DEVELOPMENT AND CHARACTERISATION OF ADVANCED ENERGY STORAGE DEVICES FOR STATIONARY APPLICATIONS

Ashkan Kavei

Department of Earth Science and Engineering

Imperial College London

Supervisor: Prof. Nigel P Brandon

April 2020

SUBMITTED IN PARTIAL FULFILMENT OF THE REQUIREMENTS FOR THE DEGREE OF DOCTOR OF PHILOSOPHY IN ENGINEERING AND THE DIPLOMA OF IMPERIAL COLLEGE

Plagiarism Declaration

Plagiarism declaration I hereby declare that all of the work presented in this thesis except that which is appropriately acknowledged and referenced as such is my own, and that it has not been submitted in fulfilment of the requirements of any other degree at Imperial College London or elsewhere.

Ashkan Kavei

31st April 2020

Copyright

Abstract

The growing demand for energy and increasing attention on environmental challenges outline the requirement to optimise the electrical grid, and gradually replace the current energy sources with sustainable and renewable alternatives. The electrical grid at present forms an enormous infrastructure to instantaneously transmit the primary generated energy to the end users. However, due to the lack of storage capabilities to store the primary energy, the existing grid must conform to the oscillations due to the changes in customer demand. Grid-scale energy storage devices such as redox flow batteries (RFBs) have emerged as key technologies to accommodate the transition from finite fossil fuels to renewable energies and improve the sustainability of the electricity generation sector. This thesis focuses on characterisation and development of novel RFB systems for energy storage applications.

Firstly, a novel Regenerative Fuel Cell (RFC) utilising inexpensive manganese electrolyte in the cathode and facile hydrogen in the negative electrode has been examined. To understand the impact of different materials on the performance of the Regenerative Hydrogen Manganese Fuel cell (RHMnFC), various membrane electrode assemblies are tested. it was found that carbon felt as the liquid half-cell electrode, Carbon paper with Pt loading of 0.3 mg/cm^2 as the hydrogen electrode and Nafion 117 as the membrane yield the highest performance in the cell. This configuration of the membrane electrode assembly yields energy efficiencies in the range of 77% and 90%, while charging and discharging the cell at current densities in the range of 20 mA/cm^2 to 100 mA/cm^2. Furthermore, viability of scaling-up is studied, where a techno economic study has been carried out to explore the feasibility of this novel chemistry compared to the conventional energy storage devices, with an estimated 37% reduction in the levelized cost of storage compared to the all-vanadium RFB system.

RFBs with manganese redox active species have hitherto been little investigated for energy storage applications due to the instability of Mn^{3+}. To improve the lifespan of the novel RFC, an electrolyte composition, consisting of manganese as the redox active species and Ti^{4+} as an additive that supresses the Mn^{3+} disproportionation, is presented. The performance of this electrolyte composition is tested, to identify the impact of the operating conditions, such as the operating temperature of the cell, rest time between half-cycles and overcharging the electrolyte, on the stability of the RHMnFC system. This set of experiments reveals that, although the presence of Ti^{4+} supresses the Mn^{3+} disproportionation reaction, precipitation of MnO_2 is an unavoidable phenomenon. Following these findings, a method to regenerate the inevitable precipitation of MnO_2 in the electrolyte is proposed and the practicality of the method is experimentally tested and proven.

Secondly, an in-situ method was developed using X-ray radiography and tomography techniques to enable the visualisation and characterisation of electrodeposited zinc (Zn) in Zn-RFBs. Zn-Based RFBs are promising technologies for energy storage applications. However, there are a number of challenges that must overcome prior to the commercialisation of these systems. The main obstacle is the dendritic growth of Zn on the anode electrode. This part of the thesis focuses on developing a method to investigate the mechanisms which effect the morphology of the zinc deposit. This method consists of designing a novel three-electrode cell with the capability to operate under different conditions, to investigate the effect of current density and electrolyte flow on the morphology of the deposited Zn. By monitoring the real-time formation of Zn deposits and reconstructing the morphology of the deposits, the mechanisms which supresses the dendritic growth of Zn deposits have been found and analysed. Quantitative analysis showed that operating under dynamic flow improved the morphology of the electrodeposited Zn and gave a compact deposit.

Acknowledgments

First and foremost, I would like to express the greatest gratitude to my main supervisor Prof. Nigel Brandon for providing me with the support and guidance to complete my thesis and giving me the opportunity and freedom to develop as an engineer. It has been a privilege to have worked with him over the past five years on different projects. I would also like to thank my associate supervisor Dr. Billy Wu for always providing the support I needed with his patience, kindness and knowledge throughout my Ph.D. This thesis would not have been possible without his efforts.

I reserve a special thank you for Dr. Vladimir Yufit, who believed in my abilities and provided endless ideas during my tenure in Imperial College. He provided endless helps to develop and pursue my ideas throughout the course of my Ph.D. Working alongside him and learning the fundamentals of the electrochemistry from him helped me to achieve this feat. Gratitude is extended to my colleague, friend and unofficial supervisor, Dr. Dami Taiwo for his support, guidance and unwavering efforts during this adventure. Without his dedication and knowledge of microstructural analysis, and his effort and contribution It would have not been possible to finalise the work in final chapter. Also, I would like to thank Dr. Farid Tariq for introducing me to the group and always supporting me in both academic and personal life and making the group enjoyable place to work every day.

In addition, special thanks to the collaborators from the Electrochemistry group in the Dept. of Chemistry, where my journey at Imperial College started, in particular Dr. Rubio-Garcia and Prof. Anthony Kucernak for all their supports and innovative ideas during my Ph.D. Their knowledge of chemistry and electrochemistry is a gift that I was lucky to learn from. An additional thank you goes to the Electrochemistry Science and Engineering group in Dept. of Earth Science and Engineering: Moshiel Biton, Bowen Song, Yuhua Xia, Andrea Gayon Lombardo, Charlie Wood, Catalina Pino Munoz, Graham Stevenson, Barun Chakrabarti, Aayon Banerjee, Paul Boldrin and Enrique Ruiz Trejo for their encouragement throughout my journey in Imperial College.

The staff in the Dept. Earth Science and Engineering: Jackie Hughes, Amanda Allotey, Emma Watson, Katie Rycraft, Samantha Symmonds, Jason Hoadley, Christopher Woodsford have been of great help on many occasions and treated me like family. Gary Jones and Graham Nash, the engineers in the department, who have always offered me best advices to deliver my design ideas and helped me to manufacture these. Zacharias Zacha and Geraldo Neto, friends and colleagues who always welcomed me to their office and solved my problems on the spot.

Alexander Griffiths and Sope Badejo have been a constant source of support and amusement and I am very lucky to have shared my Ph.D journey with such enthusiastic and good natured scientists. An

extra thank you to Alexander Griffiths who, despite working on his papers, took the time to read an early draft of every chapter of this thesis and gave an immensely detailed feedbacks, words are short to describe how grateful I am for his helps.

Thanks are of course due to Tim von Werne, CEO at RFC Power, who introduced me to the technological aspect of the energy storage and helped me to understand the connection between academic research and industry. I have had the benefit of his support for a wide variety of projects beside my Ph.D project.

Finally, I would like to express my sincere gratitude to my family for their encouragement and genericity over the years and embracing my achievements and failures with love. Despite the long distance, and not being able to see them for a very long time, their tireless support and patience, as well as their wisdom, have been a great example for me.

To my parents, Ghassem and Mahin

Table of Contents

List of Figures

List of Tables

List of Abbreviations

AC	Alternating Current
AEM	Anion Exchange Membrane
AFM	Atomic Force Microscope
ARPA	Advanced Research Projects Agency
BP	British Petroleum
CAPEX	Capital Expenditure
CC	Constant Phase Elements
CDR	Current Density Ratio
CE	Coulombic Efficiency
CL	Catalyst Layer
CP	Carbon Paper
CPE	Constant Phase Elements
CRF	Capital Recovery Factor
CT	Computed Tomography
CV	Cyclic Voltammetry
DC	Direct Current
DHRE	Dynamic Hydrogen Reference Electrode
DHSE	Dynamic Hydrogen Standard Electrode
EDX	Energy Dispersive X-Ray Spectroscopy
EE	Energy Efficiency
EIS	Electrochemical Impedance Spectroscopy
ESS	Energy Storage System

FC	Fuel Cell
FDK	Feldkamp Davis Kress
FIB	Focused Ion Beam
GC-MS	Gas Chromatography–Mass Spectrometry
GDA	Gas Diffusion Layer
GDL	Gas Diffusion Media
GDM	Global Energy Outlook
GEO	Global Energy Outlook
GHG	Greenhouse Gasses
HER	Hydrogen Evolution Reaction
HFR	High Frequency Resistance
HHNL	Hocherl & Hackle Nl
ICP-MS	Inductively Coupled Plasma Mass- Spectrometry
IEA	International Energy Agency
IEC	Ion Exchange Capacity
IEM	Ion Exchange Membrane
LCOS	Levelised Cost of Storage
MEA	Membrane Exchange Assembly
MEP	Membrane Electrode Production
MPL	Microporous Layer
NASA	National Aeronautics and Space Administrations
NL	National Laboratory
NMR	Nuclear Magnetic Resonance

OCP	Open Circuit Potential
OCV	Open Circuit Voltage
OPEX	Operation Expenditure
PEM	Proton Exchange Membrane
PEMFC	Proton Exchange Membrane Fc
PHP	Pumped Hydropower
RDE	Rotating Disk Electrode
RFB	Redox Flow Battery
RFC	Regenerative Fuel Cell
RHMnFC	Regenerative Hydrogen Manganese Fuel Cell
RHVFC	Regenerative Hydrogen Vanadium Fuel Cell
RPM	Round Per Minuet
SA	Surface Area
SEM	Scanning Electron Microscope
SHE	Standard Hydrogen Electrode
SI	International System of Units
SOC	State of Charge
SSA	Specific Surface Area
TDC	Three Dimensional Crystallite
UK	United Kingdom
USA	United States of America
UV-Vis	Ultraviolet – Visible Spectroscopy
VE	Voltage Efficiency

VRFB	Vanadium Redox Flow Battery	
XCT	X-Ray Computed Tomography	

Latin Symbols:

A	Cross sectional area	m^2
C	Capacitance	C
C_O	concentration of oxidant	mol/L
C_R	Concentration of reductant	mol/L
CPE	Constant phase element	$\Omega^{-1}s^n$
d	Diameter	m
d_e	Hydraulic diameter	m
D_{hc}	Hydraulic diameter in channel	m
D	Diffusion Coefficient	m^2/s
E	Energy	Wh
E^0	Standard Redox Potential	V
E_{OCP}	open-circuit potential	V
e^-	Electron	$-$
F	Faraday constant	$96{,}485\ C/mol$
f_c	Friction resistance	N
ΔG	Gibbs free energy	J
H^+	Proton	$-$
h	Height	m
I	Current	A
I_o	Intensity of x-ray beam	A

i_{limt}	Limiting current	A
j	Complex component	$-$
j_{lim}	Limiting current density for flowing electrolyte	A/m^2
$j_{lim(0)}$	Limiting current density for static electrolyte	A/m^2
K_{form}	Minor resistance coefficient	$-$
L	Length	m
L_c	Length of Channels	m
M	Molar mass	Kg/mol
M_i	Molar mass of species i	Kg/mol
m_i	Mass of species i	g
N	Number of Moles	$-$
n	Number of electrons	$-$
O	Oxidant species	$-$
P	Power	W
p	Pressure	Pa
Q	Flow rate	m^3/s
Q	Capacity	Ah
R	Reductant Species	$-$
R	Universal gas constant	$8.314\ J/mol.K$
R	Resistance	Ω
Re	Reynold's number	$-$
R_s	Series resistance	Ω
R_{CT}	Charge transfer resistance	Ω

R_{diff}	Diffusion resistance	Ω
S	Specific area of Reaction	m^2/m^3
SG	Specific Geometry	$-$
Sc	Schmidt number	$-$
Sh	Sherwood number	$-$
s_i	stoichiometric coefficient	$-$
T	Temperature	K
T_d	Deposition time	s
T_R	Rest time	s
t	Time	s
V	Voltage	V
$\hat{Z}$	Complex resistance vector	Ω
Z_{im}	Imaginary resistance	Ω
Z_R	Real Component resistance	Ω
Z_{wa}	Warburg impedance	Ω

Greek Symbols

σ_a	Warburg parameter	$-$
ρ	Density	Kg/m^2
μ_i	electrochemical potential of the redox species	V
η_E	Energy Efficiency	$\%$
η_v	Voltage Efficiency	$\%$
H_c	Coulombic Efficiency	$\%$
μ	Linear velocity	m/s

η_a	Activation polarisation	V
η_c	Mass-transport Polarisation	V
η_{ohm}	Ohmic Polarisation	V
$\boldsymbol{v}$	Kinematic Viscosity	m^2/s
θ	Phase shift	$-$
$\boldsymbol{\delta_P}$	Pulse diffusion layer	m
$\boldsymbol{\delta_S}$	Stagnant diffusion layer	m
$\boldsymbol{\delta}$	Length of diffusion layer	m

Chapter 1 Introduction

1.1 Overview

Over the past two decades, the global energy landscape and its environmental challenges have experienced drastic changes. Analysis and projections of the world's energy consumption in 2018 show a 2.9% growth in compare to 2017. This represents the fastest growth in the past decade, where an average 1.5% increase per year was recorded [1]. It is predicted that world primary energy supply will increase by 20%-30% beyond 2040 [2]. This growth is led by the growing population and economical changes around the globe.

According to Global Energy Outlook (GEO) 2019, 82% of global primary energy demand was supplied by fossil fuels in 2015 [2]. British Petroleum (BP) analysis has also shown that utilisation of fossil fuels has contributed to 64% of the global greenhouse gasses (GHG) emissions, which is the main contributing factor to global warming [1]. Global warming, one of the main challenges of the century and the main factor associated with the risk and significances of the climate change, has resulted in increasing attempts by governmental authorities and scientific communities to move towards renewable energies.

The growing demand for energy and the increasing attention to environmental challenges, has brought in great attention and resulted in changes to the current polices across the globe. These changes not only address the requirements to optimise the usage of the finite reserves of fossil fuels, but also it outlines variety of approaches to gradually replace energy generation sources with sustainable and renewable alternatives. To accommodate these changes, increasing volume of renewable energy sources, such as wind and solar, has been developed and employed globally. In 2016, 24.6% of the United Kingdom's (UK) gross energy consumption was generated from these sources [3]. The report on the energy outlook, which explores the forces shaping the global energy transition, suggests that less than 10% of world primary energy was generated by renewable energies sources in 2017 [4]. Furthermore, BP by taking different transition scenarios into consideration, including how fast the transition from generating the global energy from fossil fuels to generating by renewable energies might occur, have predicted that the deployment of renewable energy sources will exceed 30% of the overall energy supply across the world by 2040 (Figure 1-1) [5]. International Energy Agency (IEA) has estimated the changes in generating electricity from renewable energies between 2018 and 2040 and suggested a 24% increase of renewables-based power generation by 2040 [6].

Within recent years, there has been a significant success in the transition from fossil fuels to renewables. However, solar and wind, as intermittent renewable resources, come with unique drawbacks. These challenges are mainly due to the changes in climate conditions which affect the-energy frequency fed into the grid. Therefore, to overcome these barriers, added flexibility is necessary for the entire system [7]. In order to remedy the demand response, the capacity to balance the sudden supply and demand must be introduced. This need is where energy storage comes into play.

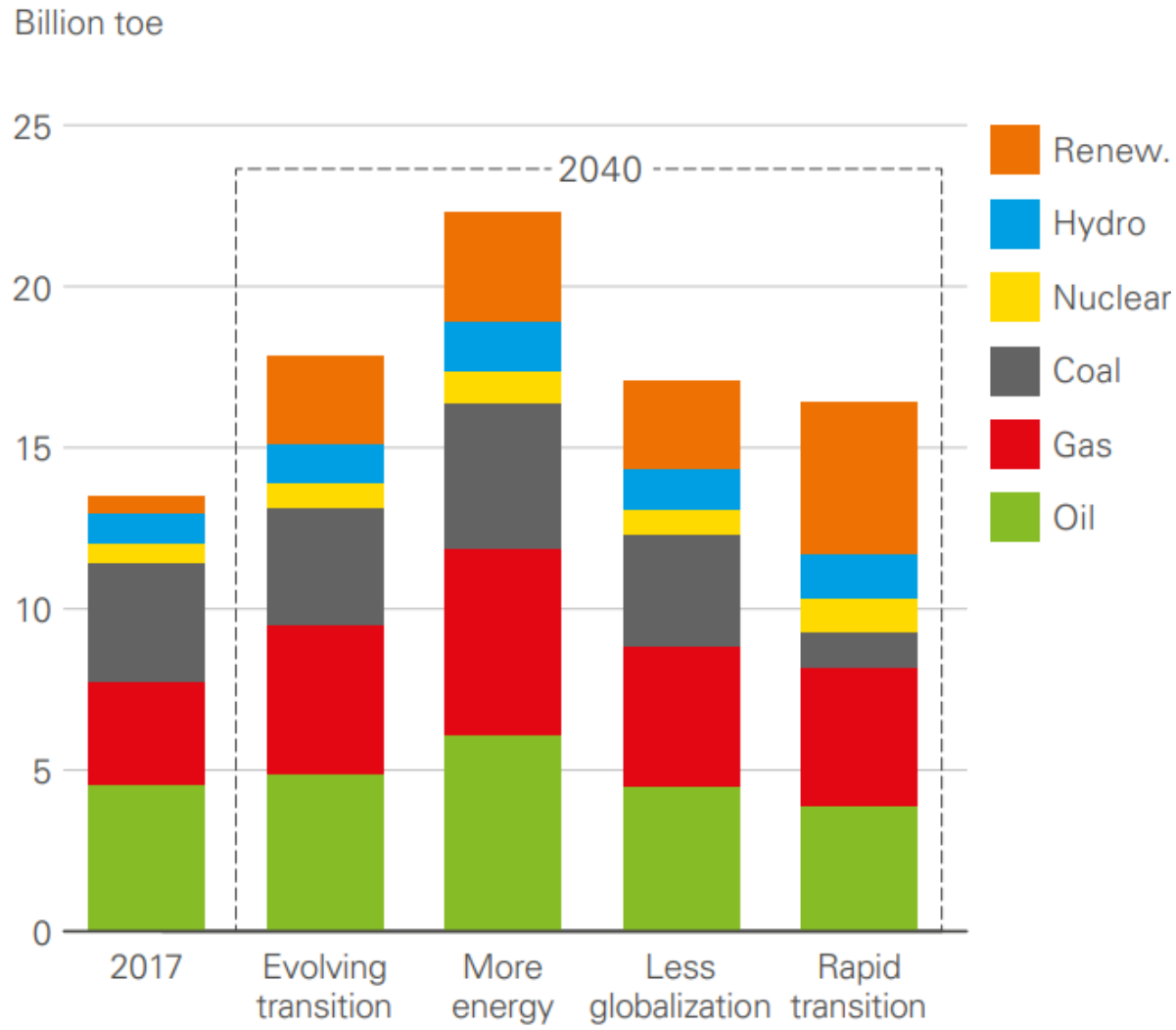

Figure 1-1: The energy outlook in 2040 which considers a range of scenarios to explore the contribution of different energy sources to primary energy consumption by fuel [5]

Energy storage, apart from its potential for storing the energy generated from renewables, can also be implemented for seasonal storage, daily peak energy shifting and grid support [8]. Currently, with significant increases in the use of renewable energy sources and the growing demand for energy in economically advanced countries, such as Germany, UK and U.S., there is an increasing challenge in managing the electrical grid systems which lack the capacity to store and provide peak energy

demands [9]. Therefore, the importance of energy storage systems becomes paramount to be able to accommodate these peaks.

Different types of energy storage technologies can be deployed based on their storage time. These technologies consist of: thermal, mechanical, chemical and finally electrochemical [10]. However, since factors such as technical characteristics and cost of some of these technologies are not well defined, it makes the implementation of these technologies challenging. According to Table 1-1 [8,10], which shows various available technologies and their properties, different systems can be employed based on their operational principles. Among these technologies, pumped hydropower (PHP) is the main current form of storing energy at the grid scale [11]. Although PHP facilities have reached a mature and commercially available stage, expanding these facilities, in accordance to the predicted future energy generation and storage growth, will face challenges due to the limited available sites [12].

Table 1-1: Energy storage technolgies based on their charastrictics and cost [8,10]

Energy Storage Technologies				
	Response Time	Efficiency %	Daily Discharge %	Cost per cycle $/kwh/Cycle
Pump Hydropower	Seconds - minutes	70-85	0.5	0.01-0.1
Compressed Air	minutes	50-75	10	0.01-0.1
Flywheel	Milliseconds – minutes	85-98	5-20	0.01-1
Supercapacitors	milliseconds	80-90	10-30%	0.1-1
Thermal Cycle	Seconds - minutes	55-80	1	0.01-0.1
Electrolyser	minutes	40-55	0	1-10
Lithium-ion Battery	milliseconds	80-90	0	0.1-1
Lead-acid Battery	milliseconds	65-80	20	0.1-1
Redox Flow Battery	milliseconds	65-85	0	0.01-0.1

Colour Codes	Mechanical	Electrical	Thermal	Electrochemical

Therefore, in order to store the energy generated from renewable sources, an efficient and reliable storage method must be implemented. For residential and commercial end-use, the identified methods must also be able to meet combination of criteria such as: efficiency, lifetime, flexibility in size and safety. In this context, electrochemical energy storage (ESS) technologies offer the required measures to meet these criteria [13]. ESS is a method of storing energy by converting the electrical energy into chemical energy by a reversible electrochemical oxidation and reduction reaction [14].

Among various energy storage technologies rechargeable batteries offer a variety of advantages, such as site independency, high efficiency, fast response and high power and energy density. A number of rechargeable batteries have been demonstrated for energy storage purposes, including conventional secondary batteries, metal-ion batteries, metal-air batteries, high temperature batteries, and redox flow batteries (RFBs).

Apart from the aforementioned benefits of rechargeable batteries, RFBs also possess some unique advantages, such as modularity, independence of power and energy, tolerance of deep charge and discharge, very little self-discharge, long cycle life, low cost and enhanced safety. The modular design of stacks and systems allows RFBs to be scaled up easily. The power and energy capacity of RFB systems are associated with cell size (active area) and tank size (volume of electrolytes) respectively and independently, allowing customising the RFB systems according to their application. RFBs can undergo deep charge and discharge operations without adverse effects on the system. The self-discharge of RFBs is small because the anolyte and catholyte are stored separately in two tanks which avoids the mixing and neutralization of these two electrolytes. Since electrolytes are stored outside the cell, the potential amount of energy generated during accidents of RFB systems are relatively low which therefore cause less hazards. Lastly, RFBs are expected to have a lifetime of up to 20 years subject to the use of durable membrane technologies, whereas the lifetime of Li-ion batteries is much shorter [15].

1.2 Motivation

In this work the characteristics of novel energy storage devices for energy storage application will be investigated. An initial technological study will be carried out on a novel Regenerative Hydrogen Manganese Fuel Cell (RHMnFC). This part of the thesis will focus on further understanding the performance of the RHMnFC, first developed by Rubio-Garcia et al. [16], by optimising the cell performance and identifying the limits associated with this technology. Later, another type of flow battery with the potential to provide secure and affordable access to clean renewable energy will be studied. In this work a novel characterisation method will be developed and demonstrated to evaluate the growth of zinc dendrites in zinc-based flow batteries. Based on the findings from the investigation of the RHMnFC system (in Chapter 4 and Chapter 5), the novel characterisation technique developed to study the dendritic growth of Zn redox couples on the electrode (Chapter 6), can be optimised to further analyse the precipitation of MnO_2 in the RHMnFC electrolyte.

Based on detailed reviews on current state-of-the-art RFBs, despite the technological success of the vanadium redox flow batteries or other redox flow batteries chemistries reviewed in detail in Chapter 2, their widespread adoption is hindered by their capital cost. The current price of RFB systems, with

4 hours discharge capacity, is over 3.5 times higher than the price target recommended by The Department of Energy in 2018 [17]. Therefore, the overarching focus of this thesis will aim to develop a novel energy storage device that offers higher performance as well as lower material cost (electrolyte and component), and then develop this device, showing the progression from an experimental small cell design to a larger cell.

The thesis has the following structure:

Chapter 1: This section presents the necessity of moving towards renewable energies, as well as challenges associated with these changes. This chapter will also investigate methods of storing the energy generated from renewables, and it will further identify the need for storage systems.

Chapter 2: Initially, different concepts, principles and chemistries of RFBs will be the focus of this chapter. Then a comprehensive review on RFB components is carried out. This chapter (Chapter 2) also reviews the current state-of-art RFBs, through which the focus of this thesis is defined based on the identified gaps in the literature. Furthermore, Section 2.6 also highlights the fundamental theory, which is essential in order to understand RFBs.

Chapter 3: This chapter introduces the experimental setups, conditions and methods used to study the two identified RFB technologies. The first two sections of Chapter 3 (Sections 3.1 and 3.2) will focus on the methodology used in this work to investigate the factors effecting the performance of the RHMnFC. Section 3.3 will illustrate a novel characterisation technique, which enables the visualisation and quantification of the growth of metal deposits on a substrate.

Chapter 4: By establishing the research question that will be answered in this chapter, the methodology and materials that are used to optimise the RHMnFC performance will be described. Further on, results obtained from experiments will be analysed to determine the optimum achievable performance using Hydrogen-Manganese chemistry.

This work will also try to investigate the feasibility of scaling up. For this purpose, the performance of flow battery in a single 150 cm^2 unit cell will be tested and analysed. In this part, steps to successfully move from a small 5 cm^2 cell towards a large 150 cm^2 will be investigated. This consist of demonstrating a design, which takes into consideration the requirement to accommodate the necessary engineering properties to make a stack. Also, the pressure drop associated with this design will be calculated. Results obtained from experiments on the performance of the RHMnFC will be used to calculate the levelized cost of storage for this technology, and feasibility of this technology for energy storage applications will be investigated compared to the existing RFB technologies.

Chapter 5: As demonstrated in Chapter 4, the RHMnFC operates over certain voltage range. However, due to internal reactions within the electrolyte, there are limitations that result in lower efficiency in the cell. These limits will be identified by reviewing the current works in relation to the Mn electrolyte. According to identified limitations, a novel method will be demonstrated, where the electrolyte can be regenerated electrochemically. Methods and experiments to recycle the electrolyte will be described and results will be analysed.

Chapter 6: This part of the thesis will demonstrate a novel characterisation technique, developed to study the morphology of dendritic growth in Zinc secondary flow batteries. Initially, challenges in regards with dendritic growth in these batteries will be reviewed. By identifying the gaps in this area, detailed design of experiment of three electrode cell will be described. Finally, recorded data will be analysed and quantified.

Chapter 7: As the final chapter of this thesis, the main findings will be concluded and suggestions for future work will be presented.

Chapter 2 Flow Batteries: A Review

In this chapter, an overview of various flow battery technologies will be explored. These electrochemical devices will be categorised based on their principle and configuration of operation. Additionally, advantages and challenges associated with each chemistry will be investigated. This comparison will be followed by introducing each component in the technologies of interest in this work. Finally, necessary critical terms and the fundamentals in relation to flow batteries will be defined and described.

2.1 Types of Flow Batteries

Among electrochemical systems, RFBs represents one of the most promising technologies for energy storage applications [13]. RFBs are electrochemical devices, which exploit the chemical energy of redox couple species in solution by redox reaction [15]. Redox flow batteries can be divided into two categories, consisting of all-liquid RFBs and Hybrid RFBs. Currently, some of the technologies following these two concepts, have reached a commercial stage and are deployed in combination with different renewable energy sources, while, more recently developed systems, illustrated in the diagram in Figure 2-1, are still in the research and development (R&D) stage [18].

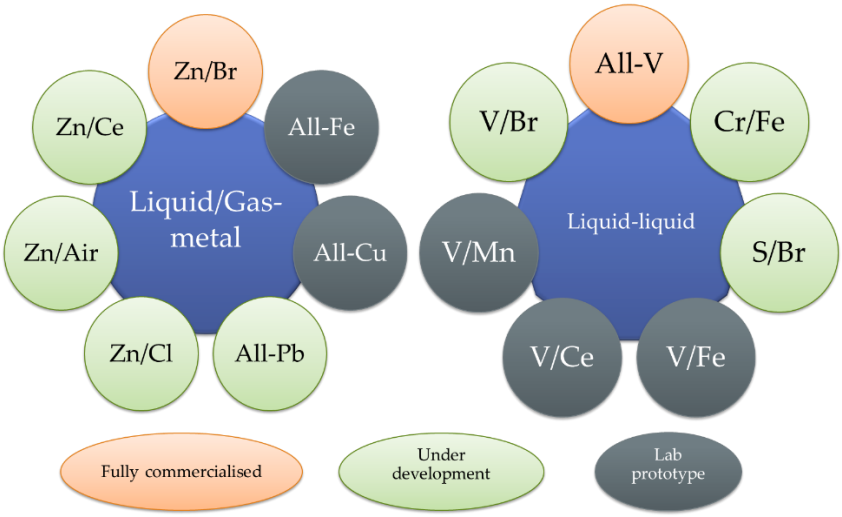

Figure 2-1: Development stage of different flow battery technologies

2.1.1 All-Liquid RFB

Since the proposition of the first RFB by Thaller [19], different chemistries, mainly focusing on inorganic redox species have been developed. This type of RFB contains two soluble redox metals, stored in two separate reservoirs. Generated energy is stored and released in the form of electricity, through oxidation and reduction reactions in the electrochemical cell. RFB electrochemical cell configurations consist of three main compartments: anode and cathode electrodes, and an ion exchange membrane

(IEM). These compartments are discussed in more detail in section 0. In these electrochemical cells, anode and cathode refers to the half cells, where oxidation and reduction occurs respectively during discharge [a].

Energy conversion within the all-liquid RFBs, as illustrated in Figure 2-2, is achieved through reversible electrochemical reactions. According to oxidation and reduction reactions [b], stated in eq. 2-1 and eq. 2-2 , both redox metal species in the anolyte and catholyte participate in the electrochemical reactions. In this electrochemical cell, the direction of electron transfer from anode to cathode is dependent on whether the cell is being charged or discharged. While charging the cell, electron transfer occurs from catholyte to anolyte, and during discharge, the reverse process occurs. During both charge and discharge, charge carrying species migrate through the IEM. The main advantage of these type of RFBs is their capability to decouple power and energy densities. The energy density of the system is determined by the size of electrolyte reservoirs, whereas the power density of these electrochemical cells depend on the size of the active area and number of cells [15,20].

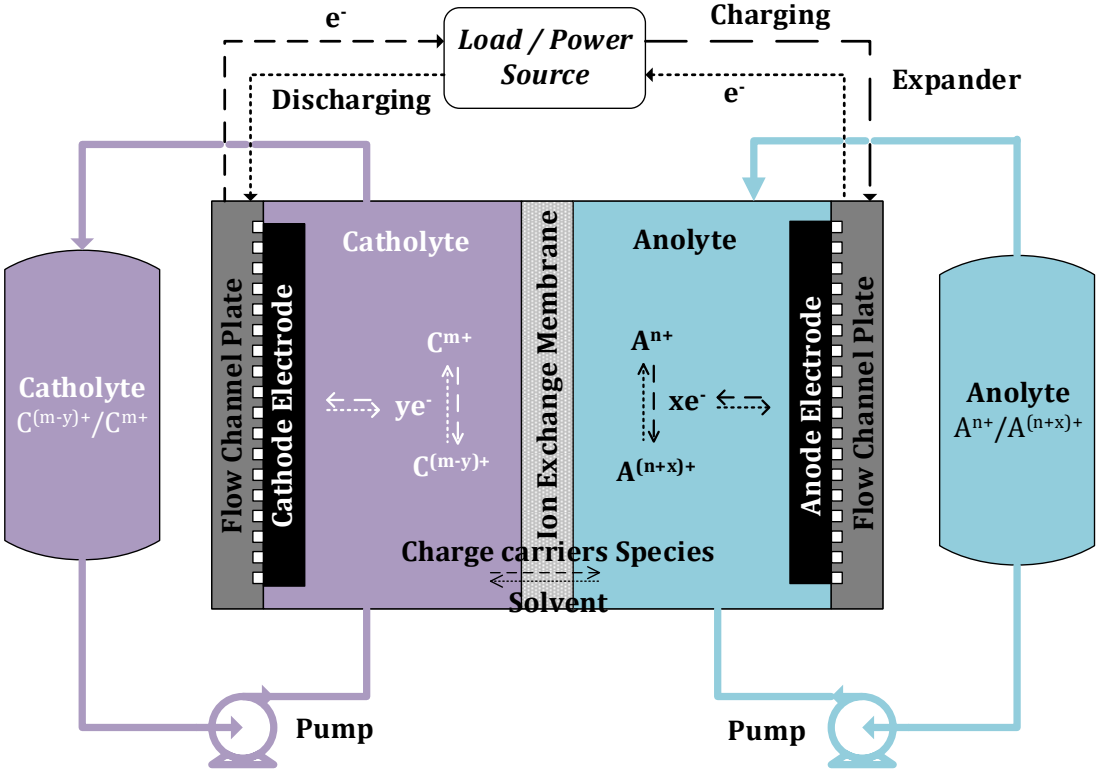

Figure 2-2: Schematic of all-liquid flow batteries

Anode Electrode: $$A^{n+} \rightleftharpoons A^{(n+x)^+} + xe^- \quad \text{eq. 2-1}$$

Cathode Electrode: $$C^{m+} + ye^- \rightleftharpoons C^{(m-y)^+}, m > y \quad \text{eq. 2-2}$$

[a] Throughout this thesis, these terms will be used based on this definition.
[b] Reactions are written: Discharge left to right, and charge right to left

Since the development of the first RFB concept, several systems, utilising different redox species, have been evaluated by different groups. However, among all the developed systems, only the all-vanadium flow battery (VRFB) proposed by Skyllas-Kazacos et al. [21] has reached commercial fruition. This system had been regarded as a promising technology by using all four oxidation states of this single element as an anolyte and catholyte. VRFBs, in comparison to other investigated systems, offers the elimination of cross-contamination and irreversible capacity losses [18]. This system will be reviewed in more detail throughout this thesis.

2.1.2 Hybrid RFBs

Beside all-liquid flow batteries, there are systems that involve non-aqueous reactants within the cell. This concept of RFBs, as various types are illustrated in Figure 2-3, are referred to as hybrid RFBs, which consist of gas-liquid and solid-liquid flow batteries [22].

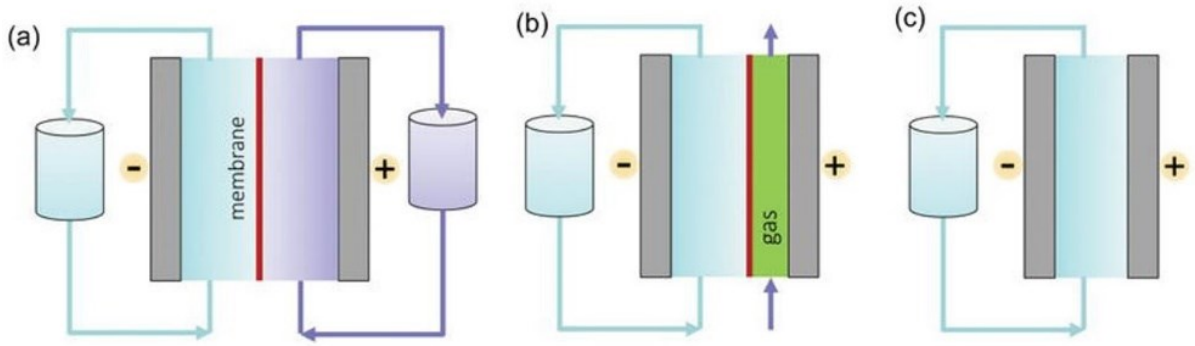

Figure 2-3: simplified schematic of hybrid RFBs [23] a) all liquid RFB, b) gas-liquid and c) solid-liquid

In hybrid flow batteries such as Zinc-cerium and Zinc-bromine systems, zinc (Zn) metal deposition on the anode electrode occurs during charge, where the other side consist of one of the soluble flowing electrolytes. Unlike the conventional concept, energy capacity in this configuration depends on the available electrode surface area to accommodate the metal deposition [24]. Although, zinc-based batteries exhibit voltage stability during charge and discharge, they are hindered by the dendritic growth of the zinc deposition at anode electrode [25]. In general, zinc batteries, due to their low cost and their abundance in ores, have the essential merits to be used as the next generation energy storage devices, and therefore, a part of this project, the growth of Zn dendrites will be investigated.

Another type of hybrid flow battery that has attracted significant scientific interest for energy storage applications, is the gas-liquid RFB. In this type of hybrid RFB, gases such as O_2, Cl_2 and H_2 is used as the reactant [23]. This concept, in comparison to conventional RFBs, enhances the cell lifetime by eliminating challenges such as mass transport limitation and cross-contamination associated with liquid-liquid RFBs. This configuration will be the main focus of this work, while similar systems will be investigated in more depth for comparison in next chapters.

2.2 Redox Flow Battery Compartments

In this section, the basic structure and components of a unit cell of RFB will be discussed. This section will focus to identify the purpose of each component and the mechanisms associated with each part that result in losses in the overall system.

The initial concept of the RFC was described in section 2.3, and was illustrated in the RFC schematic in Figure 2-6, these hybrid RFBs can be categorised into three sections, consisting of negative electrode (anode), a selective ion conductor (IEM) and a positive electrode (cathode). It must be noted that, in rechargeable batteries, the polarity of the electrodes depends on the direction of electrons. In any electrochemical cell, the electrode that oxidation occurs is defined as anode, and reduction occurs in the cathode. In this work, negative and positive electrode are identified following the discharge mechanisms.

RFBs and RFC compartments, similar to proton exchange membrane fuel cell (PEMFC) configuration, consist of endplates for mechanical support, anode, cathode and membrane exchange assembly (MEA) compartments. As demonstrated in Figure 2-4, each of these three compartments include different components. RFC assembly components are explained in more detail below.

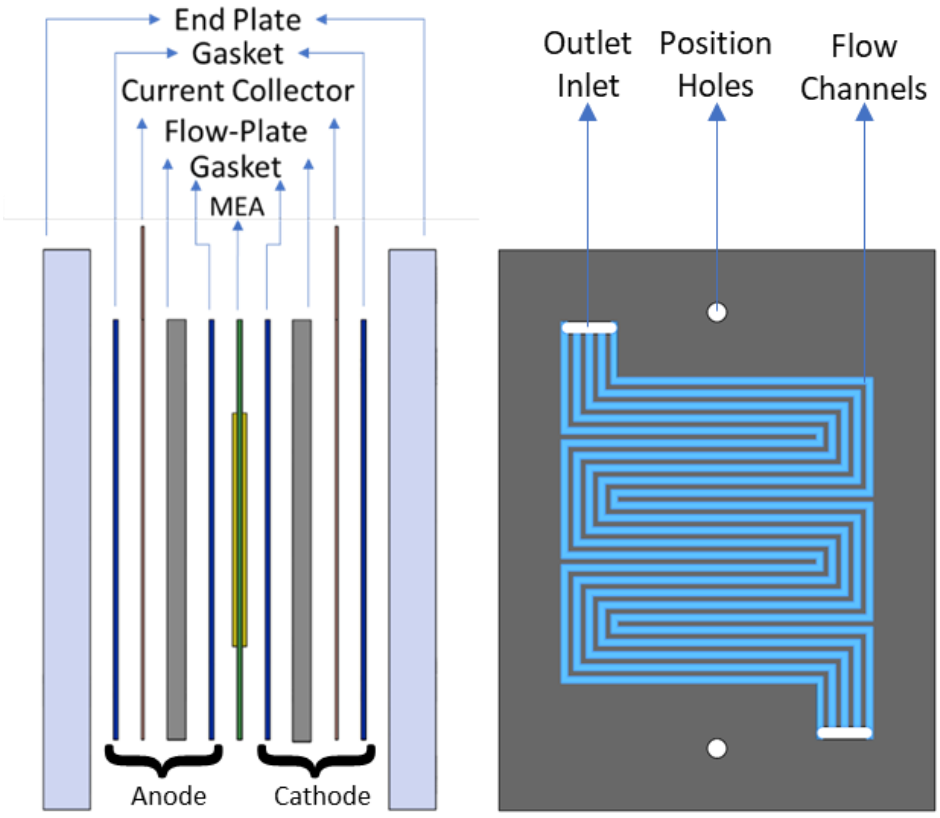

Figure 2-4: Conventional Redox Flow Battery cell and its serpentine flow design

- **Anode electrode assembly** consist of a highly conductive metal (such as copper) as a current collector, a flow plate[c] to distribute the supplied gas uniformly to the active surface area, gaskets to provide sealing to the assembly as well as uniform compression to enhance electron conductivity in the MEA.
- **Cathode electrode assembly** symmetrically to the anode, this contains the same components. However, depending on the solvent used to dissolve the redox metals and the operating voltage of the cell, it is necessary that the components in cathode electrode assembly are chemically stable in the presence of the corrosive chemicals in the electrolyte.
- **Membrane electrode assembly** is the most crucial compartment in any electrochemical cell, as the reactions in both half-cells occur in this region. MEAs consist of:
    - **Anode electrode**, similar to the material used in PEMFCs and shown in Figure 2-5, this contains three interpenetrating networks, generating the required properties, such as adequate porosity for rapid gas distribution, balanced hydrophilicity to enhance water transport during discharge, low electron resistivity and high active surface area on the catalyst layer for fast oxidation and reduction kinetics.

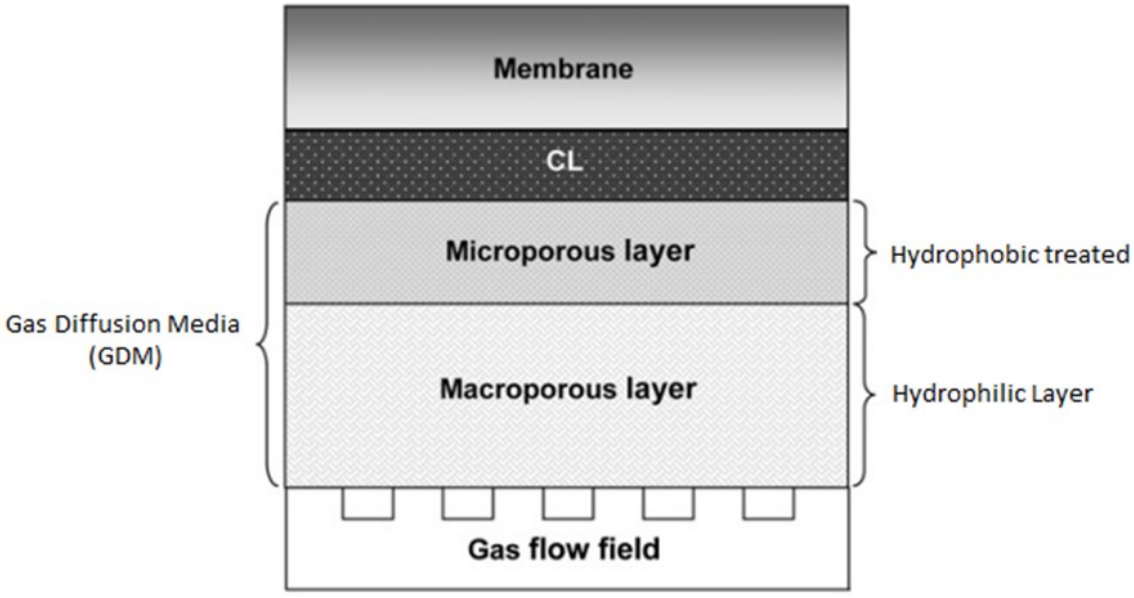

Figure 2-5: Anode electrode assembly used in PEMFC and RFCs

- **Ion exchange membrane** or separator is to ensure the division of the two reactants in both half-cells, while maintaining the continuity of the both reactions. Depending on the concept and the charge carrying ions, anion or cation exchange membrane is

[c] In some designs, this is used as current collector, as it is chemically inert.

used. In RFBs with proton being the charge-carrier ion, proton exchange membrane (PEM) is used. These polymeric membranes, while acting as a conductor to the generated ions, must act as an insulator to electrons produced during oxidation reactions.

- **Cathode Electrode** acts as liquid diffusion layer, as opposed to the gas diffusion layer used in RFC anode. Ideally, carbon-based materials, such as graphite felt, carbon paper or cloth is used in RFBs. These materials must retain their stability over prolonged periods of operation.

Understanding the effect of each compartment is critical to enhance the electrochemical performance. In particular, relating each component to the fundamental changes in performance can accelerate the optimisation of these emerging technologies. The following section (0) will discuss the current state-of-the-art related to each component in the MEA.

2.3 Development of Redox Flow Batteries

The initial concept of RFBs was introduced in 1974, in a project by the National Aeronautics and Space Administrations (NASA) [19]. In this concept, chromium (Cr^{2+}/Cr^{3+}) and iron (Fe^{2+}/Fe^{3+}) redox couples were used as anolyte and catholyte respectively. In Fe/Cr RFBs, the half-cell reactions are as illustrated in eq. 2-3 and eq. 2-4, with an overall standard cell voltage of 1.18 V vs SHE.

Anode Electrode: $$Cr^{2+} \rightleftharpoons Cr^{3+} + e^- \quad (E^0 = -0.41V\ vs\ SHE)$$ eq. 2-3

Cathode Electrode: $$Fe^{3+} + ye^- \rightleftharpoons Fe^{2+} \quad (E^0 = +0.77\ V\ vs\ SHE)$$ eq. 2-4

Overall: $$Fe^{3+} + Cr^{2+} \rightleftharpoons Fe^{2+} + Cr^{3+} \quad (E^0 = 1.18\ V\ vs\ SHE)$$ eq. 2-5

Since this system consist of two different chemistries, it results in inefficiencies such as: cross-contamination of the anolyte and catholyte, which results in irreversible capacity losses in the system. Furthermore, slow kinetics of the oxidation reaction in the anolyte, results in low power density. Since the creation of this system, different solutions, such as using catalyst on the anode [26], have been investigated to improve the anode reaction kinetics, but challenges associated with the high cost of catalyst has proven to be an important factor.

The successful development of the VRFB by Skyllas-Kazacos et al [21] demonstrated a promising system, where it had the potential to be used in various applications, consisting of power quality, load-levelling and most importantly technological capacity to be coupled with other renewables [24,27]. This concept benefits from utilising a single element in four different oxidation states, consisting of V^{2+}/V^{3+} in the anolyte and V^{4+}/V^{+5} in its catholyte [18,28]. Therefore, VRFB benefits from using the same redox couple

species in both half cells, such that the electrolyte can be regenerated in case of cross-contamination. This concept maintains an overall reaction shown in eq. 2-8, with standard potential of 1.26 V vs SHE.

Anode: $V^{2+} \rightleftharpoons V^{3+} + e^{-} \quad (E^0 = -0.26V\ vs\ SHE)$ eq. 2-6

Cathode: $V^{5+} + e^{-} \rightleftharpoons V^{4+} \quad (E^0 = +1.0V\ vs\ SHE)$ eq. 2-7

Overall: $V^{2+} + V^{5+} \rightleftharpoons V^{3+} + V^{4+} \quad (E^0 = 1.26\ V\ vs\ SHE)$ eq. 2-8

While this technology is the most developed and studied RFB, and various efforts have been made to optimise the compartments of this technology (including design, electrodes and IEM), this system still faces several challenges:

- VRFB have low specific energy density of 25-30 Wh/kg, due to low solubility of vanadium in H_2SO_4 (Sulfuric acid), which results in limited energy density [18,29].
- The installation costs of VRFB, which includes the capital and operating cost, is around $500 kW/h and 54% of the cost is due to the high price of vanadium [16,30,31].
- high oxidizing nature of V^{5+}, limits the choice of IEM and the electrodes [21,28,32].

To improve the energy density, different vanadium based flow batteries were proposed and tested. Skyllas-Kazacos et al, (2003) investigated the vanadium-polyhalide RFB [33]. In this system, with an overall redox potential of 1.30 V, VCl_2/VCl_3 and Br^-, $Cl^-/ClBr^-$ is used as the electroactive species in the-anode and cathode half-cells respectively. In comparison to all-vanadium system, where H_2SO_4 is used as the solvent medium, HCl is used in this system, which vanadium ions concentration can be as high as 3 M at room temperature. This improvement results in a higher specific energy density of 50 Wh/kg in comparison to VRFB [33,34]. Although this system could provide higher specific energy density compared to VRFB, it also faces several challenges. One of the most addressed challenges in this concept, is the rapid loss of capacity. This is caused by the transfer of vanadium ions to the cathode half-cell. However, it is possible to overcome this limitation by adding vanadium bromide to both half-cells [18]. Thus, this method of stabilising the cell, results in extra cost to the system, which makes this technology impractical for commercial uses.

Subsequently, apart from these three systems, different chemistries were tested, where each of these systems had their advantage and disadvantages. Commercialisation of low-cost systems, such as Bromine-polysulphide, with high redox potential and high specific energy density, have faced engineering challenges, due to the mixing of electrolytes, which can result in generation of heat and toxic Br_2 and H_2S gases.

In parallel with the development of the initial RFB system in 1974, two different systems were investigated in the USA [35]. The developed hybrid flow batteries, consisting of Zinc-bromine and Zinc-

chlorine demonstrated a high energy density close to 75 Wh/kg [22], which in contrast to conventional flow batteries features twice the achievable specific energy density . In these hybrid RFBs, at the anode, electrochemical reaction occurs on the surface of the electrode, where during charge, Zn is plated from the electrolyte on to the electrode. During this process, bromide is converted to bromine at the surface of the cathode which is then stored in the electrolyte reservoir [36]. Due to the electrodeposition of the Zn dendrites on the electrode, the energy density of the cell is correlated to the available active surface area on the electrode [37].

Another type of hybrid RFBs, to further reduce the material cost, was introduced by coupling a liquid electrolyte with gases. Among this type of RFBs, hydrogen or oxygen gases were combined with different chemistries [18,27,38]. However, systems using oxygen as charge carrier suffers from slow kinetics of oxygen reduction reaction, which results in a low power density [22]. On the other hand, systems using hydrogen as their anolyte have shown a promising improvement in RFB performance, as well as significant cost reduction. Hydrogen-bromine, hydrogen-iron, hydrogen-vanadium [39] and hydrogen-cerium [40] are among the hybrid RFBs with the capability of reaching the commercial targets required for RFB technologies. This concept of RFBs, which is also referred as a regenerative fuel cell (RFC), was initially introduced in 1960s [41,42]. This system was designed, following the concept of ordinary hydrogen-oxygen (air) fuel cell, for automotive applications, but due to slow reduction reaction of bromine into hydrogen bromide. However, it was soon understood that hydrogen-bromide system is more applicable for energy storage applications [41], where power density is not the main determining factor in performance.

Although, this low cost system eliminates the use of expensive catalyst for reduction reactions, this system faced drawbacks such as high ohmic resistance at high state of charge, corrosive environment due to the production of halogen vapour; and most importantly, contamination of the anode electrode due to the cross-over of bromine species [43].

Combining the findings from previous studies and technologies, Yufit et al. [39] developed a regenerative fuel cell which benefited from using low cost hydrogen as its anolyte and vanadium (V^{+4}/V^{+5}), with high standard potential (0.99 V) as its catholyte. This system, which will be discussed in more detail in Section 2.4.2, featured several advantages over different types of RFBs. This system could successfully overcome the problems associated with the cost of vanadium in VRFB, safety concerns in H_2/Br_2 systems and low power density in metal-air systems.

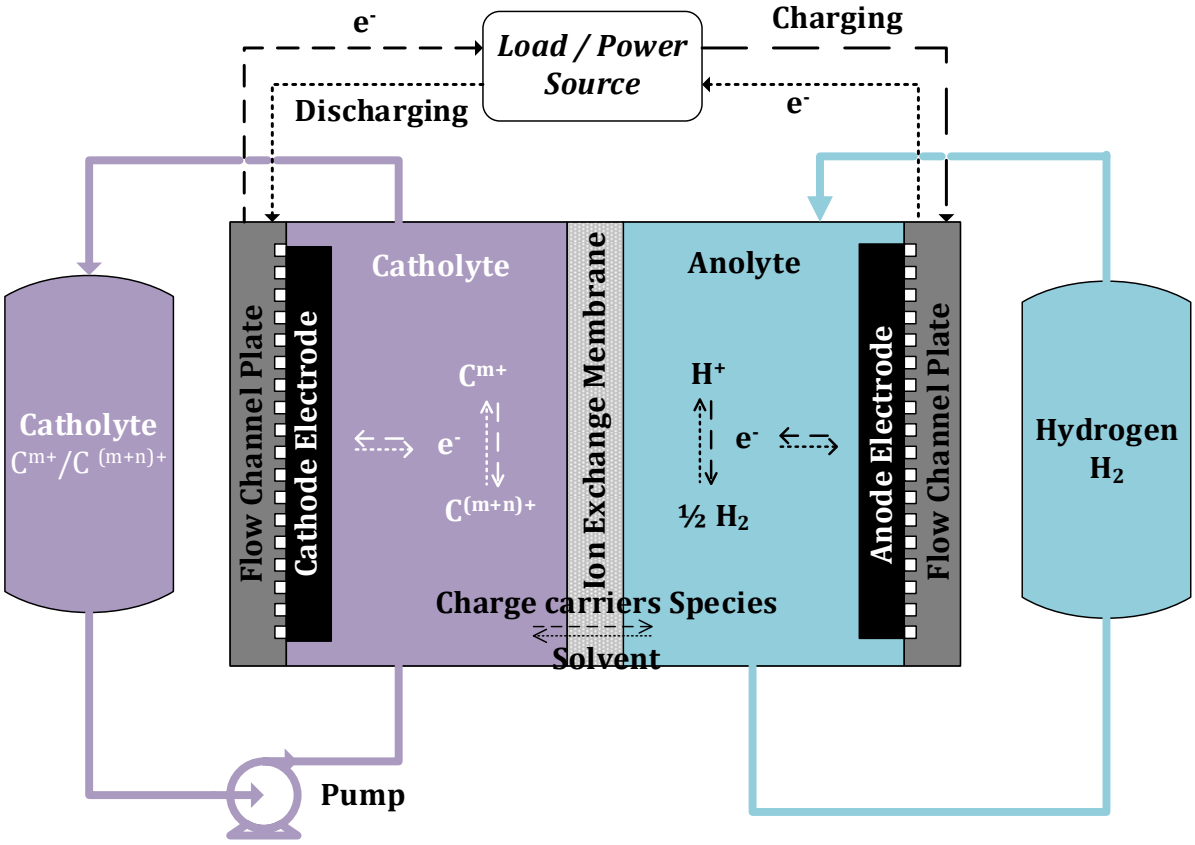

Figure 2-6: Schematic of Regenerative Hydrogen Fuel Cell

The regenerative hydrogen vanadium fuel cell (RHVFC), illustrated in Figure 2-6, maintains a 0.99 V open circuit potential. In this cell, catholyte at its V^{4+} redox state is oxidised to V^{5+} while charging. In the anode, protons migrate through the proton exchange membrane (PEM), combine with the electrons transferred through direct circuit from the cathode, and it is reduced into hydrogen. During discharge, reverse reaction occurs in the cell, where hydrogen is oxidised and V^{5+} is reduced to V^{4+} [39].

In this configuration, adverse phenomena associated with irreversible losses, caused by the crossover of the reactants are resolved. Although, crossover of the catholyte is reported, this could be successfully collected at the anode, which is pumped back to the catholyte reservoir. Furthermore, in this system, apart from storing the generated energy in the electrolyte, it is also stored in gas phase, since hydrogen is produced during charge.

The table below (Table 2-1), illustrates different available systems. This table consist of the operational parameter of each system and their reported specific energy densities. As it appears, hybrid RFBs employing Zn as their active species have higher specific energy density. This is due to the high solubility and high negative electrode potential of Zn in both alkaline-media (-1.22 V vs SHE) and acidic-media (-0.76 V vs SHE) in these electrochemical cells [44].

Among these systems, as it was described previously, some of the technologies were unable to pass the R&D stage and reach commercialisation. This was mainly due to technological challenges, such as cross-contamination, safety concerns in Br systems or the high cost of redox active species for vanadium-based flow batteries. Although the RHVFC demonstrated a significant cost and performance improvement, it still was not capable of competing with the existing systems in the market for energy storage applications.

Table 2-1: Three different types of RFB systems, including their efficiency, theoretical Potential and their specific energy density from literature [18,22,35]

Redox Species	Redox Reactions	E^0	Current Density	Specific Energy Density	Energy Efficiency
		V	mA/cm^2	Wh/kg	%
Fe-Cr [45]	$Fe^{3+} + Cr^{2+} \rightleftharpoons Fe^{2+} + Cr^{3+}$	1.18	30	15	86
V-V [13,46]	$V^{2+} + V^{5+} \rightleftharpoons V^{3+} + V^{4+}$	1.26	85	20-25	83
V-polyhalide [18]	$VCl_2 + Cl^- + ClBr_2 \rightleftharpoons VCl_3 + 2Br^- + Cl^-$	1.3	20	40	66
V-Fe [47]	$V^{2+} + Fe^{3+} \rightleftharpoons V^{3+} + Fe^{2+}$	1.02	50	-	80
V-Mn [48]	$V^{2+} + Mn^{3+} \rightleftharpoons V^{3+} + Mn^{2+}$	1.77	25	35	63
V-Ce [49]	$V^{2+} + Ce^{4+} \rightleftharpoons V^{3+} + Ce^{3+}$	1.93	22	23	68
Polysulfide-Br2 [50]	$2S_2^{2-} + Br_3^- \rightleftharpoons S_4^- + 3Br^-$	1.36	40	-	77.2
Zn-Ni [25]	$2NiOOH + 2H_2O + \mathrm{Zn} + 4OH^- \rightleftharpoons Ni(OH)_2 + 2OH^- + Zn(OH)_4^{2-}$	1.71	10	60	86
Zn-Br_2 [51]	$Zn + Br_2 \rightleftharpoons Zn^{2+} + 2Br^{2-}$	1.85	15	70	80
Zn-V [52]	$Zn + 2V^{5+} \rightleftharpoons Zn^{2+} + 2V^{4+}$	1.76	20	-	70
Zn-Cl_2 [44]	$Zn + Cl_2 \rightleftharpoons Zn^{2+} + 2Cl^-$	2.12	22	-	66
Zn-air [53]	$Zn + 4OH^- + {}^1/_2\, O_2 + H_2O \rightleftharpoons 2OH^- + Zn(OH)_4^{2-}$	1.62	20	40	72
V-air [54]	$V^{2+} + 4H^+ \rightleftharpoons V^{3+} + 2H_2O$	1.49	2.4	-	46
H_2-Br_2 [41,42,55,56]	$2HBr \rightleftharpoons Br_2 + H_2$	1.09	75	60	76
H_2-V [39]	$V^{4+} + H^+ \rightleftharpoons V^{5+} + {}^1/_2\, H_2$	0.99	70	25	73
H_2-Mn [16]	$Mn^{2+} + H^+ \rightleftharpoons Mn^{3+} + {}^1/_2\, H_2$	1.51	100	35.5	80

Colour Codes	All Liquid	Hybrid RFB (I)	Hybrid RFB (II)

Rubio-Garcia et al. [16] proposed a system in 2019, where it could further reduce the cost in comparison to RHVFC. In this system, expensive vanadium was replaced with a cheaper and the 16th most abundant element, manganese (Mn) [57]. This system also benefits from a high standard potential of 1.51 V, in comparison to the 0.99 V theoretical open circuit potential (OCP) in RHVFC. Initial tests and

experiments on this concept have demonstrated its potential to attain a potentially inexpensive system for energy storage applications. More detailed analysis of this system, including its advantages and challenges, will be investigated in Chapter 4.

This project will focus on further developing the technology, consisting of optimising the cell compartments, the range of operating conditions, effective factors on scaling up as well as a method to be able to develop a sustainable system.

2.4 Current State-of-Art RFBs

Previously, in Section 2.3, the role of redox flow batteries in grid and energy storage applications was discussed. Currently, there are a number of companies which focus on developing and deploying these technologies for energy storage applications. RedFlow Ltd., an Australian based company, has recently installed a 450kWh zinc-bromine system for renewable energy storage applications [58]. Due to the reliability of the VRFB, different companies such as RedT (UK), Sumitomo Electric Industries (Japan) and SCHMID Energy Systems (Germany) have chosen to develop this technology for commercialisation [59–61]. Sumitomo Electric Industries recently established that the VRFB has the potential for grid application by installing a 60 MWh system [61]. However, according to the targets set by Advanced Research Projects Agency – Energy (ARPA-E), in order for these technologies to be able to implementable, their capital (installed) cost must be as low as 5 cents/kWh-cycle [17].

It therefore stands to reason that the cost per kWh of the battery must be reduced over different set of variables, such as cost of the electrolyte and cost of cell components. Any new long-duration electricity storage systems can only be viable by reducing the capital cost, or improving the performance to be able to match the aggressive target [62].

To pursue a new technology within the introduced capital costs, it is necessary to improve existing RFBs from different aspects. Previously, in Section 2.1.1, it was discussed that all-liquid VRFBs are the most studied, and most commercialised system. However, according to capital cost analysis by Zhang et al. [63], it was shown that the storage time and cost of vanadium have the greatest effect on capital cost. According to different analyses, the cost of electrolytes in these systems account for 47%-53% of their capital cost [31,63,64].

It is clear that, according to these findings, in order to be able to introduce flow batteries as a potential candidate for energy storage applications, further improvements on energy density and life cycle of the current technologies must be investigated. These two parameters can only be improved by either introducing a new chemistry for higher energy density or optimising the components to extend the life cycle of the electrolyte and/or components. Improving the lifetime and achieving higher energy

density for energy storage systems will reduce the cost of storage, which is the main factor in determining the success of implementing a system for energy storage applications.

Systems such as hydrogen-bromine have lower cost per kWh, due to the higher solubility of hydrogen bromide in water (8.8M), used in one side, and utilising inexpensive hydrogen on the other side. Despite the lower cost of the reactants, extra measures are required, for safety purposes, due to the corrosivity of the HBr produced during discharge, and high vapour pressure and hazard of bromine release, for which expensive complexants need to be used to maintain safety, which increases the capital cost of the system. In addition, Pt poisoning due to adsorption of bromide on platinum is known as an critical factor in life cycle degradation of this system [55,65].

2.4.1 Organic Redox Flow Batteries

The volumetric and gravimetric energy density of the discussed RFBs are more than 4 time lower than lithium ion batteries (LIBs). The overall energy storage capacity in RFBs can be increased by using larger volumes and higher concentrations of both the anolyte and catholyte [66]. However, as discussed in Section 2.1, a rise in the cost of redox active species in RFBs, such as VRFB, have motivated researchers to investigate and develop organic redox active molecules to ameliorate the issues associated to the performance and energy density of inorganic RFBs.

The abundance of organic molecules in the earth's crust, renders these molecules to be easily scalable at a low cost, where they also provide ample advantage of engineering these molecules, via simple synthetic methods, to increase their redox potential, solubility and stability. Redox mediators such as anthraquinone, quinone and viologens have been the focus of studies at this nascent stage [67–69], where their electrochemical properties including the diffusion coefficient, exchange current density, capacity, cell voltage and reaction rate have been adjusted by additional molecular tuning in aqueous medium [70].

Quinone-based organic compounds have extensively been investigated and the merits of these materials, such as their low cost and fast kinetics have been demonstrated in different studies. Chen et al. [71] reported a peak power density of 0.4 W/cm^2 (during discharge) for a quinone-bromide redox flow battery system, comprising 9,10-anthraquinone-2,7 disulfonic acid (AQDS) and hydrobromic acid as its redox couples in the electrolytes [71]. Huskinson et al. [72] demonstrated that modifying the AQDS compound by adding two additional hydroxy groups, increases the open circuit potential of the cell by 11%, resulting in a volumetric energy density of 16 Wh/L, which is comparable to the 20 Wh/L volumetric energy density reported for all-vanadium RFBs.

Other organic redox active molecules that have gained notoriety to exploit their attractive attributes are N-methylphthalimide (NMP) and 2,2,6,6- tetramethyl-1-piperidinyloxy (TEMPO). Li et al. [73] investigated the electrochemical performance of NMP and TEMPO as the negative and positive material, respectively, in the RFB, which resulted in an average discharge potential of 1.36 V at a constant current density of 35 mA/cm^2. This increase in discharge potential is the most effective approach to reduce the cost of storage [74]. However, the constrain associated with these two organic molecules in a RFB configuration is the high average voltage of the system during charge half cycle, which requires components with higher voltage stability to the conventional RFBs.

Taking the electrochemical behaviour of the exploited organic molecules into the consideration, optimisation of the cell components and increasing the solubility concentration of these molecules, to obtain a competitive level of performance is required. It is clear that the modification and selection of organic molecules for RFBs application requires further investigation to be able to achieve a practical chemistry for the RFB systems.

2.4.2 Regenerative Hydrogen Manganese Fuel Cell:

To reduce the capital cost of energy storage devices, Yufit et al. [39] suggested the RHVFC system, and since it demonstrated a number of advantages compared to the conventional VRFB systems, it attracted attention from the researcher community. This system, a combination of VRFB and PEMFC, previously discussed in Section 2.1.2; results in cost reduction, as the amount of vanadium used in the system is halved. Another advantage, which focuses on the lifetime of the system, is the ease of recovering any capacity loss due to the crossover of vanadium during discharge. It is well known and reported in different studies that, during discharge vanadium migrates through the membrane to the anode side, which results in capacity decay and a reduction in energy efficiency in the system [75].

Both VRFBs and PEMFCs are well known technologies in their own rights but have drawbacks that limit their complete acceptance by end users. On their own, both technologies seem to suffer from incompatible material platforms and misalignment of engineering aspects. Therefore, researchers have looked at developing a strong materials-based platform by combining both of these technologies that has the potential to introduce a major step change in the stationary energy storage market.

Aligned with pursuing a lower cost technology, Rubio-Garcia et al. [16] demonstrated the newly developed RHMnFC (presented in Figure 2-7) with high energy density of 33.4 Wh/L. Mn as electrolyte had been tested previously by different research groups, where the stability of the electrolyte at 100% SoC was identified as a hindering factor in the feasibility of this technology [76].

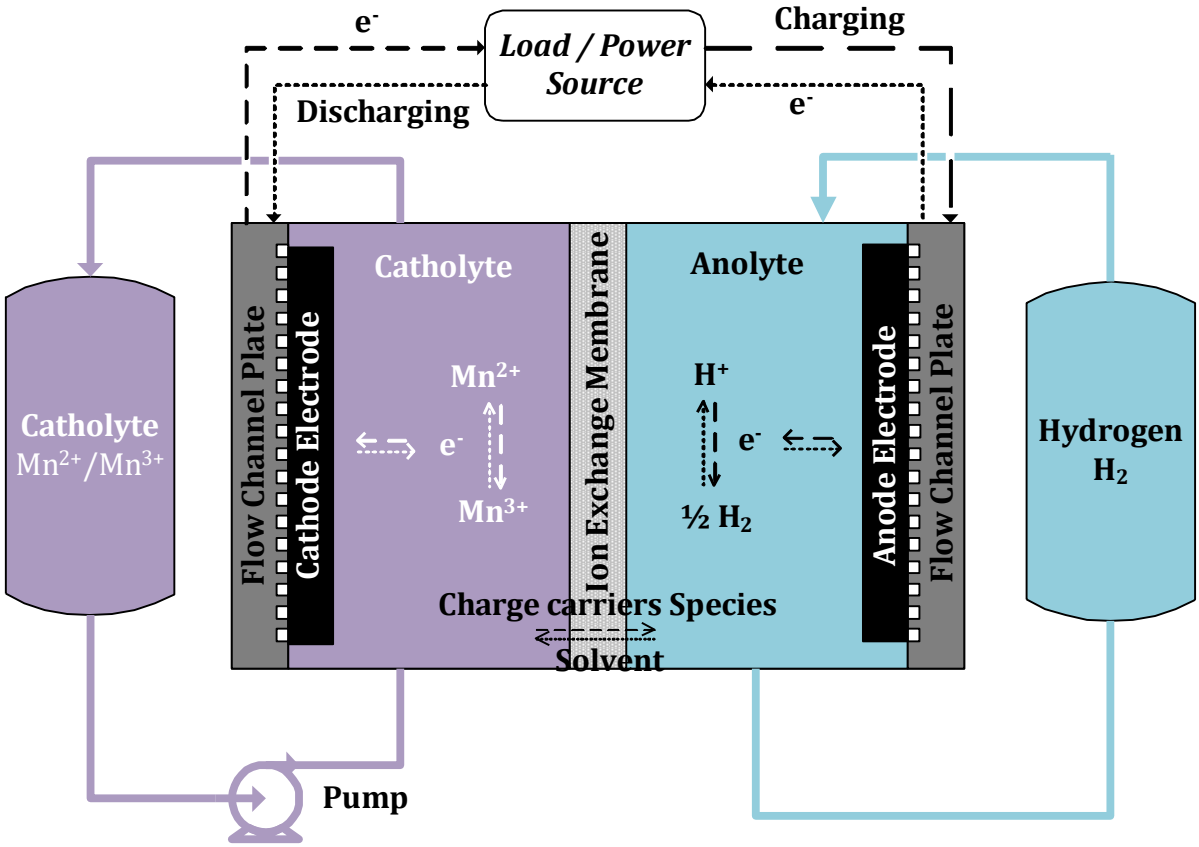

Figure 2-7: Schematic of Regenerative Hydrogen Manganese Fuel Cell, including the reactions during charge and discharge half-cycles

2.4.2.1 Manganese Redox Metals in Redox Flow Batteries

One of the technical problems associated with Mn based flow batteries is the disproportionation of- Mn^{3+}. In Mn batteries, during the charge process, as the concentration of the Mn^{3+} increases, it goes through a spontaneous disproportionation, where, as illustrated in eq. 2-9, it reacts with the water (H_2O) and produces MnO_2 [77]. The produced component, due to precipitation, has a very limited solubility in the acidic environment, and it is not soluble in the water. Therefore, this results in decay in achievable capacity, as it cannot be recovered, which effects the energy efficiency of the cell.

$$2Mn^{3+} + 2H_2O \rightleftharpoons Mn^{2+} + MnO_2 \downarrow + 4H^+ \qquad \text{eq. 2-9}$$

From a technological perspective, in order to achieve a stable charge-discharge cycle, it is therefore necessary to suppress the precipitation of MnO_2. Davies et al. investigated the chemistry of Mn^{3+} in aqueous solution, where according to his findings, oxidation of Mn^{3+} to Mn^{4+} can be stabilised by increasing the acidity of the solution. However, this method resulted in the formation of an unstable complex, where their energy density would be much lower [78,79]. Dong and Kaku investigated the use of Mn as a redox active metal in redox flow batteries, and achieved an EE of 86.7% at 50mA/cm^2 [76,80]. In their proposed novel RFB system, stable performance was demonstrated over 40 cycles, which was

achieved by adding titanium to the solution [80]. Although the mechanism through which Ti^{4+} supresses the Mn^{3+} disproportionation is not fully understood, studies have suggested that the manganese-titanium complex limits the particle size of the manganese active species, enhancing the reversibility of the oxidation and reduction reaction of Mn^{2+} to Mn^{3+} and vice versa [80,81].

Sumitomo Electric Industries worked on implementing these findings into an RFB. Although shown to be promising, the performance of the cell was identified to be the main aspect that required further improvement. The highest achieved current density in their flow battery was reported to be 50mA/cm^2, with voltage efficiency of above 80%. This performance when compared to other available chemistries required further development to achieve higher energy efficiencies at higher current densities [76].

In 2018, Nature published work from Stanford University that demonstrated a new hybrid flow battery operating with Mn deposition and dissolution reactions. In this method the production of MnO_2 was utilized as part of the reversible reaction, which improved the cell energy density significantly, as the reaction would be a two electron reaction [82]. In this study, the energy efficiency of the cell at 10mA/cm^2 was reported to reach 70%. In comparison to the commercially available VRFBs, capable of achieving energy efficiency of 85% at 80 mA/cm^2 [83], it is clear that the performance of the cell must be further optimised in order to achieve similar performance at higher current densities. Low energy-efficiency reported from work by Chen et al. was attributed to the exfoliation of thick MnO_2 layers from carbon fibres of the cathode electrode, leading to the loss of active material and decreasing the concentration of active species in the electrolyte [82].

2.4.2.2 Manganese Electrolyte for RHMnFC

In Section, it was shown that using titanium as an additive in the electrolyte supresses the disproportionation reaction of the Mn^{3+}. However, precipitation of manganese at a higher state of charge remains a signification challenge to the lifespan of the system and in developing a system that is viable for energy storage applications. In order to overcome this challenge, it is necessary to have a clear understanding of the mechanisms that can lead to the disproportionation reaction of Mn^{3+}, as well as the rate of this phenomena.

Previously, the performance of the RHMnFC was evaluated based on experiments with a minimum rest time (5 minutes) between charge and discharge cycles. Hence, even with the occurrence of a possible disproportionation reaction, the amount of precipitation would be minimal over this time period. However, taking the application of the energy storage devices into consideration, it is clear that this rest time is not always possible or practical. As highlighted in Section 2.1, flow battery

technologies can be implemented for different operation timescales. These energy storage devices can have a long rest period between charge and discharge cycles [84].

It is possible that the increase in rest time will increase the amount of precipitation, which may result a reduction in the energy efficiency and capacity of the system [82]. Hence, there are two possible strategies that could be used to overcome this. Firstly, the cell can be charged to a certain state of charge (depth of charge), where the disproportionation reaction is less favourable, which will be discussed in more detail in Section 2.4.2.3 . This strategy will lead to an increase in the LCOS of the technology, as a larger volume of active species will be required to be able to supply the energy demand. Secondly, the implementation a sustainable method that dissolves the precipitated MnO_2 in the cell, back into the electrolyte.

Qu et al. investigated the reversibility of charge and discharge cycles of MnO_2 and found that MnO_2 dissolved in an alkaline media is only rechargeable to the extent of a one electron transfer reaction, where practically only about 30% of the theoretical capacity is accessible [85]. Godunov et al, studied the dissolution of MnO_2 in different concentrations of sulfuric acid and found that rate of MnO_2 dissolution back into the electrolyte decreases as the concentration of sulfuric acid increases [86].

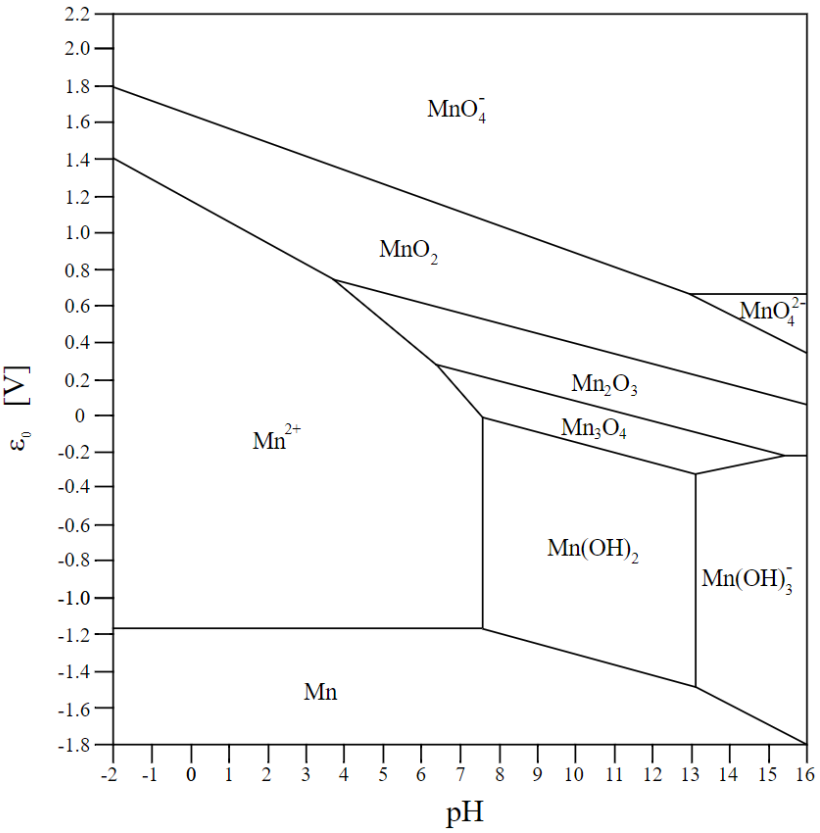

Figure 2-8: Pourbaix Diagram for Manganese [87]

According to these studies, it is necessary to initially understand the mechanisms that can lead to the degradation of the electrolyte capacity caused by the precipitation of MnO_2 in the flow cell. According to the Pourbaix diagram of manganese (Figure 2-8), at a voltage above 1.2 V, the dominant form of manganese in a highly acidic solution is MnO_2. However, this graph does not take into consideration the existence of intermediate forms of manganese such as Mn^{3+} and MnOOH [78].

2.4.2.3 Stability of Manganese at the Presence of Titanium:

According to Figure 2-8 and eq. 2-9, Mn^{3+} is thermodynamically unstable. In addition, based on Ostwald's Rule of Stages, precipitation of manganese oxides is often initiated by the growth and nucleation of metastable manganese oxides and oxyhydroxide, prior to the formation of the manganese precipitate [88]. Sun et al. [89] estimated the Gibbs formation free energy of MnO_2 to be 54.64 KJ/mol lower than Mn^{3+}. Therefore, the rate of disproportionation reaction can be limited by the introduction of a thermodynamic or kinetic barrier to this reaction [89].

Considering the concentration of the products of the disproportionation reaction, shown in eq 2-9, Mn^{3+} stabilisation in the solution is achieved at a higher acid and Mn^{2+} concentration and lower Mn^{3+} concentration. However, in a fully charged cell, opposite of this condition exists in the solution, the concentration of protons (H^+) decreases, and all the Mn^{2+} active species are oxidised to Mn^{3+}. Therefore, rate of forward reaction is higher to reach the equilibrium [90].

Dong et al. [76] suggested that, although the Mn^{3+} can be stabilised by forming metal complexes and changing the coordinate structure of Mn^{3+} ions, it still remains a significant challenge to stabilise Mn^{3+} in the solution at high concentration. Additionally, these methods affect the electrochemical activity of the active species, and therefore leads to the diminution of the performance. However, based on their suggested chemistry, it was shown that the presence of titanium in the Mn electrolyte suppresses the MnO_2 precipitation reaction [80]. Structural analyses and molecular dynamic simulations of Mn and Ti in H_2SO_4 indicate that, $Ti(SO_4)_2$ exists in the solution, beside presumed $Ti(OH)_2$ molecules, which will be discussed in more detail in Section 5.1.1 [77]. This promotes the proton dissociation from HSO_4^- and increases the H^+ concentration in the solution. As the disproportionation of Mn^{3+} releases protons, the concentration of sulfuric acid can therefore affect the equilibrium of the disproportionation reaction. Therefore, at higher H_2SO_4 concentrations and consequently higher H^+ concentration in the solution, the disproportion reaction is less favourable [78,91].

Based on these explanations, it is clear that the addition of Ti^{4+} to the Mn electrolyte suppresses the precipitation of MnO_2 in the solution. According to the pourbaix diagram of Mn (Figure 2-9), overlaid with the pourbaix diagram of Ti, this ion only exists in the form of Ti^{4+}, in the electrolyte, at the

operating voltages during charge (upper cut-off voltage of 1.65 V) and discharge half-cycles (lower cut-off voltage of 0.65 V) of the Mn-based flow batteries.

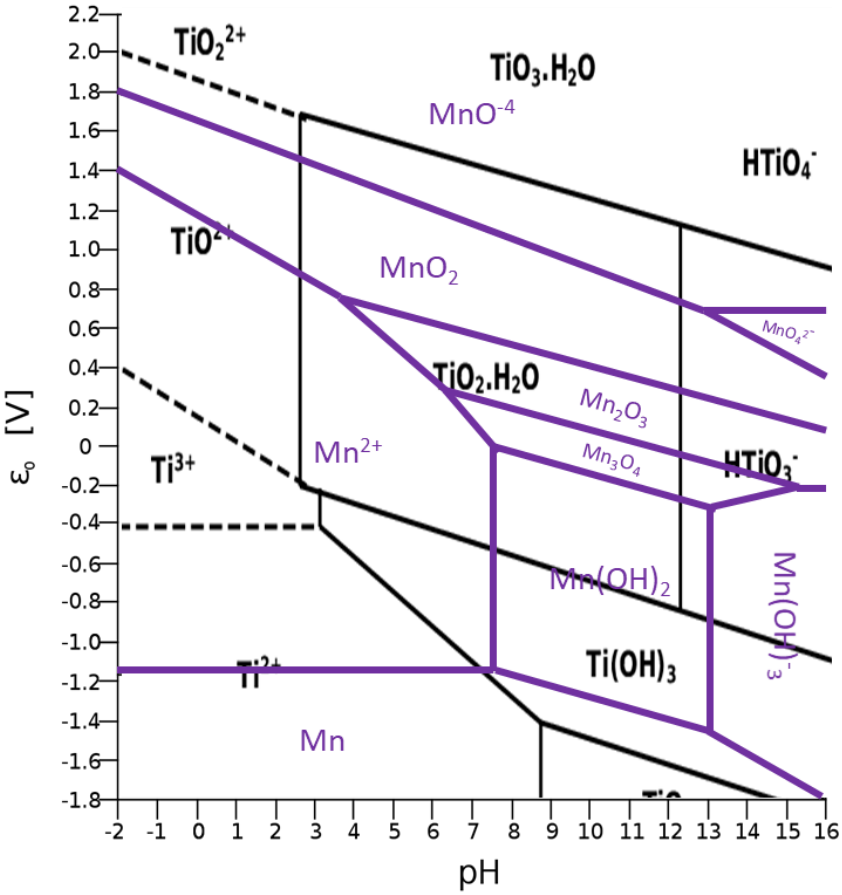

Figure 2-9: Pourbaix diagram of Mn overlaid with Ti, presenting the state of each element in the solution at different voltages

2.4.2.4 Material Selection for Regenerative Hydrogen Fuel Cells

Previously, it was established that both anode and cathode electrodes must display certain characteristics. Different studies have been orientated towards understanding these characteristics and affecting mechanisms in terms of the performance of these components. Initially, a detailed review of the required characteristics of each component will be discussed. This will be followed by looking into different works conducted in the field, to provide the latest progress in optimising the performance of each electrode and achieving optimum performance in RFCs. However, since RFCs have only been developed recently, there is limited information on their MEAs. Currently, these systems employ conventional RFB materials in their cathode and PEMFC materials in their anode, with lower amount of Pt loading on the catalyst layer; hence, current state-of-art for RFB cathode and PEMFC anode will be investigated.

2.4.2.4.1 Anode Electrode Material

It was discussed and shown in Section 2.3 and Figure 2-6, at the anode of RFCs, that during the charge and discharge process, hydrogen evolution and oxidation reaction occur respectively. Hydrogen oxidation during discharge follows a similar mechanism to that demonstrated in PEMFCs. Different reviews on PEMFCs have shown that, the main voltage losses are due to the slow kinetics of the oxygen reduction reaction [92]. In contrast to the slow oxygen reduction reaction, hydrogen oxidation reaction in the anode, using Pt as its catalyst, is so fast that the voltage losses associated with the anode can be neglected [93].

Durst et al. studied the reaction kinetics of different electrocatalysts, such as Pt, Ir, Rh and Pd on carbon. This work concluded that the hydrogen oxidation and evolution reaction, using Pt on carbon is faster than other catalysts [94]. In 2009, Neyerlin and co-workers investigated the effect of Pt loading on the kinetics of these two reactions [95]. This study concluded that, even low Pt loading of 0.05 mg/cm^2 only results in less than 5mV losses at 1.2 A/cm^2.

Another problem, associated with using carbon electrocatalysts as support, is known to be the oxidation of the carbon material at high voltage. This phenomenon in PEMFCs leads to degradation of the carbon material, which hinders the performance of the cell due to the loss of active surface area [96]. Nevertheless, it has been observed that the degradation of carbon material mainly occurs on cathode electrode. In RFBs, degradation of carbon materials heavily depends on the chemistries of the system; thus, this mechanism will vary in each system [97].

Hydrogen electrodes, as illustrated in Figure 2-5, contains two different layers, where each layer has their own unique function in the cell. Gas diffusion media (GDM), consists of a gas diffusion layer (GDL) and microporous layer (MPL), which combine to provide the means to transfer the supplied gas to the catalyst layer (CL), where the electrochemical reaction occurs. It was explained previously that in RHVFC, electrolyte can migrate from the cathode to anode electrode, during charge or discharge. Therefore, it is necessary to efficiently facilitate the migration of the droplets, accumulated in the anode, out of the system.

This mechanism can be achieved by either applying a hydrophobic polymer agent on the GDL, or by introducing a thin layer, sandwiched between CL and GDL, to ease the transfer of the water out of the CL. In this approach, hydrophobic treated MPL reduces the contact resistance between GDL and CL by enhancing gas diffusion to the system.

2.4.2.4.2 Cathode Electrode Material

The cathode electrode material plays a key role in the performance of the RFBs. In VRFBs, due to the high electrochemical stability, favourable permeability and large surface area carbon (or graphite) material is currently the most favoured material [98]. Skyllas-Kazacos et al. demonstrated a peak power density of 85 mW/cm^2, using graphite felt as electrodes on both half-cells [21]. Since then, extensive research has been focused towards improving the performance of RFBs by studying different carbon-based materials and modifying and increasing their reactivity.

One of the influencing factors, that has been the focus of research in the field, is the effect of reducing ohmic resistance and increasing the mass transport of the electrolyte in the electrodes. Extensive studies on different carbon electrodes have revealed that, by compressing the electrodes, higher performance is achievable in VRFBs [99,100]. Park et al. investigated the influence of compression on VRFBs, where they reported that by compressing a graphite felt to 80% of its initial thickness, the specific resistance of the electrode can be reduced by approximately 60% from 0.16 Ωcm to 0.095 Ωcm [101]. It was also shown that, by enhancing the electrode conductivity at 20% compression, a 5% increase in energy efficiency was achievable, in contrast to what was reported at 10% compression at various current densities [101].

Different studies have reported that further increase in compression results in additional gain in the cell performance [100,102]. However, this mechanism also depends on the design of the flow plates. The effect of different flow designs, explored by Brown et al, have shown that using a flow through design, it is possible to achieve high performance by compressing the electrode to 75% of its initial thickness. By increasing the compression to less than 75%, although a decrease in specific surface area was observed, it also resulted in 44.5% increase in pressure drop. Obtained results indicated that the pressure drop was due to the reduction of the electrode porosity, will result in efficiency losses in the system [103]. Bin-Tsang et al. investigated the influence of introducing flow patterns, to the flow field, on performance of the flow cell, where optimum compression to achieve high cell performance was reported to be between 20% and 25% [104].

Although most of the work in the field has focused on carbon felt electrodes, which is due to the high specific surface area of these materials, dramatic improvement on the performance of VRFBs was reported by researchers in University of Tennessee who replaced the conventional carbon felt with carbon paper (10 AA Carbon Paper), where an increase of performance by five-fold was reported when three layers of these electrodes were stacked on top of each other [105].

Research was conducted to improve the active site of the electrodes for vanadium redox reactions, by different types of surface treatments such as thermal and plasma treatments. Sun et al. exhibited a

10% performance gain in energy efficiency (at current density of 20 mA/cm^2) of the VRFB, by thermally treating the graphite felt at 400 °C [106]. Dixon et al. investigated the effect of plasma treatment of the electrodes on performance of VRFBs [107], and found that using this method of treatment, the energy efficiency of the VRFB at current density of 80 mA/cm^2 was improved by 7%, reaching close to 82%, in comparison to the performance of the flow battery using heat treated electrodes [107].

2.4.2.4.3 Proton Conducting Membrane Material

The IEM, as was discussed in Section 2.2, is an important component in redox flow batteries. In order to achieve a high performance in RFBs, enormous effort is generally focused on selecting a suitable membrane depending the chemistry of the redox flow systems. An ideal membrane for, RFBs with redox metals dissolved in acidic environment, should offer characteristics such as: compatibility and stability to highly acidic environments, resistance to high oxidising conditions at the cathode, low permeability to redox ions, high conductivity to proton carrying hydrogens, mechanically stable and most importantly low cost [108].

In general, membranes used in redox flow batteries can be classified to two groups. The first group consist of membranes, cations (H^+) or anions (OH^-) are exchanged through the membrane, between two half cells. The second group is classified as non-ionic porous membranes, which the permeation of the charge carrying ions are through physical barriers, where due to the size of pores it can prevent larger ions migrating across the membrane [109–111].

Development of membranes to be used in flow batteries have tended to follow the findings from works carried out on fuel cell membranes. These membranes which fall into the first classification of the membranes, can be categorised into five groups [110]: Perfluorinated ionomers, partially fluorinated polymers, non-fluorinated hydrocarbons, Non-fluorinated membranes with aromatic backbone and Acid-base blends. Among these five group of materials, the perfluorinated membranes have the most desired properties to meet the requirement of the RFBs employing cation exchange membranes. Perfluorinated ion exchange membranes contain a hydrophobic fluorocarbon (C_xF_y) backbone, where strongly hydrophilic sulfonic acid groups (SO_3H) are attached to it by the perfluoroether side chains [112]. The effective proton transport across the membrane occurs through the hydrolyzation of the sulfonic- acid groups into $SO_3^-H_3O^+$.

Nafion® membranes produced by DuPont, shown in Figure 2-10 [113], are the most widely researched and employed membrane in the flow battery industry. The perfluorinated sulfonic acid cation exchange membranes have their remarkable properties but also, they have few shortcomings. These membranes, while used in VRFB, suffer from crossover of vanadium ions, which decreases the energy efficiency of the system [114].

In order to understand the crossover phenomena in these membranes, it is important to understand the mechanism of migration of the water molecules from one side to another. Proton transport occurs through two plausible mechanisms, where both these mechanisms are not independent of each other. In first mechanism, illustrated in Figure 2-10 (b), known as the Grotthuss mechanism (also referred as proton jumping), protons transfer from one site to another through breaking and reforming the hydrogen bonds of the pronated molecules (H_3O^+). In the second mechanism, illustrated in Figure 2-10 (c), known as the vehicle mechanism, protons migrate with proton solvent (H_3O^+), which results in movement of water molecules from one side to another [115].

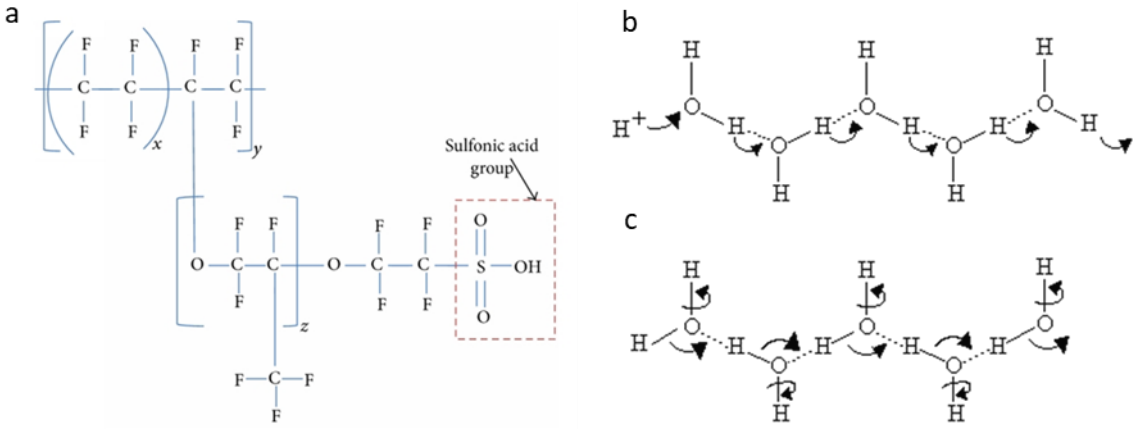

Figure 2-10: Nafion® proton exchange membrane, a) illustrates the chemical structure of the membrane [113], b) Grotthuss proton transfer mechanism and c) vehicle proton transfer mechanisms.

Typical Nafion products consist of the extruded series, such as N112, N115 and N117, and dispersion cast products such as NR211 and NR212. Since the chemical structure of these products is similar, their properties can be determined by their ionic conductivity and difference in thickness. According to the work by Shi et al. [109], Nafion® products, depending on their thickness, have different conductivity and ion exchange capacity (IEC) [109,116].

Table 2-2: Comparison of different Nafion® membranes [109,116]

Types	Thickness	IEC	Conductivity
	µm	mmol/g	ms/cm
N112	50	0.84	98
N115	127	0.87	100
N117	183	0.88	96
NR211	25	-	-
NR212	50	0.88	101

Studies on the effect of different Nafion® membranes, comparing the performance of N212, N115 and N117 in VRFB, have shown that Nafion 117 has lower crossover rate in contrast to Nafion 212. Jeong et al. work concluded that crossover rates in N117 is approximately 55% lower than N212, with N212 showing a crossover rate of 0.0125 M/hr [117]. This finding indicated that, higher crossover using N212 will result in loss in energy and columbic efficiency at longer operation period.

In another work by Jiang et al., the performance of N115, N117 and N212 at different current densities, between 40 mA/cm^2 up to 320 mA/cm^2, and their capacity retention at different number of cycles, in VRFB was studied and compared [116]. According to the results, using N212 as the IEM shows a 2% and 5% higher voltage efficiency, at 120 mA/cm^2, in comparison to the cell employing N115 and N117 respectively. This is due to the higher conductivity of the N212, which leads into lower ohmic losses during charge or discharge. However, it was also shown that due to the higher crossover of the electrolyte between two half cells, capacity retention of the cell with N212 as its IEM was 25% higher than both cells with N115 and N117 as its IEM [116].

Recently, research has focused on modifying Nafion to increase the ionic selectivity, and as a result of that to reduce vanadium permeability. Researchers have investigated the possibility of replacing the conventional perfluorosulfonic acid with a variety of sulfonated hydrocarbon membranes, such as sulfonated poly(arylene ketone), sulfonated polyimides. These works have shown that hydrocarbon membranes can exhibit reduced crossover of the vanadium ions at lower cost when compared to Nafion [118,119]. Choi et al. work concluded that using hydrocarbon membranes exhibits a 2% and 5% gain in both energy and coulombic efficiency respectively [120].

2.4.3 Feasibility of Scale-Up

Despite many reviews and extensive studies carried out on the performance of RFBs over the last three decades, there is a dearth of information on the feasibility and engineering challenges associated with up-scaling. Although there are many experimental and computational studies on the engineering aspects of RFB scale-up, the majority of these studies have focused on the influence of flow-field orientation and geometry on battery performance.

Therefore, more focus is required on the engineering aspects of the cell and a reliable comparison between figures of merit in scalability of these technologies. The ‘concept RFB laboratory tested cell’ passes through several stages to achieve an improved scaled-up system. This development is to ensure adequate electrolyte flow, current distribution and reaction kinetics within the scaled-up cell.

According to a number of papers published on the performance of VRFBs, by increasing the active area of the cell, the mass transport within the cell is significantly affected by the flow field channels in

the electrodes [13,29,121]. Gundlapalli et al. tested a short stack of four unit cells with an active area of 414 cm^2, where they reported an energy efficiency of 84% over 25 cycles [121]. Ma et al. also investigated the effect of charge and discharge current density on the efficiency of the VRFB, where a stack of 15 cells, with an active- area of 875 cm^2 was designed for testing. It was concluded that, at 45 mA/cm^2, 5% higher efficiency is achievable compared to a higher current density of 75 mA/cm^2 [46]. Thus, direct comparison of the effect of increasing the cross-sectional area in a unit cell (under the same conditions) is not reported in the literature.

2.4.4 Review on Zinc Flow Batteries

The need for reliable energy storage is critical in facilitating the increased use of intermittent renewable energy sources such as solar and wind, and in providing a means of efficiently balancing electrical power generation and demand particularly during peak periods. Among various energy storage technology options, zinc-based rechargeable batteries are another promising energy storage system due to zinc's low cost, naturally abundant supply, non-toxicity, scalability and ability to operate in ambient conditions. However, a primary issue that limits their application is poor cycle life performance due to zinc dendrite formation during charging [122,123], which can eventually cause a short circuit within the battery if the dendrites grow progressively and eventually reach the cathode.

Numerous studies have been reported on zinc electrodeposition in electrolyte solutions, some of which have demonstrated relationships between the structure of electrodeposited zinc and variables such as zincate concentration, electrode surface roughness, growth rate of deposit, temperature condition and total overpotential [124–128]. Despite this, there still remains an incomplete understanding of the relationship between zinc deposit microstructure and device performance.

Dendritic growth of electrodeposited zinc can be suppressed with the use of flowing electrolyte, electrolyte additives and pulse charging protocols [129]. However, a comprehensive understanding of effective application and implementation of these control strategies is yet to be achieved: although additives may suppress dendrite growth, they could also have adverse effects on the species transport and the electrode and electrolyte conductivities; large pulsed currents may damage the positive electrode in the secondary-zinc battery which is an inconvenience in practical applications; and there is insufficient information in the literature on the relationship between electrolyte flow dynamics and battery performance. Hence, in order to alleviate the effects of dendrite growth and improve morphological control of electrodeposited zinc, it is crucial to gain further insight into their mechanisms of formation particularly during battery operation.

Amongst the various characterisation techniques that have been used to facilitate the investigation of metal dendrite formation and growth behaviour, X-ray radiography and computed tomography (CT)

have been demonstrated as powerful tools that can be used to study dendrite microstructure in-situ and operando and at remarkable resolution. Yufit et al. used synchrotron X-ray computed tomography to analyse and quantify the growth and morphology of the zinc dendrites in a charge and discharge cycle using a static cell [124].

The choice of low-cost redox metals for secondary flow battery applications is still limited to the metals which are highly abundant in the earth's crust, such as zinc, iron, manganese and lead [57,130,131]. Hence, their widespread accessibility makes these metals attractive for energy storage applications. Due to their relatively high redox potential and fast kinetics, zinc redox active species possess significant potential for energy storage application, particularly in zinc-RFBs, which are considered to be amongst the next generation of energy storage devices [37].

Zinc-RFBs can be categorised based on the phase of the active species present in the system. Zinc (Zn) metal, similar to iron and lead metals, incorporates electrodeposition from dissolved electroactive species, and serves as the negative electrode and substrate in RFBs. Since, flow batteries with Zn as their negative electrode can operate in both acidic and alkaline media, this has facilitated their development and coupling with different positive electrode chemistries [132].

Depending on the phase of the electroactive material utilised in the positive electrode half-cell (i.e. whether it is solid, liquid or gaseous phase), Zn-based flow batteries require unique cell architectures. Figure 2-11 illustrates hybrid Zn flow batteries with positive electrodes of different phase, in which the reactions of each phase is facilitated with specific cell configurations. In these flow batteries, the reaction at the negative electrode involves the electrodeposition of Zn active species (which are present in the electrolyte) on the negative electrode substrate (typically zinc metal) during charge, and dissolution of the electrodeposited Zn back into the electrolyte during discharge. This implies that the accessible capacity in Zn-RFBs depends not only on the concentration of the redox active species present in the electrolyte but also on the available surface area for electrodeposition, thus highlighting the importance of the zinc electrodeposition process in these flow batteries [130].

Depending on the phase of the active species existing at the positive electrode and the reactions that occur at the positive electrode half-cell, Zn-RFBs may consist of a porous membrane separator or an ion-exchange membrane (IEM). In Zn-RFB systems such as zinc-bromide and zinc-cerium, shown in Figure 2-11 (c), where two electrolytes with different active species exist as anolyte and catholyte, the battery system is split into two electrochemical half-cells separated by an IEM to prevent cross contamination of the analyte and catholyte species [133,134]. However, system configurations containing a single flowing electrolyte (such as Figure 2-11 (a) and (b)) can be operated without a separator while preventing the direct reaction or cross contamination of the active species - this contributes to

reducing the capital cost of the systems with the single flow configuration compared to those requiring separators or membranes to facilitate the reactions in each half-cell [135,136].

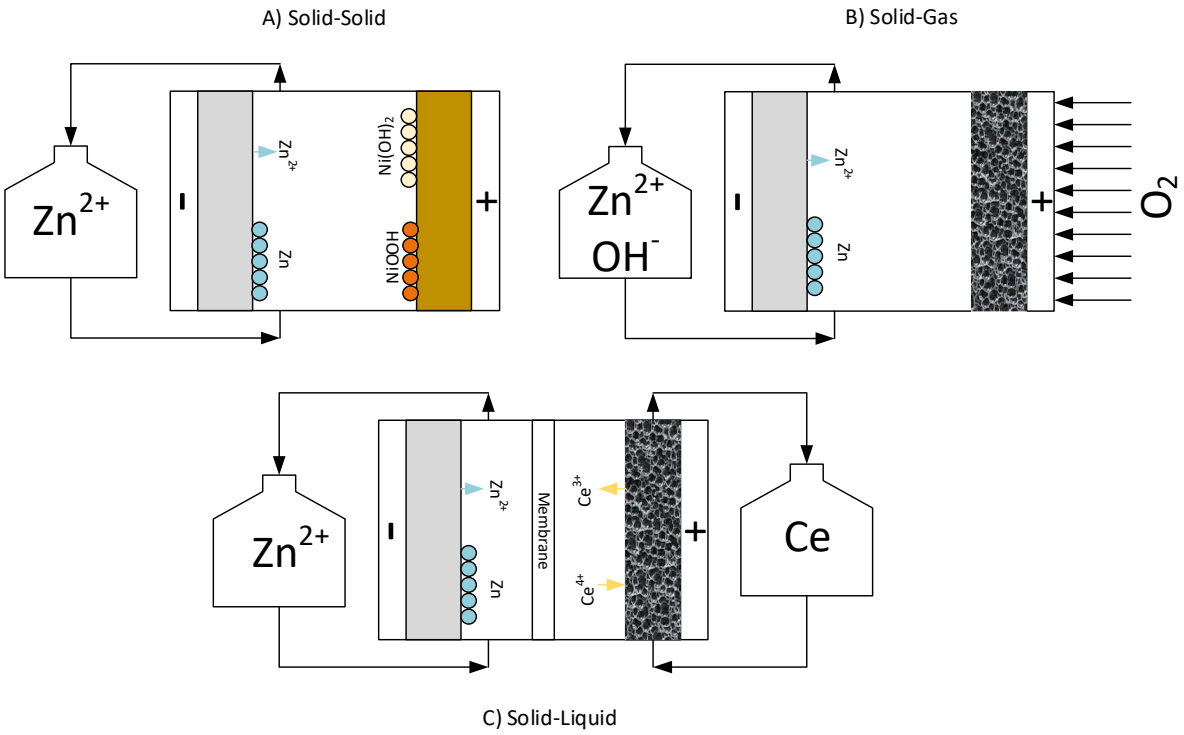

Figure 2-11: Zinc-RFBs with: a) solid phase reaction, b) gaseous phase reaction and c) liquid phase reaction at the cathode (positive) half-cell

Despite their low cost, high energy density and environmentally friendly properties, rechargeable zinc-based batteries are regarded as prospective candidates for energy storage applications [137], as they inevitably suffer from two main limitations: the growth of zinc dendrites during electrodeposition of zincate on the negative electrode surface and the occurrence of hydrogen evolution side reactions [138]. There are numerous studies reported in the research literature on these limitations; however, a clearer understanding of these limitations under realistic operating conditions and how they may be alleviated is crucial to be able to improve the cell performance and cyclability of Zn-based RFBs

2.4.4.1 Electrochemistry of Zinc Electrodeposition

The Pourbaix diagram of zinc, shown in Figure 2-12, presents the state in which zinc species exist at different pH values [139]. As indicated by this diagram, electrodeposited zinc during the reduction process occurs in the form of Zn^{2+} in acidic media and $Zn(OH)_2$, $Zn(OH)_3^-$ and $Zn(OH)_4^{2-}$ in alkaline media. The different forms of dissolved zinc species at different voltages and pH have been extensively studied and confirmed by Raman Spectroscopy [140], nuclear magnetic resonance (NMR) [141] and other

analytical techniques.

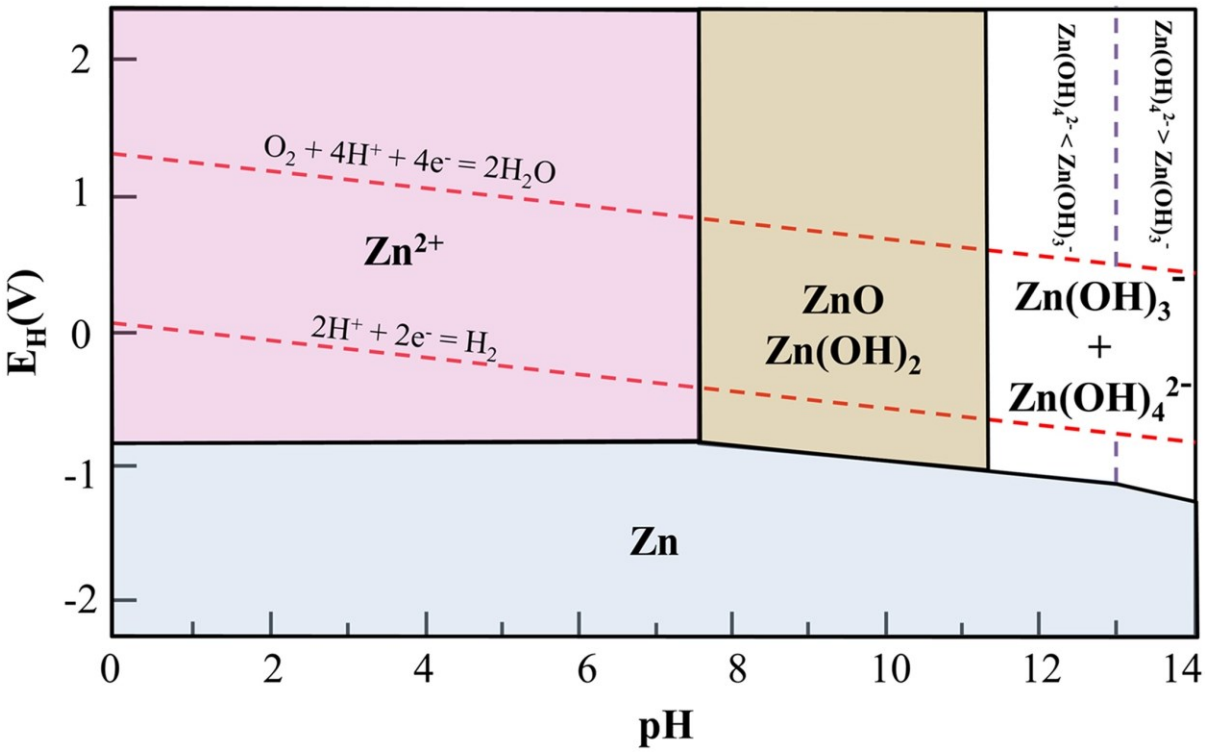

Figure 2-12: Pourbaix diagram of zinc at 25 °C [139]

In highly alkaline systems with pH above 13, electrodeposition of Zn occurs during the charge step, with the reduction of $Zn(OH)_4^{2-}$ to Zn and deposition of Zn onto an inert substrate. During discharge, the reverse reaction occurs where deposited Zn oxidises to $Zn(OH)_4^{2-}$ and dissolves in the alkaline electrolyte. This reversible electrochemical reaction, shown in eq. 2-10, has a high standard redox potential of -1.248 V vs SHE (Standard Hydrogen Electrode) [126,128].

$$Zn(OH)_4^{2-} + 2e^- \leftrightarrow Zn + 4OH^- \quad \text{eq. 2-10}$$

Bockris et al. [128] studied the mechanism of Zn electrodeposition and processes that take place during this reaction. Based on this work, it was proposed that Zn deposition on the electrode occurs through a four step process, which is demonstrated in the schematic shown in Figure 2-13. The reduction reaction for these four steps can be written in the order shown in eq. 2-11 to eq. 2-14.

Step 1 $$Zn(OH)_4^{2-} \leftrightarrow Zn(OH)_3^- + OH^- \quad \text{eq. 2-11}$$

Step 2 $$Zn(OH)_3^- + e^- \leftrightarrow Zn(OH)_2^- + OH^- \quad \text{eq. 2-12}$$

Step 3 $$Zn(OH)_2^- \leftrightarrow ZnOH + OH^- \quad \text{eq. 2-13}$$

Step 4 $$ZnOH + e^- \leftrightarrow Zn + OH^- \quad \text{eq. 2-14}$$

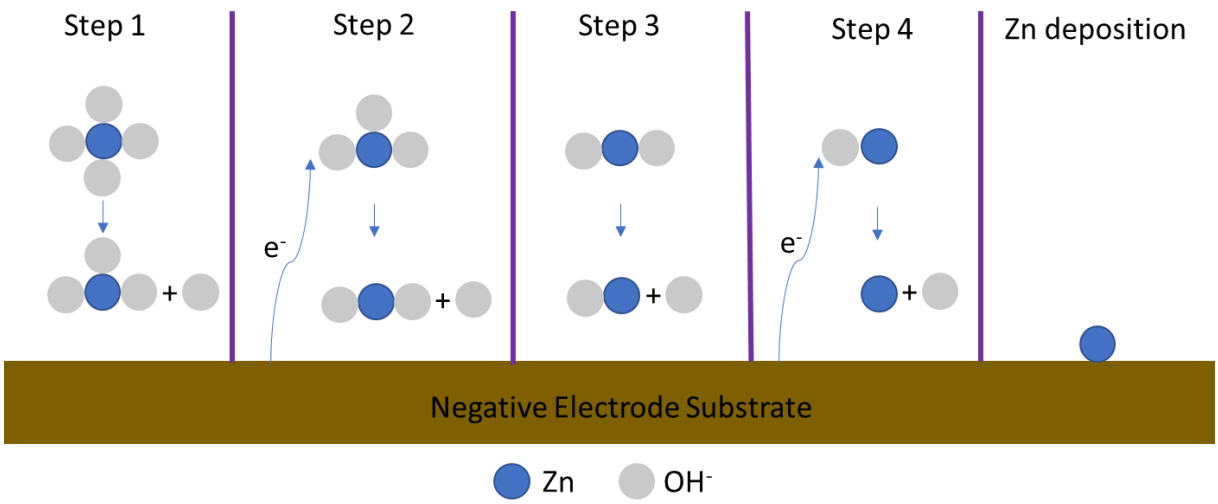

Figure 2-13: Schematic of four-step mechanism for zinc electrodeposition

According to the linear sweep voltammetry of zinc electrodeposition in a static electrolyte, shown in Figure 2-14, the physical process of Zn deposition can take place in three regions. In the initial region (I) at low current density, deposition usually occurs at a slow rate, which is limited by charge transfer rate. In the second region (II), initially the magnitude of current density increases sharply, where bulk deposition occurs [130,142]. The steep decrease of the magnitude of current density at more negative overpotential, resulting in a cathodic peak at -1.4 V vs SHE, is attributed to the diffusion control of the electrodeposition process in this region. In the final region (III), the steep increase in the current density is associated with a combination of hydrogen evolution reaction and zinc deposition reaction.

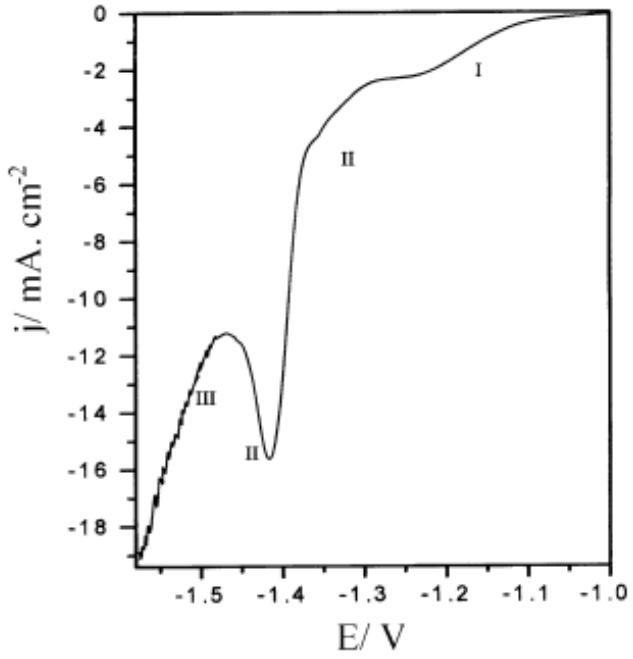

Figure 2-14:Linear voltammetry curve (vs SHE) for electro deposition of zinc on to a steel substrate in alkaline solution (v =10 mV/s) [142]

Hence, the driving force for the electrodeposition of zinc on the substrate, beside the concentration of $Zn(OH)_4^-$, is also considered to be related to the deposition overpotential [143]. However, in practical systems, two main determining factors affect the performance of the cells. One of the factors, referred to previously, is the morphology of the zinc electrodeposit, which if left uncontrolled, can lead to mechanical removal of the deposited zinc from the substrate which reduces the coulombic efficiency of the cell. The other factor is parasitic hydrogen evolution, which can occur during zinc reduction. Hydrogen evolution reaction competes with the zinc electrodeposition process to form a local net reaction, resulting in energy loss in the system [144].

2.4.4.2 Morphology of Electrodeposited Zinc

Electrodeposition of metals takes place through an initial process referred as nucleation. In this process, a small number of the ions (from solution) arrange in a pattern on the deposition substrate, forming a site for additional ions to deposit and grow. Hence, fundamental aspects of electrodeposition of Zn are directly associated with the nucleation and growth mechanisms occurring during this process [143]. On the one hand, the granularity of the deposit is impacted by the competition between nucleation and growth mechanisms, where at a higher nucleation rate, a finer deposition structure is observed. On the other hand, the form of growth determines the general structure and shape of the deposits, where at a higher growth rate (compared to the nucleation rate) a fibrous structure is obtained [145,146].

Based on the fundamental aspects of the electrodeposition process, researchers have defined two growth mechanisms which can occur: coalescence growth and layer growth [143,145–147]. The schematic of these two mechanisms is demonstrated in Figure 2-15. Coalescence growth involves the formation of three dimensional crystallite (TDC) components, and layer growth is resulted by the formation of discrete two dimensional nucleation on the surface [147].

Coalescence growth: In this growth mechanism, deposition on the substrate is initiated at isolated locations across the surface, in which continuation of the deposition on these foreign substrates, results in TDC structures. Hence, dendritic formation of the Zn deposits can occur by this growth mechanism [148,149].

Layer growth: in this growth mechanism, due to the nucleation taking place on the surface of substrate, two-dimensional deposition occurs. The deposited nuclei can form an epitaxial film of the deposited metals, or upon continuation of the deposit, it can also form well defined orientation of epitaxial layers [148–150].

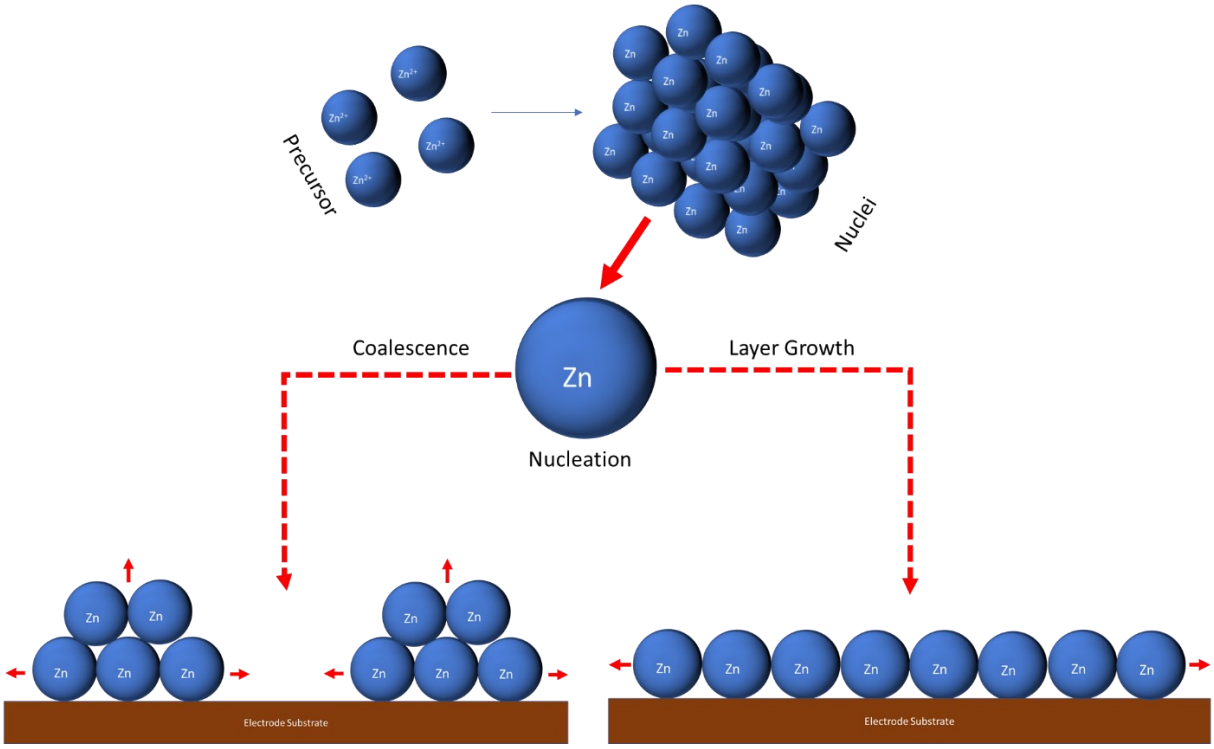

Figure 2-15: Schematic of growth mechanisms of Zn deposition on electrode substrate

The mechanisms which impact the morphology of Zn electrodeposition is fundamentally considered to depend on the mass transport of zincate to the electrode substrate [128,146], which consist of migration, diffusion and in the presence of flow, forced convection. In Zn-RFBs, migration of the zincate active species to the electrode surface is due to the potential gradient (applied overpotential) between bulk electrolyte and the electrode surface. As the zincate active species reach the electrode and are reduced to zinc deposition, their concentration at the surface of the electrode reduces, resulting in a concentration gradient between the electrode and the bulk solution.

The Nernst diffusion layer model, shown in Figure 2-16, assumed that the concentration of the active species at the distance δ (and beyond this line) from the electrode is equal to the concentration of ions in the bulk electrolyte. However, the concentration of ions in the Nernst diffusion layer decreases linearly as it gets closer to the electrode surface [150]. In this layer (Nernst diffusion layer), the migration of the ions occurs by diffusion, resulting in a concentration profile in this region. Although, the Nernst model assumes a linear concentration profile for this region, the reactant concentration in the diffusion layer reaches the concentration of the bulk solution at the boundary (δ), resulting in a curved concentration profile. However, by introducing a dynamic flow conditions into the system, the thickness of the diffusion layer will decrease. The impact of flow on the morphology of the zinc electrodeposition will be discussed in Section 2.4.4.5.

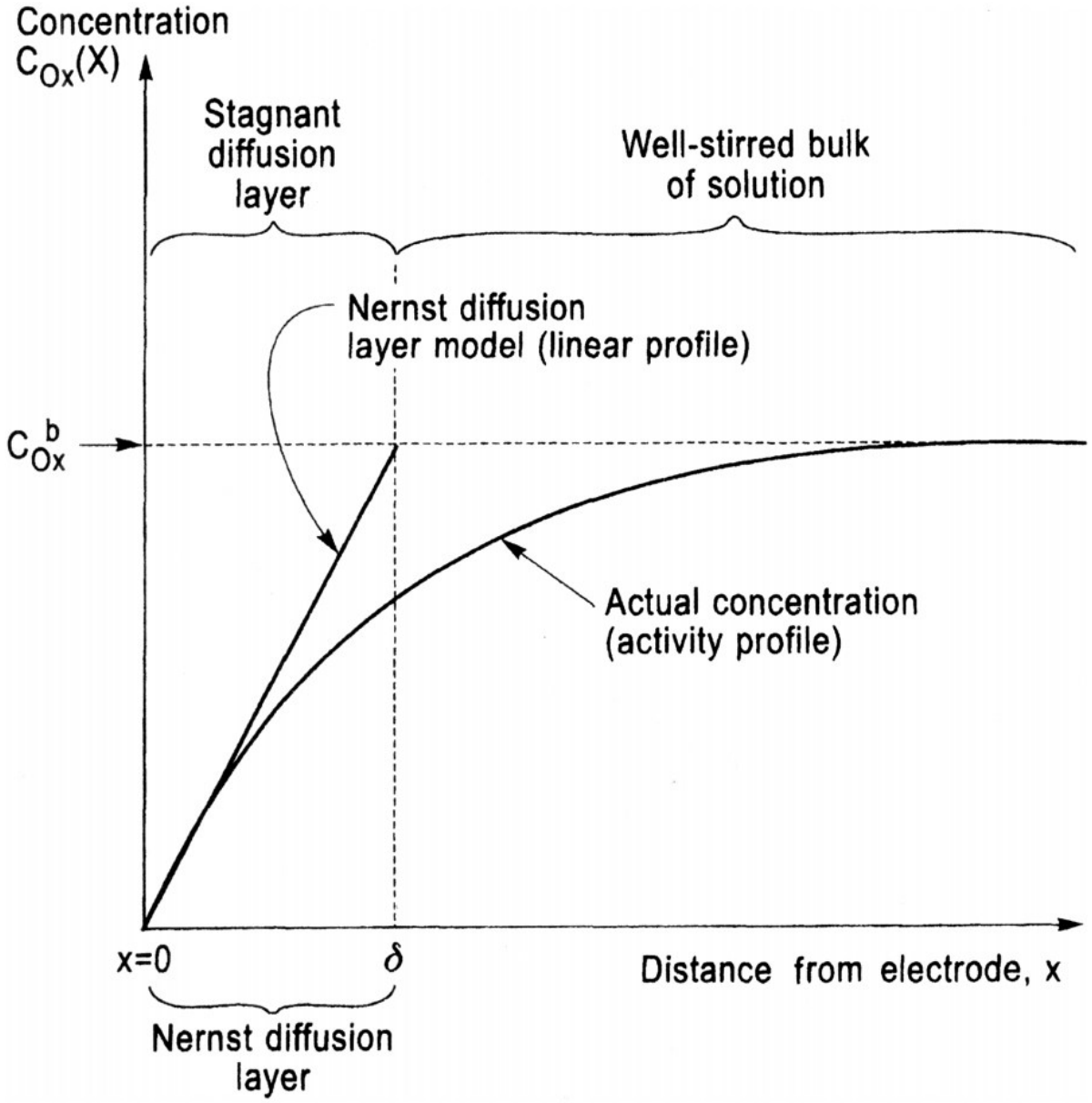

Figure 2-16: Concentration profile of zincate during electrodeposition. [150]

In general, zinc electrodeposition is classified into three main categories: dendritic, boulder-like and compact deposition morphologies. The mechanisms that result in the formation of these three distinct morphologies, shown in Figure 2-17, can be explained based on the fundamental principles of zinc deposition, discussed previously in Section 2.4.4.1. Deposition of the zincate initiates with direct deposition of zinc metals on the flat surface, at the direction normal to the substrate [151]. As the concentration of the active species ions reduces (as a result of reduction of zincate to zinc), coalescence deposition predominantly occurs. With the presence of the zinc deposits on the surface within the diffusion layer, it is more preferential for the ions to deposit on these to form boulder-like agglomerates.

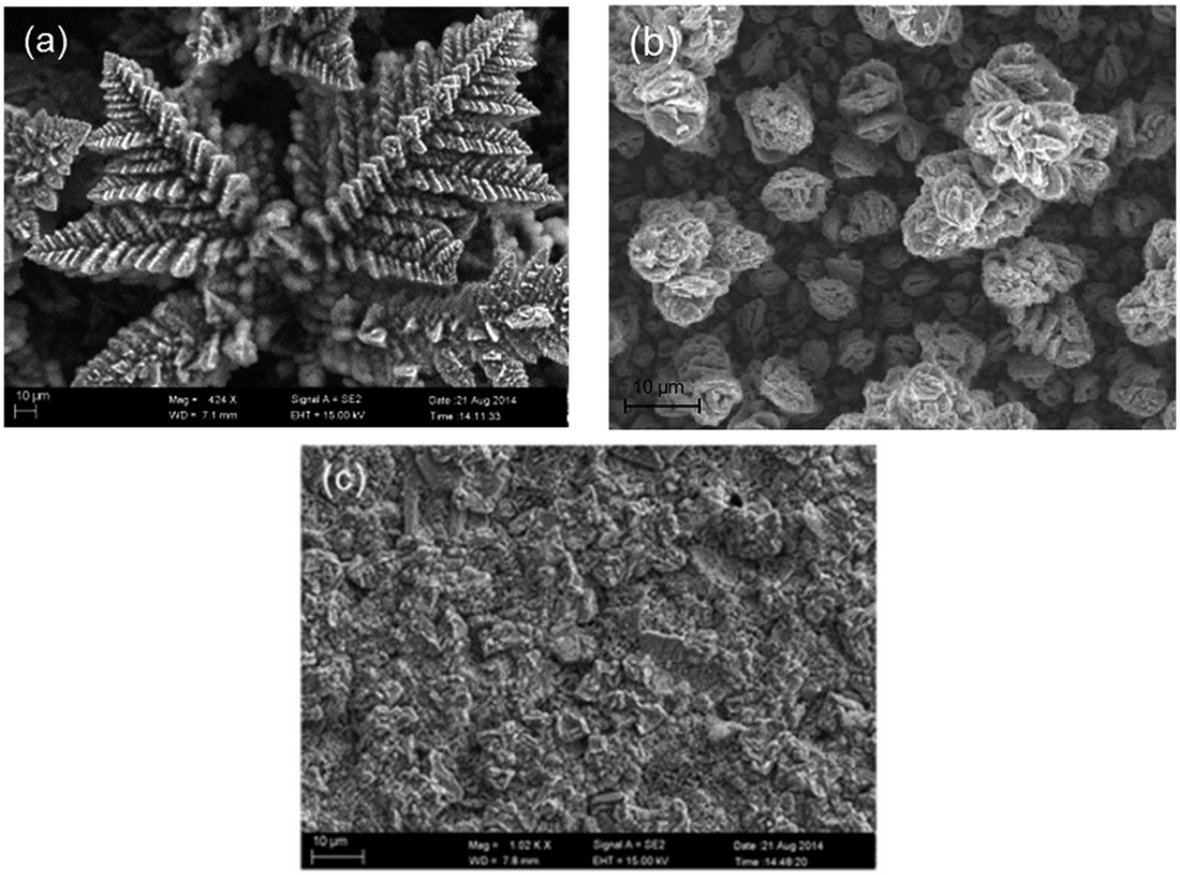

Figure 2-17: Three different morphologies of Zinc deposition: a) dendritic, b) boulder and c) compact deposition. [151]

As the deposition continues and the height of the prolonged deposits exceed the thickness of the diffusion layer, the tip of the deposited structure will be exposed to a higher concentration (equal to bulk electrolyte concentration). The deposited Zn on the electrode acts as a substrate for Zn active species in the electrolyte, hence a secondary spherical diffusion layer will be developed around the tip, and zincate ions will diffuse from the bulk electrolyte to the surface of the tip of the deposition from different directions, resulting in the formation of rapid multi-directional dendrites [128,130,150].

As the rate of nucleation increases, more sites become available for secondary deposition to take place (growth mechanism). This results in the formation of agglomerated zinc deposit on the surface of the electrode. As the current density further decreases (resulting in lower diffusion layer thickness), the rate of nucleation on the surface of electrode increases, and it becomes preferential for the zincate to reduce on the surface of the substrate, forming a compact (layer) zinc deposits [150,152].

Zinc electrodeposition morphology is a determining factor in the performance of the Zn-RFBs and controlling the electrodeposition morphology is essential in improving the lifetime of these systems. Dendritic growth during Zn deposition is an undesirable feature, which entails the risk of short

circuiting, damaging the IEM or operator, and most importantly self-discharge of the cell, due to mechanical detachment of the dendrites, resulting in a reduction in the coulombic efficiency.

2.4.4.3 Hydrogen Evolution Reaction Impact on Electrodeposit Morphology

Another determining factor of Zn deposition morphology is hydrogen evolution reaction (HER) on the surface of the electrode. HER can occur as a parasitic side reaction, while operating the cell at higher current densities than its limiting current density [153,154]. Studies carried out by Dundalek et al. on the role of hydrogen evolution reaction on Zn electrodeposition, suggested that; although, this phenomenon results in coulombic efficiency losses, it is also possible that the produced hydrogen bubbles result in enhanced mass transport of the active species from the bulk electrolyte to the surface of the electrode, by introducing an extra convection within the diffusion layer [155]. The redox potential of the HER in alkaline media, shown in eq. 2-15, is more positive than the Zn redox potential (-1.28 V vs SHE). Hence, thermodynamically, hydrogen evolution reaction has more tendency to occur at higher overpotentials. However, due to the faster kinetics of zincate reduction, zinc electrodeposition occurs prior to hydrogen evolution reaction on the electrode [128,150].

$$2H_2O + 2e^- \rightarrow H_2 + 2OH^- \quad (-0.83\ V\ vs\ SHE) \qquad \text{eq. 2-15}$$

An additional phenomenon affecting the morphology of the deposits is the undesired parasitic reaction between the deposited Zn and water molecules present in the electrolyte, which also results in hydrogen production (eq. 2-16). This phenomenon, which occurs as a result of zinc corrosion in highly alkaline media, causes a gradual self-discharge of the cell, and impacts the active material utilisation [156].

$$Zn + 2H_2O \rightarrow Zn(OH)_2 + H_2 \qquad \text{eq. 2-16}$$

The presence of the HER, as a side reaction of Zn electrodeposition, contributes to the current densities in which the electrodeposition occurs, and thus complicates the description of this process. As the overall current density of the electrode includes the current densities contributed by both HER and Zn electrodeposition, the current density that the cell operates at will not be a true representative of the amount of Zn ions deposited on the electrode [94,123].

2.4.4.4 Current State-of-the Art of Improving Zinc Electrodeposition Morphologies

Dendritic growth of the Zn deposits on the negative electrode has been studied and investigated using different characterisation techniques. Techniques such as scanning electron microscopy (SEM) and focused ion beam SEM have been used to characterise different morphologies of Zn electrodeposition previously [125,157–159]. Yufit et al. employed operando X-Ray computed tomography (XCT) technique to analyse and quantify the growth and dissolution of the Zn metal and the morphology of the zinc

dendrites in a charge and discharge cycle, using a static cell [124]. This technique was used to study the failure mechanisms in zinc batteries, and it was established that the growth mechanism of the dendrites is affected by the surface inhomogeneities caused by the substrate (Zn electrode) erosion during dissolution of the zinc dendrites in the previous cycle [124]. It was also observed that the morphology of the dendrites, in the second electrodeposition cycle, had changed compared to the initial growth. The second dendrite deposition step resulted in the growth of denser dendrites at the tip, with narrower (i.e. smaller diameter) growth on the surface of the electrode. Hence, dendrites in the second cycle were more likely to undergo mechanical detachment, which in a practical system, this would result in loss of discharge capacity and lower coulombic efficiency [124].

Therefore, it is important to introduce different strategies to improve the morphology of zinc electrodeposition for long-term cycling of Zn-RFBs [36]. The undesired growth of the dendrites is influenced by different mechanisms, discussed in Section 2.4.4.2, consisting of forced convection introduced by hydrogen bubble formation and detachment, and differences in nucleation rate and growth rate. Hence, to overcome these mechanisms which enhance the rate of dendrite propagation, suitable operating conditions are required. The two main strategies suggested to improve the morphology of zinc electrodeposition are through introducing a flowing electrolyte and modifying the electrolyte composition with the aid of additives, and both strategies for obtaining favourable morphologies will be discussed in the following.

2.4.4.5 Use of Flowing Electrolyte to Improve the Zinc Electrodeposition Morphology

The use of flowing electrolyte, proposed for the first time by Naybour, is an effective method to minimise the dendritic growth during zinc depositions in Zn-RFBs [36,160]. Introducing a flow of the electrolyte to the system has two effects; firstly it enhances electrolyte mixing, causing uniform distribution of the Zn active species (zincate), and secondly, it reduces the thickness of Nernst diffusion layer, improving the nucleation rate of the deposition on the surface of the electrode [130,150,160,161].

Studies on improving Zn-RFB performance by controlling the morphology of zinc electrodeposition, have shown that there is a direct correlation between the limiting current density and the resulting deposit morphology. Moseley et al. reported that it is possible to achieve compact growth by operating below the limiting current density of electrodeposition [162]. Previous studies reported that in static electrolyte conditions and depending on the composition of the electrolyte (i.e. the concentration of zincate and pH of the solution), dendritic growth could take place at a low current densities, as low as 8 mA/cm^2 [162]. Thus, in order to operate the cell at typical current densities of 20 to 80 mA/cm^2, electrolyte circulation is necessary.

Under forced convection (by flowing the electrolyte), the corresponding limiting current density (i_{lim}) for the electrodeposition of zinc in static electrolyte, shown in the eq. 2-17, will increase. According to this formula, where F is the Faraday constant, D refers to the diffusion coefficient of zinc ions, and C_0 is the concentration of the zincate in the bulk electrolyte, the presence of flow in the system will decrease the thickness of the Nernst diffusion layer (δ). Thus, the dendritic morphologies tend to develop at a higher limiting current density, compared to a stagnant electrolyte, as a consequence of more uniform concentration gradients on the surface of the electrode [163].

$$i_{lim} = \frac{nFDC_0}{\delta} \qquad \text{eq. 2-17}$$

Weng et al. assessed the dependency of the morphology of the zinc electrodeposition under a wide range of conditions [138]. Similar to previous works [155,160] , it was found that the morphology of the deposit can be improved by operating at current densities below the diffusion limiting current density, and that the diffusion boundary depends on the condition in which electrodeposition occurs [138].

Ito et al. investigated the transition of the zinc morphology under a flowing alkaline electrolyte in a comprehensive study [164]. The author related the relationship between zinc growth and current density to the ratio of the effective current density and limiting current density. Based on the defined relationship, it was found that (as evidenced by SEM and micro-computed tomography (µCT)), compact zinc deposition is achievable at current density ratios above 0.9, while at current density ratios below 0.4, a mossy and porous morphology was observed [164].

Yu et al. investigated the effect of flowing electrolyte on the lifespan of Zn-based flow batteries [165]. The authors demonstrated that by introducing a flow of the electrolyte into the system, its lifespan (at current density of 10 mA/cm^2) was increased from 900 cycles (60 hours) with static electrolyte to 2850 and 4725 cycles (315) at electrolyte flow rates of 4.5 mL/min and 7.5 mL/min respectively [165]. This improvement in the lifetime of the cell was correlated to the more uniform distribution of the zinc ions in the presence of flowing electrolyte, therefore, suppressing dendritic growth during Zn deposition.

2.4.4.6 Use of Additives to Suppress Dendritic Growth

Previous studies reported in the literature have shown that additives utilised in the electrolyte formulation lead to finer deposition grain sizes, by promoting the two-dimensional growth of the zinc deposits on the substrate [166]. The formation of finer crystal grains can be attributed to the growth mechanisms explained in Section 2.4.4.2, and the previous theories suggesting that the deposition at a lower overpotential could result in a higher nucleation rate [128,167].

Metals such as mercury, lead and cadmium have been previously added to the electrolyte to improve the Zn electrodeposition morphology [36,168]. These metals have been used due to their high HER overpotential and are effective inhibitors of dendritic growth of the Zn deposits on the electrode. These additives suppress the dendrite growth by blocking the active deposition sites on the previously deposited Zn metals, facilitating the deposition on the substrate [169]. However, due to the environmental impacts caused by these metals, have made the use of these additives' undesirable.

Organic additives have recently received considerable attention as their presence in electrolyte promotes more refined grain sizes, resulting in uniform zinc deposition [170]. In one of the most recent studies on the use of additives in Zn RFBs, Trudgeon *et al*. examined sixteen different electrolyte additives to assess the effect of additives on the morphology of zinc deposition and on the performance of the zinc-nickel RFB [169]. The authors found that tetraethylammonium hydroxide and tetraethylammonium bromide were the most promising amongst the tested additives [169]. At a current density of 20 mA/cm^2, these additives in alkaline electrolytes demonstrated a 10% improvement in energy efficiency when compared to electrolyte without any additives, and maintained a cycling coulombic efficiency of 95-97% [169].

2.4.4.7 Characterisation of Zinc Electrodeposition Morphology and Microstructure

Since the very first study on the morphology of zinc electrodeposition by Naybour [160], different characterisation techniques have been used to investigate the microstructural and morphological compositions of the Zn deposits. Nabyour used scanning electron microscopy (SEM) to study the morphology of zinc deposition at different flow rates and was able to identify compact, boulder-like and dendritic deposition morphologies [160]. Bockris et al. also used SEM to examine the effect of overpotential and electrolyte concentration on zinc electrodeposition morphology [125].

Bannik and Akolkar used optical microscopy to perform live observation and tracking of dendrite evolution during Zn electrodeposition in alkaline electrolyte [171]. In this study, the authors mainly focused on characterising the effect of polyethyleneimine additive concentration on dendrite suppression and performed the study under static electrolyte conditions.

Popoola et al. using focused ion beam scanning electron microscopy (FIB-SEM) and atomic force microscopy (AFM) conducted a comparative study of microstructural properties of the plated Zn and Zn-Alloy coating, and found that the presence of aluminium alloy resulted in a homogeneous deposition [172]. Wu et al. also used FIB-SEM to study the cross-section of the zinc electrodeposition and found that the presence of iron (Fe) suppresses the dendritic growth of zinc deposition [173].

Surface characterisation techniques such as optical microscopy and SEM enable imaging of deposition structures at remarkably high resolutions and provide a wealth of microstructural information; however, most of the Zn deposition studies employing these techniques are ex-situ as developing more realistic in-situ experimental setups to facilitate real time tracking of deposition growth (particularly under realistic flowing conditions) using these techniques is not trivial.

It is clear that most of the prior work on the electrochemical formation of zinc deposition involved studying the morphology of the final deposit and comparing the final surface composition of the deposits, obtained at different conditions, such as different electrolyte flow velocities or different electrolyte compositions at the presence of additives. Hence, using these ex-situ characterisation techniques, such as SEM, does not provide any information related to the intermediate processes which leads into the final growth morphology.

However, recent advances in electrochemical cell designs and scientific instrumentation have enabled operando and in-situ studies of metallic dendrite formation. Gallaway et al., using synchrotron X-ray computed (XCT) tomography carried out an in-situ study on the effect of bismuth additives on morphology of zinc electrodeposition and it was observed that bismuth suppressed the dendritic formation of the Zn deposition [174]. Biton et al. used FIB-SEM tomography to obtain high resolution 3D images of a single zinc dendrite which was used to model mechanical failure of dendrites upon their detachment from the substrate [175].

X-ray microscopy techniques have rapidly advanced in recent years and has enabled characterisation of metallic dendrite structures in 3D with remarkable resolution. Unlike FIB-SEM imaging, the non-invasive nature of X-rays makes X-ray imaging techniques particularly suitable for conducting in-situ and operando studies at multiple time and length scales. Time-resolved X-ray computed tomography (XCT) has been successfully used to investigate the evolution of morphologies of the 3D microstructure of various metallic alloys during solidification in metal casting processes; however, it has only recently been extended to the operando study of electrochemical systems [175–180].

Yufit et al. presented operando visualisation and multi-scale tomography studies of dendrite formation and dissolution in zinc-based batteries [124]. The authors reported, for the first time, on the use of synchrotron X-ray radiography and tomography to capture the real-time growth and dissolution of electrodeposited zinc dendrites in 2D and 3D. The X-ray imaging experiments in their work were conducted using a bespoke X-ray transparent cell which did not enable flowing electrolyte conditions.

The following work reported in this Chapter 6 takes into consideration the limitations of the work from Yufit et al. to develop a more sophisticated electrochemical cell design that facilitates the use of X-ray

radiography and XCT to study in real time the morphological evolution of zinc electrodeposition microstructure under flowing electrolyte conditions, as well as other phenomena affecting deposition morphology such as hydrogen evolution reactions.

2.4.4.8 X-Ray Computed Tomography

X-ray radiation, due to its penetrating nature, has been extensively employed in imaging applications. X-ray radiography, a non-destructive technique, uses this nature of X-ray radiation for visualising the interior features of a solid object. In this characterising technique, information is obtained by measuring the amount of the transmitted X-rays, and these measurements are presented in the form of a 2D image. X-ray computed tomography (XCT) generates a 3D image of the internal features by reconstructing the 2D X-ray projection images or radiographs, while the object of interest is rotated about a single axis perpendicular to the X-ray beam [181–183].

Figure 2-18, illustrates the basic principle of the XCT imaging technique. In a standard XCT, when a beam of X-rays, generated from an X-ray source, is directed to a rotating sample, they are absorbed, scattered, or transmitted through the sample. The transmitted X-rays are recorded by the X-ray detector. Scintillator converts the recorded X-rays by the detection system to a visible light, resulting in visible images. These 2D images are progressively obtained and digitised into a computer, where by further processing, a 3D image of the object can be created [181,183]. The 3D image can be produced by mathematically reconstructing the acquired 2D projection (radiographs) images.

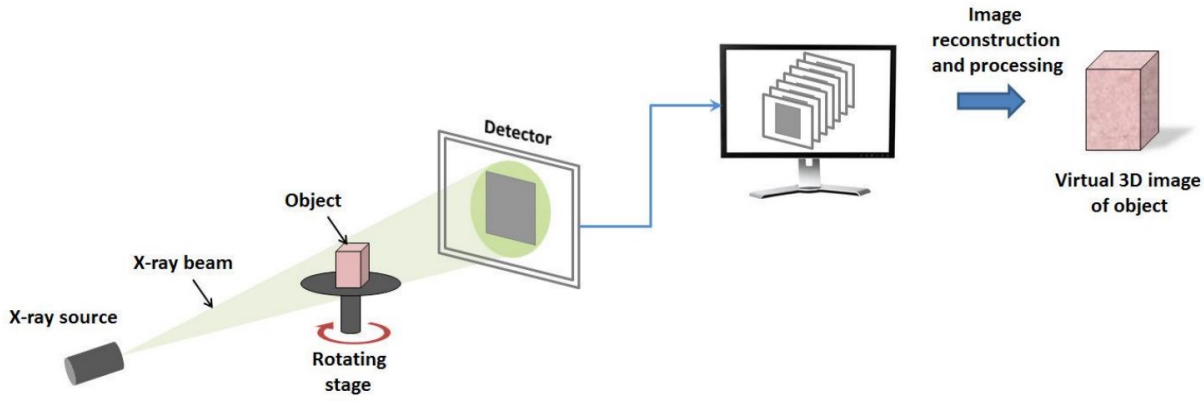

Figure 2-18: Schematic of the basic principle of X-ray computed tomography [183]

While 2D projection images are composed of picture elements (pixels), CT images are composed of volume elements (voxels) from which, through a specialized algorithm the distribution of x-ray attenuation of the volume that is being imaged, a 3D image is reconstructed. Attenuation reflects the amount of X-ray energy absorbed. The attenuated X-ray is a function of the density and composition of the object that is being imaged, which this relationship is defined by the Beer-Lambert's law (eq. 2-18), where I is the intensity of the X-ray beam (with length of X) after passing through the object, I_0

refers to the intensity of the X-ray beam incident to the object, and μ (cm^{-1}) is the linear attenuation coefficient of the object.

$$I(x) = I_0 e^{-\mu x} \qquad \text{eq. 2-18}$$

In most laboratory X-ray sources, X-ray attenuation is function of two dominant physical processes:

Photoelectric absorption: In this process the total energy of the incoming X-ray beam (photons) are transferred to the inner electrons of the elements in the material and this energy ejects the electron. This process is the dominant mechanism at low X-ray energies, between 100-150 keV.

Compton scattering: This is the process in which the incoming X-ray photons interact with the outer electrons. In this process, only part of the photon energy is lost by ejecting the electrons, hence, the photons are deflected in a different direction [182]. This process becomes predominant at higher energies compared to the absorption process [184].

2.5 Redox Flow Battery Fundamentals

The key distinction between an electrochemical and chemical redox reaction is that, in a chemical reaction, both reactions (oxidation and reduction) occur in same compartment while in an electrochemical cell, reactions are spatially separated from each other. Thus, the complete reaction takes place in separate half-cells (electrodes). Although the redox reactions occur at separate half-cells, but the rate of the reactions are in correlation with "*the principle of conservation of charge and electroneutrality*". Consequently, all the electrons or the current leaving an electrode, must enter the opposite terminal. This also applies to the ions at their IEM interface with the electrodes, where the flow of ions is continuous from one half cell to the other.

2.6 Electrochemical Principles and Reactions

The general form of reaction, in any electrochemical cell, is the combination of oxidant (O) in the anode, and reductant (R) in the cathode, as given by eq. 2-19. In this section, two half-cells are referred as left and right electrodes. In batteries and fuel cells, **polarization** refers to the change in potential from its equilibrium conditions, due to the flux of electrons. **Overpotential** refers to the drop of potential caused by the resistance in flux of electrons in the cell.

Overall cell reaction $$O + xe^{-} \rightleftharpoons \mathrm{R} \qquad \text{eq. 2-19}$$

The rate of this reaction is related to the flow of electrons (current) by Faraday's law. According to this, the total mass produced from this reaction is in correlation with "the amount of charge passed multiplied by the weight of species. eq. 2-20 demonstrates, the relationship between producing mass of species *i* (m_i), with its molar mass (M_i), stoichiometric coefficient (s_i), number of electrons that are

transferred (*n)*, total amount of charged transferred (*I*) in period of *t* and *F* is the Faraday's constant (96,487 coulombs/mol).

$$m_i = -\frac{s_i M_i I t}{nF} \qquad \text{eq. 2-20}$$

In any electrochemical cell, the maximum electrical energy that can be stored in or supplied by the cell depends on the change in Gibbs free energy (ΔG) of each half cell reactions, given in eq. 2-21. This indicates that the Gibbs free energy is the difference between free energy of the products (right electrode) and reactants (left electrode), where μ_i is the electrochemical potential of the redox species. This also indicates the direction of electrons flow in the cell, where if ΔG is negative, electrons will flow from left to right, and if positive, the opposite will occur.

$$\Delta G = \left(\sum_i s_i \mu_i\right)_{Right} - \left(\sum_i s_i \mu_i\right)_{Left} \qquad \text{eq. 2-21}$$

However, at a certain potential, which is also referred as equilibrium, there will be no electron transfer between two half-cell electrodes. This potential is referred as **open-circuit potential** (E_{OCP}), which is written in form of eq. 2-22 relating it to Gibbs free energy. According to this definition, there is no net current flux in the system, but there are internal reactions among the existing species in two electrodes. However, the rate of forward reactions and opposite (backward) reactions are equal. Thus, OCP is a function of the intrinsic nature of the present species, their concentration as well as the temperature.

$$\Delta G = -nFE_{OCP} \qquad \text{eq. 2-22}$$

Equilibrium potential or E_{OCP} of the electrons can be related to the concentration of the oxidants and reductants (reactant and Products) by the Nernst equation. As stated in eq. 2-23, concentration of the oxidant (C_O) and the reductant (C_R) depends on the state of charge (SOC), which effects the thermodynamic potential of the cell. In this equation, *R* is the universal gas constant (8.314 J/mol.K), *T* is temperature in Kelvin and E^0 is the standard potential of the species in the cell, independent of the concentration.

$$E_{OCP} = E^0 + \frac{RT}{nF} ln\left(\frac{C_O}{C_R}\right) \qquad \text{eq. 2-23}$$

The electrochemical potential of electrons within the cell can be controlled, where by perturbing the equilibrium, reactions in the cell can be facilitated. By the means of an external power- supply or a load-bank, negative or positive potential can be applied to the electrodes. Applying a negative potential (relative to the OCP potential) to the cell initiates the transfer of electrons from the reactant

to electrode in the anode (oxidation). Contrary to the anode, at the cathode electrons transfer from electrode to the reactant, where reduction occurs. Opposite to this, when a positive potential applied to the cell, which is higher than the equilibrium potential, electrons in the half-cell with a lower overpotential will transfer from the reactant to the electrode, and migrate to the other half cell, where they will be transferred to the reactant from the electrode. This mechanism is summarised in Table 2-3.

Table 2-3: Oxidation and Reduction reaction depending on the applied potential to the electrochemical cell in relation to the equilibrium potential

E_{OCP}	$E_{applied}$	E_{cell}	Left	Right
A	B	A+B>A	Cathode	Anode
A	B	A+B<A	Anode	Cathode

2.7 Electrochemical Overpotential and Electrode Kinetics

In any system, it would be desirable to convert all the energy in the system (or supplied to the system) into useful electrical energy. However, different phenomena accompanying the electrochemical reactions, result in losses due to the polarization in the system. Polarization can be defined as "*an electrochemical process, which deviates overall potential from the equilibrium potential due to inducing a flow of electrical current though the cell*" [185]. These losses, illustrated in eq. 2-24, consist of:

$$E = E_{OCP} - \eta_a - \eta_{ohm} - \eta_c \qquad \text{eq. 2-24}$$

- **Activation polarization (η_a)**: is the difference in potential, in relation to the equilibrium potential, required to transfer the electrons from electrode interface into the reactant.
- **Ohmic polarization (η_{ohm})**: is the loss due to charge transport. This is a product of the intrinsic resistance of the cell components. This includes electronic resistance of the components such as, electrodes, current collectors, electrolyte and the flow plates; and ionic resistance of the IEM.
- **Mass transport polarization (η_c)**: arises due to the difference in concentration of the reactant and product at the flow plate surface and the electrode, as a result of mass transfer.

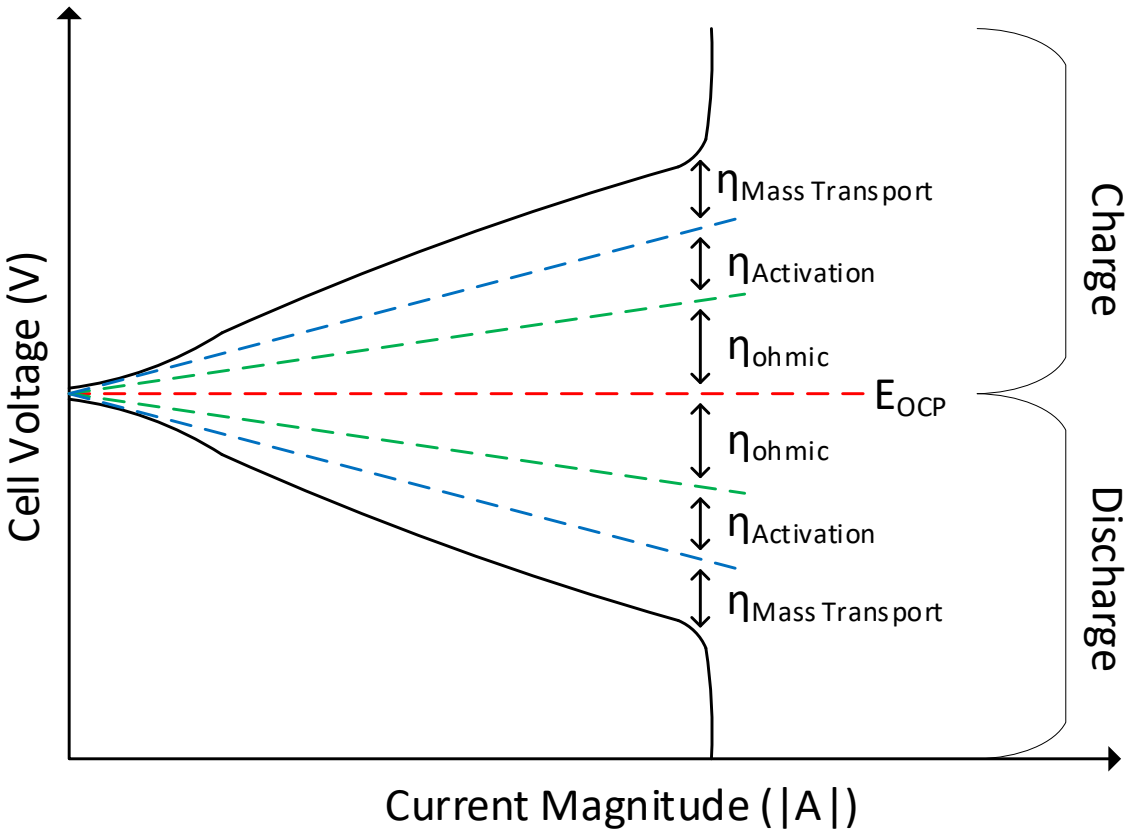

Figure 2-19: Cell polarization as function of operating unit current

Although the amount of the storable energy in an electrochemical system depends on the electrochemical reactions at the anode and cathode compartment, there are different factors that influence the magnitude of the diffusion rates, charge-transfer reaction and as a result, the magnitude of the energy loss. These factors include flow plates design and material, electrolyte conductivity, and nature of the IEM (or separator). Based on the electrochemical principles, there exists certain essential rules, which dictate the design of flow batteries to achieve a high efficiency with minimal energy loss.

Figure 2-19 demonstrates the inefficiencies in a flow battery, as discussed previously, each of the polarizations relates to different components in the cell. In order to be able to optimise the cell performance, it is crucial to understand these losses:

2.7.1 Activation Polarization

Activation polarization is associated with the energy required to activate the electrochemical reactions in the electrode. The activation polarization overpotential (η_a) can be determined by the Butler-Volmer equation in form of eq. 2-25, where i_0 is the exchange current density, i is the current density and α is the charge transfer coefficient. The charge transfer coefficient can be defined as "*the fraction of the electrostatic potential energy affecting the reduction rate in an electrode-electrolyte interface*

reaction" [186]. The Butler-Volmer equation applies to the charge transfer controlled region, where the difference in concentration between bulk and reaction media solution is less than 10%. The activation overpotential can be further simplified to eq. 2-26 and expressed in the form of Tafel equation.

$$i = i_0 \left[exp\left(\frac{\alpha_a n F \eta_a}{RT}\right) - exp\left(\frac{-\alpha_c n F \eta_a}{RT}\right) \right] \quad \text{eq. 2-25}$$

However, this is only applicable to the high overpotential region. As it can be seen in Figure 2-20, at small overpotentials.

$$\eta_a = a - bln(i) \; when \; \eta_a \ll E_{OCP} \quad \text{eq. 2-26}$$
$$\eta_a = a + bln(i) \; when \; \eta_a \gg E_{OCP}$$

2.7.2 Ohmic Polarization

Ohmic drop or polarization is the intrinsic resistance of the components during the transport of electrons and/or ions through the cell. Ohmic drop relates to components such as flow plates, current collectors and the IEM. In RFC, since IEM has the role of transferring protons, the ohmic drop (eq. 2-27) is dominated by the ionic resistance (R_{ionic}).

$$\eta_{ohm} = iR_{ohmic} = i(R_{ionic} + R_{electronic}) \quad \text{eq. 2-27}$$

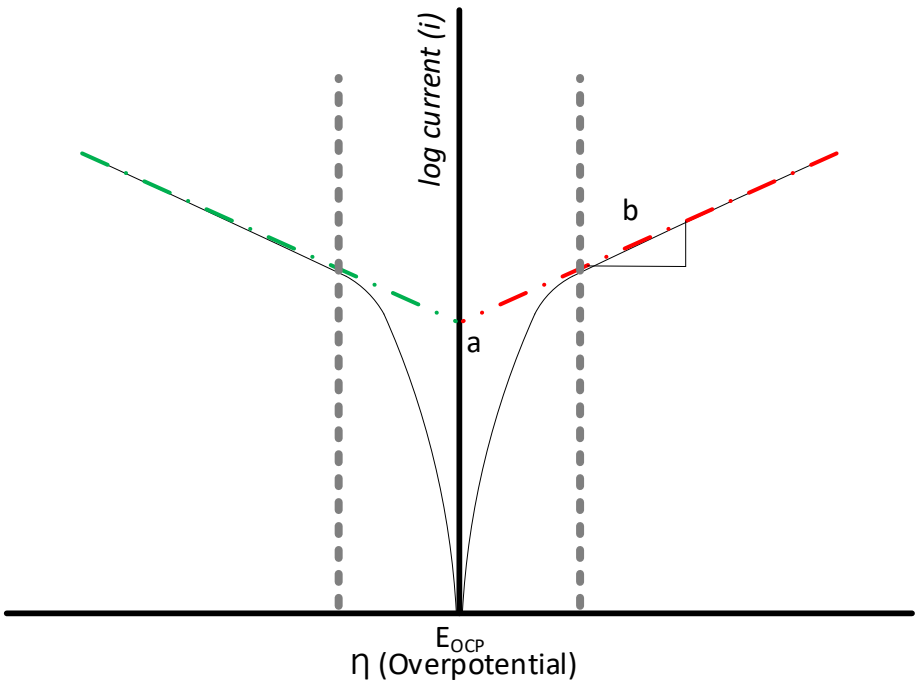

Figure 2-20: Tafel Plot showing different logarithmic current at different overpotentials, where a represents the exchange current density and b is the Tafel slope

2.7.3 Mass Transport Polarization

As can be seen in Figure 2-19, mass transport or concentration polarization usually dominates in the high current density region. At high current density ranges, the current flowing in the cell largely

depend on the diffusion of active species from the bulk electrolyte to the electrode surface. However, it is possible that, due to slow kinetics of the electrochemical reactions or high internal resistance in the cell, mass transport losses may not become apparent in the polarization curve. This polarization is best described in the form of eq. 2-28, where i_{lim} is the liming current density.

$$\eta_c = \frac{RT}{nF} ln\left(\frac{i_{lim} - i}{i_{lim}}\right) \quad \text{eq. 2-28}$$

2.7.4 Extra Losses Associated With an RFC

Beside the main three electrochemical losses introduced previously, in RFBs, due to crossover of the electroactive species from one half-cell to another through the IEM, loss in capacity can occur. Depending on the chemistries used in the flow battery, these losses can lead into a permanent loss capacity. However, in RFCs, utilising hydrogen or other gasses as one of the reactants, permanent capacity loss can be limited by collecting the electrolyte that appears in the gas half-cell, but this by itself requires some extra measures to be able to retrieve the lost capacity.

2.8 Critical Performance Evaluation Terms

The specific energy of different flow battery systems was listed in Table 2-1. These values are usually obtained in optimum design and performance conditions. Thus, the performance of the batteries may differ under different operating conditions. In this section, influencing factors on performance characteristics of batteries will be discussed. Important merits in evaluating electrochemical systems performance are power and energy density, capacity and energy, voltage and coulombic efficiencies.

Previously, in Section 2.1, it was noted that in flow batteries power and energy densities can be decoupled. **Power density** (W/cm^2) is the amount of energy transferred at a given time per active unit area of the electrochemical cell and can be calculated using eq. 2-29, where $P_{(t)}$, $V_{(t)}$and $I_{(t)}$ are the power, current and voltage respectively. This figure of merit is characteristic of the single unit cell (depending on the RFB chemistries); thus, in order to achieve higher power[d], it is possible to either increase the number of the cells or increase the active surface area.

$$P_{(t)} = \frac{V_{(t)} . I_{(t)}}{A} \quad \text{eq. 2-29}$$

On the other hand, the amount of energy available in the system is referred to the **capacity**. Capacity, contrary to the power density, depends on the volume and concentration of the active species. Charge

[d] Power = power density X Area X Number of the cells

or discharge capacity (Ah), shown in eq. 2-30, measures the amount of current flown through the cell at given period.

$$Q_{exp} = \int_0^{t_{max}} I_{(t)} dt \qquad \text{eq. 2-30}$$

It must be noted that for a given electrolyte, the maximum measured capacity can differ from the maximum **theoretical capacity**. The latter is determined according to eq. 2-31, where N is the number of the moles of the active species in the electrolyte, n refers to the number of electron per mole, and F is the Faraday constant.

$$Q_{theory} = \frac{N.n.F}{3600} \qquad \text{eq. 2-31}$$

Energy density of the system, described in eq. 2-32, provides the amount of extractable energy stored in per unit mass of the electrolyte. Energy density, measured with SI unit of Wh/kg, where $I_{(t)}$ refers to the current and m is the mass of the electrolyte.

$$\mathrm{E} = \frac{\int_0^t V_{(t)}.I_{(t)} dt}{m} \qquad \text{eq. 2-32}$$

The mentioned parameters are important factors in determining the suitable applications for each system. However, in order to understand the feasibility of different systems for different applications, it is important to be able to define the evaluation parameters, where it can relate to their performance. Thus, different efficiencies are used as a figure of merit to make each system comparable to other systems.

Voltage efficiency (VE) determines the effects of cell voltage losses or polarization, which represents the ratio between average discharge and charge voltage. Various losses, defined in section 2.7, will reduce this efficiency; by reducing these losses, it is possible to maximise the cell efficiency. Voltage efficiency (η_v) is calculated via the following equation:

$$\eta_v = \frac{\langle V_{discharge} \rangle}{\langle V_{charge} \rangle} \times 100\% \qquad \text{eq. 2-33}$$

Current efficiency or **coulombic efficiency (CE)** determines the ratio between the total charge extracted and the total current flown into the electrochemical cell. This performance evaluation parameter can be calculated using eq. 2-34.

$$\eta_c = \frac{\int_0^{t_d} I_{discharge}.dt_d}{\int_0^{t_c} I_{charge}.dt_c} \qquad \text{eq. 2-34}$$

Finally, energy efficiency defines ratio between the energy that could be extracted from cell and the energy that could be stored in the cell. Energy efficiency can also be expressed in terms of voltage and coulombic efficiency, as shown in eq. 2-35.

$$\eta_e = \eta_v \times \eta_c = \frac{\int_0^{t_d} V_{discharge}.I_{discharge}.dt_d}{\int_0^{t_c} V_{charge}.I_{charge}.dt_c} \quad \text{eq. 2-35}$$

2.9 Electrochemical Characterisation Techniques

Electrochemistry embraces the study of chemical changes across the medium caused by the flow of an electrical current, as well as the energy produced by chemical reaction. In addition, electrochemistry also deals with exploring electrolyte solutions and the chemical equilibrium that occur in the solutions. Using electrochemical analysis, electric potential and electric current in an electrochemical cell can be measured. The two main aspects of a cell can be measured by two different methods, consisting of **Potentiometry** and **Voltammetry.** Potentiometry is the measurement of the change in Potential of the cell over time and voltammetry relates to controlling potential and measuring current. Another technique to characterise the electrochemical behaviour of the system is **electrochemical impedance spectroscopy** (EIS). EIS measures the resistive and capacitive properties of the materials in the system [35,187]. In this section, fundamentals related to both cyclic voltammetry (CV) and EIS methods will be investigated.

2.9.1 Cyclic Voltammetry (CV)

CV as an electrochemical technique that measures the change in current developed by changing the potential at a given rate. This measurement involves applying a potential to the working electrode such that the current flowing through the working electrode (as a function of applied potential) is recorded. Using this method, information related to the electrochemical process, such as reversibility of reaction and diffusion coefficient of the active species in the electrolyte, can be determined.

To carry out this type of measurement, the potential between a lower and upper limit is swept at different rates (mV/s). Due to the cyclic nature of the potential scan both the cathodic and anodic responses are seen during the scan and, because the scan covers a large potential window, areas of high and low overpotential are imposed. This produces an anodic and cathodic curve, often referred to as a wave.

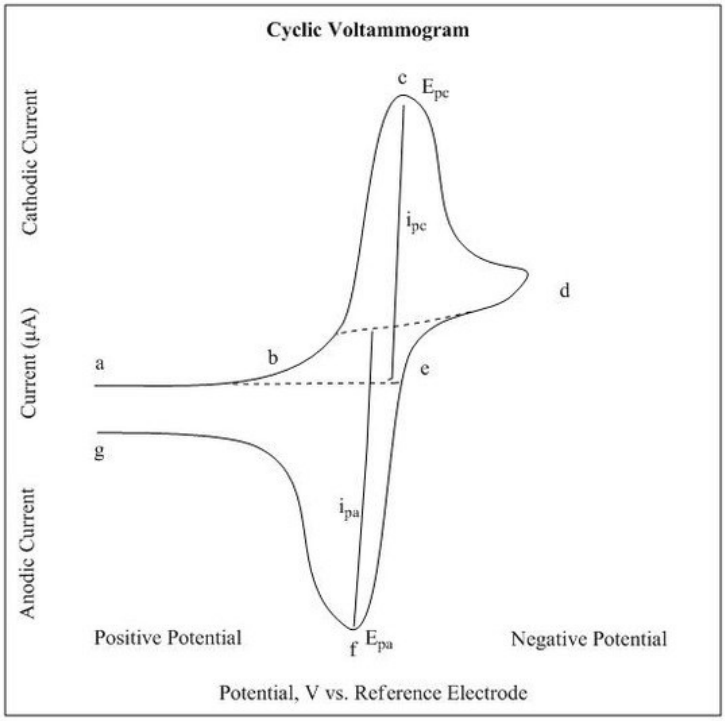

Figure 2-21: Cyclic voltammetry of electrochemical process in a single electron process

According to Figure 2-21, the points of anodic (I_{pa}) and cathodic (I_{pc}) peak currents represents the point where oxidation and reduction process occur in the cell respectively. The separation of these peaks indicates the reversibility of these processes. Anodic (E_{pa}) and cathodic (E_{pc}) peak potentials are reached when all the redox couple active species at the surface of the electrode has been oxidised and reduced respectively.

2.9.2 Electrochemical Impedance Spectroscopy

EIS is a characterisation technique with the ability to evaluate electrochemical mechanisms at the interface of the electrode with the electrolyte. This technique is a quantitative method to determine the resistance of elements in the cell to current flow, from which a wide range of information can be obtained. In this section, the EIS technique will be explained, where most of the information are summarised from three different books [188–190].

Electrical resistance (R) in an ideal resistor is defined by Ohm's law, shown in eq. 2-36. The relationship between potential (E) and current (I) is only applicable for direct current (DC). However, this law can also apply to alternating current (AC), where the frequency is 0 Hz. impedance (Z), measures the opposition of the components or circuit in a system to the flow of alternating or direct current.

$$R = \frac{V}{I_{DC}} \qquad \text{eq. 2-36}$$

In electrochemical systems, when the frequency of the AC current is non-zero, impedance takes into account the resistance contribution from capacitors, resistors and inductors. Following this explanation, the impedance is described as complex resistance vector ($\hat{Z}$), which can be presented in form of a polar equation (eq. 2-37) and in terms of Cartesian coordinates (eq. 2-38). Complex impedance in Cartesian form consists of the real component resistance (Z_R) and imaginary resistance (Z_{Im}) contributed by both inductance and capacitance.

Polar Form: $$\hat{Z} = Ze^{i\theta}$$ eq. 2-37

Cartesian Form $$\hat{Z} = Z_R + iZ_{Im}$$ eq. 2-38

In EIS measurements the magnitude of the signal excitation determines the noise to signal ratio. This ratio must be sufficiently low that the system remains in the linear region. The magnitude and phase of voltage or current, resulted from signal excitation, provides insight about the processes occurring in the tested system.

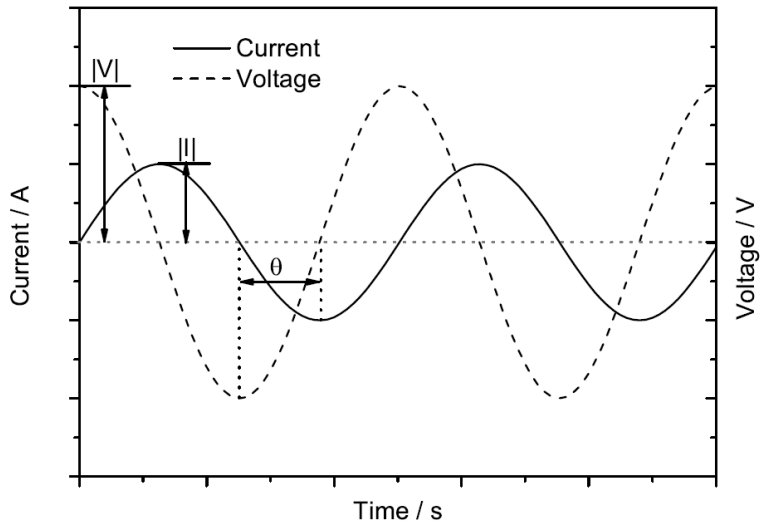

Figure 2-22: Current and voltage oscillation in EIS measurements [191]

According to Figure 2-22, it can be seen that by applying a sinusoidal current, which is known as EIS under galvanostatic control, the voltage response to changes in applied current is measured. The applied current with an amplitude of $|I|$ at a frequency f results in voltage response with an amplitude of $|V|$ at the equivalent frequency and a phase shift θ with respect to the current signal. According to these definitions, the current and voltage response can be written as eq. 2-39 and eq. 2-40.

$$V(t) = |V|\sin(\omega t)$$ eq. 2-39

$$I(t) = |I|\sin(\omega t + \theta)$$ eq. 2-40

According to these equations, the impedance of the system can be therefore defined as the ratio between applied current and measured voltage response. The impedance of a such system is given in eq. 2-41.

$$Z(\omega) = \frac{V(\omega)}{I(\omega)} \qquad \text{eq. 2-41}$$

Representing the described impedance in terms of Cartesian coordinates, illustrated in Figure 2-23 (a), can evaluate the contribution of the real and imaginary components into impedance. Therefore, combination of these two components can be used to find the magnitude of the impedance ($|Z|$), using eq. 2-42, and phase angle θ using eq. 2-43.

$$|Z| = \sqrt{{Z_R}^2 + {Z_{Im}}^2} \qquad \text{eq. 2-42}$$

$$\theta = \arctan\left(\frac{Z_{Im}}{Z_R}\right) \qquad \text{eq. 2-43}$$

Using the impedance vector, it is possible to produce a Nyquist plot, shown in Figure 2-23 (b), which can be used to evaluate the real and imaginary impedance. In this plot, along the x-axis, real impedance data is plotted, and negative imaginary components impedance is graphed along the Y-axis of the plot. This plot can be used to characterise the frequency dependency of the electrical component exist in the system to impedance responses. As demonstrated in the Nyquist plot, it is possible to identify the various processes occurring in the system, where the low frequency region on right end of the semi-circle represents the sum of the ohmic and non-ohmic resistances, and the higher frequency intercept at the origin of the graph represents the contribution of ohmic resistance.

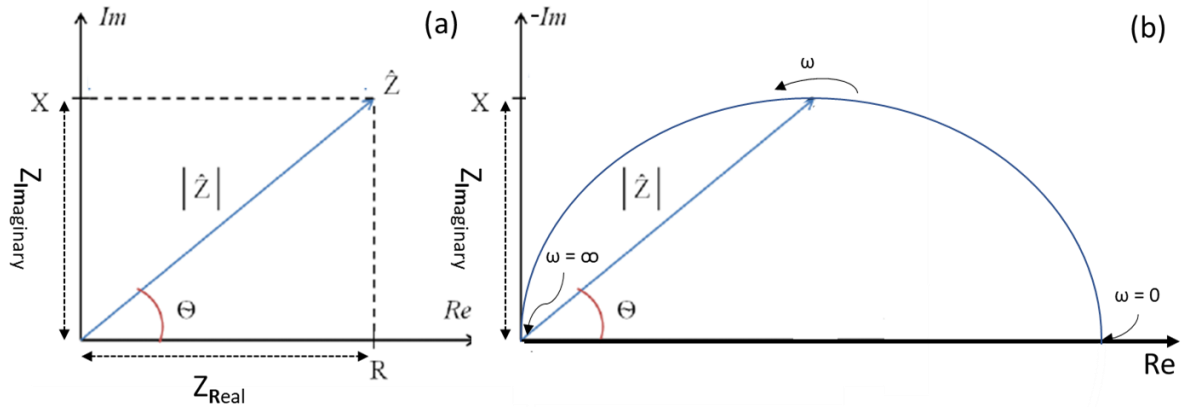

Figure 2-23: a) Cartesian form of the impedance, taking into account the contribution of real and imaginary components and b) its representation Nyquist plot of impedance data

In order to be able to interpret and extract useful data from EIS data and identify the underlying processes from these measurements, equivalent circuit fitting can be used. Therefore, to describe the

ongoing phenomenon within the system, simplified models are introduced which establish the relationships between impedance and each circuit element.

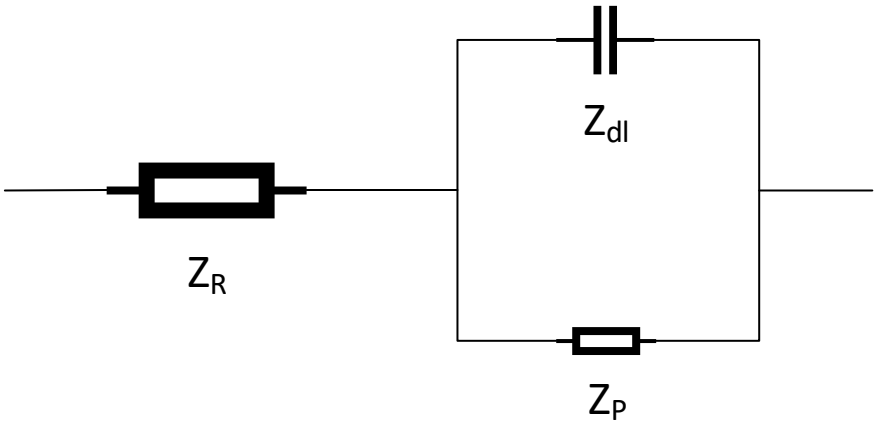

Figure 2-24: Equivalent circuit of Randles Cell

The Randles Cell circuit, illustrated in Figure 2-24, is the most common analog circuit model that represents the equivalent circuit for the electrolyte and electrode interface within an electrochemical cell. This model takes into the account the uncompensated resistances such as polarisation resistance (Z_P), series resistance (Z_S) and double-layer capacitance (Z_{dl}). Series resistance has an impedance which is independent of frequency and does not contain an imaginary part. Hence in a Nyquist plot, this resistor would be shown as a single point on the X-axis, representing the real impedance of the plot. Therefore, the series resistance can be presented as eq. 2-44, and properties such as temperature, ionic conductivity and electrodes material effect this resistance.

$$Z_R = R \qquad \text{eq. 2-44}$$

Typically, three main types of resistances are studied in EIS measurements of electrochemical systems. These consist of series resistance, which refers to the bulk resistance to flow of electrons through the conductive materials and ions in solution; charge transfer resistance, which is associated with faradaic mechanism at the electrode; and diffusion resistance, which refers to the mass transport limitations.

In regard to double-layer capacitance, it refers to the polarisation of ionic charges at the surface of electrodes. In any electrochemical cell, while charging the cell, charged ions will move toward the electrode surface, thus the surface area and size of ions will directly influence this double-layer capacitance. At 100 % state of charge, as a result of ion adsorption and double layers, the electrode will act as a capacitor to store the charge. A capacitor's impedance response is presented in eq. 2-45, and only consist of an imaginary component, where j is the complex component, C is the capacitance and ω represent the frequency.

$$Z_{dl} = \frac{1}{j\omega C} \qquad \text{eq. 2-45}$$

Polarisation resistance represents the restriction of charge transfer at the interface of electrolyte and electrode. This phenomenon occurs when the potential of the electrochemical cell is pushed out of equilibrium (by applying external potential), which initiates charge transfer through electrochemical reactions. Hence the magnitude of this resistance is affected by the kinetics of the reactions and the mechanism of current interaction with the electrode. Polarisation resistance, given in eq. 2-46, similar to double layer capacitance only includes an imaginary component. Inductive effects are predominant at high scan frequencies, mainly as a result of the inductive properties and finite length of measurement wires.

$$Z_P = j\omega C \qquad \text{eq. 2-46}$$

In a real electrochemical system, where complex processes are occurring within the cell, combination of these three resistive elements (inductor, capacitive and series resistance) do not necessarily represent the impedance response of all reaction and transport steps. Thus, in order to model the behaviour of the system impedance response, two main additional elements are used, consisting of Warburg elements and Constant Phase Elements (CPE).

The Warburg impedance, given in eq. 2-47, arises from the one-dimensional diffusion of species (a) to the electrode. In this equation the Warburg parameter (σ_a) is dependent on the properties of the species a, such as its reaction rate, concentration in electrolyte, diffusivity of the species and the current density and potential of the system [192].

$$Z_{\omega,a} = \frac{\sigma_a}{\omega^{1/2}\,(1+j)} \qquad \text{eq. 2-47}$$

CPE impedance can be expressed in form of eq. 2-48, where φ and T are CPE parameters. Using this equation, all three resistors consisting of pure resistor, pure inductor and pure capacitor can be described. A CPE, depending on its parameters, can behave in of the three resistors form. This equation represents a pure resistor when $\varphi = 0$, and when $\varphi = 1$ or $\varphi = -1$ it behaves as pure capacitor or inductor respectively. The Warburg element can also be represented as a CPE element when $\varphi = 0.5$, and in general a CPE element is used to illustrate the charge transfer resistance of a rough or non-ideal electrode.

$$Z_{CPE} = \frac{1}{T(j\omega^{\varphi})} \qquad \text{eq. 2-48}$$

2.10 summary

In this chapter different developed energy storage technologies were identified and analysed, and the necessity of using intermittent renewable energies was highlighted. The key factors impeding redox

flow batteries to be considered as a potential candidate to combine with other electrochemical devices as a mean of energy storage was studied. To be able to understand these factors, the most developed RFB technologies were explored in more detail. For systems such as hydrogen/bromine or all vanadium RFBs, factors such as the cross-contamination of active species, high cost of material and safety concerns were investigated. According to these findings, it was identified that there is still a gap to the production of a safe system at low cost. Based on the available technologies and the demand for low cost energy storage systems, highlighted in this chapter, two potential systems, RHMnFC and Zn-based flow batteries, were identified and discussed in more details.

By assessing these studies on adopting Mn chemistry for flow battery applications, there is a lack of knowledge in terms of choice of components, consisting of liquid half-cell electrode, hydrogen electrode and IEM. In addition, it is important to be able to understand the limiting mechanisms affecting the stability of the electrolyte, temperature dependency of the cell performance and achievable capacity using this technology. In next chapters to explore the factors determining the performance of RHMnFC, these gaps will be experimentally investigated.

Disproportionation of charged manganese (Mn^{3+}) active species is an inevitable phenomenon in Mn based flow batteries, given sufficient time. Different studies have been carried out to understand the mechanisms of Mn^{3+} oxidation and MnO_2 precipitation, where different methods to supress the disproportionation reaction have been recommended. The most common and effective method to supress manganese disproportionation is known to be the addition of Ti^{4+} as additives. An overview of the current state-of-the-art related to this method was given and discussed in detail. Analysis in different studies also suggested that increasing the H^+ concentration in the solution may be an effective method to supress the MnO_2 precipitation.

Reviews on the current state of research present a significant gap in understanding the mechanism by which Ti^{4+} supresses Mn^{3+} disproportionation. By elucidating the contributing mechanisms, there is the potential to develop a system for energy storage applications. Therefore, mechanisms that will determine the lifetime of the RHMnFC, such as the reversibility of the disproportionation reaction, stability of electrolyte at different temperatures and performance of the cell at different temperatures, requires further investigation.

Also, from an engineering point of view, it is necessary to understand the feasibility of scaling up and how the information obtained from experiments at the lab scale (small active area) cell translates into a larger active area. Therefore, it is important to identify the performance indicator factors affecting the viability of scale up.

Section 2.4.4 reviewed the fundamental principles of zinc electrodeposition in Zn-based RFBs. Additionally, mechanisms that affect the formation of different deposition morphologies were also discussed. It was also explained that the growth of Zn metal on the electrode substrate depends on different mechanisms such as nucleation rate and growth rate, where higher nucleation rates resulted in a more compact deposition compared to the bulbous or dendritic formation of Zn at higher growth rates. Another phenomenon that has an impact on the morphology of the deposition was shown to be the hydrogen evolution reaction, whose presence could enhance the mass transport and improve surface morphology.

Furthermore, Section 2.4.4.4 explored the methods through which formation of dendrites could be suppressed, resulting in a smoother deposition of the Zn metal on the electrode. Prior experimental studies showed that introducing a flowing electrolyte could result in improved deposition, by increasing the limiting current density. Also, studies on different electrolyte compositions have shown that additives could suppress dendritic growth.

In addition, characterisation techniques that were used in prior studies to investigate the morphology of the deposits were discussed. However, it was highlighted that using ex-situ techniques such as SEM would only enable analysis on the final deposit, and that intermediate processes were not well understood. Thus, previous studies did not capture the initial deposition steps, and the role of different phenomena on the formation of different morphologies, which are pivotal in providing quantitative evidence for growth mechanisms.

Therefore, to understand intermediate processes (such as initial growth) and the effect of suggested battery performance improvement methods (flowing electrolyte and/or additives in the electrolyte), it is necessary to develop an in-situ technique, where growth and dissolution of the Zn electrodeposition process could be studied in real-time. X-ray computed tomography characterisation, which will be the main method to study the Zn electrodeposition at different conditions, was briefly explained.

Finally, to be able to develop new system with potential to meet the technological requirements for energy storage applications, the fundamental theory of electrochemical systems was studied. In addition to these theories, the main parameters to be able to compare the performance of different technologies were defined, where these terms will be used throughout the thesis to evaluate the performance of the technology in question. Following introducing the fundamental equations and terms associated with electrochemical systems, two different electrochemical characterising techniques were investigated in detail.

Chapter 3 Experimental Set Up and Methodology

This chapter will be separated into three sections, where in the first section, primary the experimental methods such as cell assembly, electrolyte preparation and materials used to investigate the effect of each factor on the performance of the RHMnFC will be explained. This will be followed by discussing the experimental techniques used to take measurements to determine the performance of the technology in question. In addition, in order to scale up, several iterations to achieve an optimum design of larger flow plates will be demonstrated. Second section will explain the experimental methods used to investigate electrolyte stability, and the methods able to regenerate the degraded electrolyte as a result of the disproportionation of Mn^{3+} and the precipitation of MnO_2.

Third section of this chapter will present the design of a bespoke cell which enables the visualisation of Zn deposits on the surface of the electrode as they form in real-time. This will consist of illustrating the design of the test rig and explaining the material used to manufacture the cell. Furthermore, an overall schematic of the experimental setup and the equipment used to carry out these tests will be discussed. This will be continued by discussing the techniques used in this work to visualise and quantify the morphology of the electrodeposited zinc particles under different conditions.

3.1 Experimental Set Up to Investigate the Performance of Regenerative Hydrogen Manganese Fuel cell

3.1.1 Regenerative Fuel Cell Configuration

A commercial cell from Scribner Associates, shown in Figure 3-1, with a 5 cm^2 active area, was used throughout the project for lab testing. For ease of assembly, first the gold-plated copper current collector for the hydrogen half-cell was placed on top of the end plate. End plates are crucial components in any electrochemical flow cell, as they provide the mechanical support while applying the necessary compression to the cell components. Ultra-high purity POCO® graphite, with single serpentine flow channel, is placed on top of the current collector.

As the next step, a hydrogen electrode, which was explained in detail previously in Section 2.4.2.4, is cut to size and placed on the graphite plate along with the Tygerflo gaskets. Tygerflo gasket is a composite glass fibre material with a PTFE coated matrix, which gives sufficient sealing to eliminate any gas or liquid leakage from the active areas. Tygerflo gaskets are incompressible, thus the amount of compression applied to the electrodes will depend on the thickness of the gaskets used. This mechanical property of Tygerflo makes the use of these gaskets advantageous over conventional compressible Viton (FKM) gaskets.

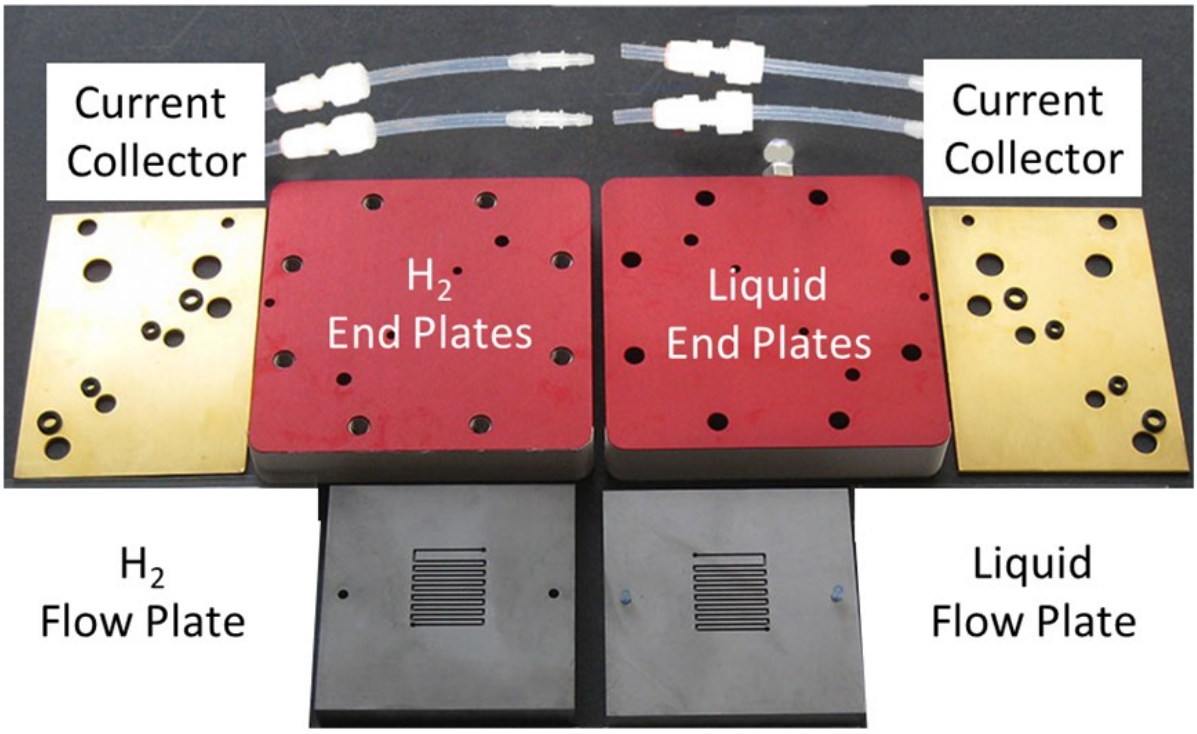

Figure 3-1: Scribner flow battery assembly with 5 cm^2 active area

As discussed in Section 2.4.2.4.2, to achieve an optimum performance, a certain level of compression is required for different electrodes, and according to these findings, the hydrogen electrode was compressed to 80% of its initial thickness, and the graphite felt was compressed by 25%. Following the placement of the gaskets and MEA, similar to the hydrogen side, on the liquid side, a serpentine graphite plate was placed on top of the MEA and gaskets, which was followed by placing a current collector and an aluminium end plate on top of the flow plate.

3.1.2 Selection of Membrane Electrode Assembly components

In order to achieve desirable performance and identify the best MEA components, different electrodes and membranes were tested. The different MEA components used in this phase of the work are discussed below.

3.1.2.1 Anode Electrode (Hydrogen Electrode)

The role of the hydrogen electrode in electrochemical cells, utilising hydrogen as its fuel, has been explained in Section 2.4.2.4.1. It was also identified that Pt loading can determine the kinetics of the hydrogen evolution and oxidation reaction. In this work, in order to understand the effect of Pt loading on the performance of the RHMnFC, two different hydrogen electrodes were tested. Hydrogen electrodes with 0.3 mg/cm^2 and 0.03 mg/cm^2 Pt loading on a Vulcan-Carbon cloth, with 400 µm thickness, were used to compare the effect of Pt loading on cell performance. These electrodes also

contained 40% PTFE content to facilitate liquid transport, which accumulates during discharge or crossover, out of the cell.

Previously, in the Electrochemistry group, in order to understand the effect of Pt loading on hydrogen oxidation during discharge, two different carbon electrodes with 0.4 mg/cm^2 and 0.3 mg/cm^2 Pt loading and thickness of 200 µm, produced by Johnson Matthey, were used, where electrochemical experiments were carried out to identify the difference in performance [16,193]. These electrodes in comparison to the carbon cloth electrodes lacked the existence of MPL with PTFE coating.

3.1.2.2 Cathode Electrode (Electrolyte half-cell):

In order to understand the effect of the electrode thickness, which directly effects the residence time of the electrolyte in the active volume of the electrochemical cell, two different electrodes were tested. Initially carbon paper (SGL Group, Germany, Sigracet® SGL 10 AA) with a thickness of 400 µm was tested. The effect of thickness was studied by testing a single layer of the carbon paper as the cathode electrode (liquid half-cell) and comparing the performance to the results obtained by increasing the number of layers from one layer to three layers. In addition to this, the effect of increasing available surface area and electrolyte residence time was tested by comparing the difference in performance of the RHMnFC using carbon paper electrode and graphite felt with 4.6 mm thickness (SGL Group, Germany, Sigracet® GDA 4.6).

3.1.2.3 Ion Exchange Membrane Selection and Activation:

Previously it was discussed that one of the major challenges in RFBs includes the crossover and cross-contamination of the electrolyte. In RHMnFC, it is possible to collect and recirculate the electrolyte, which migrates to the opposite half-cell. However, this adds to the system cost. In this work, two different commercially available membranes were tested. Nafion® 117 and Nafion® 212, with typical thickness of 183 µm and 51 µm respectively.

Nafion membranes were initially cut and prepared (activated) by going through a standard activation process. For cleaning purposes, the membrane was soaked in 1M Hydrogen peroxide (VWR, 30% (W/V)) solution and heated at 80 °C for 1 hour. This was followed by rinsing the membrane with deionised water and heating it in 1M H_2SO_4 (VWR, 95%) solution at 80 °C 1 hour. Finally, it was rinsed and left in deionised water for future use.

3.1.3 Manganese Electrolyte Preparation

The introduction of RHMnFC by Rubio-Garcia et al. [16] showed that, in order to produce a stabilised electrolyte, and prevent Mn^{3+} from going through disproportionation and precipitating, it was necessary to use Ti^{4+}. Although, the method used to produce the Mn electrolyte with Ti additive in the

solution resulted in consistent performance of the cell, this method consisted of a heat intensive process to dissolve TiO_2 in a high concentration acid. In addition to the overall inefficiency (heating up the solution) of this method, it also proved to be time consuming.

Therefore, a different method was developed in this work, to eliminate heating in high concentrated acid to dissolve TiO_2. In this work to produce a 40 mL solution with 1M Ti, 1M Mn and 5M sulfuric acid content, 6.4 g titanium (IV) oxysulfate ($TiOSO_4.xH_2O$) (Sigma-Aldrich, ≥29% Ti) was first dissolved in water. In the second step, 11.2 mL of H_2SO_4 (VWR, 95%) of the stock solution was added. Finally, after the solution was cooled down to room temperature, 4.6 g of $MnCO_3$ (Sigma-Aldrich, ≥99.9% trace metal basis) was added and left to stir and dissolve. This method reduced the electrolyte preparation time from two days period [16], in the previously reported method, to a two hour process.

3.1.4 Experimental System Configuration

In order to carry out the experiments, the system was set up according to the schematic illustrated in Figure 3-2. In this set up, the electrolyte is supplied at a flow rate of 50ml/min using a PTFE-diaphragm pump (Masterflex® L/S® - WZ07090-62, Cole Parmer®). In order for the electrolyte, in a flow-by flow field (serpentine flow channels), to diffuse through the graphite felt electrode, the inlet was connected to the bottom of the cell and recirculated back to the reservoir tank from the top outlet. Contrary to Mn electrolyte, hydrogen was supplied at the rate of 100 mL/min, using a hydrogen flow controller (Bronkhorst®) to the cell from the top manifold.

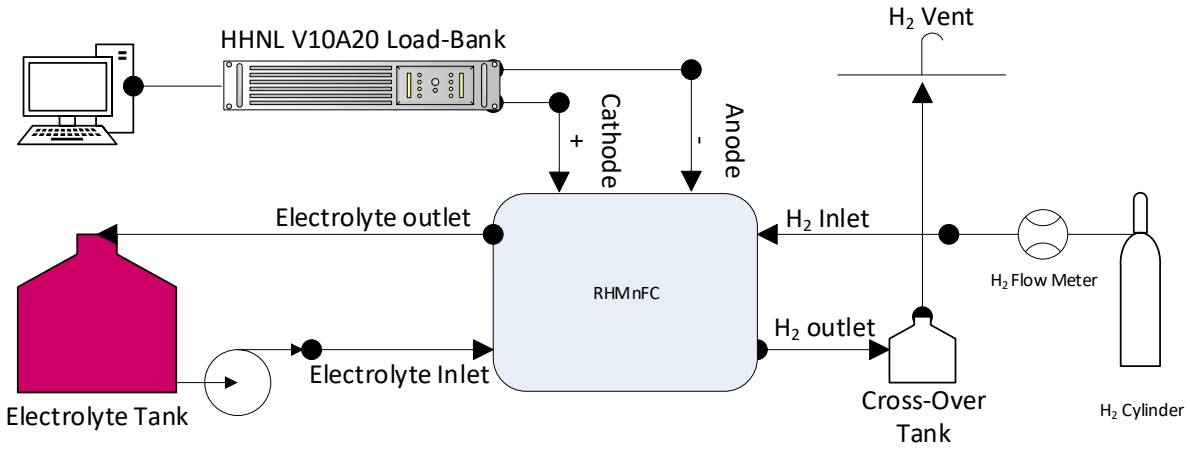

Figure 3-2: Experimental set-up configuration for RHMnFC with open hydrogen supply

In the gas half-cell, as hydrogen tends to flow upward upon expansion, it was necessary to supply hydrogen from top to bottom, to diffuse through the carbon electrode. In this set of experiments, hydrogen is vented out of the cell from the bottom fitting, which passes through the crossover

collection tank. Any electrolyte migrated to the hydrogen side is collected and recirculated back to the main electrolyte tank, and hydrogen gas leaves the system and goes to vent.

As part of this work, in order to understand the proposed RFC performance and its round trip efficiency, charge and discharge cycles are performed using different components, and different conditions. In this setup, a Hocherl & Hackle NL (HHNL) series-2 200W power source-load bank was used to perform charge and discharge. This device was connected directly to a computer for data acquisition purposes.

3.1.5 Cell Performance Conditioning

Once the cell is set up, it was found that, due to the low performance observed from the experiments using a fresh electrolyte (will be discussed in Section 4.1.7), that the cell and/or the electrolyte required a conditioning step, where it would allow the cell to reach its operating condition. In order to achieve the optimum operational conditions, the- following steps were carried out:

- The cell was charged at a low current density of 20 mA/cm^2.
- Once the cell potential stabilised, and dV/dt has reached to +2mV/s, the current density was increased in 10 mA/cm^2 increments until it reached an operating current density of 100 mA/cm^2.

The importance of this step in the performance of the cell was investigated and is discussed in detail in Section 4.1.7.

3.1.6 Experimental Conditions for Performance Evaluation

To perform the performance studies, different conditions were applied for the testing. These parameters are explained below.

3.1.6.1 Determining Efficiency and Capacity Utilisation

- To determine the energy, voltage and coulombic efficiency of the electrochemical cell, all the charge and discharge cycles were performed at a constant current (galvanostatic) condition, where minimum of 10 cycle was carried out at 20 mA/cm^2, 40 mA/cm^2, 60 mA/cm^2, 80 mA/cm^2 and 100 mA/cm^2.
- In order to avoid producing MnO_2, a cut off voltage of 1.65 V was set as the upper limit. Therefore, once the voltage of the cell reached this value, the power source would stop supplying current. A lower limit of 0.65 V was also introduced as the cut-off voltage for discharge.
- Charge and discharge capacity measured experimentally was compared to the theoretical capacity. Since the Mn^{2+} to Mn^{3+} reaction is a one electron reaction, the theoretical capacity

of the electrolyte is determined using eq. 3-1. In this equation, n is the number of electrons transferred, F is the faraday constant 96485.3 sA/mol, m indicates the mass of the solute, and Mw is the molar mass of the solute.

$$Q_{Theoritical} = \frac{n \times F \times m}{3600 \times Mw} \ (mAh) \qquad \text{eq. 3-1}$$

3.1.6.2 Polarisation Curve to Determine Peak Power Density

For this work, the effect of different Pt loading on the hydrogen electrode was tested using different electrodes. (Choice of electrodes were discussed in Section 3.1.2.1). This was done previously as part of a project in the Electrochemistry group, but since this project focuses on the same system, the choice of hydrogen electrodes was based on the findings from work previously carried out by Rubio-Garcia et. al., in the Electrochemistry group [16], which will be illustrated and discussed in Section 4.1.2.

The maximum power of the system was measured, focusing on demonstrating the effect of Pt loading on the hydrogen electrode.

These measurements were taken as follow:

- At OCV, a constant current with 20 mA/cm^2 increments was applied
- At each current density, the current was held for 20 seconds, where using the Scribner e850 test station, high frequency resistance (HFR) values were recorded at each current.
- This was carried out until the overpotential reached the mass transport region (ie., cut-off voltage).

3.1.7 Scaling Up

To investigate the feasibility of scale up, a commercial cell was purchased and tested. Due to the commercial value and agreed confidentiality between the manufacturing company and RFC Power LTD (a spinout company from Imperial College London), it is not possible to discuss the detail of the design in depth. This single cell was designed in a way that, upon success of the single cell testing, it would be possible to develop a stack. This 150 cm^2 active area cell, illustrated in Figure 3-3, benefited from a serpentine flow field design in both cathode (liquid half-cell) and anode (hydrogen- half-cell) electrodes. The effect of surface tolerance of the plates and compressibility of these gaskets used in the cell will be discussed in Section 4.1.9.

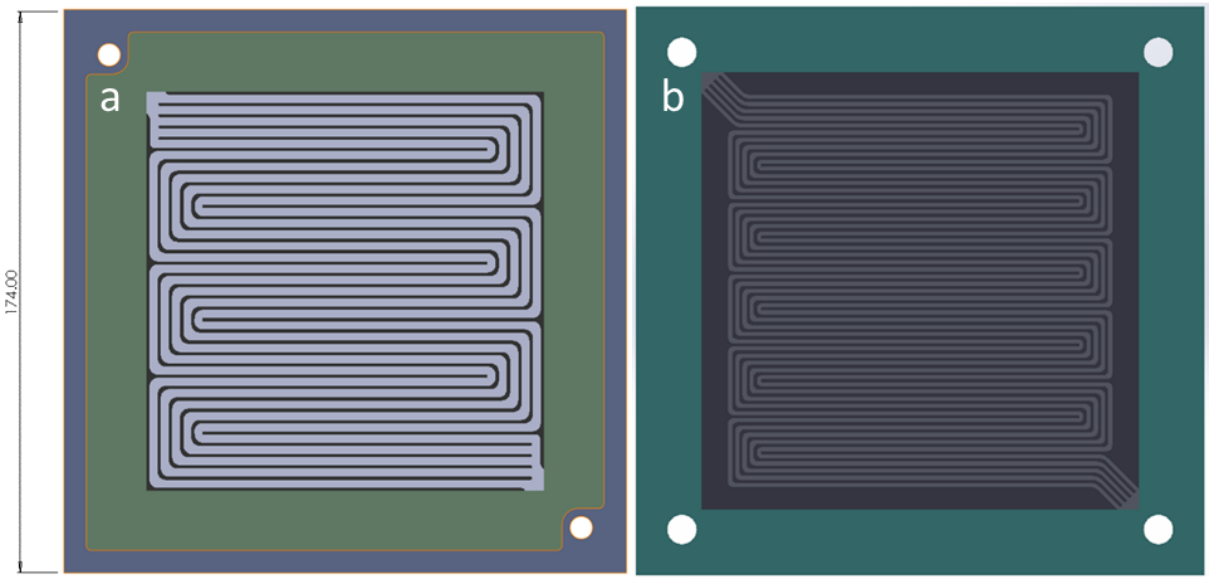

Figure 3-3: Serpentine flow field design of the single cell redox flow battery cell a) flow plate on the liquid half-cell and b) flow plate for the hydrogen half-cell

Similar experimental setup steps to those explained for the small cell in Section 3.1.6, was carried out to assemble the large cell. To carry out the performance measurements in this cell, a peristaltic pump (Masterflex® L/S®, MFLEX Easy-Load® II Head) was used to supply the electrolyte. Throughout this part of the work, Viton tubing with ¼ inch inner diameter was used, where a maximum flow rate of 250 mL/min was supplied to the cell.

One of the drawbacks identified in this commercial design was the number of components and gaskets required to assemble the electrolyte half-cell. This complexity of design consequently resulted in limited control on the compression of the electrode used for the liquid side. Also, it was found to be difficult to seal the cell to prevent leakage of the electrolyte. These challenges arise from low compressibility of the Viton gaskets that were used in the cell, as well as low surface tolerance of the manufactured components which, where coupled together, resulted in leakage.

To carry out further studies, the design of the liquid half-cell electrode was therefore further developed and improved in this work. This was done by firstly reducing the number of the components from three down to two components; secondly, the- number of gaskets was reduced from three gaskets to one gasket between the frame and the graphite plate. In this design, the pattern of the flow field was kept similar to that manufactured by the commercial partner. Other improvements to the cell design, were the changes made to the liquid side inlet and outlet fittings. In this concept, illustrated in Figure 3-4, the PTFE tubing enters the flow field frame, where the liquid travels through the channels on the PVC frame and flows into the channels in the graphite flow plate.

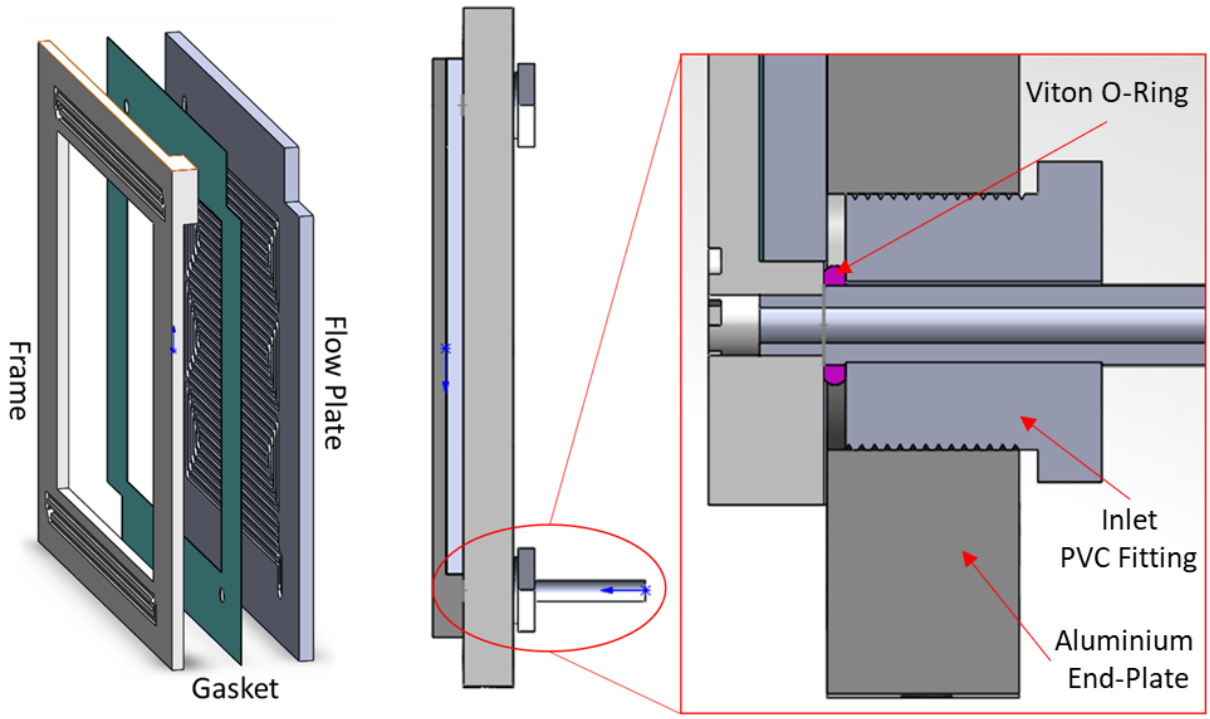

Figure 3-4: Optimised design with modified components and optimised fittings

This design, benefiting from an O-Ring between the flow frame and the screw fitting (screwed into the endplate), provides the flexibility to seal the ingoing and outcoming solution from leakage. In other words, even in cases where there is a poor surface tolerance on the interface of end plate and the frame (the electrolyte initially enters this part of the cell and flows to the graphite flow plate), it would still be possible to easily seal the inlet and outlet.

It must be noted that the use of frame in this design was to enable stack development in the future. In a RFB stack, electrolyte enters and leaves the individual cells from common inlet and outlet manifolds. Thus, shunt currents occur during operation because of the potential difference across the bipolar flow plates, separating individual cells, and the conductivity of the electrolyte [194]. Middle cells are more effected by shunt currents where their voltage is lower than the single cells closer to the start and the end of the stack. Therefore, when cells are connected in series, cells closer towards the two ends will operate at higher voltage, which, during charge, can result in the degradation of these cells, as they operate above the cut-off voltage [195]. Shunt currents are often referred as parasitic losses that reduce the current efficiency during the charge and discharge cycling of the cell. Shunt currents, due to the transport of electroactive ions in the electrolyte by diffusion and/or migration, can also exist under open circuit conditions [196]. In order to overcome this phenomenon, narrow channels with longer pathways are added to the design to increase resistance and to minimise the internal parasitic current.

3.2 Experimental Set Up to Investigate the Stability of Regenerative Hydrogen Manganese Fuel Cell and Electrolyte

3.2.1 MEA Material Selection and Electrolyte Preparation

In this part of the project, the configuration and setup were similar to the methods outlined in Section 0. The choice of MEA materials was based on their performances, which was tested and reported in the previous chapter (0). Therefore, the following MEA components were used:

- Gas Half-Cell: Hydrogen electrode with 0.3 mg_{pt}/cm^2 with 40% PTFE loading
- Proton exchange membrane: Nafion 117 (treated using the protocol explained in Section 3.1.2.3)
- Electrolyte Half-Cell: Graphite felt with 4.6 mm (Untreated)

Electrolyte preparation and final elemental composition also followed the procedure explained previously (Section 3.1.3), where the electrolyte with 1 M Mn and 1 M Ti in 5 M sulfuric acid was produced. According to the findings from Section 4.1.7, when a new electrolyte was prepared a conditioning procedure was conducted, where it was initially charged and discharged galvanostatically at 20 mA/cm^2.

3.2.2 Stability of Manganese Electrolyte

To investigate the stability of electrolyte in the absence of any additives, 1M manganese electrolyte in 5 M H_2SO_4 was prepared. In order to obtain an understanding of Mn disproportionation and its mechanism in the electrochemical flow cell, a 40 mL electrolyte was initially charged at 100 mA/cm^2 up to 1.65 V, and then discharged at a similar current density until a voltage of 0.65 V was reached (lower cut-off voltage). A 2 hour rest time was used between charge and discharge cycles, and this procedure was repeated until the electrolyte completely degraded due to precipitation of MnO_2, and it was not possible to carry out a charge or discharge cycle.

3.2.3 Stability of the Charged Manganese Electrolyte at Different Resting Times

The stability of the electrolyte is determined by the coulombic efficiency of the electrochemical cell as well as its capacity retention. To investigate the capacity retention of the electrolyte, the following procedure was followed:

1. A standard electrolyte according to Section 3.1.3 was used in the cell and charged at 100 mA/cm^2 up to 1.65 V.
2. Electrolyte was circulated in the cell and stirred in the electrolyte tank.
3. Different wait times, between 5 mins and 20 hours were introduced into the procedure between the charge and discharge cycles.

4. Cell was discharged at 100 mA/cm^2 until a cut-off voltage of 0.65 V was reached.
5. After each discharge cycle, the cell was charged and discharged galvanostatically at 100 mA/cm^2 to ensure that the electrolyte had returned to its optimum condition, established in Section 4.1.6.
6. Performance evaluation indexes of each cycle were calculated and presented.

3.2.4 Regeneration of Electrolyte

A method was developed that can be used to dissolve the disproportionated MnO_2 precipitates, this method will be reported for the first time as a part of electrolyte regeneration:

1. To obtain the performance of the cell, the system was charged and discharged at a constant current density of 100 mA/cm^2 for ten cycles.
2. To produce MnO_2, the cell was charged at a constant potential of 1.8 V, until the current density reached 10 mA/cm^2
3. To ensure that the electrolyte was fully degraded (i.e it was not possible to perform further charge or discharge half-cycles), an attempt was made to discharge the electrolyte with a current density of 100 mA/cm^2.
4. Cell was discharged at a constant potential of 0.1 V, until discharge current density had reached to 10 mA/cm^2.
5. Charge and discharge cycle, similar to step one, was applied.

In Section 5.1.3, it will be seen that, during step four an oscillation in the discharge current is observed. To understand this phenomenon and investigate the hypothesis around the mechanisms causing this oscillation, electrolyte regeneration was performed at different flow rates (10 RPM, 20 RPM and 30 RPM) and the results obtained from this experiment will be presented.

3.2.5 Temperature Dependency of Manganese Electrolyte

One of the most important criteria in the operation of the any electrochemical cell is the stability of the electrolyte used in the cell at different temperatures. In order to investigate the effect of temperature on the performance of the cell and the stability of the electrolyte, the following procedures and configurations were used.

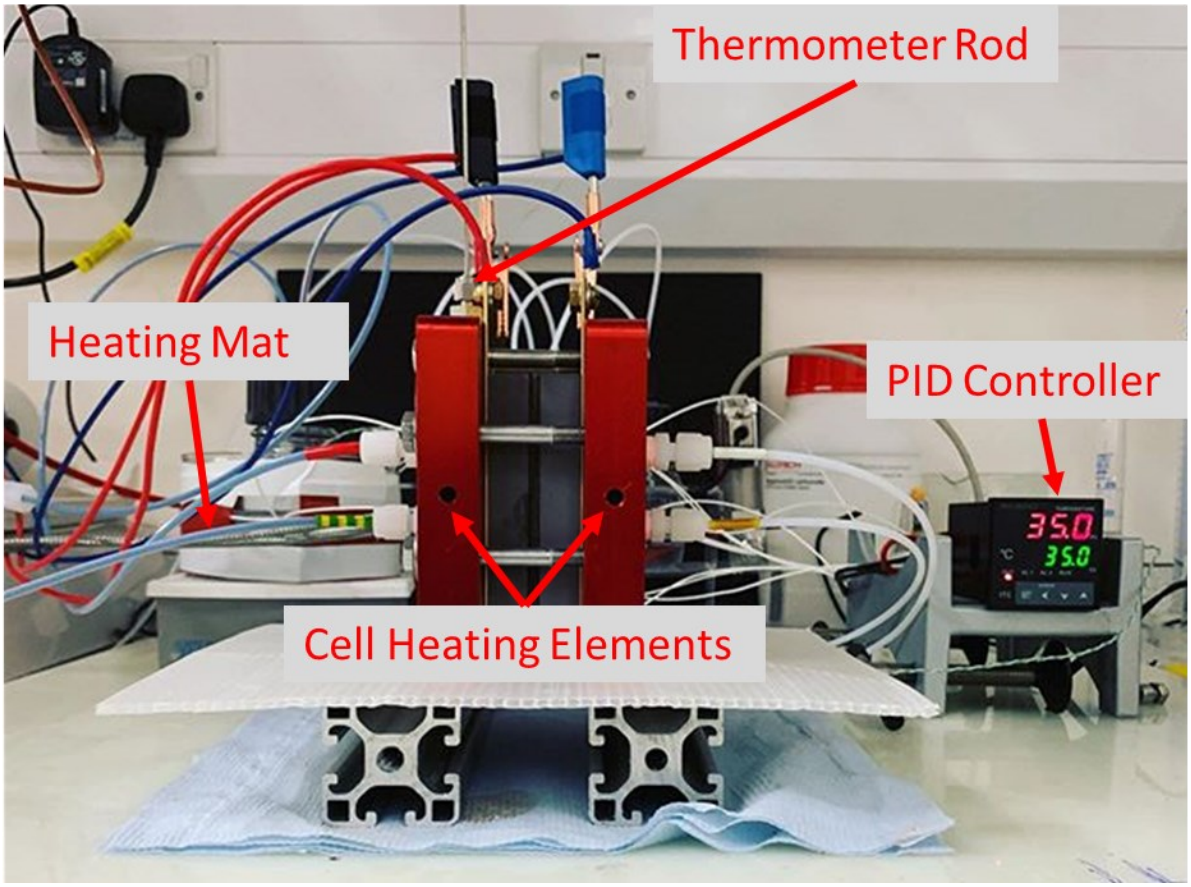

Figure 3-5: Experimental set up to understand the electrolyte stability at different temperatures

Initially, the stability of the electrolyte was tested by heating the electrolyte to temperatures above room temperature (setup is illustrated in Figure 3-5). In order to heat the cell, heating elements provided with the cell assembly (Scribner Associates) were placed inside the designated areas in the end plates. To monitor the temperature of the cell, thermocouple (Type K) was used, which was inserted into the cell.

3.2.6 Characterizing Techniques to Investigate Electrolyte composition

To understand the phenomena occurring during disproportionation and regeneration of the electrolyte, different characterising techniques, such as Inductively coupled plasma mass-spectrometry (ICP-MS) and Ultraviolet–visible spectroscopy (UV-Vis) were used. As a part of the Mn electrolyte stability work, these studies were carried out in the Electrochemistry group by A. Tan, and the relevant results from this part of the project will be presented accordingly [81].

In order to measure MnO_2 precipitation, ICP-MS 7000 was used to measure the concentration of the Mn in the solution at different times and temperatures. To conduct this experiment, an electrolyte was fully charged, and 5 mL samples were separated into different vials. Each sample was placed in

an oil bath at temperatures between 35 °C and 50 °C, at 5 °C intervals. To measure the change in concentration over time, aliquots of 200 μl were taken from each sample up to 70 hours.

To dissolve any precipitated MnO_2, each aliquot sample were initially digested using 1mL of 1M-hydrochloric acid (HCl), where all the MnO_2 would reduce to Mn^{2+}. Then each sample was diluted to a concentration below 1 ppm with 2% nitric acid (HNO_3) and in the solution. The dilution procedure was based on diluting a 1M Mn electrolyte, hence any samples with lower Mn concentration would fall below 1ppm.

3.3 Experimental Setup for In-Situ Visualisation and Quantification of Electrodeposit Morphology Under Dynamic Conditions in Zinc Secondary Batteries

3.3.1 Cell Design

In order to be able to carry out the experiments in conjunction with the electrochemical reactions in Zn flow batteries, the following test cell was designed and manufactured. In this setup, a 2.0 mm diameter zinc rod (≥ 99.99%, GoodFellow) was used as counter electrode (CE). A dynamic hydrogen reference electrode (HydroFlex®) with a tip diameter of 1.6 mm was used as a standard hydrogen electrode (SHE). The cathode electrode (working electrode) used in this setup was a carbon rod (99.997%, ultrafine 1-5 µm, GoodFellow) with a truncated tip of 200 µm upper diameter and 4.91 mm lower diameter and a height of 4.71 mm.

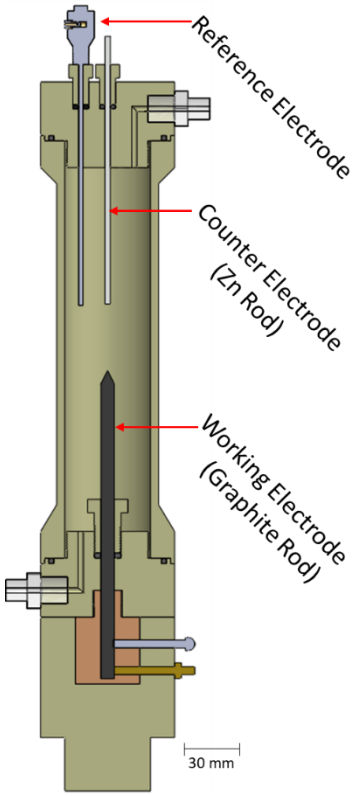

Figure 3-6: Three-electrode in-situ test cell

Since this bespoke test apparatus was built to be used in an environment sensitive to corrosive materials it was necessary to design a fully leak free test rig. Besides manufacturing a perfectly sealed product, it was also crucial to achieve a design where none of the terminal connectors, from the testing station, could interfere with the tests, or, in other words, could be exposed to the alkaline solution in the test rig. Considering these criteria, a novel test cell with different compartments, demonstrated in Figure 3-6, was built and tested.

3.3.2 Compartments of Three-Electrode In-Situ Test cell:

The three-electrode cell was designed consisting of three main compartments. These three compartments were manufactured from polyether ether ketone (PEEK, DirectPlastics). PEEK was

selected as it was transparent to the X-Ray beam, and radiography on the samples could be performed:

Top cap, shown in Figure 3-7 (a), both reference and counter electrodes (Zn rod) were assembled to this part. Beside the electrodes, PFA elbow connectors were used as the outlet manifold, with a 1/8-inch inlet diameter (NPT, Swagelok). One of the main features of this design is the use of modified connectors, which by screwing these into the cap, apply pressure onto the Viton O-ring (FKM, 90 shore, Polymax®) to enact compression and seal the pathways where liquid could possibly leak from the cell. Using these connectors, both the reference and Zn electrodes were inserted into the cell, where O-rings also help to fix these electrodes from any further movements. This part is assembled to the main hollow cylinder, and filled with the electrolyte for the electrochemical reactions to take place. As can be seen on the 3D drawing in Figure 3-7 (b), the top cap consists of a groove where the O-Ring with 21 mm inner diameter and 2 mm thickness was placed inside. Once this cap screwed in the hollow cylinder, compression on the O-ring produced the required sealing to eliminate leakage.

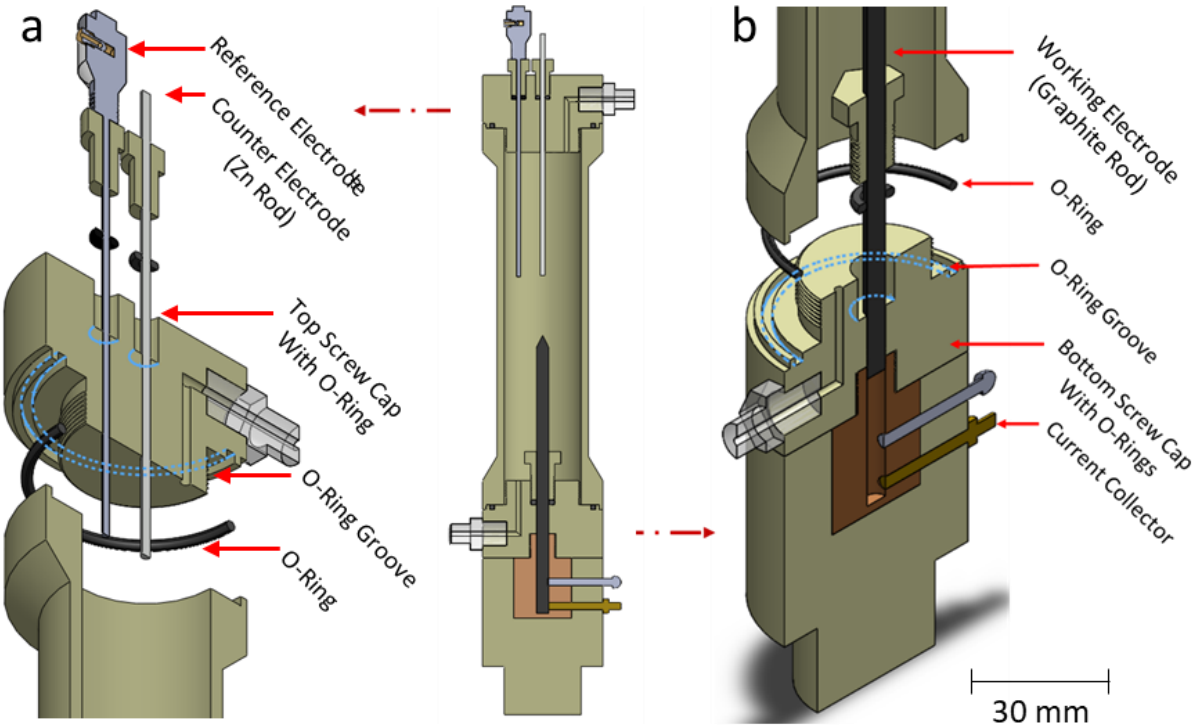

Figure 3-7: Exploded view of the cell a) top cap and b) bottom holder with their essential components of the in-situ cell

Bottom holder, shown on the right 3D drawing in Figure 3-7, holds the graphite working electrode. Similar to the top cap, it contains a customised connector, responsible for holding the electrode in place, and prevents the electrolyte from leaking further down the cell, which could interfere during measurements. At the bottom part, a hollow cylindrical brass metal was pressed into the PEEK holder, which acts as a current collector. Since the stage holder in the XCT setup contained metal jaws to hold

the rig, the brass metal was pushed into the PEEK holder, where a screw was inserted to be able to make the electrical connections required for measurements.

3.3.3 Electrochemical Reaction Characterisation Cylinder

The hollow cylinder, illustrated in Figure 3-8, was enclosed with two components explained in the previous section. The distance between the electrodes was kept constant at 25 mm for all the experiments. Although a narrower cell would be more favourable, due to the restrictions caused by different components such as manifolds and electrodes, this cylinder was designed with an inner diameter of 32 mm and a wall thickness of 3mm. According to these dimensions, the manufactured cylinder contains a volume of 109.38 ml. This cell, in dynamic flow conditions, was filled using the bottom manifold, and the electrolyte exited the cell from the top outlet.

In order to only expose the tip of the electrode to the electrolyte, such that reactions could only take place on the truncated conical shape region of the graphite electrode, a PTFE tape was used to cover the rod below the base of the conical tip. The lateral surface area of the tip (working area) was calculated to be 45.25 mm^2.

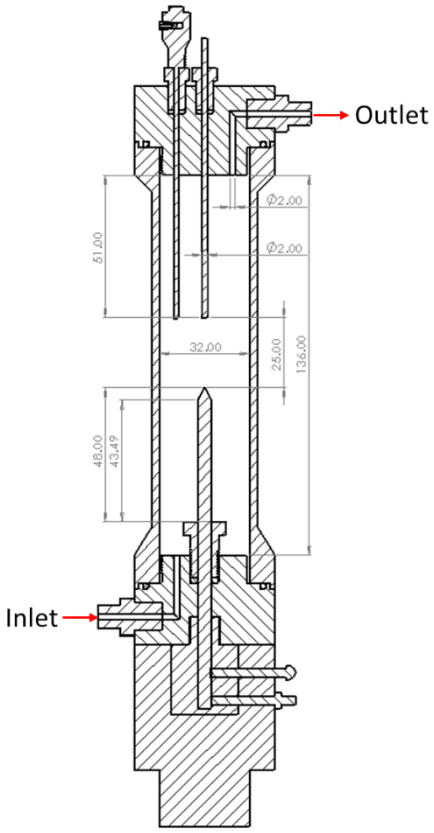

Figure 3-8: CAD drawing of the hollow test cylinder including the space between Zn and graphite electrode.

3.3.4 Electrolyte preparation

A 500 mL electrolyte solution consisting of 0.5M zinc oxide (ZnO, ≥ 99.5%, Fisher Scientific), 6M potassium hydroxide (KOH, ca. 85%, pellets, Alfa Aesar) was prepared. In order to prepare this electrolyte, initially KOH was dissolved in deionised water. Since this reaction is exothermic, the high temperature of the solution enhanced the solubility of the ZnO in the solution, hence ZnO was added immediately after KOH, while the solution was at a higher temperature (approximately 55°C) than room temperature (20 °C).

3.3.5 Experimental System Configuration

In order to carry out the experiments, the system was set up according to the schematic shown in Figure 3-9. The electrolyte was supplied to the testing area, from the 200 mL reservoir, using a peristaltic pump (Masterflex® L/S®, 77200-50, Cole Parmer®) via the bottom inlet. The electrolyte was circulated back into the main reservoir, which was stirred during the experiment from the top outlet.

During these experiments, in order to supply the electrolyte, a tube with an inner diameter of 1/4-Inch (Masterflex® L/S®, EW-06442-17, Cole Parmer®) was used.

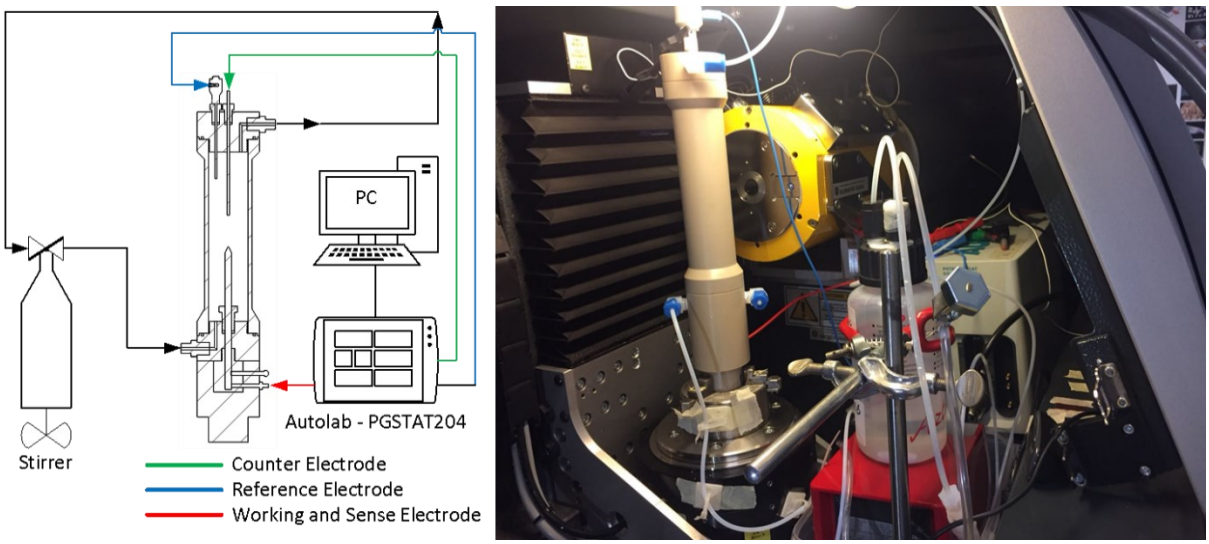

Figure 3-9: Schematic of the in-Situ cell configuration inside XCT Machine

3.3.6 Electrochemical Experimental Setup and Conditions:

3.3.6.1 Cyclic Voltammetry (CV) Experimental Conditions

Cyclic voltammetry (CV) was used in this three electrode in-situ cell to understand the effect of flow rate at the tip on current density of the deposition and dissolution. This part of the experiment was conducted at four different flow rates as mentioned in section 3.3.5. The CV was carried out at voltage range of -1.6 V (vs SHE) and -0.4 V (vs. SHE), with a scanning rate of 10 mV/s.

3.3.6.2 Chronopotentiometry at Various Current Densities

In order to investigate the effect of operating current density on the morphology of the Zn deposits, electrodeposition was carried out at negative current densities of 10 mA/cm^2 and 100 mA/cm^2 under static electrolyte conditions. Electrodeposition was continued until a capacity per unit area of 5 mAh/cm^2 was achieved. This set of experiments were designed to visualise the formation of the Zn deposits on the surface of the electrode in real-time by using X-Ray radiography and tomography, for which the experimental procedures will be explained in Section 3.3.8.

3.3.6.3 Chronopotentiometry at Various Current Densities Under Dynamic Flow of The Electrolyte

To study the difference between the evolution and morphology of the Zn deposits under dynamic flow compared and static conditions, electrodeposition was carried out at constant current densities of 10 mA/cm^2 and 100 mA/cm^2 under dynamic flow conditions. Experiments were conducted at two pump rates, 100 RPM (1.05 cm/s) and 200 RPM (2.11 cm/s), and the relevant calculation to find Reynold's number for these pump rates are demonstrated in Table 6-1. Formation of the deposits at these

conditions were monitored in real-time using X-ray radiography and the 3D structure of the morphology of these experiments were obtained by reconstructing the X-Ray tomography images.

3.3.6.4 Pulsating Chronopotentiometry with Various Duty cycles

The effect of depositing zincate on the surface of the electrode at a pulsated constant current density of 100 mA/cm^2 was studied at duty cycles of 20%, 50% and 80% (according to eq. 3-2) under static and dynamic flow of the electrolyte, and the depositions obtained from these set of experiments were compared to the morphology of the depositions obtained from experiments in Sections 3.3.6.1 and 3.3.6.3. Presented in Figure 3-10, different duty cycles correspond to different rest times at each deposition cycle. In each cycle, a deposition period of 2 seconds in applied, with different rest periods of 8 ,2 and 0.5 seconds applied at each cycle for duty cycles of 20%, 50% and 80% respectively.

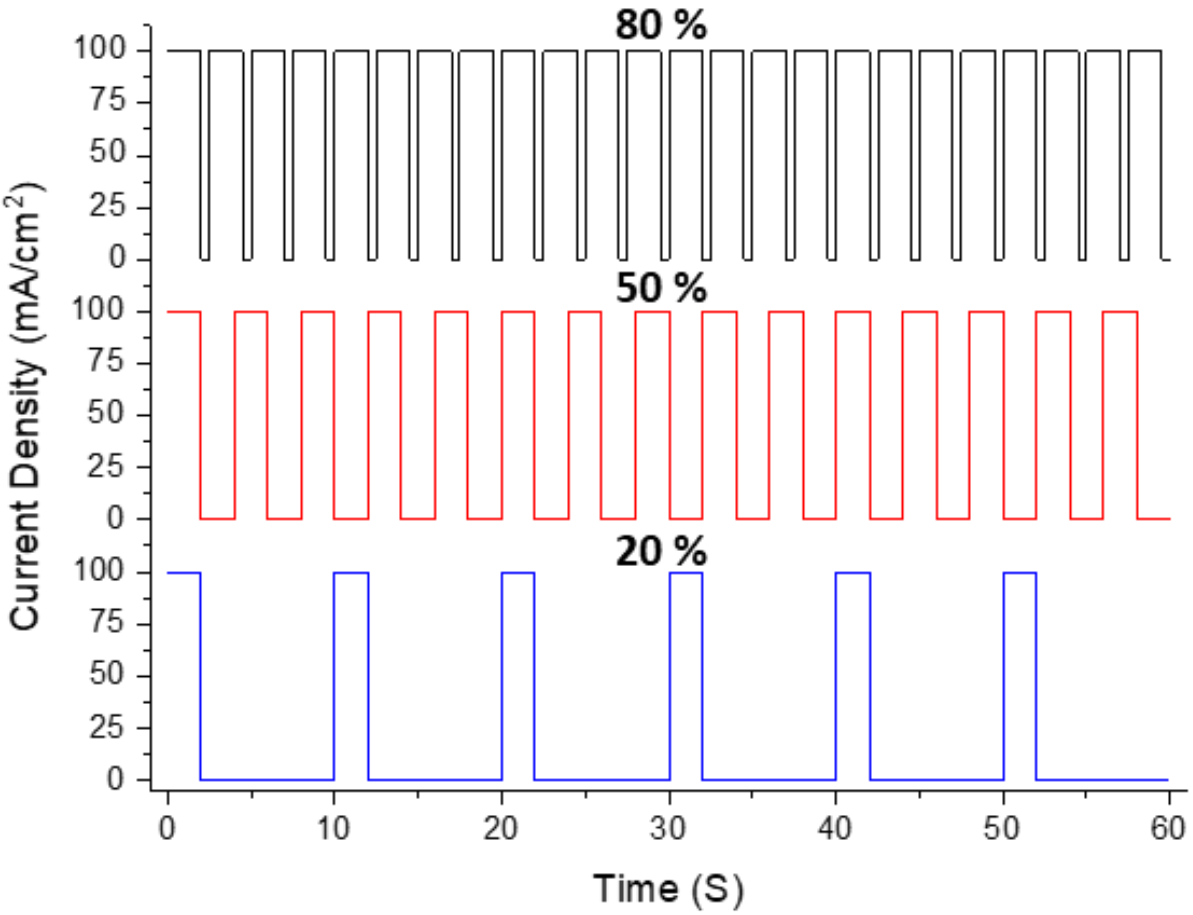

Figure 3-10: Waveform characteristics of the electrodepositions at a current density of 100 mA/cm^2 with different duty cycles

According to eq. 3-2 the duty cycle is the fraction of intermittent deposition of the Zn, with a deposition period of T_d and a rest time of T_R. For this set of experiments, the period of the electrodeposition was fixed at 2 seconds, and depending on the duty cycle in each experiment, different rest periods were introduced to the procedure, ranging from 8 seconds to 0.5 seconds. All

the depositions were continued until an areal capacity of 5 mAh/cm^2 was achieved. Figure 3-10 illustrates the initial 60 seconds of the waveform characteristics of the duty cycles used in this set of experiments.

$$Duty\ Cycle = \frac{T_d}{T_d + T_R} \qquad \text{eq. 3-2}$$

3.3.7 X-Ray Computational Topography

X-ray radiography and tomographic imaging experiments on the zinc electrodeposits under flowing electrolyte conditions were carried in the custom-built flow cell using a laboratory X-ray imaging instrument (GE Nanotom S, GE, USA). An image and schematic illustration of the experiment rig setup up is shown in Figure 3-9 and Figure 3-11.

The X-ray tube was operated at 120 kV and 100 µV for both radiography and tomography experiments as this provided optimum image contrast and signal to noise ratio within the capability of the instrument. As shown in Figure 3-11, the in-situ flow cell was mounted on a rotating sample stage with three-electrode electrical connections made between the cell terminals and potentiostat, and flow connections made between the cell, a peristaltic pump and an electrolyte storage vessel.

With the X-ray instrument in radiography mode, charge currents were applied to the cell to induce zinc deposition whilst simultaneously imaging the conical tip of the carbon composite electrode for each experiment, the charging current was applied until an areal capacity of 5 mAh/cm^2 was achieved. In order to demonstrate the capabilities of the in-situ flow cell for both electrochemical testing and 2D/3D microstructural characterisation, experiments to observe the effect of current densities and varied degrees of pulsed electrodeposition on zinc morphology and microstructural properties under different flowing electrolyte conditions were conducted.

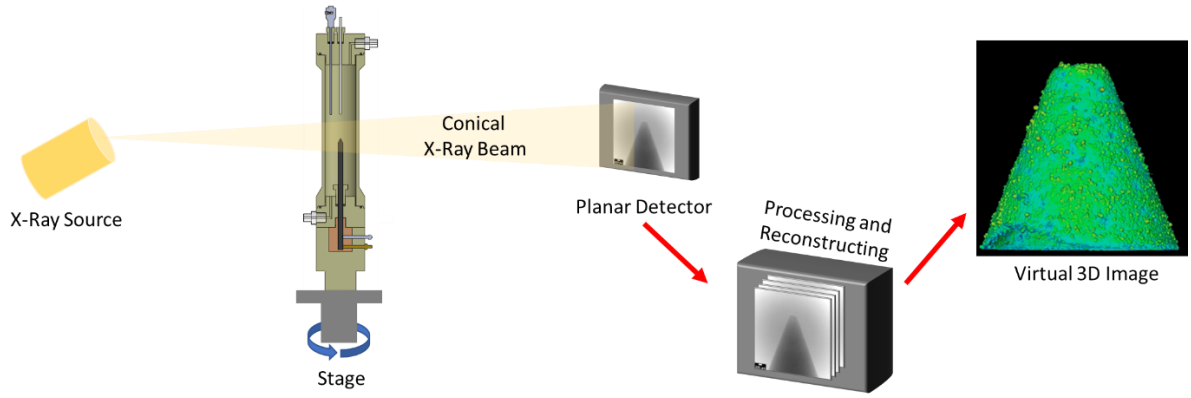

Figure 3-11: Schematic of the X-ray computed tomography of zinc electrodeposition and post processing

With an X-ray detector image integration of 2 seconds and detector image averaging and frame skip setting values of 3 and 1 respectively, radiographs were collected every 7 seconds (0.14 Hz). After each

radiography experiment, the current was stopped and an X-ray tomography scan of the conical-top of the carbon composite rod was performed. In order to obtain tomographic images with high contrast and high signal-to-noise ratio, the electrolyte was slowly drained from the cell prior to tomographic image acquisition. It is noteworthy that due to the imaging resolution limitation of the instrument and the large reliance on geometric magnification in laboratory X-ray imaging instruments, resolving any porous zinc deposition was extremely challenging. Higher Spatial and temporal X-ray image resolution at synchrotron light can aid to resolve the porous deposits.

For the tomographic imaging experiments, 1801 projection images (or radiographs) were captured over a 360° rotation of the flow cell about its long axis. Tomographic reconstruction of each set of acquired projection images was performed using a cone-beam filtered back-projection algorithm based on the Feldkamp-Davis-Kress (FDK) algorithm [197].

3.3.8 Data Analysis from XCT

Image pre-processing and segmentation of the resulting reconstructed volume was done using commercial image processing software (Avizo v9.5, Thermo Fisher Scientific). 3D median filtering was applied to the reconstructed grayscale image volumes to reduce the image noise and threshold-based segmentation was performed to extract the deposited zinc microstructures which facilitated their 3D rendering. Using the "Local Thickness" plugin in Fiji software [198], the smallest deposit feature size resolved from the experiment was calculated to be 6 um. Due to the large sizes of image volume data, a region of interest along the conical tip of the carbon composite rod was selected in each tomogram for subsequent analysis. Microstructural parameters such as zinc deposit volume, volume specific surface area, deposit height and size distributions were extracted from the 3D image volumes.

3.4 Experimental Summary

Section 3.1 of this chapter presented all the experimental methods and procedures used to obtain the data required to understand the parameters affecting the performance of the cell. In addition to the experimental protocols, the choice of materials used throughout this work was explained. Finally, the design and optimisations required, to move from a small 5 cm^2 lab scale electrochemical cell to a large cell with 150 cm^2 active surface area were explained in detail.

It is important to mention that experimental methods used to test the performance of the large cell were similar to those used to test the small cell (with an active area of 5 cm^2). The scaleup portion of this work mainly focuses on the engineering aspect of the technology, to produce a electrochemical cell where findings from small cell testing can be transferred, to understand the research questions that must be investigated in order to be able to move from a single cell to a stack with more than one individual cell.

Section 3.2 of this chapter presented all the experimental methods and procedures used to obtain the required data to understand the factors influencing the stability of the electrolyte and its effect on the performance of the cell. In addition, a method to regenerate the degraded electrolyte was analysed, where different techniques to investigate this method was explained.

As the final Section of the experimental methods (section 3.3), a novel in-situ system for operando visualisation of the formation of the Zn deposits on the surface of the electrode was proposed, and the design of the system with different components were discussed and demonstrated. This bespoke cell, which enabled the formation and growth of deposits to be measured in real-time, consists of a dynamic hydrogen reference electrode, which measured the voltage response of the working electrode while electrodepositing zinc on the surface of the electrode.

The system configuration and experimental procedures to investigate the effect of various operating conditions, such as the impact of operating current density, effect of dynamic flow and static flow and waveform electrodeposition on the formation and morphology of the Zn electrodeposition were explained. Characterisation techniques, such as X-ray radiography and tomography, employed in this project to visualise the formation and reconstruct a 3D structure of the deposited morphology was also discussed.

Chapter 4 Investigation of Regenerative Hydrogen/Manganese Fuel Cell (RHMnFC)

This chapter will contain three main parts, initially exploring the current state-of-the-art research in the field of RFBs. This will include analysing the advantages of regenerative fuel cells over conventional flow batteries and identifying gaps in the literature with regards to the Regenerative Manganese Hydrogen Fuel Cell (RHMnFC). To answer the identified questions, the methods and materials used in experiments will be explained. Finally, results obtained from sets of experiments will be shown and discussed.

4.1 Results and Discussion

This section will be divided into two sections, the first section will present and discuss the results previously obtained during different projects in the Electrochemistry group; the second section of this of this work will discuss the results obtained from experiments based on the findings from the first half of the work in this thesis.

The focus of the projects carried out in collaboration with the Electrochemistry group, in the department of Chemistry at Imperial College London, was to establish the effect of different parameters associated with the hydrogen electrode on the performance of the RFC in question. In this study, the influence of catalyst layer's Pt loading, the difference in performance of different carbon support and most importantly, the effect of PTFE content on the performance of the reactor was investigated and reported [16].

The work on this thesis, developing on the findings from the project on the effect of hydrogen electrode on the performance of the cell, the effect of different materials such as the liquid half-cell electrode and IEM was tested. It is important to note that, unlike fuel cells, the performance of energy storage devices is mainly determined by their round-trip efficiencies and the energy output. Therefore, to determine the performance of the cell, charge and discharge cycles would be the main means used to determine the performance of the technology.

4.1.1 Electrolyte Preparation

According to the tests on solubility of Mn precursor ($MnCO_3$), TiO_2 and $TiOSO_4$ additives, it was observed that TiO_2, as reported in the literature, is insoluble in both sulfuric acid or water and the addition of this additive to any water-based solution resulted in a paste. Similarly, dissolving $TiOSO_4$ in sulfuric acid at different concentrations, between 1M and 5M, was tested. According to these tests, similar to TiO_2, adding $TiOSO_4$ to sulfuric acid resulted in a white slurry material, which is believed to be TiO_2. However, it was seen that $TiOSO_4$ was easily dissolved in water, where its equilibrium reaction

is given in eq. 4-1. Different concentrations of Ti additive were tested, and it was seen that it is possible to achieve a 2.5M Ti solution. In case of Mn precursor, as given in eq. 4-2, it was observed that, 1M of this compound could easily dissolve in any acidic solution with concentration above 1M. Therefore, following these steps, it became apparent that, in order to produce 1L of the electrolyte, 1M $TiOSO_3$ (159.95 g/mol) was dissolved in 400ml of water. 228 ml of sulfuric acid was added to the solution, and once cooled down, 1M of $MnCO_3$ was dissolved to achieve the final product.

Titanium reaction: $$TiOSO_4 + H_2O \rightarrow TiO(OH)_2 + 2H^+ + SO_4^{2-}$$ eq. 4-1

Manganese reaction: $$MnCO_3 + H_2SO_4 \rightarrow MnSO_4 + CO_2 + H_2O$$ eq. 4-2

4.1.2 Hydrogen Electrode Performance Based on Pt loading and PTFE Content

In order to investigate the performance of hydrogen electrodes as a function of Pt loading in the catalyst layer, hydrogen electrodes with 0.4 mg_{pt}/cm^2 and 0.03 mg_{pt}/cm^2 Pt loading were tested in a RHMnFC system. Polarisation and power curves obtained from these two cells at 100% SoC electrolyte, shown in Figure 4-1, demonstrates that at current densities up to 1 A/cm^2, the Pt loading on electrode will not affect the performance of the cell [16,193]. However, it can be seen that, using the electrode with Pt loading of 0.4 mg_{pt}/cm^2, a high power density of 1400 mW/cm^2 was achieved.

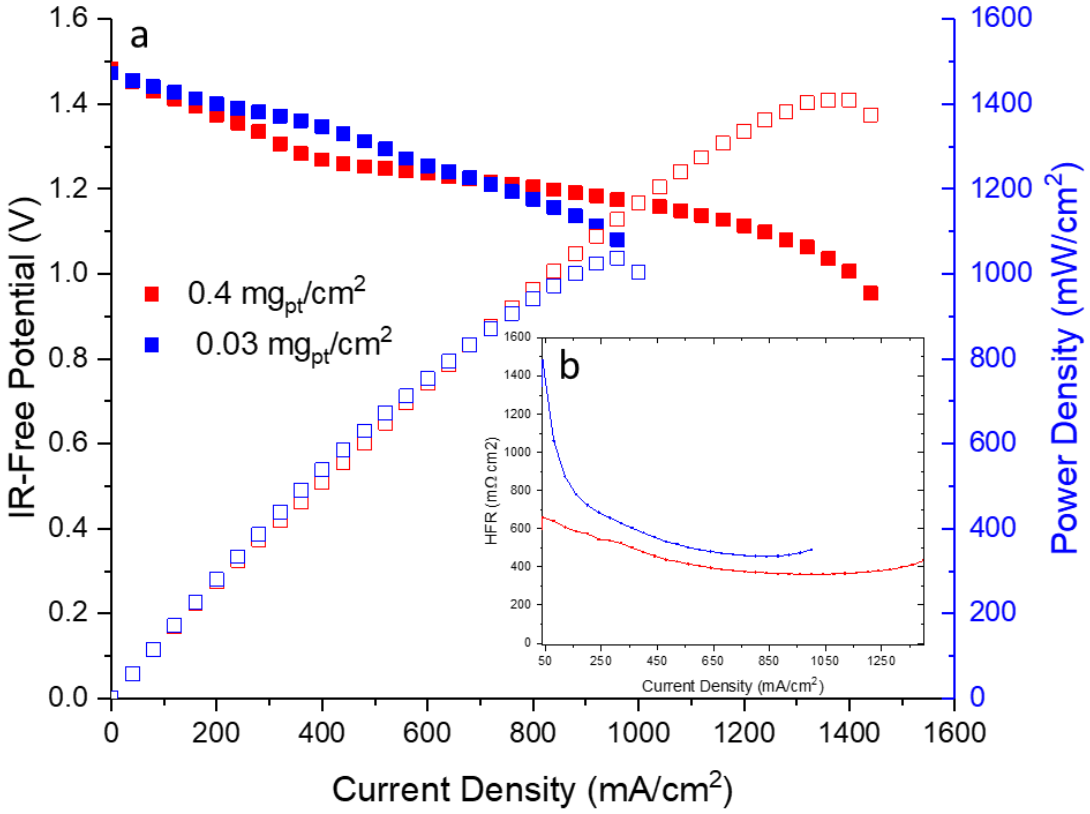

Figure 4-1: a) Polarisation and power curves of 0.4 mg_{pt}/cm^2 and 0.03 mg_{pt}/cm^2 Pt loading on hydrogen electrode in RHMnFC and b) HFR values recorded by the test station (Scribner e850) to take the ohmic losses to the account [16]

A significant potential error occurs during electrochemical measurements when the uncompensated resistance gets high. In all electrochemical cells, there is a specific resistance between the surface of the working electrode where reactions are occurring and the surface of the electrode where measurements are taken from. This resistance is generally referred to as the uncompensated-resistance. As current flows through the cell, an increasing potential is developed across the uncompensated resistance in the cell. Due to this potential, it is possible that the measured potential is lower than the voltage applied to the cell. Hence in order to take into the account for these losses, polarisation curves for both electrodes were iR-corrected using the HFR values recorded (presented in Figure 4-1 (B)) by the test station (Scribner e850) to take these ohmic losses into account.

As discussed previously in Section 2.2, RFB technologies prioritise the energy efficiency of the system over its maximum power density; consequently, the performance of the cell at higher current densities, which result in lower energy efficiency, are not a dictating factor in determining its advantages. Following these findings from experiments, to eliminate any effects of Pt loading on cell performance, hydrogen electrodes with 0.4 mg_{pt}/cm^2 Pt loading and 30% PTFE content were used.

4.1.3 Cathode (Liquid half-cell) Electrode Performance

The effect of different liquid half-cell electrodes (Mn electrolyte half-cell) was investigated using three different set ups. As reviewed in Chapter 2, the performance of the electrochemical systems is directly related to the electrode material and their properties. Following cathode electrode material selection from previous RFB work, galvanostatic charge and discharge cycles at 100 mA/cm^2 were carried out, and changes in the overpotential of the cell compared to OCP were recorded. In this part of the work, single layer and three layer carbon paper and graphite felt was used as the electrode in electrolyte half-cell, where their performances in terms of voltage, energy and coulombic efficiencies were analysed.

Prior to analysing the data obtained from testing these electrodes as the liquid half-cell electrodes, it is important to understand two main properties of these electrodes. These properties consist of the specific surface area (SSA) of each electrode and the available volume in the electrode after compression, which will directly impact the residence time (RT) of the electrolyte in the cell. As can be seen in Table 4-1, which presents the properties for each sample tested in the cell; for a 5 cm^2 cross section area, 3 layers of SGL 10AA carbon paper electrode has a greater surface area (SA) than the two other samples. However, graphite felt electrode (GFD 4.6), due to its thickness, will a have higher electrolyte residence time per pass with the electrolyte flow rate of 50 mL/min.

Table 4-1: Electrode properties of different samples tested as liquid half-cell electrodes (Numbers provided by SGL)

Sample	Thickness	Weight	SSA	SA	Porosity	Volume	RT
	cm	g	m^2/g	m^2	%	cm^3	S
SGL 10AA	0.04	0.01572	3.3	0.051876	88	0.132	0.1584
SGL 10AA[e]	0.12	0.04476	3.3	0.147708	88	0.396	0.4752
GFD 4.6	0.46	0.2169	0.4	0.08676	94	1.6215	1.9458

According to galvanostatic charge and discharge cycle of these three different electrode configurations, shown in Figure 4-2 (a), a capacity of 17.12 Ah/L was achieved using a single layer carbon paper, which represents only 65% of the theoretical capacity. Low electrolyte capacity utilisation of single layer carbon paper can be related to its low electrochemical surface area. Hence lower active surface area of single layer carbon results in a higher activation overpotential within the cell, which induces the starting voltage at the charge half-cycle to be closer to the cut-off voltage.

Arenas et. al. investigated the dependency of the electrolyte residence time and rate of conversion on RFBs and concluded that by reducing the residence time in the modules, conversion efficiency of the active species reduces [199]. Consequently, for the electrodes with lower residence time, it is only possible to charge a limited amount of the electrolyte before the cell reaches to 1.65 V. Furthermore, voltage, energy and coulombic efficiencies of the cell (i.e., the performance indicating factors) using single layer CP were calculated to be 66 %, 64% and 98%, respectively, demonstrated in Figure 4-2 (b). By increasing the number of layers of CP, stacked on top of each other, a dramatic increase in the-performance of the cell is observed. It can also be seen that, using 3 layers of the CP as the cathode electrode increased the capacity utilisation by 28%, from 65% to 92% of the electrolyte theoretical capacity (Figure 4-2 (a)). This can be attributed to two different mechanisms, including an increase in electrochemical surface area and increase in residence time of the electrolyte in the reaction site (presented in Table 4-1). Hence, this electrode adjustment, also reduces the activation overpotentials, which allows the system to charge for longer duration.

Following the mentioned drop in overpotentials, improvements in performance parameters are also recorded. Galvanostatic charge and discharge cycles at 100 mA/cm^2 performed on this electrode configuration exhibit an increase in the performance of the cell, where VE, EE and CE are calculated to be 76%, 75% and 99%, respectively.

[e] This sample consisted of 3 layers of SGL 10AA

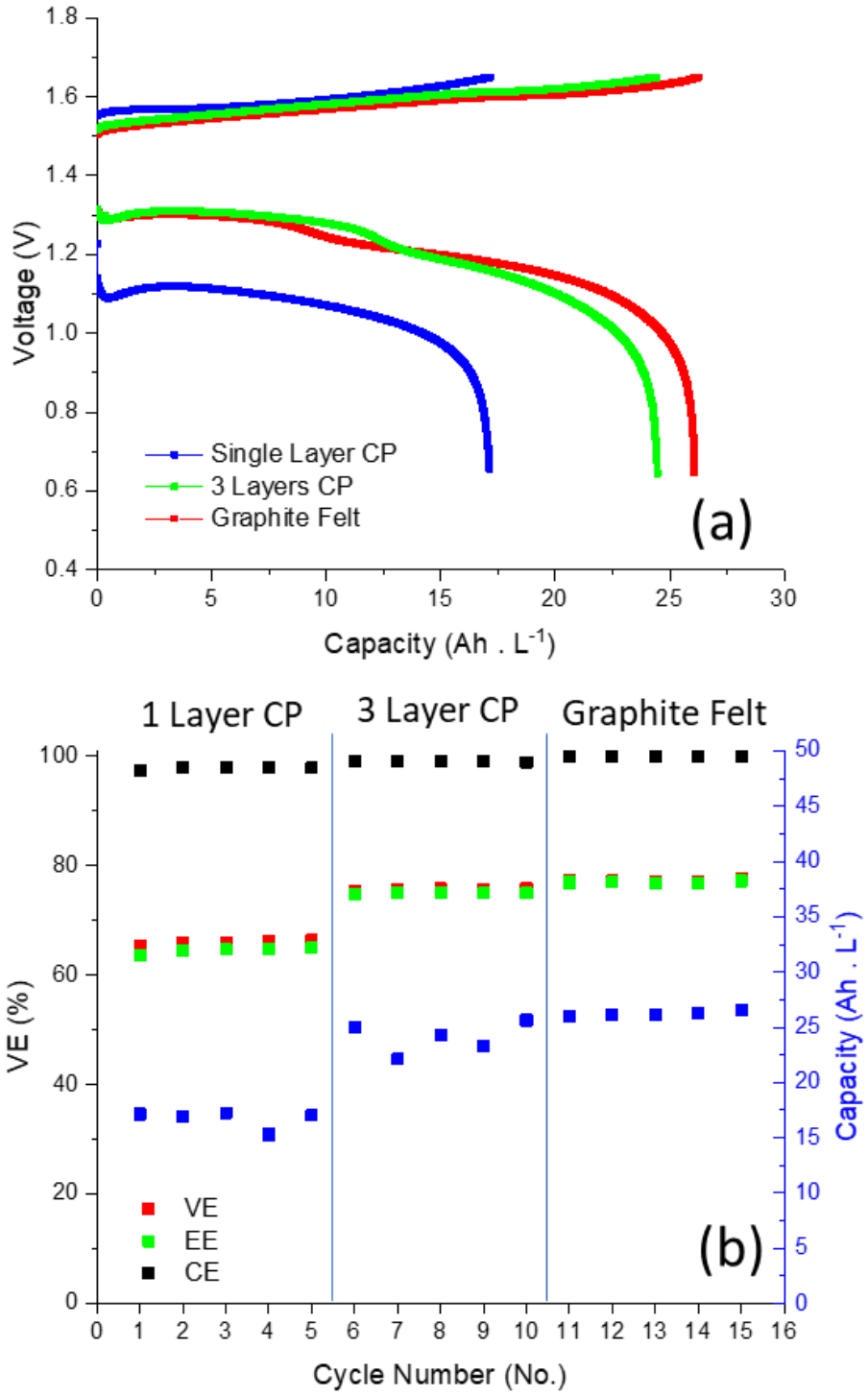

Figure 4-2: a) Galvanostatic charge and discharge of different electrode in RHMnFC and b) their performance analysis, consist of voltage efficiency (VE), Energy efficiency (EE) and coulombic efficiency (CE) during five cycles at 100 mA/cm²

By replacing the previously tested CP electrode with graphite felt in the liquid half-cell, there was an improvement in the performance of the cell, close to the performance achieved by the 3 layered CP configuration. The graphite felt configuration achieved a 98% capacity utilisation, approximately 6% higher than the 3 layer CP setup. Moreover, the VE and EE of the cell was observed to increase by 2% relative to the 3 layer CP setup. In addition to voltage and energy efficiency improvement, the

coulombic efficiency of the cell exhibited a more uniform performance in 5 galvanostatic charge and discharge cycles, when compared to the cells using CPs as their electrode, achieving coulombic efficiency of 99.97% in average.

According to these results, the changes in overall efficiencies of the RHMnFC cell using three different setups align with the findings from the literature, discussed in Chapter 2. As it was suggested, the performance of the electrochemical cells is in direct correlation with both active surface area of the electrodes and residence time of the electrolyte, reported in Table 4-1, in this compartment. Therefore, using graphite felt, which has higher active surface area compared to CP, higher performance was achieved in comparison to cells assembled with CP as their liquid half-cell electrodes. Following the findings from these experiments, it was decided to use graphite felt as the cathode electrode for rest of the study.

4.1.4 Ion Exchange Membrane Selection

The role of the IEM in the performance of RFBs was discussed in Section 2.4.2.4.3, where researchers demonstrated that using a Nafion 212 (thickness of 50 µm) in VRFBs resulted in a 4% higher voltage efficiency in the cell. However, it significantly reduced the lifetime of the system, as higher crossover rate was observed compared to Nafion 117 (Thickness of 183 µm) [116,120].

Therefore, to further investigate the RHMnFC choice of components, the performance of two different Nafion membranes were investigated, to understand the impact of different membrane thickness on the performance of the cell, as well as the impact this might have on the electrolyte crossover from the liquid half-cell to hydrogen half-cell.

In this part of the experiments, RHMnFCs were assembled according to the aforementioned electrodes (Sections 3.1.2.1 and 3.1.2.2). To compare the losses in performance and degradation in capacity over number of cycles, both assemblies, with Nafion 212 or Nafion 117 as their membranes, were charged and discharged at 100 mA/cm^2 for 150 cycles. Since in these two assemblies, identical configuration of hydrogen and electrolyte electrode were used, the performance evaluation indexes were primarily affected by the performance of different IEMs in each assembly. However, in order to carry these tests in shorter times, the concentration of the Mn active species was reduced from 1M to 0.2M. Hence, an electrolyte with 0.2M Mn and 0.2M Ti in 3M H_2SO_4 was used to perform these experiments.

According to the galvanostatic charge and discharge cycles performed on both setups, where their performance is illustrated in Figure 4-3, the energy efficiencies of both cell configurations are above 70% at the start of the experiments. However, there is a lower coulombic efficiency, and thus lower

energy efficiency, in the cell with Nafion 212 as its membrane (Figure 4-3 (a)), compared with the EE of the cell with Nafion 117 membrane (Figure 4-3 (b)). This effect can be attributed to capacity losses caused by the crossover of the- electrolyte through the thinner membrane (N212).

Looking at the charge and discharge cycles of the assembly with Nafion 212, fluctuations in VE can be observed, which can be attributed to the mass transport limitations caused by flooding of the hydrogen electrode as a result of electrolyte crossover from the liquid half-cell to the gas side. This limits hydrogen gas permeability through the electrode and hence reduces its permeation from GDL to CL, where hydrogen oxidation reaction takes place during discharge. The presence of the electrolyte in the hydrogen side during charging also limits the diffusion of the produced hydrogen through the CL to GDL and eventually to exit the cell. This phenomenon induces a decrease in the accessible surface area for hydrogen reduction during charge, which increases the mass transport overpotential.

This hypothesis around the efficiency loses, due to crossover of electrolyte, can also be investigated by measuring the capacity retention in each cycle. The graph (a) in Figure 4-3 shows that the specific capacity of the electrolyte in the cell with the Nafion 212 membrane decreases by 35% compared to its initial capacity over 50 cycles. However, as an advantage of this hybrid flow battery system, mixing of the liquid electrolyte with hydrogen analyte does not occur, thus the capacity of the electrolyte can be retained by recycling the electrolyte collected on the hydrogen side back into the electrolyte reservoir.

On the other hand, the cell assembly with Nafion 117 as its membrane, has shown a consistency in performance levels as it retains its cycle efficiencies across the 150 performed cycles. This demonstrates a negligible crossover of electrolyte from the liquid side to gas half-cell during discharge, resulting in stable energy efficiency during its operation period. In these experiments, no accumulation of electrolyte in recovery tank on the hydrogen side was observed, which is consistent with the steady capacity retention of the electrolyte during its operation.

Consequently, according to the experiments carried out on the effect of two different membranes on the performance of the cell, the results indicate that Nafion 117 will result in no or minimal energy density losses while operating the RHMnFC, corroborating other studies reported previously in Section 3.1.2.3. However, this will be further investigated and reported in Section 4.1.8.

Furthermore, although fluctuations of the VE and EE were related to the mass transport limitation due to the crossover of electrolyte, it could also be argued that electrolyte crossover also results in activation polarisation and a form of ohmic overpotential during charge and discharge due to blockage of the reaction sites and transport required through the liquid that would coat the electrode surface.

As a result of crossover, active surface area (where hydrogen evolution and oxidation occur) is decreased. Therefore, at the start of cell charge or discharge, higher energy is required to initiate the reaction in the CL, which results in higher activation overpotential.

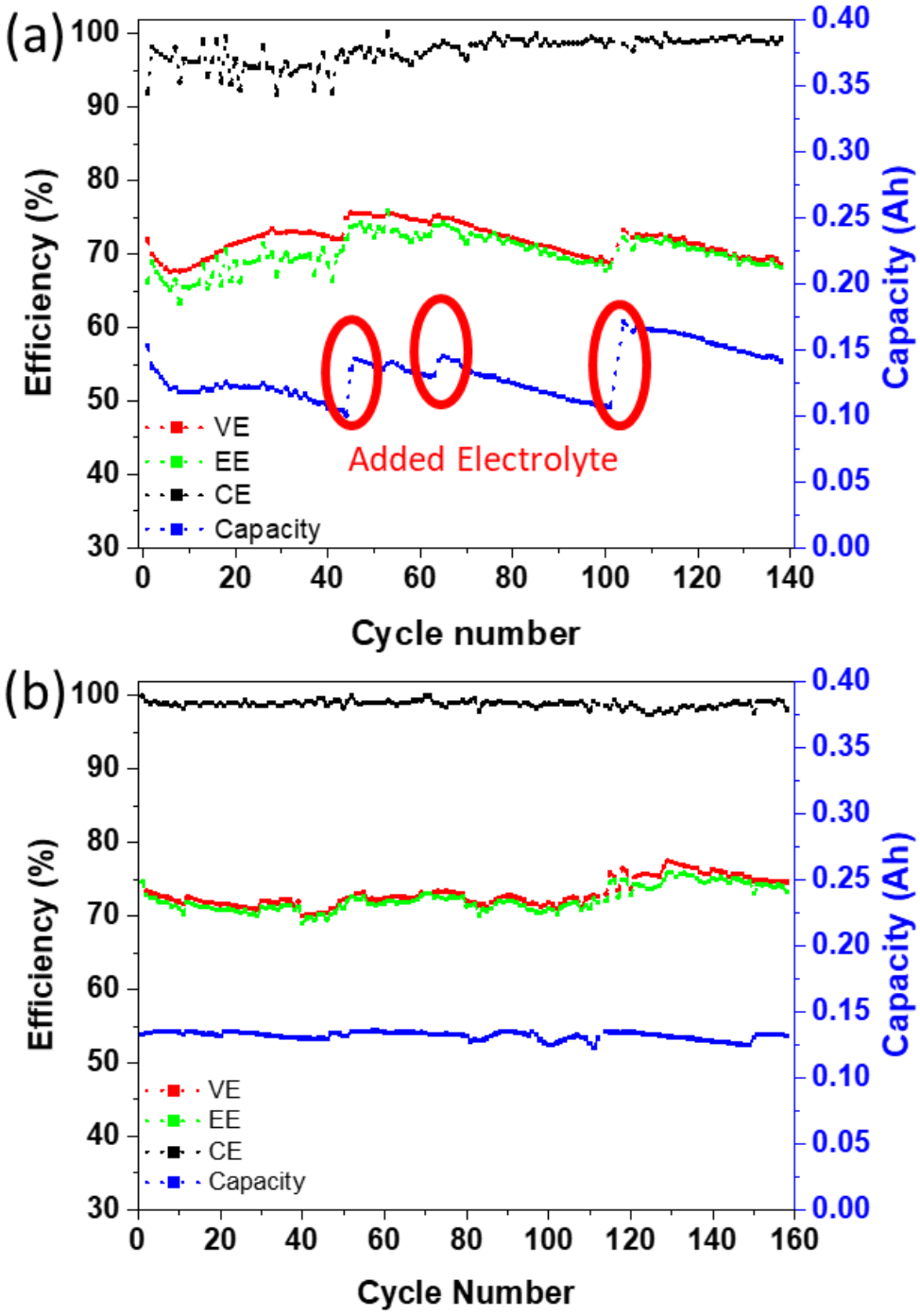

Figure 4-3: Galvanostatic charge and discharge performance of cell at 100 mA/cm² with (a) Nafion 112 (b) and Nafion 117, 0.2M Mn and 0.2M Ti in 3M H_2SO_4

Also, it could be argued that, due to the existence of liquid electrolyte on the surface of membrane/electrode interface and surface of the fibres throughout the hydrogen electrode, ionic and electronic conduction will be affected, producing an ohmic drop during the operation. Therefore, it is

concluded that the effect of crossover is more complex than is immediately obvious and may have significantly more impact than just the increase in the mass transport overpotentials.

4.1.5 Sulfuric Acid Concentration of Electrolyte

The concentration of H_2SO_4 has an influence on the ionic conductivity and viscosity of any flow battery electrolyte. In order to investigate the effect of H_2SO_4 concentration as the electrolyte support in the performance of the flow cell, three different concentrations of H_2SO_4 in the electrolyte were tested. According to the preliminary results, shown in Figure 4-4 (a), the best performance was obtained using 3M of H_2SO_4 in the electrolyte.

By increasing the concentration of H_2SO_4 from 3M to 5M, there was a 4% drop in EE, which can be related to the change in the viscosity of the electrolyte. At a higher viscosity, the diffusion of electrolyte is hindered through the porous graphite felt electrode. Although other studies on H_2SO_4 based flow batteries have also shown a decrease in energy efficiency at higher H_2SO_4 concentrations as viscosity increases [200], work on Mn flow batteries has suggested that the sulfuric acid concentration effects the life time of the electrolyte [91]. As will be discussed in Section 4.1.7, at 100% SOC, where Mn^{3+} is produced through the oxidation reaction during charge, disproportionation occurs, where MnO_2 is produced as particulates. This reaction releases protons; hence the concentration of sulfuric acid can affect the equilibrium of the disproportionation reaction. Therefore, at higher H_2SO_4 concentrations, when the concentration of protons is increased, the disproportion reaction is less favourable, which affects the stability of the electrolyte [91].

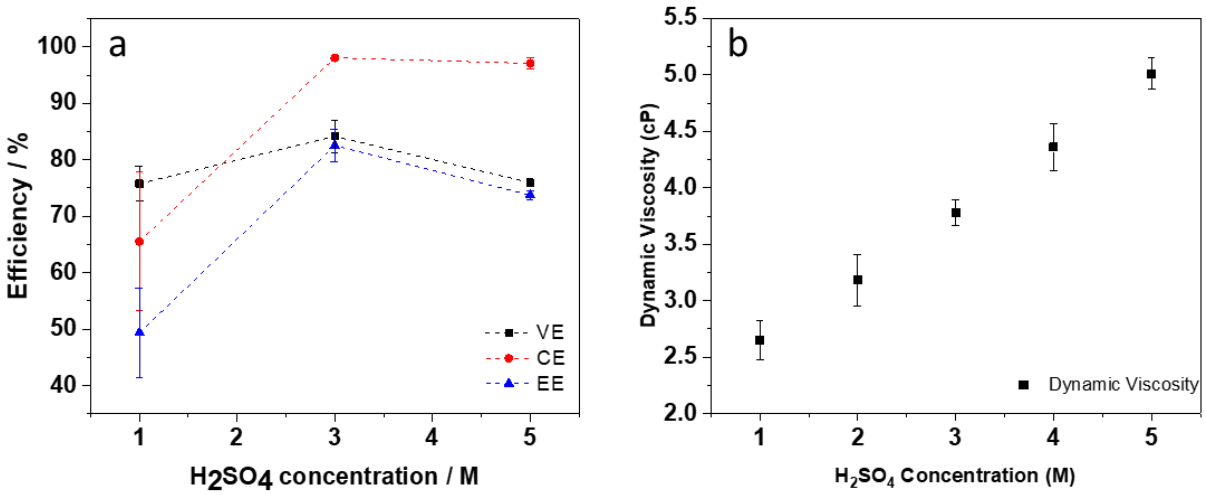

Figure 4-4: The performance of the RHMnFC with different H_2SO_4 concentration a) energy efficiency, voltage efficiency and coulombic efficiency of the cell and b) dynamic viscosity of the electrolyte

In order to understand the relationship between the change in viscosity of the electrolyte and its acid content, drop ball dynamic viscosity measurement was carried out and is presented in Figure 4-4 (b). According to these measurements, as expected, the dynamic viscosity of the H_2SO_4 electrolyte

increases with increasing acid concentration in the solution. Therefore, it is possible that the decrease in the EE of the cell, with H_2SO_4 concentration of 5M in the electrolyte, is resulted by the increase in the mass transport overpotential.

Therefore, taking all the findings into consideration, it was decided that the electrolyte with 5M sulfuric acid concentration will be used in this work. Although, this will decrease the energy and voltage efficiencies of the RHMnFC, it will increase the stability of the electrolyte at a high state of charge, which is a crucial index for the lifetime of the cell for commercial applications.

4.1.6 RHMnFC performance at Different Current Densities

To further investigate the cell performance and achieve an optimum current density, building on previous findings of best performing MEA components, the cell was tested under different current densities, using 40 ml of 1M Mn and 1M Ti in 5M sulfuric acid electrolyte. According to the previous results, in this assembly a hydrogen electrode with 0.4 mg_{pt}/cm^2 Pt loading and 30% PTFE loading was used. In the liquid half-cell, untreated graphite felt with 4.6 mm thickness was used as the electrode and Nafion 117 was employed as the proton exchange membrane. The cell was operated at different current densities between 20 mA/cm^2 and 120 mA/cm^2.

Galvanostatic charge and discharge of the RHMnFC at different current densities, illustrated in Figure 4-5, indicates that high VE and EE is achievable using this set up. It can be seen that, at current densities between 20 mA/cm^2 and 50 mA/cm^2 energy efficiencies above 80% are achievable. By increasing the current density above 50 mA/cm^2, the EE of the cell drops to 78% at 100 mA/cm^2, which can be attributed to the increase of the activation and mass transport overpotentials at higher current densities. The most important performance evaluation factor, which makes this chemistry comparable and more successful than alternative chemistries discussed in Chapter 2, is the achievable discharge capacity (compared to theoretical capacity) of this chemistry.

It can be seen that at current densities between 40 mA/cm^2 and 100 mA/cm^2, capacities close to 100% of theoretical capacity can be achieved. According to these measurements, at 40 mA/cm^2 capacity of 1.067 Ah (99.68% of the theoretical capacity) was achieved. Further increase in the current density demonstrated a high charge and discharge capacity of 1.061 Ah (99.46%$_T$) and 1.059 Ah (98.33%$_T$) at current densities of 60 mA/cm^2 and 80 mA/cm^2 were obtained respectively. It was also observed that, at a higher current density of 100 mA/cm^2 it was possible to achieve 97.67% of the theoretical capacity (1.047 Ah).

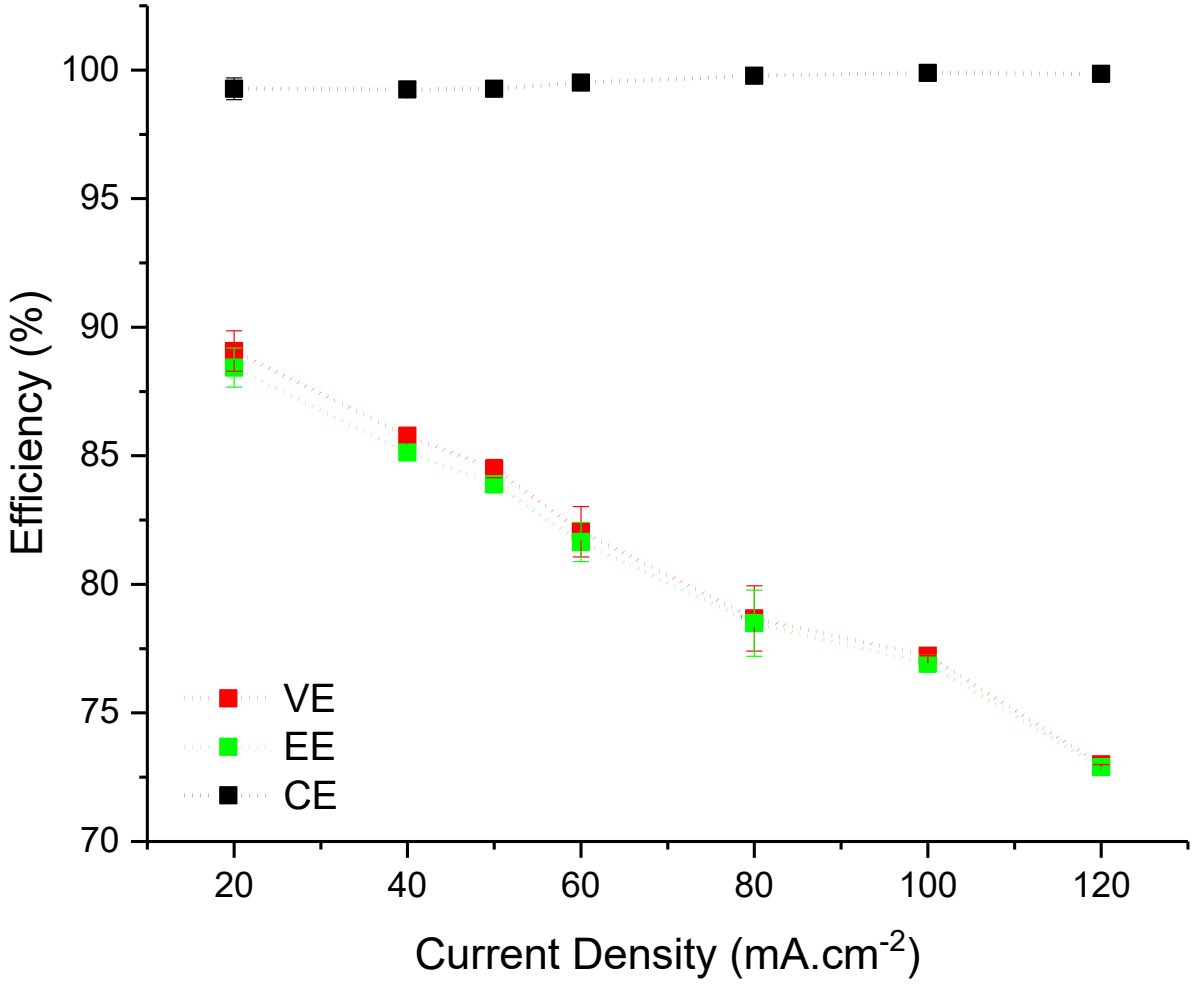

Figure 4-5: Performance evaluation analysis of RHMnFC at different current densities. 40 ml electrolyte with 1M Mn and Ti in 5M H_2SO_4 with 50 ml/min flow rate and 100 ml/min H_2 flow rate.

By increasing the current density to 120 mA/cm^2, there is a 6% drop in EE compared to the level achieved at 100 mA/cm^2. Although the voltage and energy efficiencies of the cell are determined to be above the acceptable threshold according to U.S. Department of Energy [17], its specific capacity drops below 70% of the theoretical capacity. Considering the charge and discharge cycle of the cell, it can be seen in Figure 4-6, at 120 mA/cm^2, the starting overpotential is very close to the cut off voltage. Due to the high activation overpotential of the cell at this current density, the electrolyte can only be charged for a short time, which results in a capacity utilisation of 67.38% compared to the theoretical capacity of the electrolyte.

The most interesting outcome of these sets of experiments was the performance observed from charge and discharge cycles at 20 mA/cm^2, where a capacity 46% higher than theoretical discharge capacity was achieved. This phenomenon was demonstrated to be highly reversible, where a coulombic efficiency of 99.91% was obtained from the analysis on the charge and discharge cycles carried out at this current density.

Previously, in Section 2.4.2.1, the stability of manganese at high state of charge was reviewed, and it was discussed that Mn^{3+} in the absence of additives, is believed to go through a disproportionation reaction, whereby, according to eq. 4-3, two Mn^{3+} active species react with each other and produce Mn^{2+} and MnO_2 (Mn^{4+}). The mechanism, by which MnO_2 forms, is through an intermediate reaction given in eq. 4-4. Even with Ti additive in the electrolyte, which helps to suppress the disproportionation of Mn^{3+} to Mn^{2+} and MnO_2, this reaction still occurs at a lower rate. However, this composition of the electrolyte, beside suppressing the disproportionation, also affects the morphology of the precipitated manganese dioxide [76].

$$2Mn^{3+} + 2H_2O \rightarrow Mn^{2+} + MnO_2 + H^{4+} \quad \text{eq. 4-3}$$

$$Mn^{3+} + 2H_2O \rightarrow MnOOH + 3H^{+} \quad \text{eq. 4-4}$$

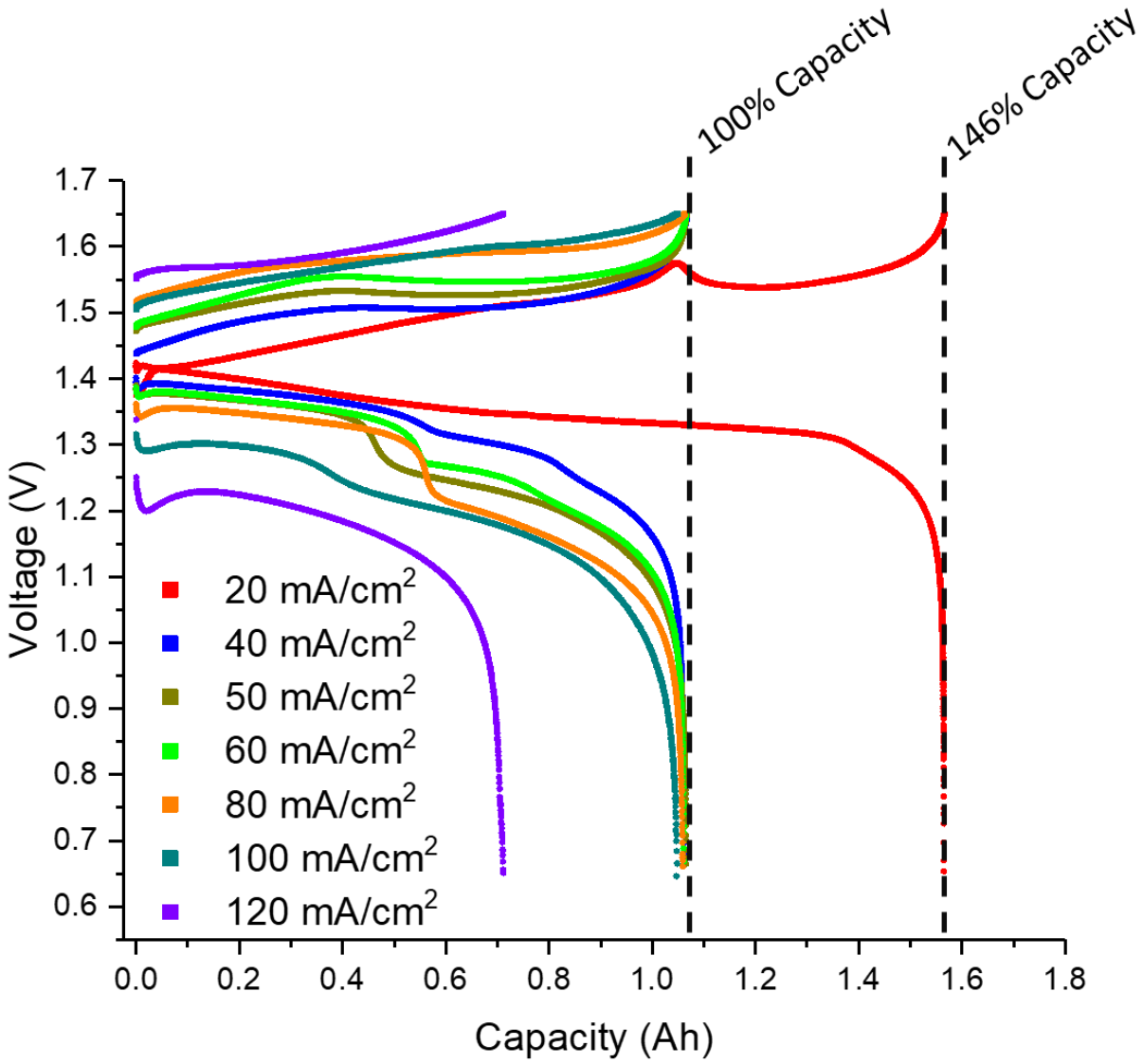

Figure 4-6: Galvanostatic charge and discharge of RHMnFC at different current densities; 20 mA/cm² up to 120 mA/cm². 40 ml Electrolyte with theoretical capacity of 1.072 Ah.

According to these aforementioned mechanisms, due to the charging period of the cell at low current density, it is believed that the produced Mn^{3+} goes through the disproportionation reaction. Due to the occurrence of this phenomenon, all the Mn^{3+} is converted into 0.5M Mn^{2+} and 0.5M MnO_2, which, in this case 50% extra Mn^{2+} becomes available in the solution. According to this hypothesis, it is possible to achieve a capacity utilisation close to 150% of the theoretical capacity.

However, based on this assumption, the duration of galvanostatic charging is the key indicator on the amount of disproportionation reaction that takes place in the electrolyte. In order to investigate this hypothesis, the duration of charge was reduced from 10 hours to 7.5 hours by reducing the electrolyte volume from 40 mL to 30 mL. As expected, and illustrated in Figure 4-7, the achievable specific capacity is reduced from 146% using 40 mL electrolyte to 131.2% with 30 mL electrolyte. This indicates that, as the charging period decreases, the disproportionation reaction occurs for shorter time, which results in 15% less Mn^{2+} production.

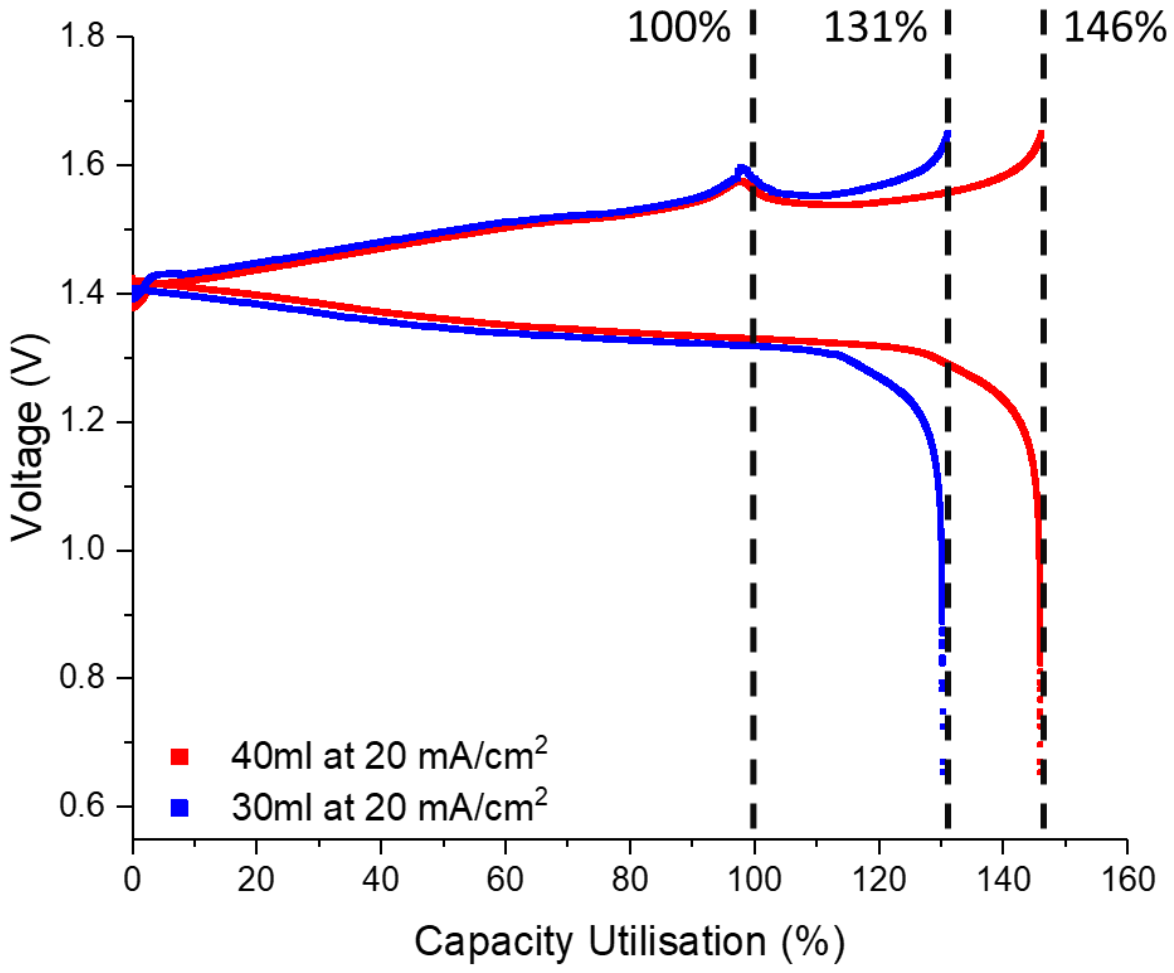

Figure 4-7: Comparison of charge and discharge cycle of 30ml and 40ml electrolyte at 20 mA/cm²

In order to be able to understand and explain the observed phenomenon, Mn^{3+} disproportionation was modelled in the Electrochemistry group by Prof. Anthony Kucernak, using the kinetic model given

in eq. 4-5. According to this equation, the change in concentration of the Mn^{3+} is calculated over time (t) at different temperatures (T), where k is the rate constant of Mn^{3+} ($6.53 \times 10^{-7}\ dm^3/mol.s$) [201]. ΔG refers to the Gibbs energy of formation of the aqueous ions of manganese (72 KJ/mol) [201].

$$\frac{d[Mn^{3+}]}{dt} = -k\ exp\left(\frac{-\Delta G}{R}\left(\frac{1}{T} - \frac{1}{298}\right)\right)[Mn^{3+}]^2 \qquad \text{eq. 4-5}$$

Using eq. 4-5, the change in Mn^{3+} is predicted over time at temperatures between 20 °C and 65°C, illustrated in Figure 4-8, where according to this graph, it can be seen that concentration of Mn^{3+} disproportionation occurs at a faster rate as the temperature increases. However, at room temperature, where all the experiments are carried out, the change in concentration is lower than 3% in first 20 hours.

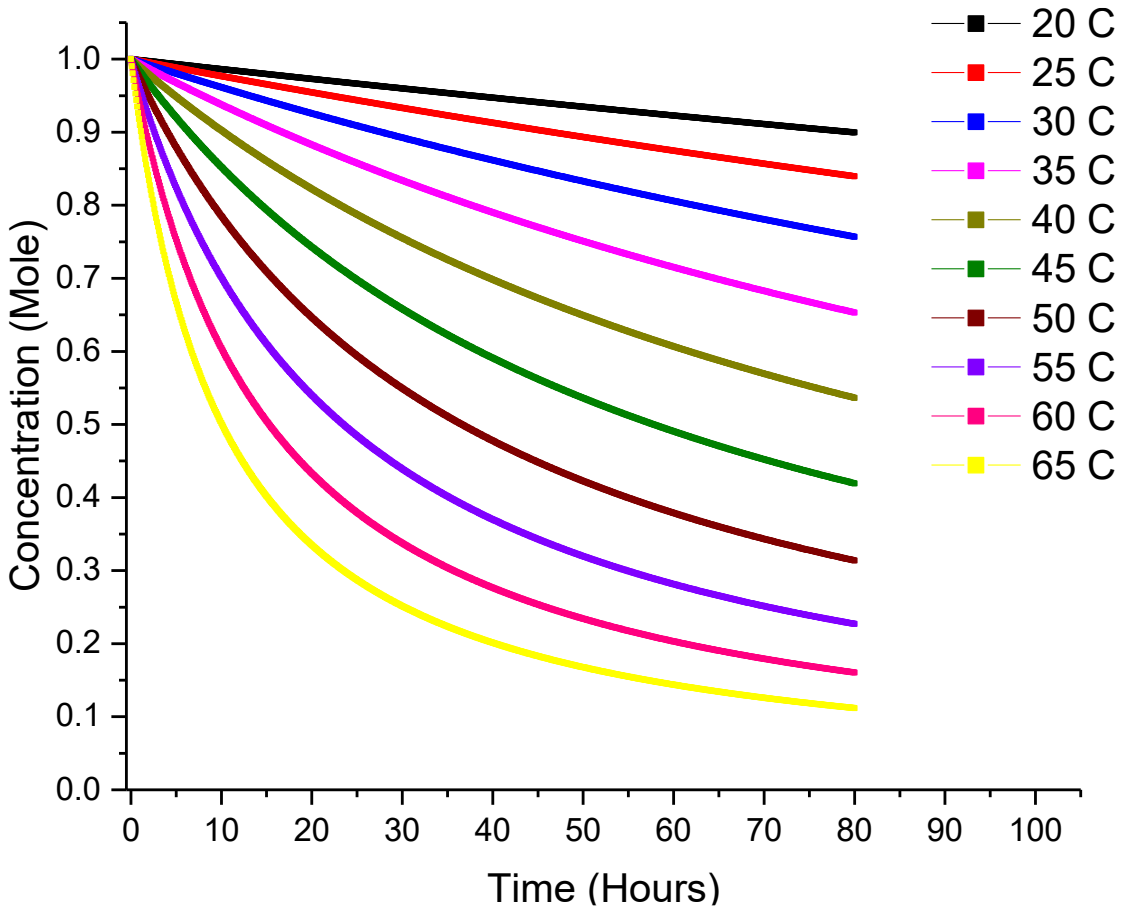

Figure 4-8: Calculated Mn^{3+} concentration at different temperatures over time

Therefore, according to this model, the disproportionation reaction increases when the cell temperature is above room temperature (20 °C). It is important to understand that the model only takes into account the disproportionation of the Mn^{3+} in the electrolyte at 100% SOC, and during the reaction 50% of the disproportionated species turn into Mn^{2+} and no further reaction occurs. However, according to the configuration of the experimental setups, the cell is constantly being charged and

hence the concentration of Mn^{3+} is constantly increasing. Additionally, this model shows that at higher concentrations of Mn^{3+}, disproportionation reaction occurs at a faster rate, while at lower concentrations, the rate of disproportionation is reduced. During galvanostatic charging, Mn^{3+} concentration is retained at higher concentration, and therefore its rate of disproportionation is faster. The reversibility of this reaction will be discussed in the next chapter (Chapter 5).

Another hypothesis that could explain this observation, is the intermediate reaction given in eq. 4-6. According to this hypothesis, it is possible that manganese exists as a suspension in the electrolyte, at its intermediate state. Thus, intermediary MnOOH provides the extra electron, which according to the reversible reaction shown in eq. 4-6, then transforms into MnO_2 precipitates.

$$MnOOH \leftrightarrow MnO_2 + H^+ + e^- \quad \text{eq. 4-6}$$

It is important to note that, in the electrode where the reaction occurs, it is possible that both the intermediate reaction and final precipitation reaction contribute to extra achieved capacity. However, since both reactions form precipitates, it would be expected that these precipitates would increase the ohmic resistance and block the channels and prevent further charging. It is also possible to hypothesise that when charging at low current densities, despite the precipitation and deposition of Mn onto the electrode's fibre surface, the change in active surface area of the electrode has little impact on the possibility of the cell to reach the cut-off voltage. This is due to the low current density approximating a low enough rate of reaction such that the limitation in active surface area is not yet an issue.

During discharge at a low current density of 20 mA/cm^2, a similar process is expected to occur, whereby the existing Mn^{3+} redox species are reduced to Mn^{2+}. Once all the existing Mn^{3+} is converted into Mn^{2+}, the remainder of the reactions, suggested by lee et al. [202], can happen in two possible ways. It is possible that the reduction reaction, given in eq. 4-7, is a 2 electron transfer process, whereby MnO_2 precipitates exist as a suspension in the solution that will directly reduce to Mn^{2+}, and produce manganese active species soluble in the supporting electrolyte.

$$MnO_2 + 2H^+ + 2e^- \leftrightarrow Mn^{2+} + 2H_2O \quad \text{eq. 4-7}$$

The second route would involve a two-step process, similar to what was proposed while charging, including an intermediate step were MnO_2 is initially reduced to MnOOH. According to this assumption, during discharge, MnO_2 initially reduces to MnOOH in a one electron process, shown in eq. 4-8. Then the produced MnOOH reduces into Mn^{2+} through a second electrochemical reduction reaction, given in eq. 4-9.

$$MnO_2 + H^+ + e^- \leftrightarrow MnOOH \quad \text{eq. 4-8}$$

$$MnOOH + 3H^+ + e^- \leftrightarrow Mn^{2+} + 2H_2O \quad \text{eq. 4-9}$$

According to the exhibited charge and discharge cycle of the cell at 20 mA/cm^2, it was understood that the reactions occurring in the cell are reversable reactions. However, this will depend on the rest time of the electrolyte between charge and discharge at each cycle. The reversibility of the disproportionation reaction will be investigated in Chapter 5, where the electrolyte will be overcharged to produce MnO_2 and will be discharged with different resting times between charge and discharge half cycles.

4.1.7 Cell Performance at Initial Cycle

Following the findings in the previous experiments, electrolyte composition and flow cell components for the MEA have been established. According to the results in Section 4.1.6, a current density of 100 mA/cm^2 was chosen to be the optimum current density to perform the experiments. However, after using a fresh electrolyte and attempting to charge and discharge the cell at the mentioned current density, a low energy efficiency was observed to be 45% lower than the theoretical capacity.

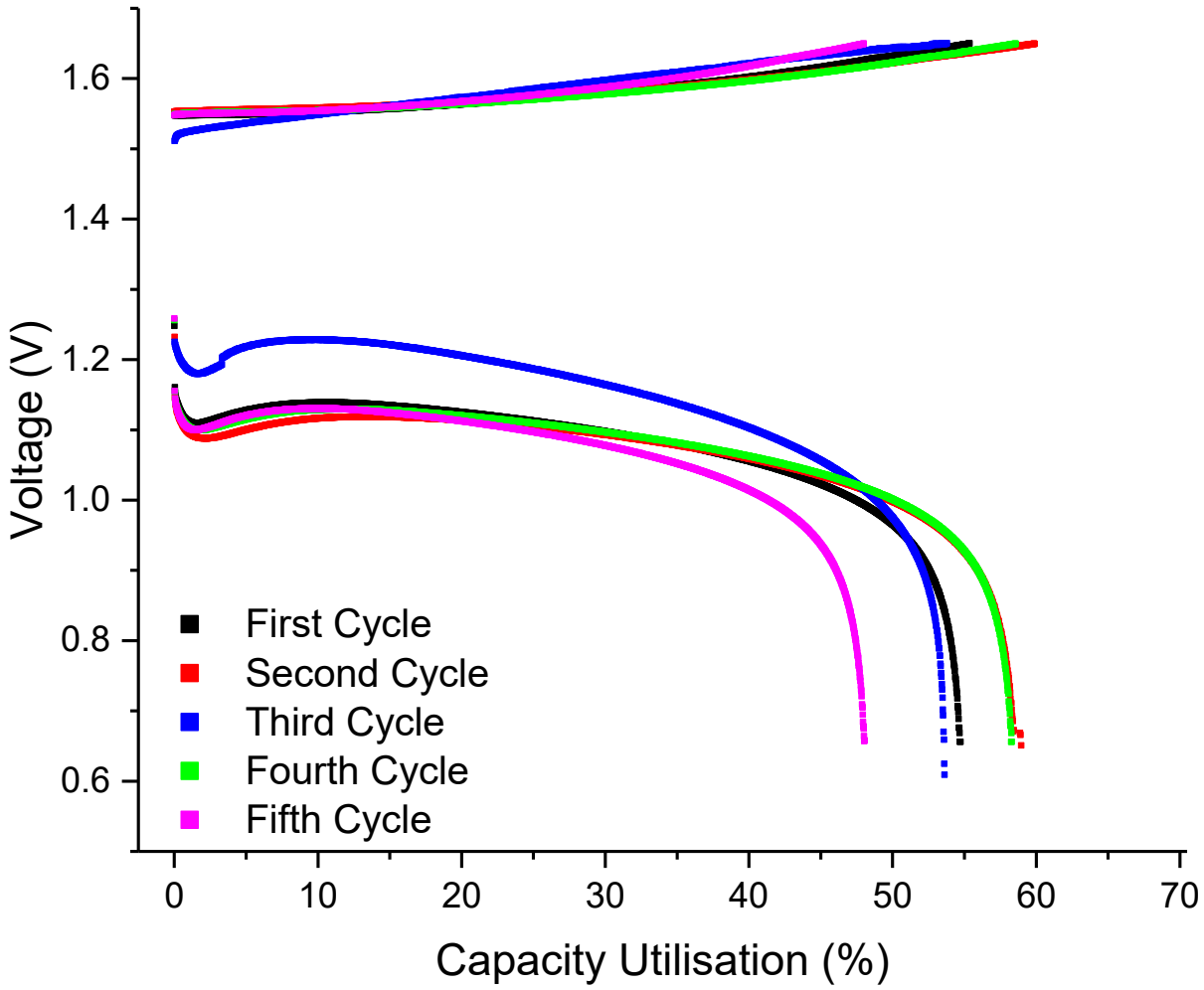

Figure 4-9: 5 galvanostatic charge discharge cycle of fresh electrolyte at 100 mA/cm^2

As the experiment used a cell that had been used previously, and the components were not replaced, it was expected that the performance of the cell would not be affected by changing the electrolyte. As presented Figure 4-9, with a fresh electrolyte, the achievable capacity was limited to an average of 55% theoretical capacity. The limited achievable capacity and lower EE, in comparison to what was reported previously at current density of 100 mA/cm^2 (Figure 4-6), can be related to the composition of the Mn-Ti complex in the fresh electrolyte.

Comparing the performance evaluation indexes, analysed and presented in Figure 4-10, for both fresh electrolyte and what was achieved as a standard performance for this chemistry, also indicates a considerable drop and inconsistency in efficiencies of the cell using a fresh electrolyte. It can be seen that EE and VE drop significantly to 68% on average, which is 9% lower than what could be achieved previously using a conditioned electrolyte. This drop in the performance could be attributed to the wettability and surface treatment of the electrode in a newly assembled cell, but this phenomenon is not consistent with the experimental set up, where a cell that had been previously tested was being used.

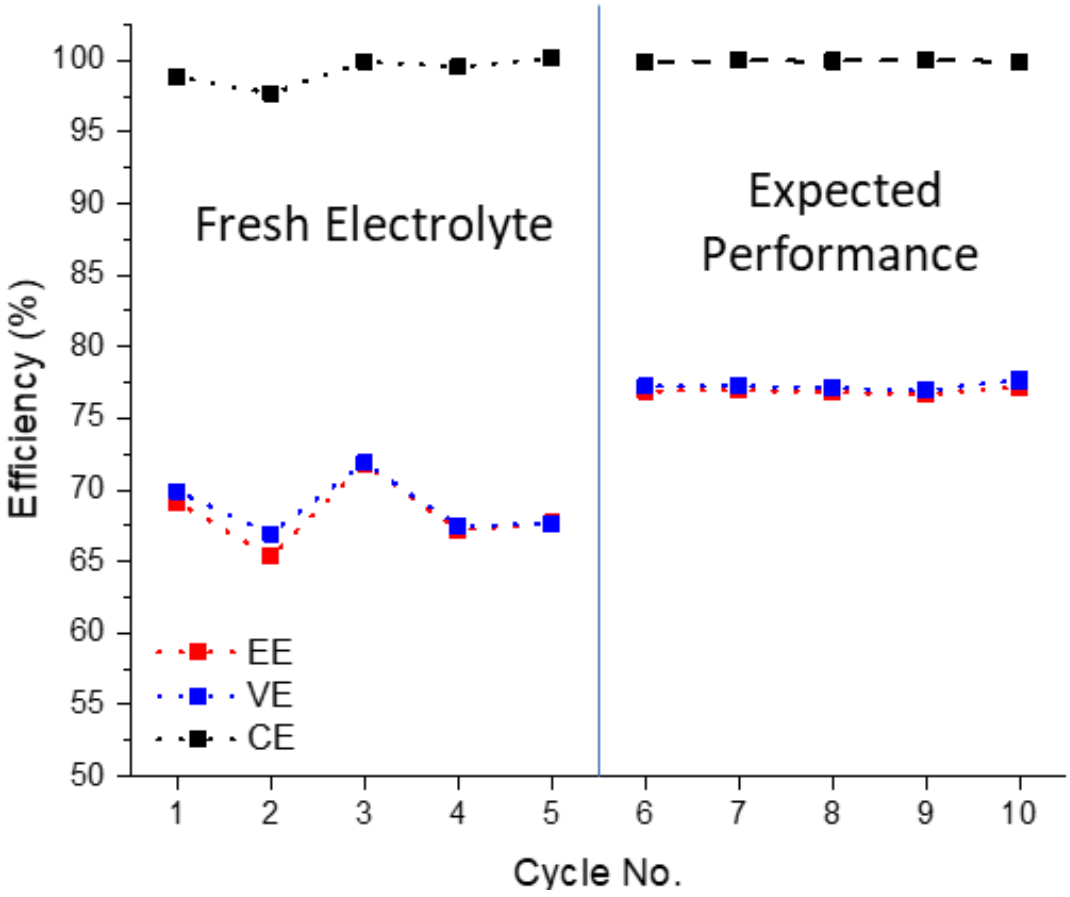

Figure 4-10: Performance analysis of 5 galvanostatic charge and discharge cycle of fresh electrolyte at 100 mA/cm^2

However, by reducing the current density to 20 mA/cm^2, using the same electrolyte and set up, and following running a cycle at low current density, charging and discharging the cell at 100 mA/cm^2, a higher capacity was achieved. A galvanostatic charge and discharge cycle, presented in Figure 4-11, shows that after charging the cell at lower current density, a capacity comparable to that reported in Section 4.1.6 could be reached.

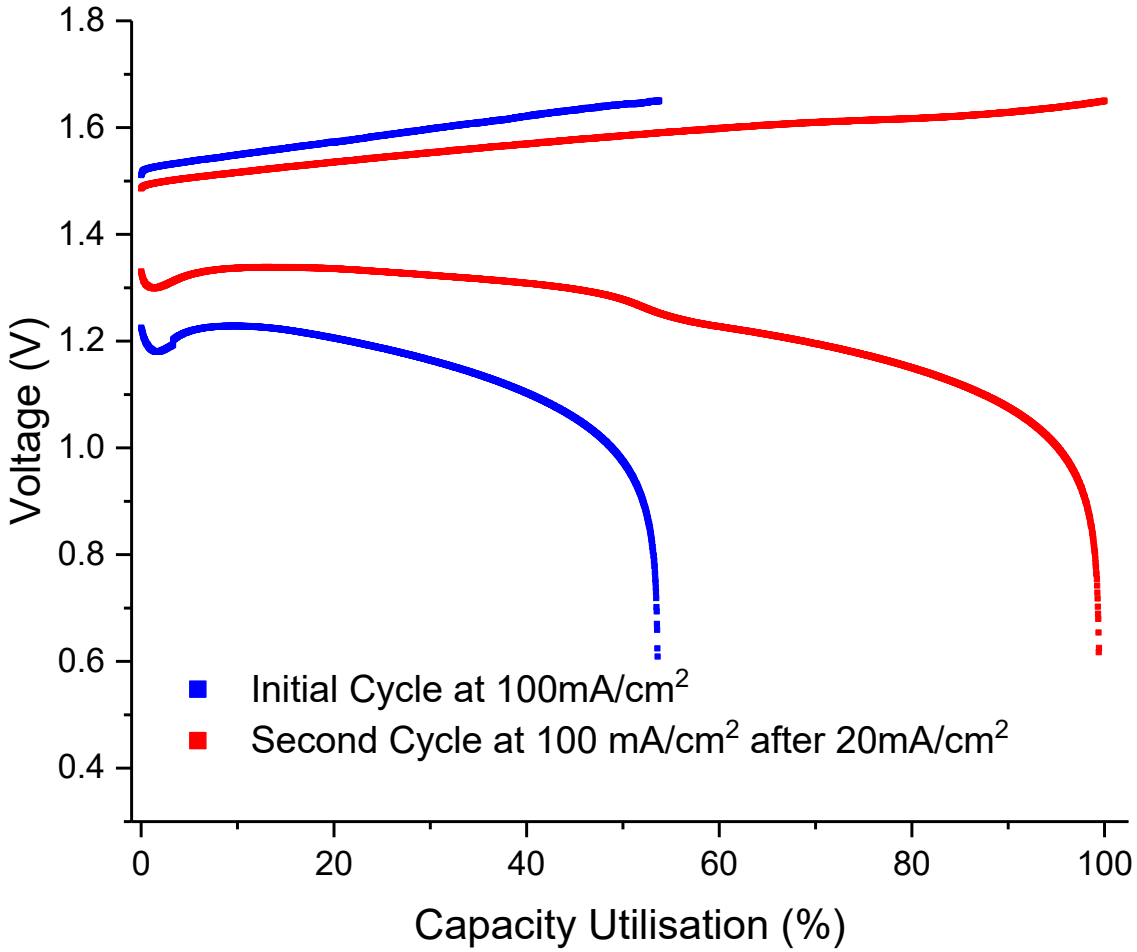

Figure 4-11: Initial charge and discharge cycle at 100 mA/cm^2 with fresh electrolyte and charge discharge cycle after running the electrolyte at 20 mA/cm^2 and performing charge and discharge cycle at 100 mA/cm^2

Therefore, observed irregularity in performance is believed to be as a result of the electrolyte composition, which can be related to a number of mechanisms:

1. From a mechanical point of view, it could be hypothesised that the inconsistent performance of the cell at the start, is due to the surface tension of a fresh electrolyte, which leads into limited interaction of the active species with the available surface area of the electrode. Hence, it can be assumed that the high surface tension of the electrolyte results in a higher charge transfer resistance between the electrode and the electrolyte. Additionally, high

surface tension of the electrolyte inhibits electrolyte movement, which consequently lowers the transport of the electrolyte through the porous graphite felt electrode.

2. Due to the use of Ti in the electrolyte as an additive, it is possible that these elements interact with each other to produce complex chains [203]. Thus, it is possible that there are Mn active species that are in shorter chains, and some of the dissolved Mn are in longer complex chains. Therefore, charging the electrolyte at high current density, which requires higher rates of mass transport, only Mn redox metals in shorter chains are able to participate in the reaction, as they will have higher diffusion coefficients. Hence, Mn in longer chains will have a lower diffusion coefficient, such that in order to be able to access these electroactive species lower charge rate is required.

3. At low current density, as charge transfer occurs at lower rate, Mn^{2+} active species present in long complex chains participate in the oxidation reaction, and, due to this reaction, bonds between the chains breaks to form smaller chains. According to this hypothesis, once smaller polymer chains are produced, polarisation due to mass transport limitation decreases. Hence, according to this mechanism, it is possible to access all the Mn present in the electrolyte.

EIS data collected at 0% SoC for the RHMnFC system before and after changing the electrolyte are displayed by the Nyquist plot in Figure 4-12. It is clear that the EIS measurements of the cell with the used electrolyte and fresh electrolyte exhibit similar values for the series and charge transfer resistance of the cell. These two resistances are characteristic properties of the cell components such as IEM and MEA, and since the same cell components are being used, similar values are obtained for all three different measurements.

The Nyquist plots reveal that a lower frequency semi-circle, which indicates the losses that are associated with the diffusion processes in the porous media [39], the cell with a fresh electrolyte have a higher resistance value. However, the diffusion resistance obtained from EIS measurements for the fresh electrolyte after performing the conditioning step, by charging and discharging at a constant current density of 20 mA/cm^2, reduces by 3 Ωcm^2, and exhibits a similar values to the impedance data obtained from the electrolyte, which was used previously in the cell.

Therefore, low VE obtained from the charge and discharge cycles can be attributed to the high diffusion resistance of the fresh electrolyte, which effects the diffusivity of the Mn^{2+} active species from the bulk electrolyte to the surface of the electrode, where the oxidation reaction occurs. The difference in the diffusion resistances, for the cells with different electrolyte conditions (fresh and

conditioned), demonstrates the importance of the conditioning step. Although, the collected data helps to explain the losses in the fresh electrolyte, mechanisms that contribute to these losses in the cell must be further studied.

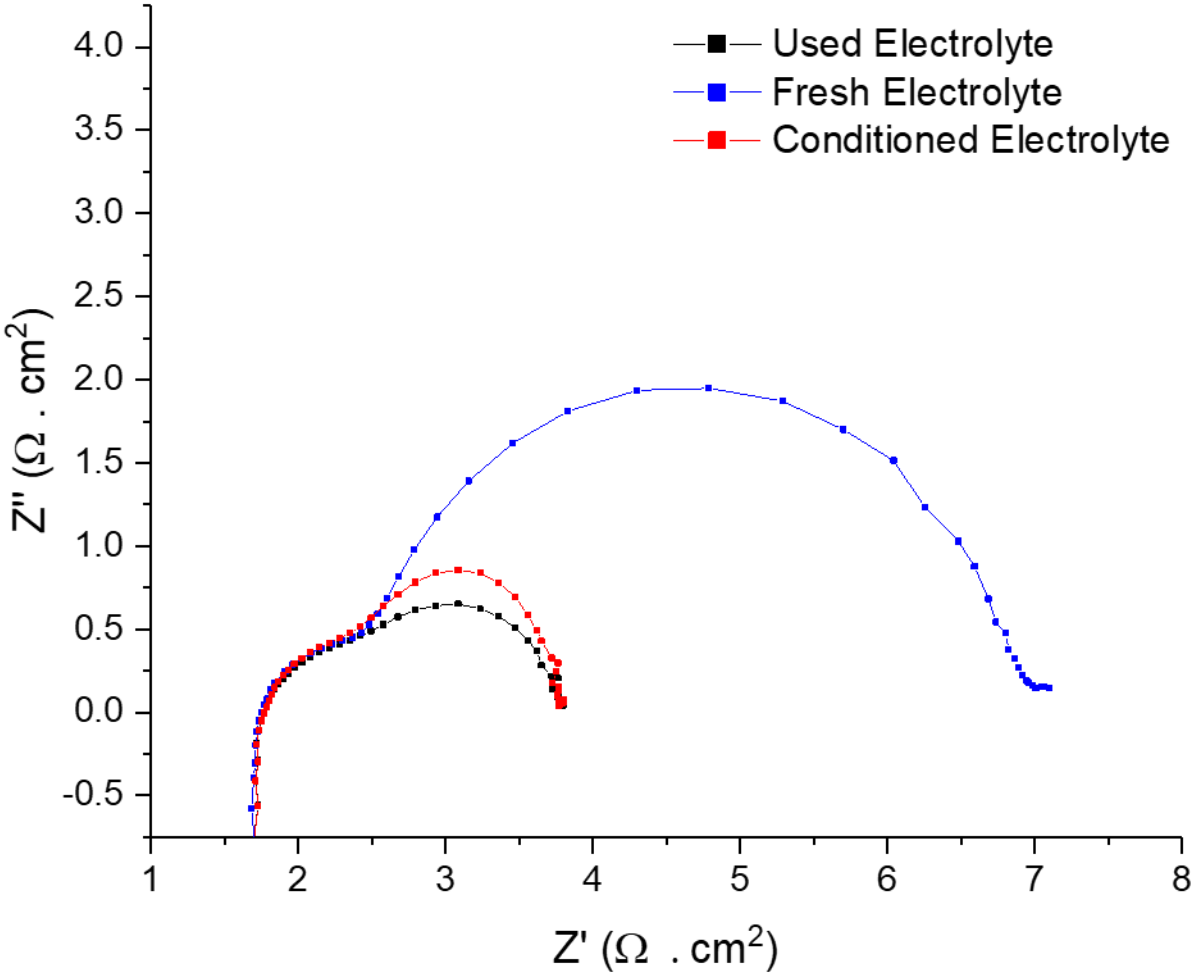

Figure 4-12: Nyquist Plot for the RHMnFC cell at 0% SoC, before and after changing the electrolyte to illustrate the effect of conditioning step on the diffusion resistance of the system (frequency range (100 kHz to 10mHz)

4.1.8 Crossover During Discharge

One of the main limitations of flow batteries, as discussed in the review of flow batteries in Chapter 2 and Section 2.4.2.4.3, is the crossover of the active species between two half-cells. Although it is easier to collect and recirculate the electrolyte crossover in hybrid Gas-liquid RFBs, there are still inefficiencies relating to these systems.

From a visual perspective, there were no observable traces of Mn electrolyte or water droplets, due to condensation of water vapour, in the electrolyte collecting tank. Also, as decay in capacity was not observed during lifetime testing, it could be hypothesised that the electrolyte crossover during the charging of the cell, where protons from the oxidation reaction of Mn^{2+} migrate through the

membrane, is negligible. To further investigate the possibility of crossover, Gas chromatography–mass spectrometry (GC-MS) was used to identify the presence of different gas substances within the cell.

In this analysis, in order to collect a standard reading, gas coming directly from hydrogen cylinder was initially analysed, where the presence of deferent standard gases was recorded. Afterward, a drying column (Drierite 26800, Cole-Parmer®) was connected in line with the outlet of the hydrogen half-cell, to trap any moisture or vapour coming out of the hydrogen side due to crossover of electrolyte. This test was repeated without drierite, to analyse the increase in water vapour, which would provide information regarding possible crossover of the electrolyte. In this method, all the measurements were obtained during cell charging, where hydrogen would be produced, and the reduction reaction of H_2 was occurring on the hydrogen electrode.

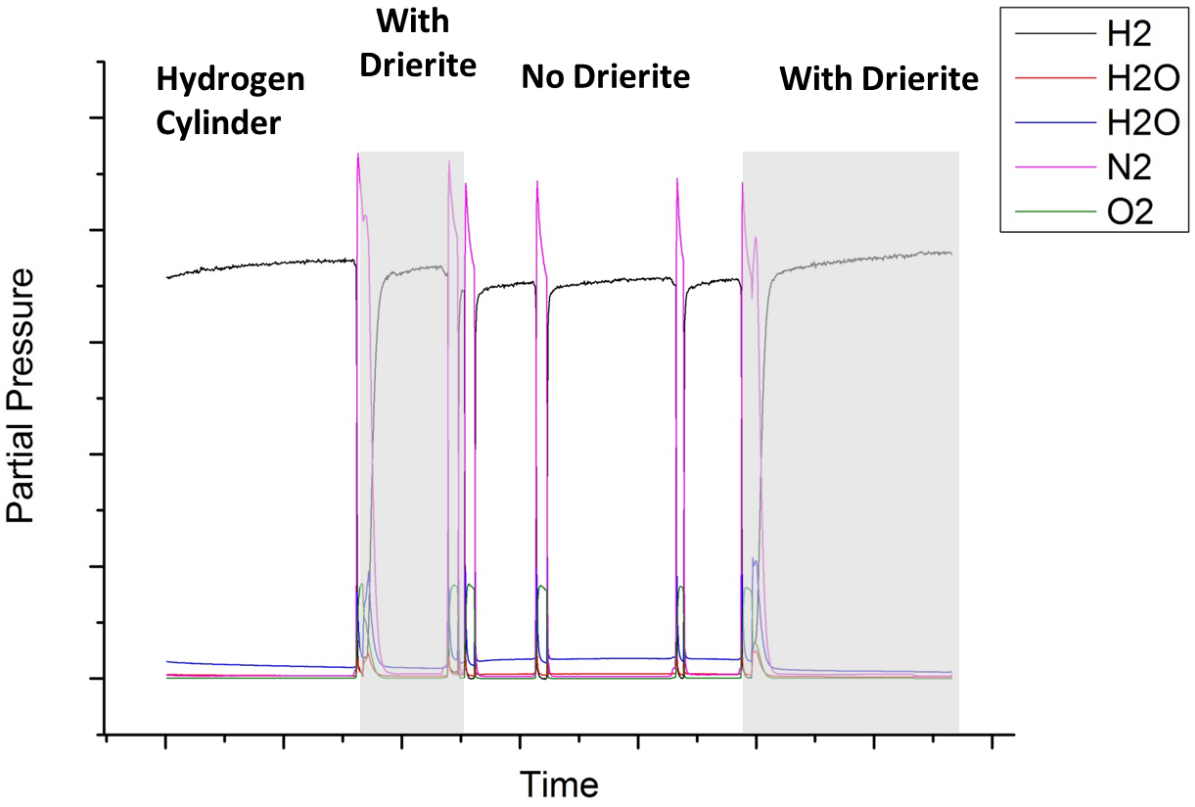

Figure 4-13: GC-MS analysis of produced gasses during charging of the cell, where hydrogen is produced [f]

According to the GC-MS measurements, illustrated in Figure 4-13, while charging the cell, there is a gain in H_2O pressure as protons move from the liquid side to the gas side. This increase in pressure

[f] Due to the COVID-19 pandemic, it was not possible to extract the raw data from the computer in the lab. Therefore, this figure will be recreated to match the format of this thesis, as soon as possible.

shows the presence of liquid in the hydrogen half-cell during reduction of H_2 on CL layer. The presence of liquid could be caused by either the migration of proton with the water molecules through the membrane, according to what was discussed in Chapter 2, or by the crossover of the electrolyte through the membrane from the liquid half-cell to the hydrogen half-cell.

To further investigate this, upon deconstruction of the cell, the CL layer of the hydrogen electrode, which is contact with the membrane in the MEA, was analysed using Energy Dispersive X-Ray Spectroscopy (EDX). Analysis on the hydrogen electrode, presented in Figure 4-14, demonstrated the presence of Mn and Ti elements on the electrode. Looking at the identified elements, Mn is the dominant element at the surface, which can be in form of MnO_2 or $MnSO_4$, where EDX analysis is not a sufficient technique to distinguish the form of compound. However, from a visual point of view, it is known that MnO_2 appears as a black/dark brown precipitate, where $MnSO_2$ tends to be cream/light brown particles. As it appeared from the deconstruction of the cell, a light brown coating could be seen on the surface, which signifies the presence of $MnSO_4$ on the hydrogen side.

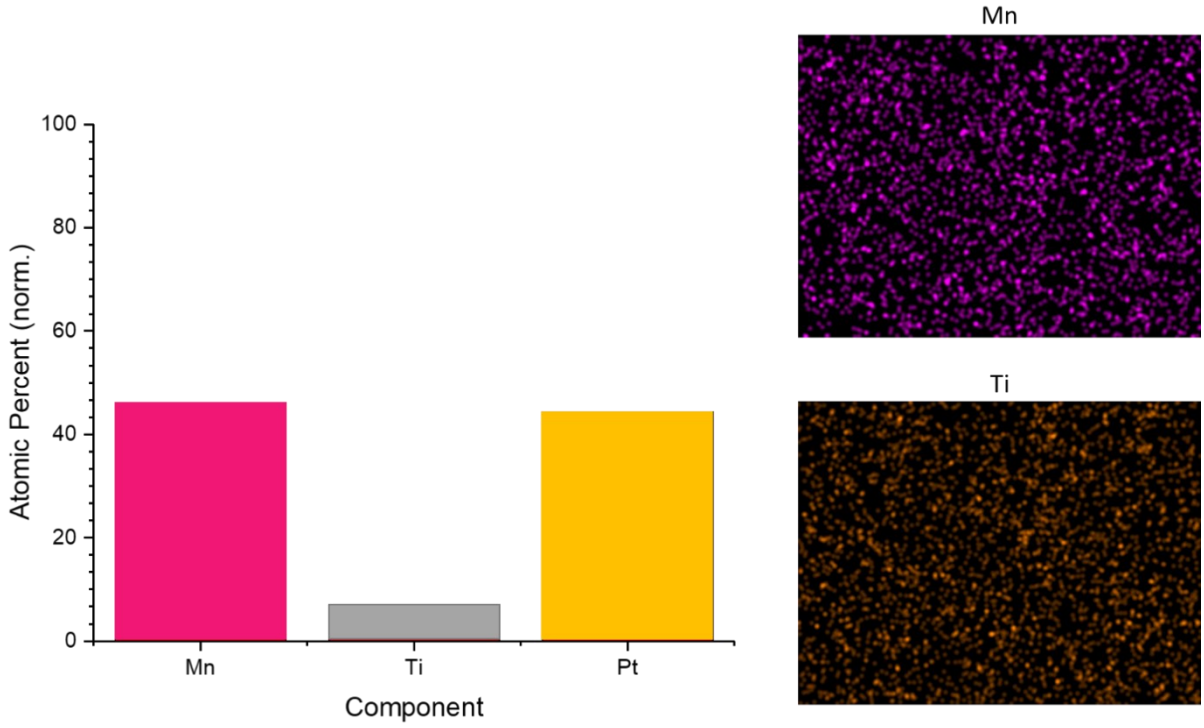

Figure 4-14: Atomic Percent of elements on the hydrogen electrode from EDX analysis [193]

Consequently, following these sets of experiments, it can be concluded that there is a sufficient amount of crossover in this hybrid flow battery to keep the membrane hydrated. Also, this crossover is not as pronounced as has been observed and reported in the literature investigating VRFBs, where a 25% decay in capacity was observed over 100 cycles in VRFBs [204]. Thus, to be able to further investigate this phenomenon, a large active area cell could help to have more conclusive results.

Crossover occurs across the membrane, which by increasing the area, the total volume of crossover will be higher than could be collected in a 5 cm^2 cell.

4.1.9 Investigating Feasibility of RHMnFC Scale Up

Following outcomes on the hybrid hydrogen-manganese regenerative fuel cell, from different experiments on a small 5 cm^2 active area flow cell, the performance of this novel energy storage technology in a large 150 cm^2 active area cell was investigated. Subsequently, the knowledge gained from investigating different configurations and materials for each compartment was attempted to be transferred to a large-scale cell, with an active area of 150 cm^2. For this purpose, a commercial cell was ordered initially, where the best performing components from previous sections, such as hydrogen electrode, graphite felt and Nafion 117 were used in this cell.

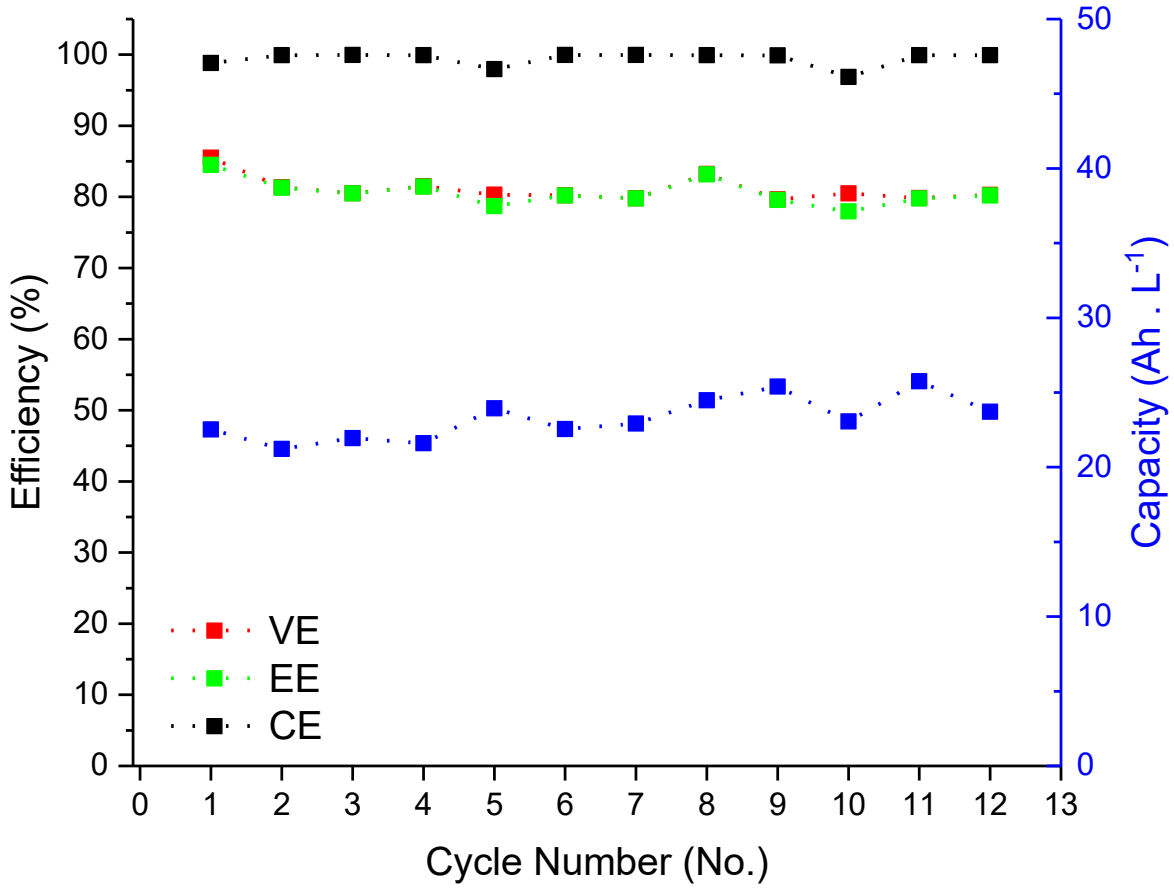

Figure 4-15: EE, VE and CE of the 150 cm^2 cell, galvanostatic charged and discharged cycles at 20 mA/cm^2. 1 L electrolyte of 1M Mn and 1M Ti with 5M H_2SO_4 concentration. Electrolyte flow rate: 150 ml/min, Hydrogen flow rate: 300 ml/min

The results from galvanostatic charge and discharge cycling of the cell at 20mA/cm^2 exhibited an average performance of 81% and 99.41% for EE and CE respectively. Comparing the obtained EEs from large (Figure 4-15) and small (Figure 4-6) cells, it could be seen that the performance of the commercial

cell (custom designed and manufactured to mitigate the needs of the hydrogen-manganese hybrid flow cell) was 8% lower than what was achieved in small cell testing (reported in Section 4.1.6).

Two different mechanisms were assumed to lead to the performance losses in this setup. Firstly, the effect of flow rate on the performance of the cell was investigated, where flow rate was increased from 150 mL/min to 200 mL/min. The change in flow rate, however, did not affect the efficiency. Secondly, the compression of the electrodes was believed to contribute to the reduction in performance. As discussed in Section 0, in fuel cells and flow batteries where porous electrodes are used for gas or electrolyte distribution, the optimum compression is between 20% and 25% [101,103].

Over compression of electrodes can introduce mass transport limitations to the reaction interface and low compression on the electrodes can affect its conductivity. By deconstructing the electrochemical cell, the compression of the graphite felt electrode was measured to be only 10% (460 μm), while the hydrogen electrode was compressed to 50% of its initial thickness. These measurements were taken based on the thickness of the gaskets and frames used in each electrode, as well as taking into the account the maximum compressibility of the employed gaskets in each half-cell.

Therefore, two different issues were participating in reducing the performance of the cell. In the hydrogen half-cell, the permeability of the electrode was reduced, hindering hydrogen diffusion from the CL to the GDL, and then outside the cell. In the liquid half-cell, the conductivity of the electrode would be affected by low compression of the cell, where the ohmic resistance would increase.

Since this manufactured cell was designed to be able to progress to build a stack, and hence PVC flow frames were used to limit shunt current between each cell, it was not possible to increase the compression. As the thickness tolerance of this flow frame was measured to be approximately ±200 µm, gaskets with a minimum compression of 200 µm must be used to mitigate the thickness tolerance of the PVC frames and eliminate the electrolyte leakage. By changing the gasket from 2 mm Viton gasket with 300 µm compressibility to a 1.75 mm gasket (with final compression of 15% on felt electrode), galvanostatic charge and discharge was carried out again.

According to the new set of tests, the results for which are presented in Figure 4-16, there was an improvement in EE and achievable capacity, where the EE of the cell was improved by 5% in comparison to the initial tests. Also it was observed that, similar to what was reported in Section 4.1.6, at 20 mA/cm^2 it was possible to reach beyond the one electron transfer reaction, where 129% theoretical capacity was achieved in 5 charge and discharge cycles carried out on the cell.

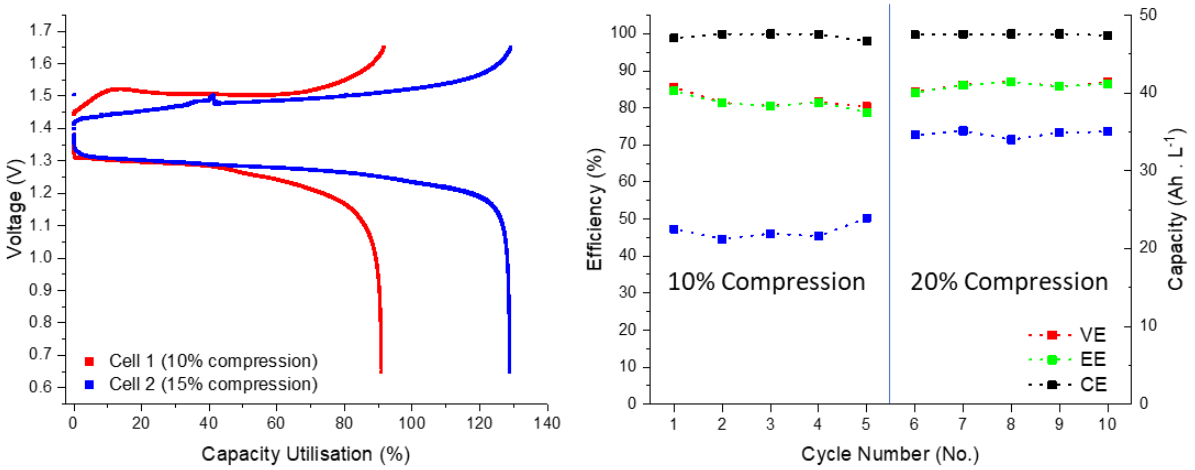

Figure 4-16: Charge and discharge cycle of 150 cm^2 with 10% and 15% achievable compression (Left) and performance comparison of these two cells (right)

This was believed to be for two reasons: firstly, the leak of the electrolyte could be due to the porous material used as manifold housings and the electrolyte progressively impregnated into the existing porous in these manifold housings and started to leak (Figure 4-17); secondly, due to the low tolerance in manufacturing parts, gaskets may not provide sufficient sealing and eventually the electrolyte reached the outer edge of the gaskets and leaked behind the liquid half-cell flow frame in contact with the current collector.

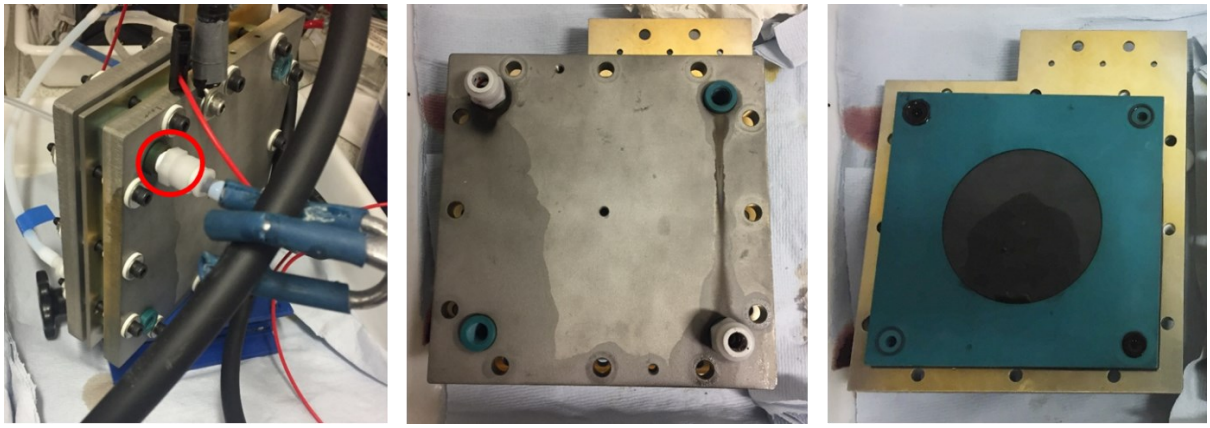

Figure 4-17: Leakage observed from the cell after one week of testing and presence of electrolyte at the interface of graphite plate and current collector upon deconstruction

The presence of liquid on the interface of the current collector not only caused degradation of the current collector, but also resulted in oscillations of the voltage measurements. Upon deconstruction of the cell, it was observed that the graphite plate on the liquid side had been bent, which this could also be the reason for presence of electrolyte on the interface of the current collector.

Following these observations and limitations in current design, a new liquid half-cell compartment was designed and manufactured by the author. In order use the commercial end plates, the dimensions of the cell were limited to the position of the inlet and outlet manifolds, as well as the

tightening screws on the endplates. This could possibly limit the sealing on the edges of the electrode compartment, as the space where the gaskets had to seal was thin and limited.

This cell was initially conditioned according the procedure outlined in Section 4.1.7. Following conditioning steps, tests were carried out by increasing the current density to 85 mA/cm^2. Performance analysis, presented in Figure 4-18, demonstrated a consistent performance over 10 cycles with average EE of 76%. The loss in voltage efficiency, compared to results obtained from the testing of the small electrochemical cell, can be attributed to the low flow rate used to carry out the tests on this cell. Due to the limited lifetime of the Viton tubes, used in the peristaltic pump, it was decided to use a flow rate of 250 mL/min for the electrolyte and 500 mL/min for hydrogen. This limitation can cause concentration polarisation at higher current density, as the rate of oxidation and reduction of the Mn active species during charge and discharge respectively increases.

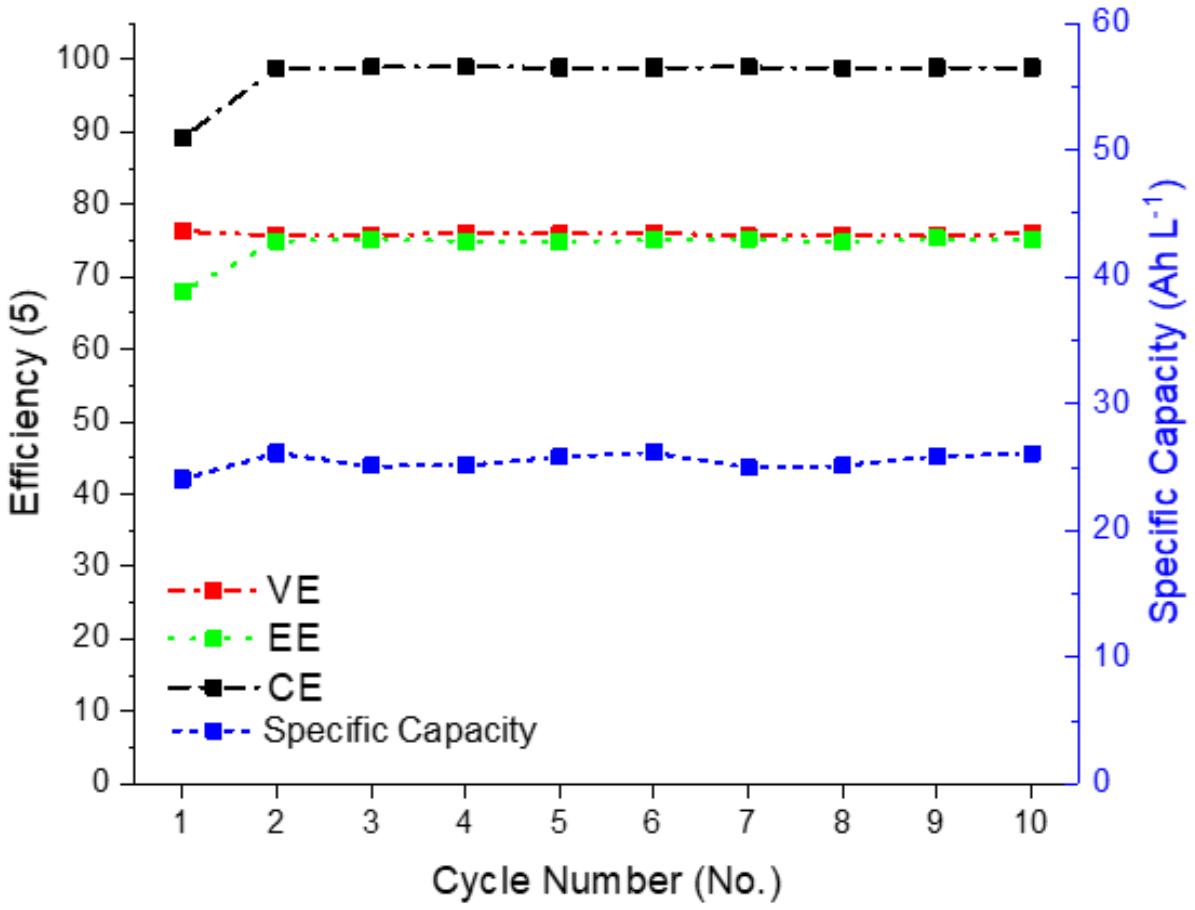

Figure 4-18: performance of in-house modified flow cell with 150 cm^2 active area, charged and discharged at 85 mA/cm^2

To be able to understand the effect of flow and flow pattern on performance of the cell, the pressure drop in the flow field across the active area was calculated, and compared to the pressure drop according to the flow parameters in the small cell. The pressure drop in the flow channels was calculated using eq. 4-10, considering pressure drop due to the friction and pressure drop caused by

a sudden change in direction of fluid flow. In this equation, f_c is the friction resistance coefficient, D_{hc} refers to the hydraulic diameter of the flow, K_{form} is the minor resistance coefficient, ρ is the density of the electrolyte flowing through the channels, A_c is the area of the channel and Q_C is the flow rate of electrolyte in the channel [205].

$$\Delta P_{FFC} = (f_c \frac{L_c}{D_{hc}} + K_{form}) \frac{\rho}{2A_c^2} Q_c^2 \qquad \text{eq. 4-10}$$

f_c can be calculated using eq. 4-11, where SG is the specific geometry of the channels, which varies depending on the geometry and ratio of width to depth of the channel [206].

$$f_c = \frac{SG \times A_c \times \mu}{\rho \times D_{hc} \times Q_c} \qquad \text{eq. 4-11}$$

According to these calculations, the velocity of electrolyte, at 250 mL/min, in a large flow cell with five serpentine channels, is threefold lower than the small cell with a single flow channel and flow rate of 50 mL/min (0.33 m/s for large cell and 1.04 m/s for small cell). The lower velocity of the electrolyte in the larger cell also produces a lower pressure difference at the inlet and outlet of the cell.

The pressure drop in serpentine flow channels has a direct impact on the flow distribution characteristics into the electrodes. Baek et al. demonstrated this effect by modelling the effect of pressure drop on the flow distribution in electrodes. According to this study, the reduction of pressure difference between inlet and outlet leads to a reduction of under-rib convection [207]. Therefore, as the under-rib convection reduces, the flow of the electrolyte into the porous electrode will decrease, which will increase the mass-transport polarisation of the cell.

In order to achieve an energy efficiency similar to the small cell, electrolyte flow into the felt must be enhanced. Assuming the flow distribution characteristics in the electrode is only dependent on the characterises of the electrolyte flow in the flow channels, the flow velocity of the electrolyte in the channels must increase. By increasing the velocity, pressure drop will also increase across the cell and result in an increase in electrolyte flow through the porous electrode. According to the generated data from the model (Figure 4-19), to achieve a similar pressure drop in the large cell, the flow rate must increase to 750 mL/min, where pressure drop will be 76.8 KPa.

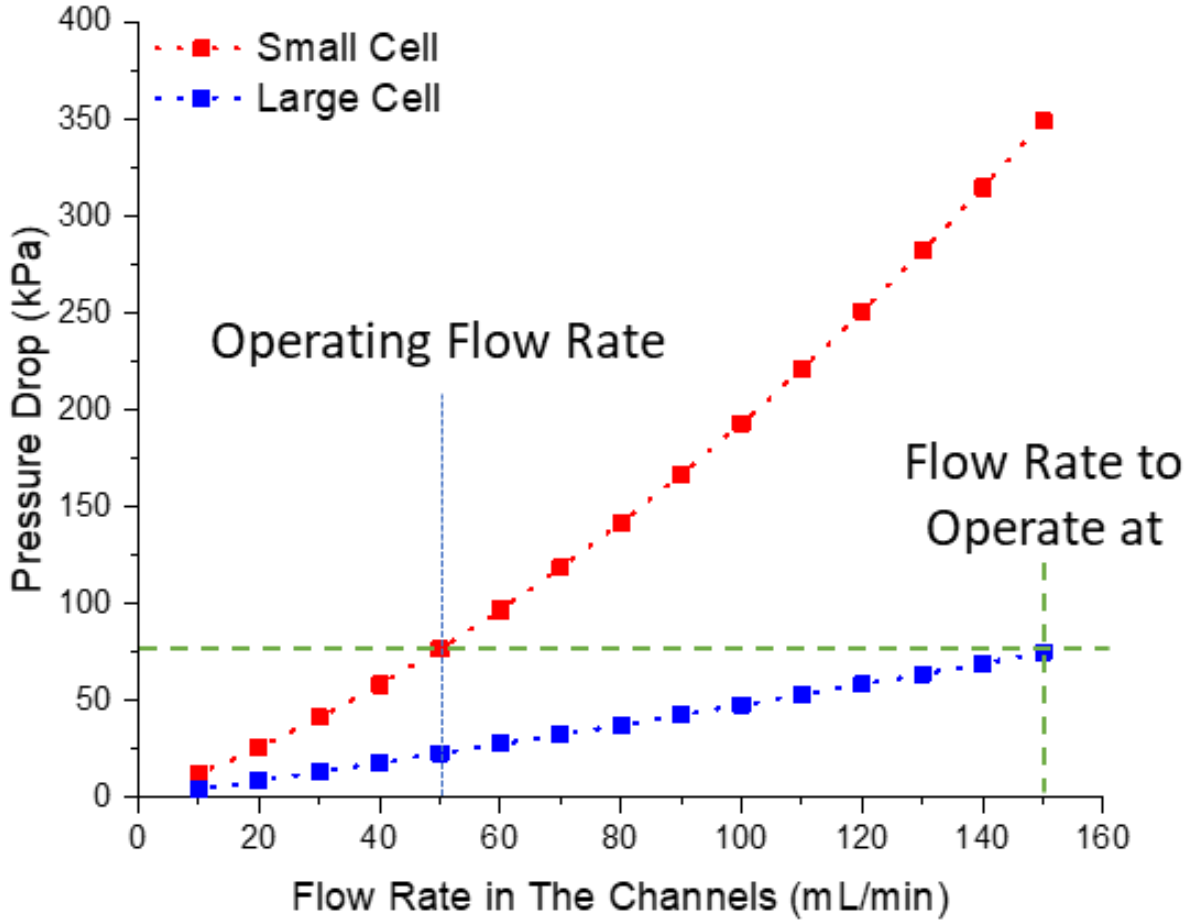

Figure 4-19: Calculated pressure drop based on different flow rates of the electrolyte in the small and large cell

4.1.10 Cost Analysis of RHMnFC and Its Comparison with Existing Energy Storage System

One strategy to reduce the cost of RFBs, as an energy storage device, is to lower the cost of the electrolyte or increase its energy density. Key characteristics of the active species in different RFB systems are the main determining factors of the electrolyte cost. These characteristics consist of active species solubility, number of electrons that can be transferred during oxidation and reduction reaction, its molar mass, cell potential and material cost. The last two characteristics have the most significant impact on the cost of the RFB. Hence, identifying active species which operate at high potential can be an effective approach to lower the cost of RFB systems. Beside electrochemical characterises of active species, another approach could rely on identifying cheap materials that could replace the existing RFB chemistries.

Abundant organic active molecules such as hydrogen, oxygen and carbon, due to large material reserves, exhibits very low cost, where their cost is not determined by their material reserves or production rates [68]. Main technical consideration when choosing these materials are the chemical stability, safety and their reaction kinetics.

The innovation of RHMnFC has shown interesting electrochemical characteristic in comparison to conventional RFBs. However, it is also important to investigate its economic advantages compared to incumbent RFB technologies. In this section, cost analysis on the newly invented system, RHMnFC, will be carried out. This analysis will include tabulated cost of all the components and balance-of-plant. Using previously reported methods, [208] the cost of four different systems such as hydrogen bromine RFB (H/Br), all-liquid VRFB (V-V), polysulfide air RFB (S/Air), will be calculated.

Cost comparison of different electrochemical devices or energy storage devices is only sensible for a clearly defined and similar application. As mentioned in Section 2.4, RFBs, due to their characteristics are used for energy storage applications, where energy density provided by these systems is the main determining factor in relation to the value added by these technologies to the specific area.

The key factor, in order to produce a comparable cost analysis on any technology, is to ensure that individual cost figures are based on comparable assumptions and are calculated at the same level of detail. Thus, in this section, different factors consisting of manufacturing costs, lifetime of the technology, upfront costs, operation costs and financing costs will be taken into consideration. These are introduced below:

Manufacturing and operation cost: RFBs, similar to any infrastructure resources, requires period servicing. These can be minor or major servicing depending on the lifetime of components and the technology. Significant additional cost can be added by the frequency of these repairs, where this will vary for different RFBs. For instance, in a RHMnFC, to store the produced hydrogen during charge half cycle; it will require and introduce different manufacturing and maintenance efforts, not needed for other flow battery technologies.

Upfront costs: In order to bring a project to a commercially operable status, there are fixed initial costs. This includes cost of components, electrolyte, and facilities needed to operate the batteries, as well as the cost of acquiring and upgrading these assets. Upfront cost or capital expenditure (CAPEX) is one of the main challenges in commercialisation of RFBs.

Lifetime: Cost of technologies, depending on their purpose, should be put in relation to their functionality over the lifetime. For RFBs, as energy storage device, lifetime refers to its projected cycle lifetime, which is the number of complete cycles expected from these systems. Usually lifetime of a battery is predicted to be until its nominal capacity decays below 80% of the rated capacity (due to degradation or irreversible loses).

There are other factors impacting the lifetime of these technologies, such as depth of discharge, which directly affects the number of cycles and their roundtrip efficiencies. Another factor that determines

the lifetime of RFBs, is the number of cycles required from the energy storage system per year. This by itself is determined from different factors, such as size of storage, energy required from the system; hence, for different systems with different energy densities, this can vary.

Residual Value: All the ESS systems consist of components in their balance-of-plant and components that will still hold a certain value at the end of main system's lifetime.

In order to reflect on the explained factors and their influence on the cost, a simple metric must be defined. The resulting cost metric assumes a constant price per kWh of the system, over its applicable lifetime and this constant as a cost metric is known as Levelized Cost of Storage (LCOS). This term is designed to enable a fair comparison of the energy storage cost against revenue cost of different systems across a range of applications [209].

To calculate the LCOS, shown in eq. 4-12, it can be formulated along all the individual components impacting upfront cost, manufacturing and operational cost, residual cost of components at the end of lifetime and charging electricity tariff. To be able to obtain comparative results, assumptions will be required. These assumptions will be constant for all the systems, but their main features that divides these systems from each other will be the main determining factor to compare these technologies.

$$LCOS = \sum_{n=1}^{N} (C_{CAPEX} + C_{Manufacturing} + C_{Opration} - C_{Residual} + C_{electricity}) / \sum_{n=1}^{N} Opration\ Time \quad \text{eq. 4-12}$$

Taking eq. 4-12 into consideration, this calculation can be expanded to different terms, with each term shown below:

$$N_{years} = \frac{Lifetime}{365 \times hours\ per\ cycle\ \times cycle\ per\ day} \quad \text{eq. 4-13}$$

$$CC = \frac{Capital\ Investment}{\eta \times rated\ capacity} \quad \text{eq. 4-14}$$

$$Capital\ Recovery\ Factor\ (CRF) = \frac{i(1+i)^N}{(1+i)^N - 1} \quad \text{eq. 4-15}$$

According to eq. 4-13, eq. 4-14 and eq. 4-15, which takes the number of years in operation (N), capital cost (CC) normalised to the characteristics of the cell, such as system energy efficiency (η_e) and rated capacity of the cell into the account. And finally, CRF calculates the ratio of annuity for given length of time, taking interest rate (i) into the account [208].

Using discussed factors and their formulas, the LCOS can then be calculated using eq. 4-16:

$$LCOS = \frac{CC}{CRF \times number\ of\ cycles\ per\ year} + \frac{C_{electricity}}{\eta_e} \qquad \text{eq. 4-16}$$

In order to calculate the LCOS of the previously mentioned systems, several existing cost estimate studies in the literature were used. Also, this cost analysis was based around an entry level system with low production volumes. However, in order to obtain comparative results, there are assumptions that must be made for each system. These assumptions consist of:

- All the calculations are based on 1 MW systems, which is chosen based on the available literature [208], with minimum energy capacity of 500 kWh and maximum of 72000 kWh, to investigate the effect of energy capacity on the LCOS.
- All the systems are assumed to provide similar round trip energy efficiency of 80%
- When considering bipolar plates, the cost of the material is approximately 50% for the material and 50% for the fabrication, including the effect of hydrogen pressure, in H-Mn and H-Br systems, on bipolar plates [210].
- pumping energy for electrolyte is accounted as 2% loss in overall EE.
- Performance of the cells are based on the information in literature [13,16,208,211].
- Faradic efficiency is assumed to be 100%, where both electrolyte and hydrogen stoichiometry is calculated based on this assumption for all the systems.
- 13% discount rate is assumed for capital investment. Also, it is assumed that there will be no tax.
- Cost of electricity is assumed to be 0.04$/kWh
- Number of cycles per day is assumed to be one cycle per day (365 cycles per year), with systems operating for 20 years.

Table 4-2: Assumptions and sets of constant parameters used to calculate the LCOS of four different energy storage systems

Parameter	Value	Unit
Lifetime	20	year
Cycles per day	1	cycles/day
Number of cycles	365	cycles/year
Depth of discharge (DoD)	95	%
Degradation rate	1	%/year
OPEX	2	1/year
Electricity tariff	4×10^{-5}	$/Wh
Discount rate	13	%
Residual value	30	%

These assumptions and set parameters that was used to calculate the Installation cost and LCOS are summarised in Table 4-2. It is clear that, since constant parameters are assumed, the main factor in determining the difference in cost of these systems will depend on the characteristics of the chemistries used in each system. These influencing characteristics consist of the solubility of the redox active species in the electrolyte, operating current densities and discharge voltage of these cells and most importantly the number of electrons transferred in the reaction. It has to be noted that, all the numbers used in this section are based on literature values used generally in calculating the LCOS of electrochemical cells such as RFBs and PEMFCs [16,208,212].

As each system has its own intrinsic materials, based on these materials different components in the stack can change, it is necessary to clearly understand different components and difference in cost of these materials and components. Since this work is to try to achieve a fair comparison of RHMnFC with other existing technologies, the highest market price of Mn and Ti in 2020 will be taken into account, while for other systems, the lowest market price in 2020 will be used to obtain their LCOS.

Table 4-3 shows sets of parameters that are used to carry out the techno-economic analysis in these four systems. In this table, it can be seen that there are parameters which are assumed constant for all different systems. However, these parameters might vary for different systems because they are influenced by different aspects of the active species.

For instance, in an all-liquid VRFB, it is necessary to balance the electrolyte after a certain number of cycles, as crossover is one of the main known phenomena in this technology. The price of membrane depends on the ion that has to migrate through the membrane; where for an S-Air system, where OH^- is the permeable ion through the membrane, an Anion Exchange Membrane (AEM) is used. It can be seen that negative electrodes used in both H-Mn and H-Br is double the price of two other system.

The difference in price of the negative electrodes is due to the high price of Pt catalyst, which is used as the catalyst in these systems.

Table 4-3: Sets of parameters used to calculate LCOS of four different systems, taking into account chemical characterises of each systems [16,31,208,213].

Parameter	H-Mn	V-V	S-Air	H-Br	Unit
Power electronics	1000	1000	1000	1000	$/kW
Labour per power	150	150	150	150	$/kW
Membrane	350	350	35	350	$/m2
Bipolar plate	300	150	300	300	$/m2
Negative Electrode	140	70	75	140	$/m2
Positive electrode	70	70	70	70	$/m2
Current collectors	5	5	5	5	$/m2
Gaskets/tubing/rods	28	28	28	28	$/m2
MEA frame	50	50	50	50	$/m2
End plates	10	10	10	10	$/m2
Flow meters/sensors	72	72	72	72	$/m2
Labour	180	180	180	180	$/m2
Electrolyte	2.7	15	0.5	1.5	$/Kg
Electrolyte preparation	0.8	0.8	0.8	0.8	$/kg
Pumps	15	15	15	15	$/L/min
Electrolyte tank	0.5	0.5	0.5	0.5	$/L
Solvent Concentration	5	5	15	0	M
Active Species Concentration	1.5	1.5	15	6.6	M
Hydrogen/Air tank	1000	-	32	1000	$/Kg
Venturi ejector	500	-	-	500	$/Kg/h
Valves	500	-	-	500	$/Kg/h
Complex MEP	-	-	-	48.5	$/Kg
Cell Voltage	1.2	1	0.7	1	V
Current Density	0.1	0.2	0.05	0.2	A/cm^2

However, the main parameters that have an impact on overall cost of the different systems is the price and solubility of the redox active materials used in the electrolytes. One of the main advantages of S-Air, beside its low price per unit weight, is high the solubility of polysulfide in potassium hydroxide (KOH), which results in a higher achievable energy density in this system.

Hydrogen price takes into account the price of all the components, included compressor and drying-column which are required to store the produced hydrogen. However, the main cost participant in hydrogen economy is the cost of storage, where special safety is required to be able to operate the system using this gas. This value, taken from LCOS calculation for H-Br [208], can be lower for RHMnFC.

As discussed and analysed in Section 4.1.8, the produced hydrogen during charge does not contain any flammable gas, which directly reduces the cost of hydrogen storage and handling.

Following assumed constant "power output" for all the systems in Table 4-2, and the nominal operational current density and cell voltage defined for each system in Table 4-3, the cell size required for each system has been calculated. The size of the cell for each system was accordingly used to calculate the overall cost of manufacturing and amount of catholyte and analyte required to produce the required energy for different hours of storage.

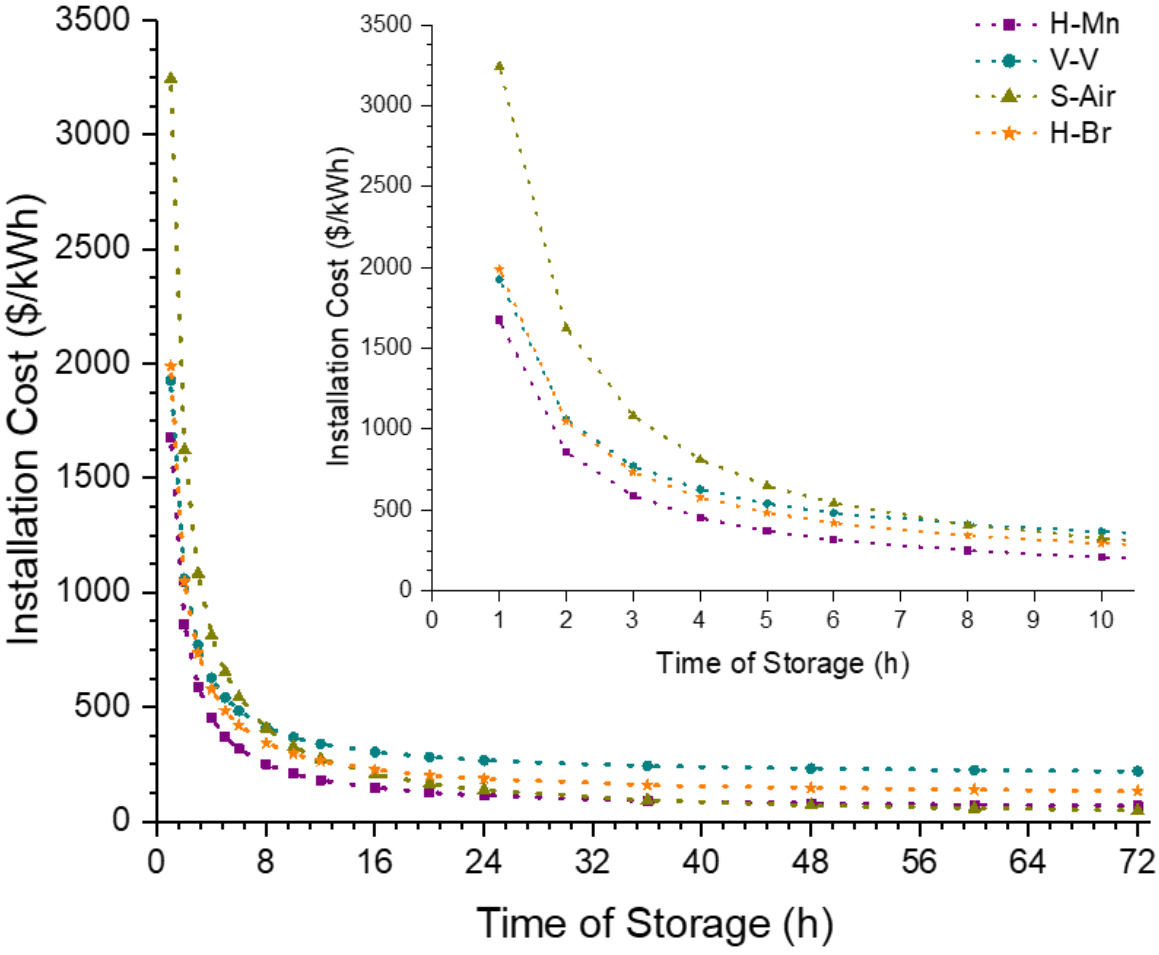

Figure 4-20: Installation cost of four different systems based on hours of storage

Figure 4-20 presents the calculated installation cost for previously discussed energy storage systems. Cost estimation, according to the parameters defined previously, takes into the consideration best operation conditions and parameters for all-liquid vanadium, S-Air and H-Br systems, and compares this to the unoptimized performance of the H-Mn, flow cell studied in this project. These evaluations show that the studied system (RHMnFC) has approximately 15% lower installation cost, for 1hr of storage, when compared to V-V and H-Br systems. However, as storage capacity increases from 1 hr

to 8 hours, there is an approximate 40% and 28% reduction in cost, compared to V-V and H-Br systems respectively, is forecasted.

Polysulphide-air hybrid-RFB, an upcoming system, investigated by Xia et al. has shown a great potential for long term energy storage applications [214]. This system, due to the solubility and price of its active species is more advantageous compared to any other systems discussed in this section. However, its low performance results in an increase in installation cost, as this directly effects the size of the cell [215]. Low power output of this system is due to the slow kinetics oxygen oxidation and reduction reaction, which directly affects the current density of this system. Additionally, previous works on this system has indicated that AEMs also transport the negatively charged polysulphide species to the positive side which results in the poisoning of the oxygen catalyst. To mitigate this effect, a dual-membrane cell design has been trialled. This consists of the addition of an extra membrane, inserted between the negative side and the existing AEM [50,214]. This can increase the cost of this system significantly, as it increases the cost of membrane material; however, this can increase the cell performance, which can reduce the overall cost of the energy storage.

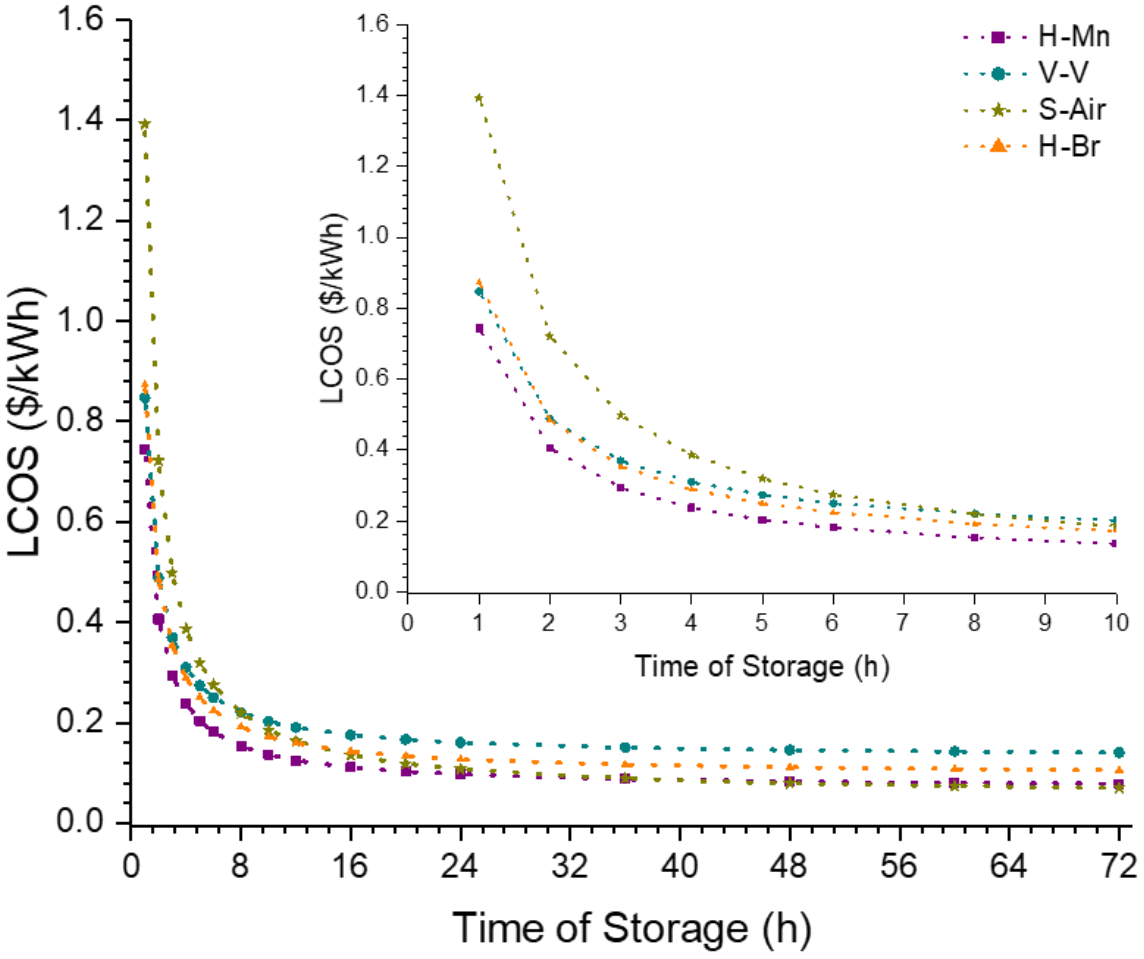

Figure 4-21: LCOS of four different systems based on hours of storage

The LCOS of these systems takes into consideration the lifetime of the systems, and its estimation is shown in Figure 4-21. Since constant parameters are used for all four systems, where it is assumed that the lifetime of each system is 20 years, with each system running one cycle per day throughout the whole year; hence, similar trend to installation cost (Figure 4-20) is seen for LCOS evaluations.

Therefore, it can be argued that RHMnFC is more beneficial for energy storage applications compared to all other commercially available RFB systems. These advantages are due to its high power output, which lowers the cost of stack and stack components. In addition to its better performance, this system benefits from low cost materials in contrast to VRFB.

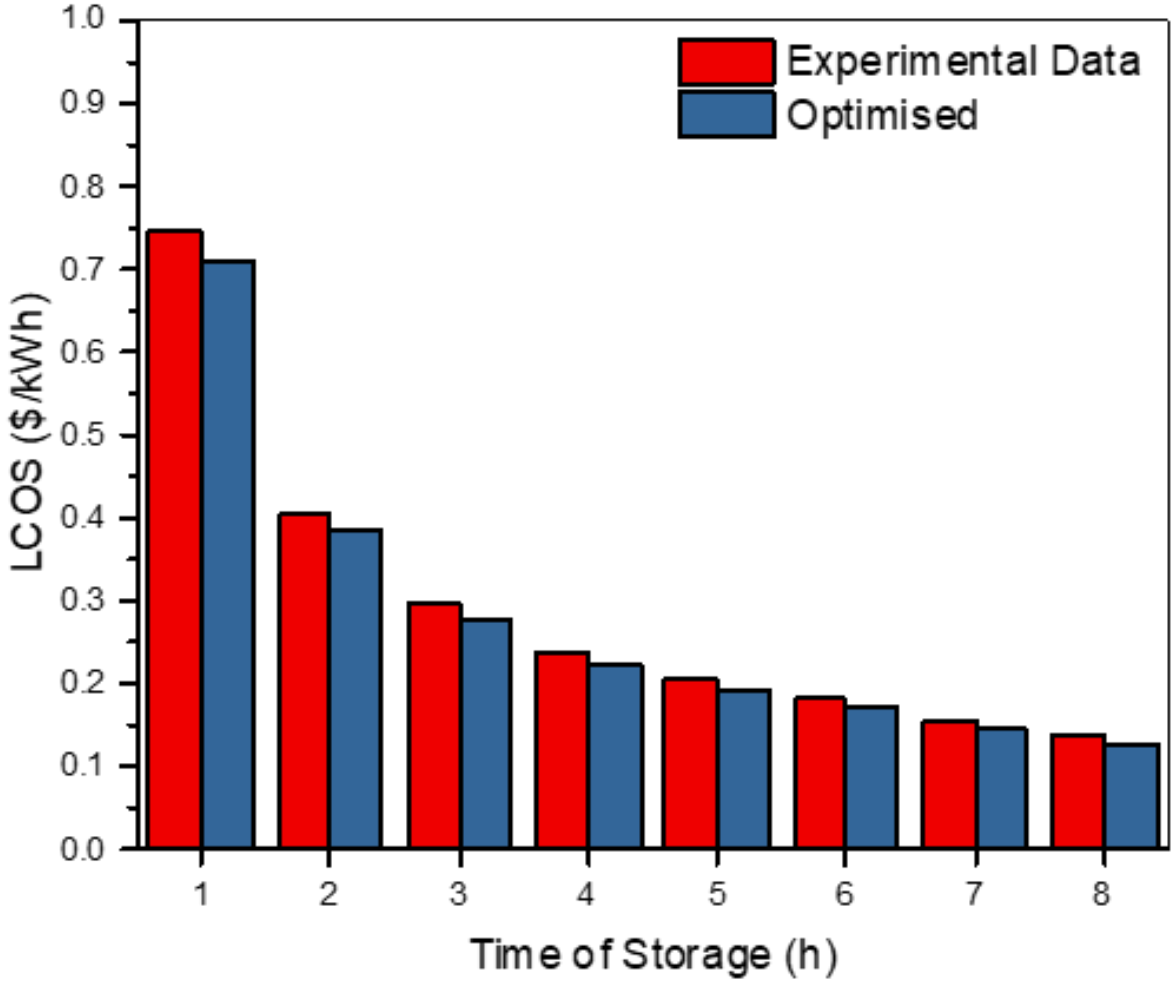

Figure 4-22: LCOS of H-Mn system based on experimental data compared to LCOS of the system with assumed optimum performance

It was mentioned that the cost of the Mn-H system was estimated using the data obtained from experiments, thus it is possible to achieve a higher performance by optimising the cell components. Based on the improvements made on the performance of V-V and H-Br systems, from their initial prototypes until reaching to a commercial state, similar trends can be applied to the RHMnFC system. Hence, it can be assumed that it is possible to operate the system at current densities close to 0.3

A/cm2 (0.1 A/cm2 was assumed previously), with improved round trip efficiency of 85% (80% was assumed previously), as well as nominal discharge voltage of 1.25 V (1.1 V was assumed previously). Figure 4-22 demonstrates the decrease in the cost of the system with optimised performance compared to the LCOS of the system with the performance metrics obtained from experiments. It can be seen that, by optimising the cell performance, LCOS can further reduce by approximately 5%.

4.1.11 Summary

In this chapter, following previous investigation on this system, different configurations of cell components were tested, and materials exhibiting reproducible and high performance were chosen. It was demonstrated that the thickness and surface area of the liquid electrode has an important role on the performance of the cell. Also, two Nafion membranes with different thicknesses were tested, and based on the capacity loss due to crossover, the best performing membrane was chosen.

The performance of the RHMnFC at different current densities was reported, and it was established that using this chemistry, it is possible to achieve a high performance at high current densities. This performance can be further improved by optimising the cell and its electrodes. Additionally, a conditioning protocol was established for this system, where hypothesis around the phenomena causing this was discussed.

As a result of the success of these tests, a commercial cell with 150 cm^2 active area was tested, where this cell was modified to duplicate the mechanical properties used in cell with 5 cm^2 active area. Finally, a cost model was produced, which using this mode LCOS and installation cost of four different systems were calculated and discussed. According to these evaluations, the proposed system has significant potential for energy storage applications.

Based on initial investigation of this novel RFB technology, further gaps were identified. Consequently, to be able to optimise the performance of this system, it is necessary to obtain a better understanding of the different phenomena determining the performance of the system. The most important gaps identified in this work, relate to the chemistry of the Mn electrolyte in the presence of Ti additives. In addition to the necessity of understanding the electrochemical characteristics of the system, the importance of engineering aspects in feasibility of scale up requires further attention. These identified gaps, from initial investigation of the RHMnFC system in this work, will be discussed in the final chapter, where detailed description of the techniques required will be suggested.

Chapter 5 Regeneration of Manganese-Titanium Electrolyte

In this chapter, for the first time, a method to regenerate the electrolyte electrochemically will be introduced and investigated. This work will study the conditions in which the capacity of the electrolyte is affected by the disproportionation of the Mn^{3+} and precipitation of MnO_2, which cause a rise in ohmic resistance of the liquid half-cell, loss of capacity and consequential inefficiencies in system performance.

The methodology and experimental procedures used to carry out the experiments will be introduced, where parameters used to study the stability of the electrolyte in the system will be described. Results obtained from these sets of experiments will be analysed and eventually, based on these findings, a standard procedure to regenerate the electrolyte will be proposed.

5.1 Results and Discussion

In this section, the results obtained from the set of experiments used to investigate the stability of the electrolyte at different operational conditions will be presented. This study will follow on from the findings in the previous chapter (Section 4.1) an attempt to investigate the limitations of the electrolyte at different operating conditions. Since this project is based on a novel flow battery chemistry, there is limited or no information of the underlying mechanisms that influence the stability of the electrolyte.

The second part of this chapter will present a new method, which explores the possibility of dissolving the MnO_2 precipitate back to the electrolyte electrochemically. The success of this method will make the RHMnFC technology a sustainable technology, as the regeneration of the electrolyte can be done internally at no cost.

5.1.1 Stability of The Manganese Electrolyte

As reviewed and discussed in Section 2.4, Mn like transition metals with intermediate oxidation states can undergo disproportionation reactions. At a high state of charge, and when Mn is the only active species present in the electrolyte, disproportionation of Mn^{3+} will result in the instability of the electrolyte. However, this depends on different mechanisms such as state of charge, waiting period between charge and discharge half-cycles, and the temperature at which the cell is operating. In order to investigate the stability of Mn electrolyte, 40 mL of 1 M Mn in 5 M H_2SO_4 was charged and discharged at constant current (without any Ti stabilisation), based on the optimum operating current density found in Section 4.1.6.

According to three charge and discharge cycles of the Mn electrolyte [g], shown in Figure 5-1, it can be seen that during the first cycle it was possible to fully charge the electrolyte, but during discharge there was a 30% loss in specific capacity. This irreversible loss in the capacity eventually resulted in full degradation of the electrolyte and subsequently charging or discharging the cell was not possible.

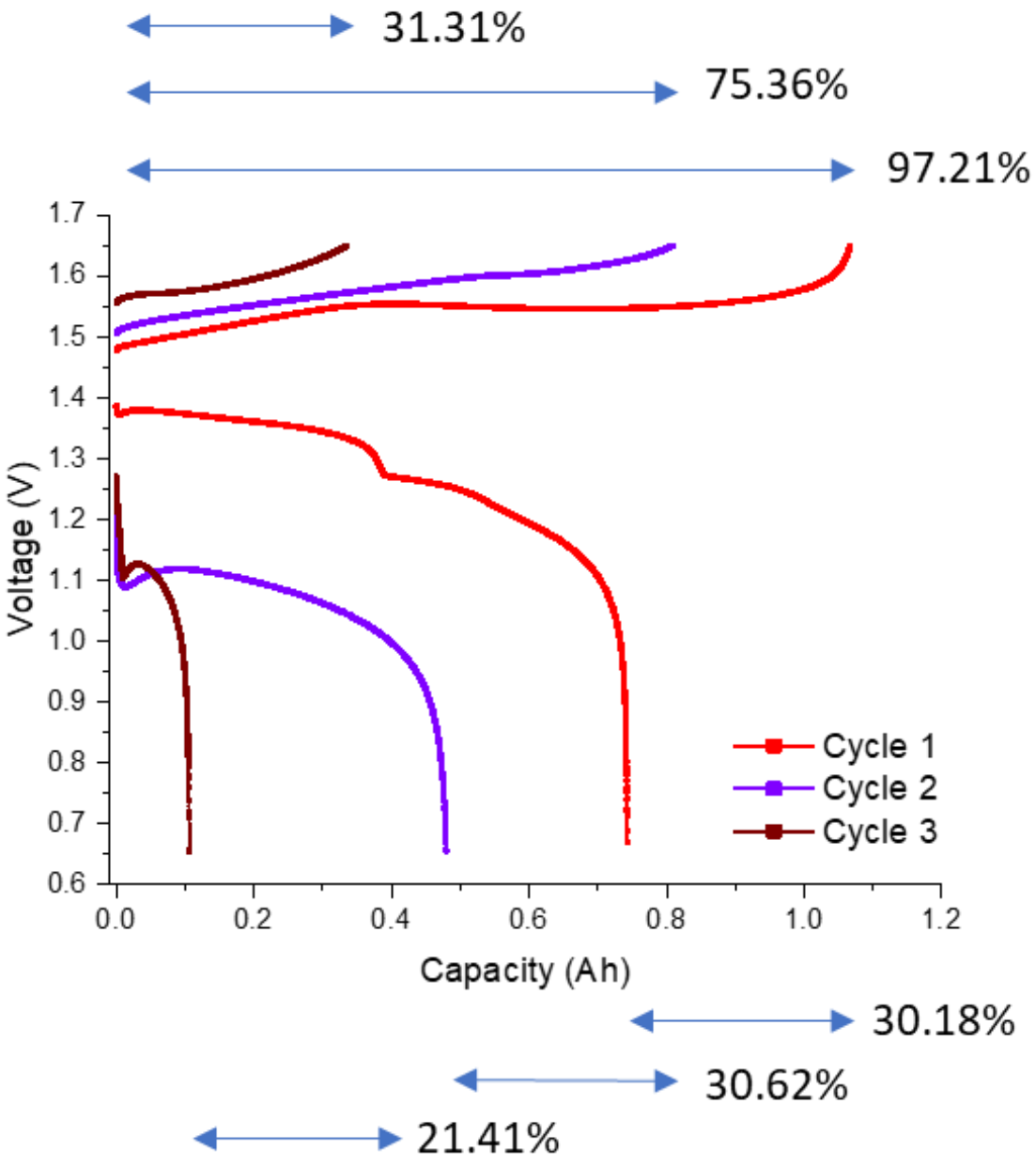

Figure 5-1: Charge and discharge cycles at constant current of 100 mA/cm^2 of electrolyte of 1M Mn in 5M H_2SO_4, without any Ti additives to suppress Mn^{3+} disproportionation

[g] Mn electrolyte referred in this section, does not contain Ti additives to stabilise the Mn^{3+} and suppress the disproportionation reaction. However, on the other sections of the thesis, the electrolyte contains the Ti stabiliser, where the method is reported in Section 3.1.3.

Comparing the three different cycles, it can be seen that during the first discharge, a capacity utilisation of 67% was reached (previously in 0), achievable capacity at current density of 100 mA/cm^2 was reported to be 97% of the theoretical capacity). Thus, it can be assumed that a 30% loss in the achievable capacity was caused by disproportionation of Mn^{3+}, and consequently producing 15% Mn^{2+} and 15% MnO_2 precipitates. Hence, while charging the electrolyte in the second cycle, it must have been possible to reach 82% of the theoretical capacity. According to the obtained results, it had been only possible to reach 75.36% of the theoretical capacity.

Repeating the charge and discharge half-cycle has shown further loss in capacity. According to the calculations and based on the discharge capacity of the second cycle, it should have been possible to reach 52%-65% of the theoretical capacity. However, as can be seen in the third charge cycle only 31.31% of capacity was achievable.

Therefore, it is possible that, during disproportionation of the charged electrolyte, precipitated MnO_2 deposits on the fibres in the electrode. This causes a reduction in the active surface area of the electrode and thus increases the ohmic overpotential, which subsequently results in reaching the cut-off voltage at shorter time. It is also possible that the graphite felt has acted as a filter and accumulates the precipitated particles in the porous electrode, thus the MnO_2 precipitates block the pore-network, which causes an increase in mass transport overpotential. In combination, these two mechanisms contribute to the degradation of the electrolyte and the cell, which subsequently makes it impossible to carry out further charge or discharge half-cycles.

5.1.2 Dependency of The Electrolyte Stability on Rest Period at High State of Charge

In conventional flow batteries, capacity fade can typically occur through two mechanisms, namely crossover of the active species through the membrane or precipitation of the reactant in the electrolyte which, depending on the source of the capacity loss, can be reversable. In flow batteries utilising a single common active species as reactants on both half-cells and hybrid gas-liquid flow batteries, capacity losses due to crossover are reversible by rebalancing the electrolyte. The second mentioned mechanism, which occurs due to precipitation of the active species, is known to be the main cause of capacity decay in RHMnFCs.

Previously, in 0, it was established that the crossover of the electrolyte is negligible in RHMnFCs and using this chemistry, reproducible results were achieved with an extended number of cycles. However, it is important to further study the electrolyte stability and capacity loss mechanisms at different conditions. Since manganese precipitation occurs due to disproportionation of Mn^{3+}, it is important to investigate the stability of the electrolyte at 100% SOC.

The stability of the electrolyte at different rest periods were tested. In these experiments, a standard electrolyte (preparation method reported in Section 3.1.3) was used, which was initially fully charged. Between the two half-cycles the electrolyte was left stirring and circulating in the cell for a period of time before applying a discharge current density of 100 mA/cm^2. According to the galvanostatic charge and discharge cycles, the performance of the cell was evaluated based on its energy efficiency and discharge capacity utilisation.

According to the evaluated performance indicating factors (i.e. EE, VE, CE), Figure 5-2 shows the decay in voltage efficiency as the resting period between charge and discharge half-cycle is increased. It can be observed that by increasing the waiting period from 30 minutes to 10 hours, the VE has dropped from 77.94% to 68.54%. Additionally, the CE evaluated for the cycles with a similar resting time up to 10 hours suggests that there is no irreversible capacity fade caused by the Mn^{3+} disproportionation reaction.

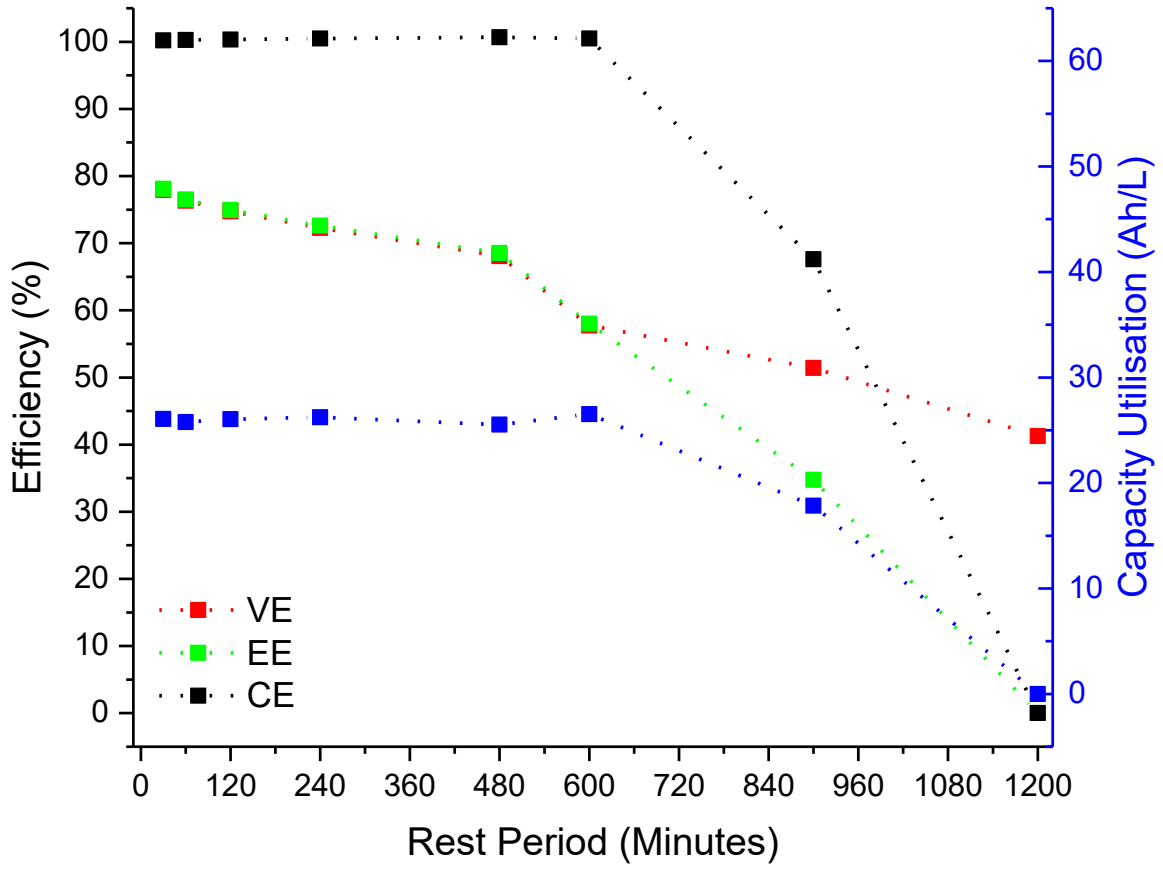

Figure 5-2: Effect of rest period between charge and discharge half cycles at different rest periods up to 20 hours, where the cell was fully charged to 100 SoC at each cycle at room temperature

As the resting period between charge and discharge half-cycle is increased beyond 10 hours (600 minutes), a decrease in discharge capacity is observed. Specific discharge capacity for the cycle with 15 hours wait time between two half cycles, drops down to 64% of the theoretical capacity. A drop in

the discharge capacity and hence decrease in coulombic efficiency for the cycle with 15 hours resting period is possibly caused by the irreversible precipitation of the MnO_2. Eventually, it was observed that by increasing the wait time to 20 hours, it became impossible to further discharge the cell.

According to these measurements, the effect of the resting period on the stability of the fully charged electrolyte and cell can be separated into two halves: less than 10 hours and beyond 10 hours resting period. In each category different phenomena lead to the certain inefficiencies in the performance of the cell, which will be discussed below:

- **0.5 hours up to 10 hours**: The drop in the energy efficiency of the cell when increasing the resting period up to 10 hours might be caused by two mechanisms. Firstly, the drop in VE is possibly caused by the increase in the activation overpotential of the cell. This is caused by the deposition of the precipitated manganese on the fibres, which could increase the ohmic resistance contributed by the electrode. The second mechanism that may cause the drop in VE is the increase of mass transport overpotential in the electrode. The increase in wait time results in more Mn^{3+} disproportion and precipitation of the MnO_2, which might block the pore networks in the electrode and limit the electrolyte flow inside the porous media. It is important to note that, as discussed in Section 4.1.7, Mn disproportionation to produce MnO_2 precipitates occur through an intermediate reaction. If the precipitates exist in this intermediate state, it is possible for a reduction reaction to take place to produce Mn^{2+} in the electrolyte.

- **Beyond 10 hours**: The main inefficiency in the performance of the cell with wait time over 10 hours is the drop in coulombic efficiency. The decrease in the achievable discharge capacity is caused by the irreversible precipitation of the MnO_2 in the electrolyte. the first hypothesis that could explain the irreversible capacity fade is that, as the rest time increases over 10 hours, precipitation of MnO_2 is initiated. Therefore, unlike the first part (rest time below 10 hours), where Mn precipitates exist as the intermediate compound (MnOOH), at the cycle with 15 hours wait time, 30% of the Mn^{3+} has reached its stable oxidation state (Mn^{4+}) [78].

  A similar mechanism can be hypothesised to explain the degradation of the cell during the cycle with 20 hours rest time. However, two different mechanism can contribute to the degradation of the cell or the electrolyte. The first mechanism is believed to be due to the complete disproportionation of the Mn^{3+} active species, which results in the generation of Mn^{2+} and Mn^{4+}. And as stated previously, since MnO_2 (Mn^{4+}) exists as a precipitate, it is not possible to discharge the cell. However, this hypothesis is against the kinetic model explained

in Section 4.1.7, which shows that at room temperature only 0.1 M of Mn^{3+} goes through the disproportionation reaction and precipitates to MnO_2. In addition, work by Tsagerli et al. on the electrochemical behaviour of MnO_2 has shown that, MnO_2 can be discharged electrochemically at the presence of Mn^{2+} in the electrolyte [216]. Thus, based on the first hypothesis it must be possible to discharge the participated MnO_2, as an equal amount of Mn^{2+} would exist in the electrolyte. Therefore, there must exist another mechanism which makes the discharge of electrolyte impossible. Based on the observations, the second mechanism that is limiting the electrolyte from being discharged is hypothesised to be the blockage of the porous in the electrode by the MnO_2 precipitates.

5.1.3 Regeneration of Electrolyte

It was seen that the main mechanism causing inefficiency in the performance and decrease in the achievable discharge capacity in RHMnFC is the precipitation of manganese redox active species at high states of charge close to 100% SoC. Although, adding Ti additive to the manganese electrolyte suppresses the disproportionation reaction, its precipitation still occurs at a slower rate. Therefore, it has become crucial to be able to dissolve the precipitated MnO_2 back into the solution to recover the performance of the cell and mitigate the capacity loss.

To find a method where faded capacity, due to the irreversible precipitation of the MnO_2 could be recovered, Rubio Garcia et al. in the Electrochemistry group studied different mechanisms. During investigations to find a method to dissolve MnO_2 in the solution, a rotating disk electrode (RDE) setup was used, where a thin layer of MnO_2 was deposited on the disc. During the experiment, it was observed that the use of $Ti_2(SO_4)_3$ (Ti^{3+}) was able to dissolve the MnO_2 residue immediately.

Based on this finding, it is possible to remove any precipitate formed in the electrolyte and the cell with Ti^{3+}. One way to adopt this to the technology would involve adding Ti^{3+} to the cell, however, this would change the concentration of the redox active species in the electrolyte. Hence, a better technique to remove any MnO_2 from the electrolyte and dissolve it back into the electrolyte would involve producing Ti^{3+} through the electrochemical reduction of Ti^{4+}.

As shown in Section 0, Ti^{4+} is used in the manganese electrolyte to increase the stability of the electrolyte at high SOC by supressing the disproportionation reaction. Hence, it must be possible to reduce the existing Ti^{4+} to Ti^{3+} electrochemically within the cell. According to the standard reduction potential of this process, Ti^{4+} can be reduced to Ti^{3+} at 0.1 V. In addition, since the reduction of Mn^{4+} to Mn^{2+} occurs at standard redox potential of 1.22 V, dissolving MnO_2 in Ti^{3+} will be a spontaneous redox process. The equilibrium equation for this redox reaction is as below:

$$2\,Ti^{3+} + Mn^{4+} \rightarrow 2\,Ti^{4+} + Mn^{2+}$$ eq. 5-1

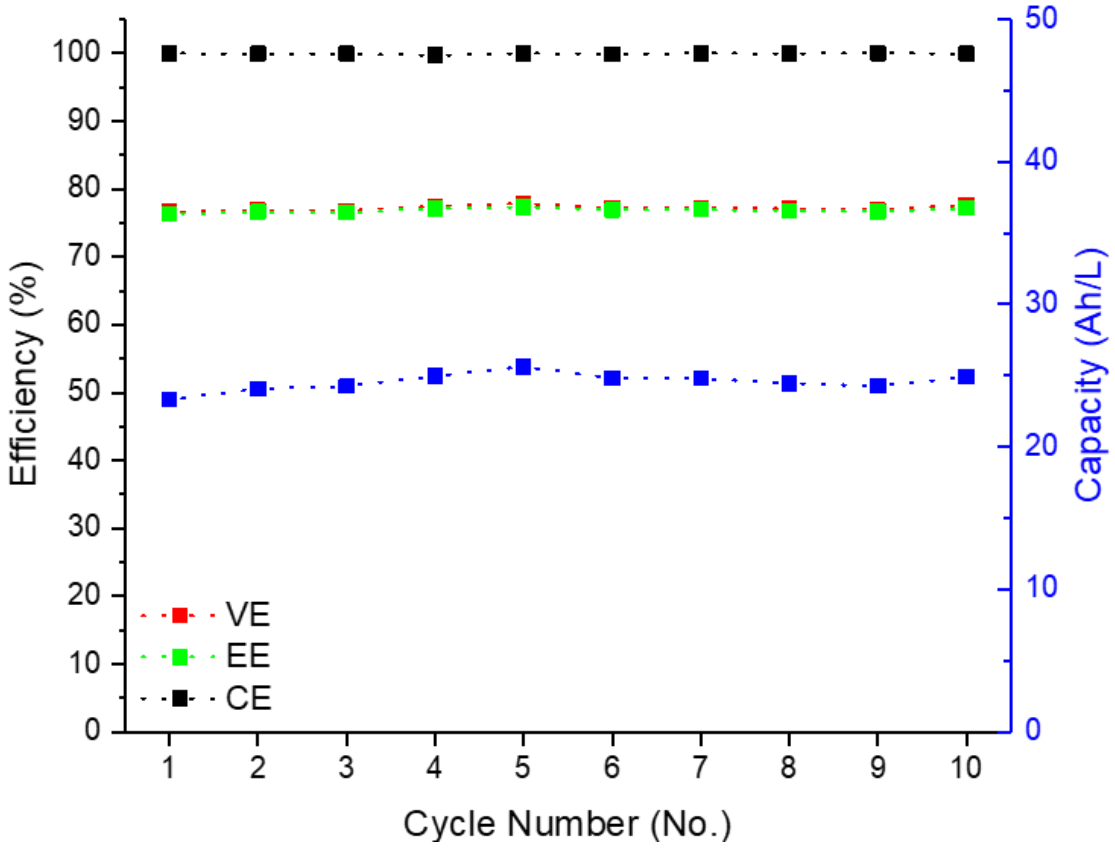

Figure 5-3: Step 1 - Galvanostatic charge and discharge cycles of the cell at 100 mA/cm²

As explained in Section 3.2.4, firstly the performance of the cell over 10 cycles was tested using a standard electrolyte (Figure 5-3). Similar to what was presented previously in Section 4.1.6, the average EE of 78% was obtained from the galvanostatic cycling of the cell at 100 mA/cm^2, and it was also possible to achieve 97.3% of the theoretical capacity.

Secondly, the cell was charged at a constant potential of 1.8 V to produce MnO_2. At the start of overcharging the electrolyte, as the concentration of the reactant (Mn^{3+}) is high, it is possible to charge at higher current. By moving forward, the charging current reduces as the concentration of Mn^{3+} reduces. According to the area under the graph, the charge capacity was calculated to be 1.59 Ah (73.87% of theoretical capacity for two electron transfer reaction).

To ensure that the electrolyte is fully degraded (precipitated), a discharge half cycle was attempted, and it was seen that by applying a discharge current, the potential of the cell immediately dropped below the 0.65 V cut-off voltage.

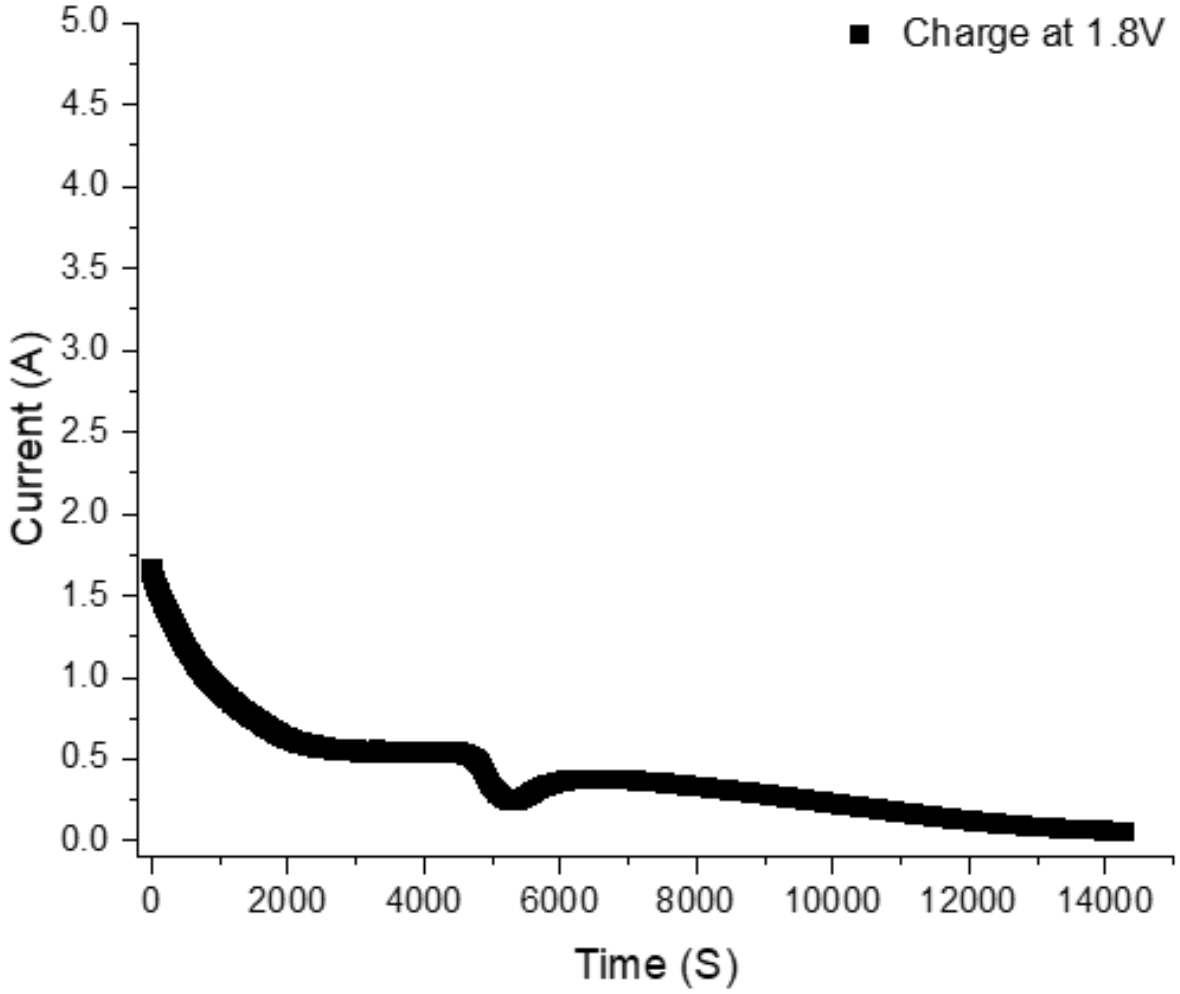

Figure 5-4: Step 2 - Charging the discharged electrolyte at constant potential of 1.8 V to produce MnO_2, in a cell with an active area of 5 cm^2

The fourth step consisted of experimentally validating the practicability of this redox reaction inside the electrochemical cell, which was discharged at constant potential of 0.1 V. According to this finding, it must be possible to discharge all the MnO_2 in the cell or the electrolyte back to the solution to form- Mn^{2+}. As can be seen in Figure 5-5, there is a massive oscillation in the measured current flux during this process. The mechanisms that are possibly causing the oscillation of the response current to the constant potential will be discussed later in this chapter. According to the area under the Time vs current plot, a capacity of 1.71 Ah (Equivalent to 78.40% of the theoretical capacity for two electron reaction) was observed, which is 0.12 Ah higher than the capacity observed for the second step (during overcharging the electrolyte). The excess capacity during discharge will be investigated later in this chapter.

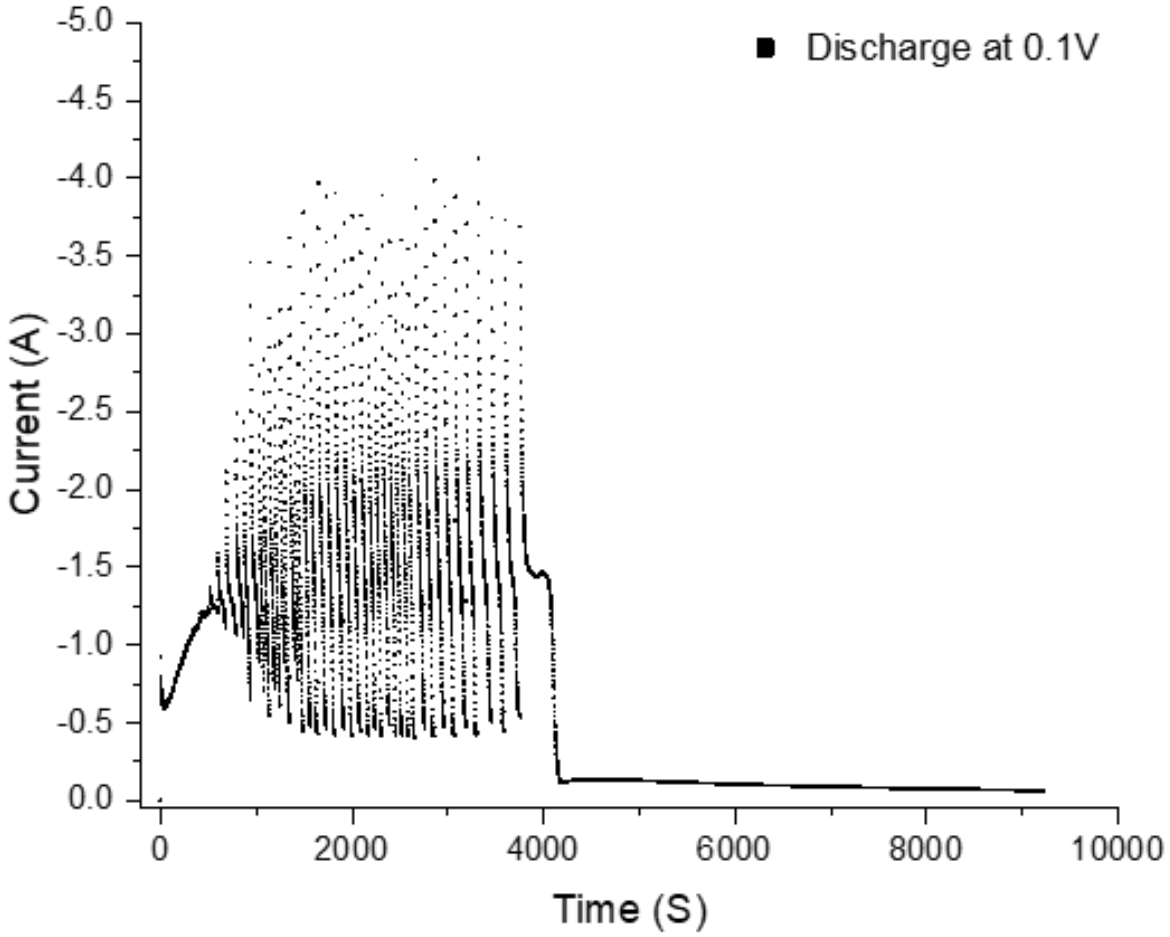

Figure 5-5: Step 4 - Regenerating the precipitated electrolyte by discharging the cell at constant voltage of 0.1 V to produce Ti^{3+}, in a cell with an active are of 5 cm^2

The final Step involved charging and discharging the cell at a constant current density of 100 mA/cm^2 for 10 cycles. Based on these cycles (Figure 5-6), the performance of the cell was evaluated to be similar to what was achieved for the cell at the initial step, before overcharging the electrolyte. These 10 cycles exhibit an average EE of 78.1% and an achievable capacity of 97.63% compared to theoretical capacity. This indicates that, this method dissolves the precipitated MnO_2 in the system and recovers the capacity loss due to disproportionation.

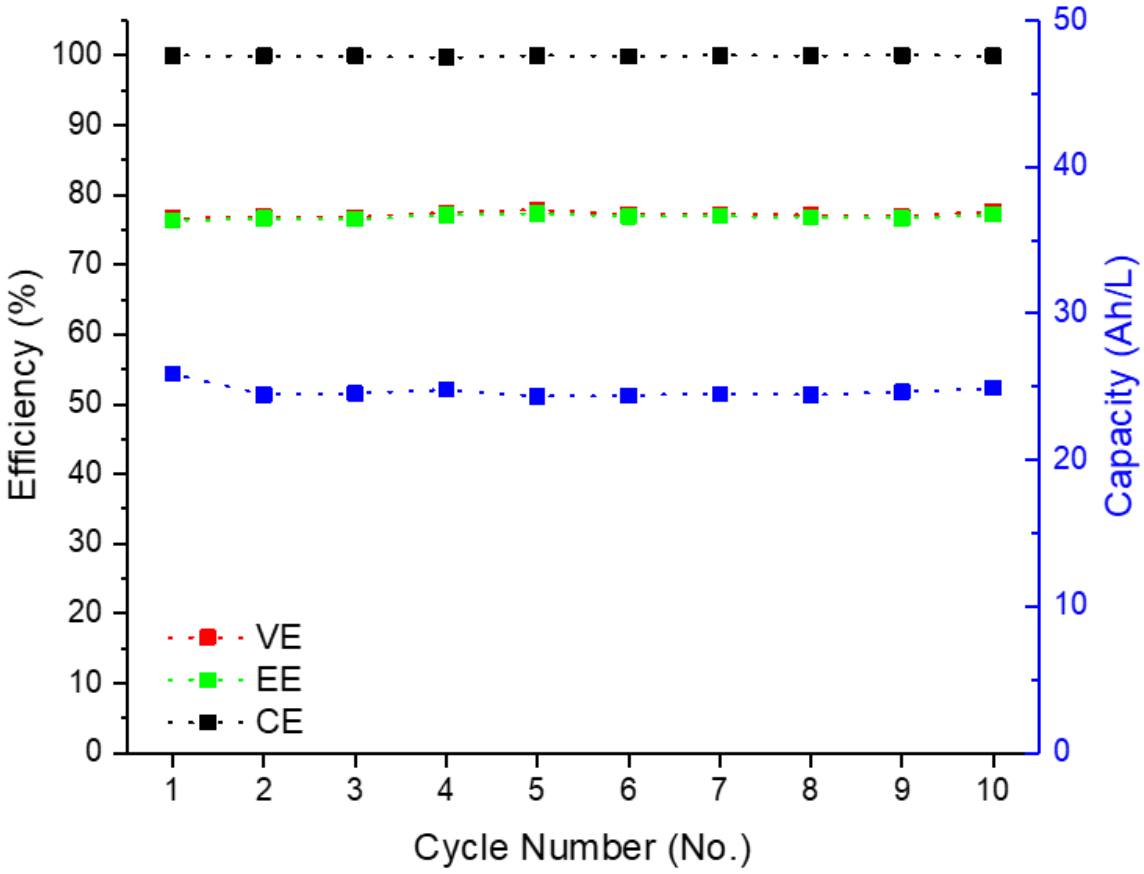

Figure 5-6: Step 5 (Final Step) - Consistent performance of the cell after regeneration of electrolyte

Based on these sets of experiments the reversibility of the MnO_2 precipitates was investigated. Although the regeneration of the electrolyte was proven to be achievable using this method, further studies are required to be able to understand the different phenomenon occurring during regeneration.

5.1.3.1 Oscillation of Current Response During Electrolyte Regeneration

In Section 5.1.3 while discharging the cell at constant potential of 0.1 V, which was used to remove the MnO_2 residues in the system and dissolve it back into the electrolyte, there was a significant oscillation of the current response. This oscillation could be related to the amount of reactant entering the cell and the residence time of the reactant in the cell. Since the cell is operating at a constant potential of 0.1 V, the rate of the reduction reaction increases. In addition, at the start of this step when the reactant concentration is higher, it is possible to reach a higher discharge current and reduce all the reactants to the products. Once all the reactant entering the cell is consumed, the current starts reducing. Hence, based on this hypothesis, the observed oscillation of the discharge current response is a function of the electrolyte residence time in the active volume.

In order to understand and investigate the credibility of this hypothesis, regeneration of precipitated electrolyte was repeated at different flow rates. By changing the flow rate of the electrolyte supply to

the cell, the residence time of active species in the cell would also change, and there should be a change in the discharge current response behaviour.

Figure 5-7 presents the current response of the system to constant potential discharging at different flow rates. According to the measured data, the oscillation of the current response shows higher amplitude at a flow rate of 25 mL/min compared to 50 mL/min (standard flow rate of electrolyte in this project). These results align with the hypothesis that the oscillation of the current drawn from the cell will be affected by the supply rate of reactants and their residence time in the cell.

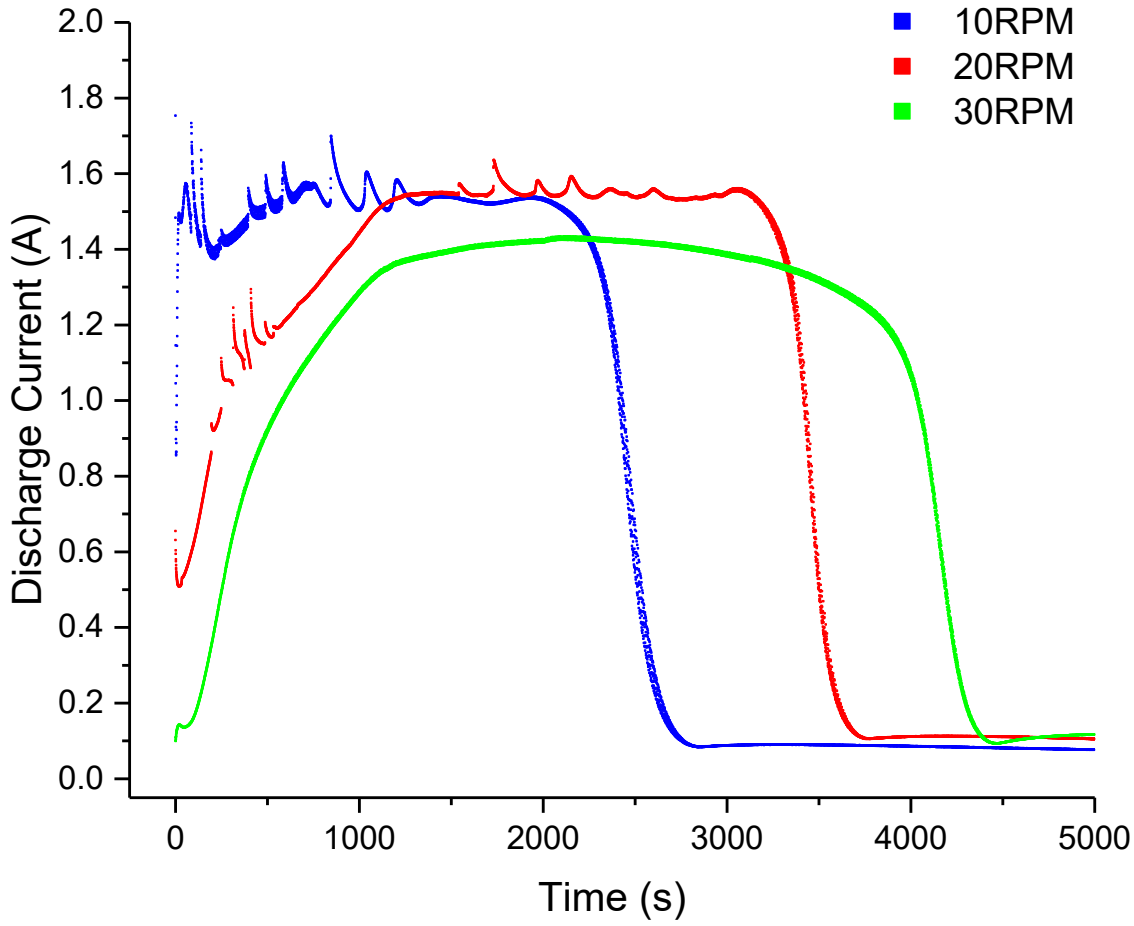

Figure 5-7: Current response of system discharged at constant potential of 0.1 V at different pump rates of 10 RPM (25 mL/min), 20 RPM (50 mL/min) and 30 RPM (75 mL/min), in a cell with an active area of 5 cm²

When the flow rate was increased to 75 mL/min, the oscillation of the discharge current response disappeared. This indicates that the time constant of the reaction in which MnO_2 dissolves in Ti^{3+} is higher than the reduction reaction rate of the active species. Hence, the limiting factor at this flow rate is the reaction between produced Ti^{3+} and the precipitated MnO_2, where at this specific residence time of the Ti^{3+} only limited amount of MnO_2 can participate in the reaction and reduce to Mn^{2+}. This hypothesis also explains the different behaviour observed at the start of the discharge current. According to the measured data, the starting current at different flow rates increases as the flow rate

decreases. By increasing the flow rate, the mass transport polarisation decreases, hence it would be expected to be able to achieve a higher discharge current as the flow rate increases. However, according to the measured current response, the opposite behaviour was observed, where the cell was discharged at a lower current. This indicates that, due to lower residence time of the produced Ti^{3+} in the cell, a lower amount of MnO_2 residue can be removed from the porous electrode. This indicates that the residence time of the Ti^{3+} inside the porous media, where MnO_2 deposits exist is a determining factor on the rate of regeneration.

5.1.3.2 Excess Capacity During Discharge at Constant Potential

In Section 5.1.3 it was reported that 0.12 Ah excess capacity was measured during discharge of the cell at 0.1 V constant potential. This excess capacity is believed to be due to the extra reduction of Ti^{3+} to Ti^{4+}. In order to understand this phenomenon, it is important to review the reactions occurring during the overcharging and the regeneration stage (potentiostatic discharging at 0.1 V).

During charging of the cell at a constant potential of 1.8 V, it was observed that a capacity of 1.59 Ah was achieved. Since a 40 mL electrolyte with a capacity of 2.16 Ah was used (full conversion of Mn^{2+} to Mn^{4+}), it is possible that either only 73.61 % of the Mn^{2+} was oxidised to Mn^{4+}, hence 26.41 % of the electrolyte was not charged, or oxidation of Mn^{2+} to Mn^{4+} goes through an intermediate reaction, where Mn^{2+} initially oxidises to Mn^{3+}. According to this hypothesis, all the active species in the electrolyte had initially oxidised into the intermediate oxidation state (Mn^{3+}), contributing 1.08 Ah to the capacity, and it was only possible to oxidise 47.2% of the Mn^{3+} into Mn^{4+} precipitates. Hence, after charging the cell at a constant potential, the final product in the cell would consist of 0.47 M Mn^{4+} and 0.53 M Mn^{3+}.

In order to reduce the Mn^{4+} in the electrolyte to Mn^{2+}, as discussed in Section 5.1.3, Ti^{4+} has to be reduced to Ti^{3+} (eq. 4-11). Based on the first hypothesis, where it was assumed 73.61% of the Mn^{2+} in the electrolyte oxides to Mn^{4+}, in order to dissolve the Mn^{4+}, all of the Ti^{4+} has to be reduced to Ti^{3+}, providing a capacity of 1.08 Ah. By producing 1M of Ti^{3+}, it can only react with 0.5 M of Mn^{4+} in the electrolyte and reduce it Mn^{2+}, leaving 0.23 M Mn^{4+} residues in the electrolyte. Hence in order to fully remove the remaining Mn^{4+} from the electrolyte and reduce it to Mn^{2+}, 0.46 M Ti^{4+} has to be reduced to Ti^{3+}, contributing a 0.51 Ah to the total capacity. Therefore, the extra 0.12 Ah capacity seen during constant potential discharge can be related to the excess reduction of 0.11M of Ti^{4+} to Ti^{3+}.

The second hypothesis assumes that, initially all the Mn^{2+} participates in the reaction, through a single electron oxidation reaction, to produce 1 M of Mn^{3+}, which contributes 1.08 Ah to the overall capacity. This is followed by further oxidation of 0.47 M of the Mn^{3+} to Mn^{4+}, contributing 0.51 Ah to the overall capacity. Hence, in order to regenerate the electrolyte, 0.94M of Ti^{3+} must be produced by reducing

the 1M TI^{4+} in the solution. However, similar to the first hypothesis, the excess capacity is a consequence of over-reducing Ti^{4+} to Ti^{3+}.

The redox potential of an aqueous solution determines the tendency of the solution to lose or gain an electron. Based on the redox potential of the Ti and Mn redox active species (eq. 5-2 and eq. 5-3), Ti with a lower redox potential will have a higher tendency to lose an electron (oxidise) during the charging of the cell, where electrons are extracted from the active species in the liquid half-cell and moved to the hydrogen half-cell [217]. Since the excess capacity is assumed to be caused by the extra reduction of Ti^{4+} into Ti^{3+}, hence, at initial charge half-cycle of the cell, Ti^{3+} must first oxidise to produce Ti^{4+}. Therefore, the excess Ti^{3+} produced during the discharge step (step 4) would be expected to affect OCP of the cell and the excess capacity must be retrievable during the first charge half-cycle.

$E_{OCP} = 0.1\ V$ vs SHE $\qquad Ti^{3+} + H_2O \leftrightarrow TiO^{2+} + e^- + 2H^+$ eq. 5-2

$E_{OCP} = 1.51\ V$ vs SHE $\qquad Mn^{2+} \leftrightarrow Mn^{3+} + e^-$ eq. 5-3

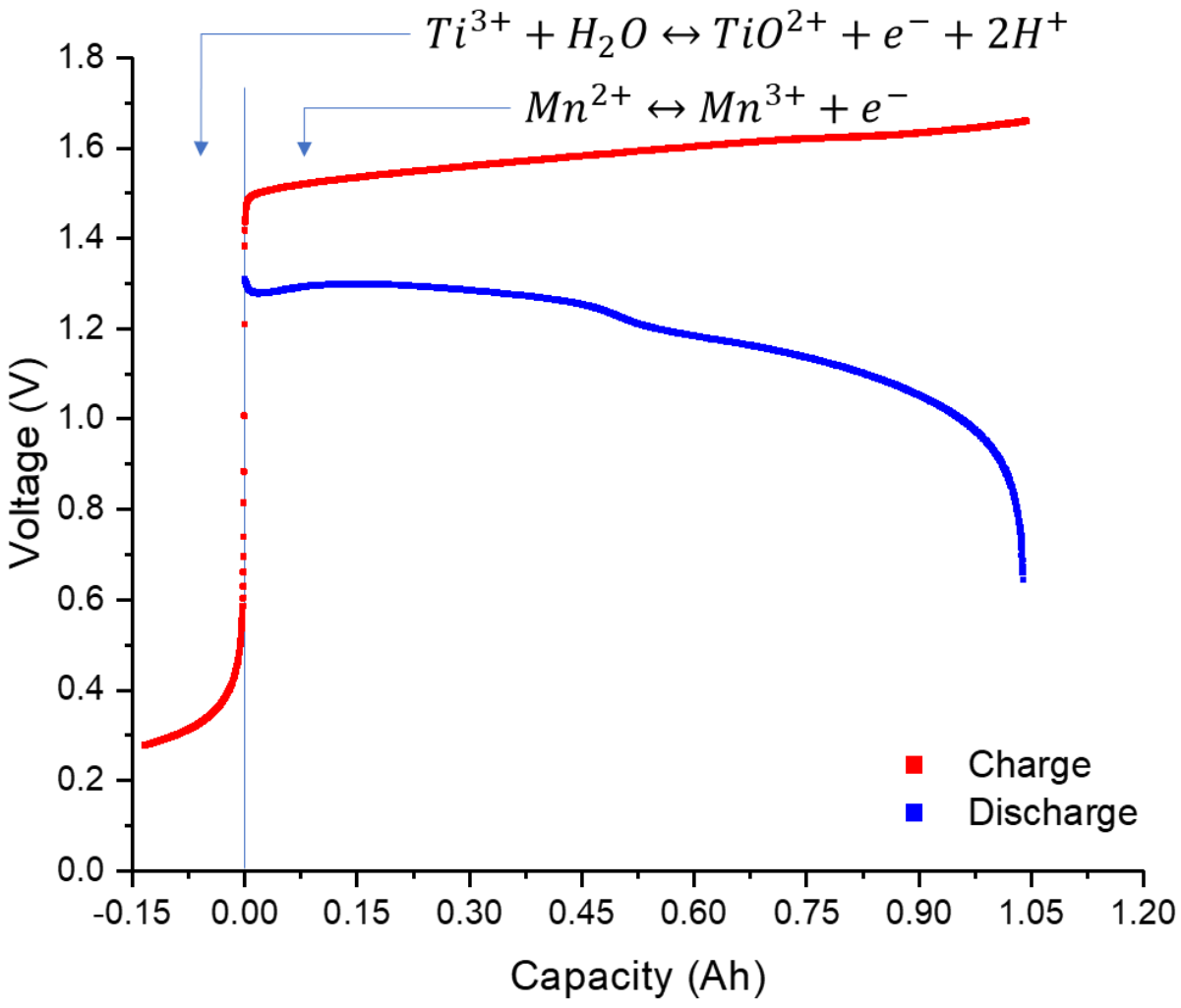

Figure 5-8: First charge half cycle of the cell after regenerating the electrolyte in the cell.

Figure 5-8 demonstrates the initial cycle after regenerating the electrolyte according to the recorded measurements from galvanostatic charging of the cell at 100 mA/cm^2, with voltage response measured to be 0.4 V. This voltage presents the electrochemical oxidation reaction of Ti^{3+} to Ti^{4+} and based on the charged capacity observed at this part of the measurement, it was evaluated to be 0.12 Ah, equal to the excess capacity achieved in step four of the regeneration procedure.

5.1.4 Influence of Temperature on Manganese Electrolyte and Cell Performance

Another mechanism that may result in capacity fade of the RFBs is the precipitation of the redox active species in the electrolyte caused by the instability of these species at temperatures higher than room temperature [218]. In VRFB, precipitation of vanadium pentoxide (V^{5+}) at a moderately high temperature is a common problem. Zhang et al. investigated the effect of temperature on the performance of VRFB system and concluded that, although increasing the temperature up to 55 °C improves the voltage efficiency of the cell by 3% (at the current density of 40 mA/cm^2), it also reduces the coulombic efficiency of the electrolyte by 4% [218].

Therefore, the performance of the cell and stability of the electrolyte at temperature higher than room temperature must be examined. In RHMnFC, since titanium is used to stabilise Mn^{3+}, the stability of the electrolyte will be affected by the stability of both manganese active species and titanium additive at different temperatures.

5.1.4.1 Stability of Electrolyte Over Time at Different Temperatures

The stability of Mn^{3+} at different temperatures was discussed previously in Section 4.1.7; where the change in the concentration of Mn^{3+} caused by the precipitation of MnO_2 at different temperatures and durations was modelled. However, this model does not take into account the change in the stability of the electrolyte with the presence of the Ti additive. In collaboration with Danlei Li, a student in the Elechtrochemistry group, the stability of Mn^{3+} as a function of temperature and time was studied experimentally [193]. In this set of experiments, the change in the concentration of manganese over time was monitored at different temperatures.

Although the mechanism by which titanium metal supresses the Mn^{3+} disproportionation has not yet been established, the existence of a weak bond between manganese and titanium metals, linked by oxo bridges could be hypothesised [81,203]. Based on this hypothesis, the change in temperature could impact the strength of the bonding between these two metals and consequently destabilise the electrolyte [81].

Comparison of the experimental data to the kinetic model of the change in manganese concentration over time is presented in Figure 5-9. Although experimental data show close approximation to the

data obtained from the model, there are different mechanisms that could affect the experimental data. The main inaccuracy that contributes to the reliability of the experimental data, is the method of preparation of the electrolyte. In this experiment, the method that was discussed in Section 4.1.1, which involved producing $Ti(SO_4)_2$ electrochemically by oxidising $Ti_2(SO_4)_3$, has been used. However, since the produced $Ti(SO_4)_2$ was not used immediately, formation of TiO_2 at the bottom of the electrolyte tank was observed. As a consequence, the reduction in Ti concentration results in the immediate disproportionation of Mn^{3+} and precipitation of MnO_2 in the electrolyte. This effect was observed at the starting concentration of the Mn electrolyte during ICP measurements (Figure 5-9).

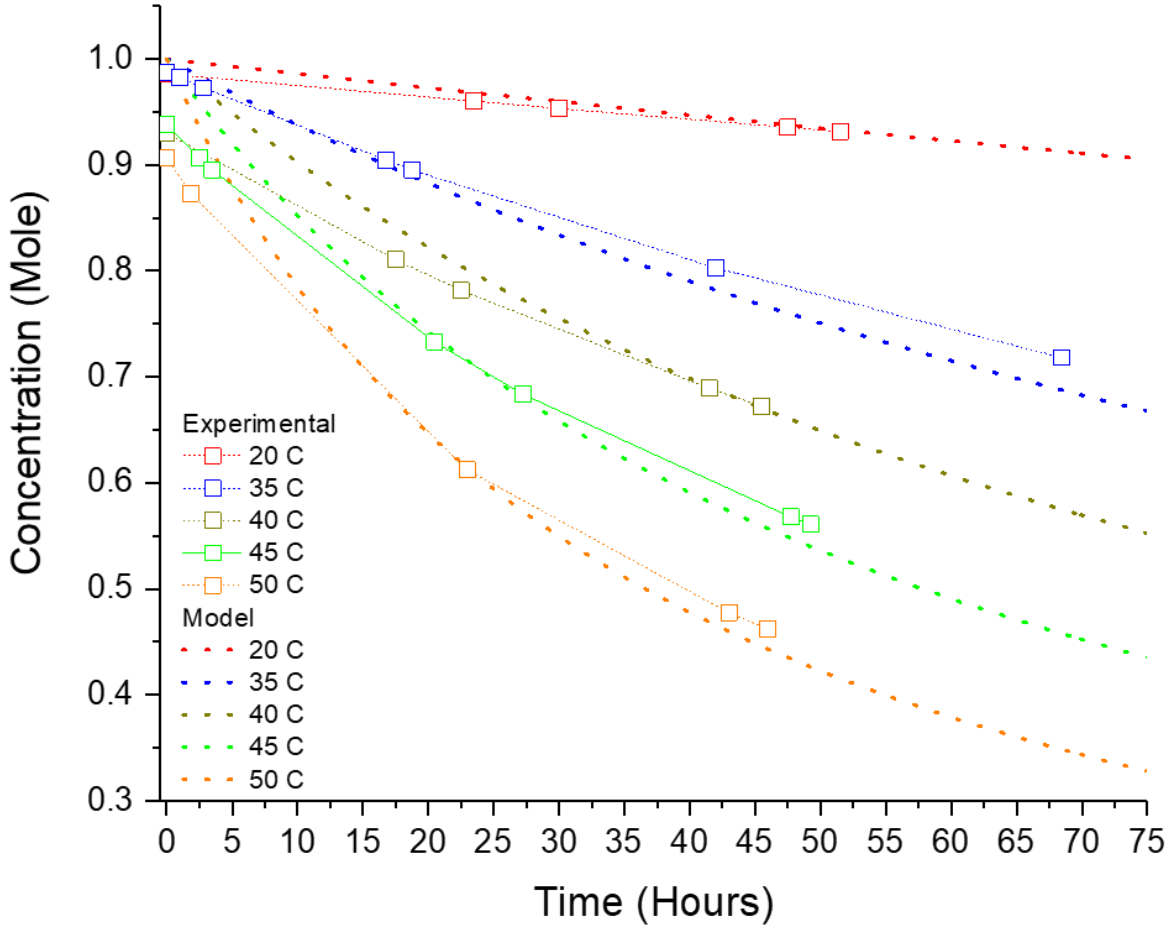

Figure 5-9: Experimental and kinetic model of the change in Mn^{3+} concentration over time at different temperatures (Experimental data by A. tan) [81]

In order to obtain comparable data, the change in manganese concentrations of the electrolyte over time at different temperatures were adjusted based on the starting concentration of the experimental samples. Based on the new model, compared to the experimental data, it was observed that the change in the concentration of the manganese electrolyte at 100% SOC over time at different temperatures exhibits a slower decrease rate.

It was expected that the fade in capacity observed during experiments would be lower than that predicted using the kinetic model. Figure 5-10 compares the precipitation of MnO_2 over time at different temperatures for the electrolytes with equal concentration at the start of the experiment. According to the obtained graph, it is observed that capacity fade of the electrolyte with the presence of Ti additives occurs at slower rate compared to the data obtained from the model predicting the decay in Mn concentration over time at different temperatures.

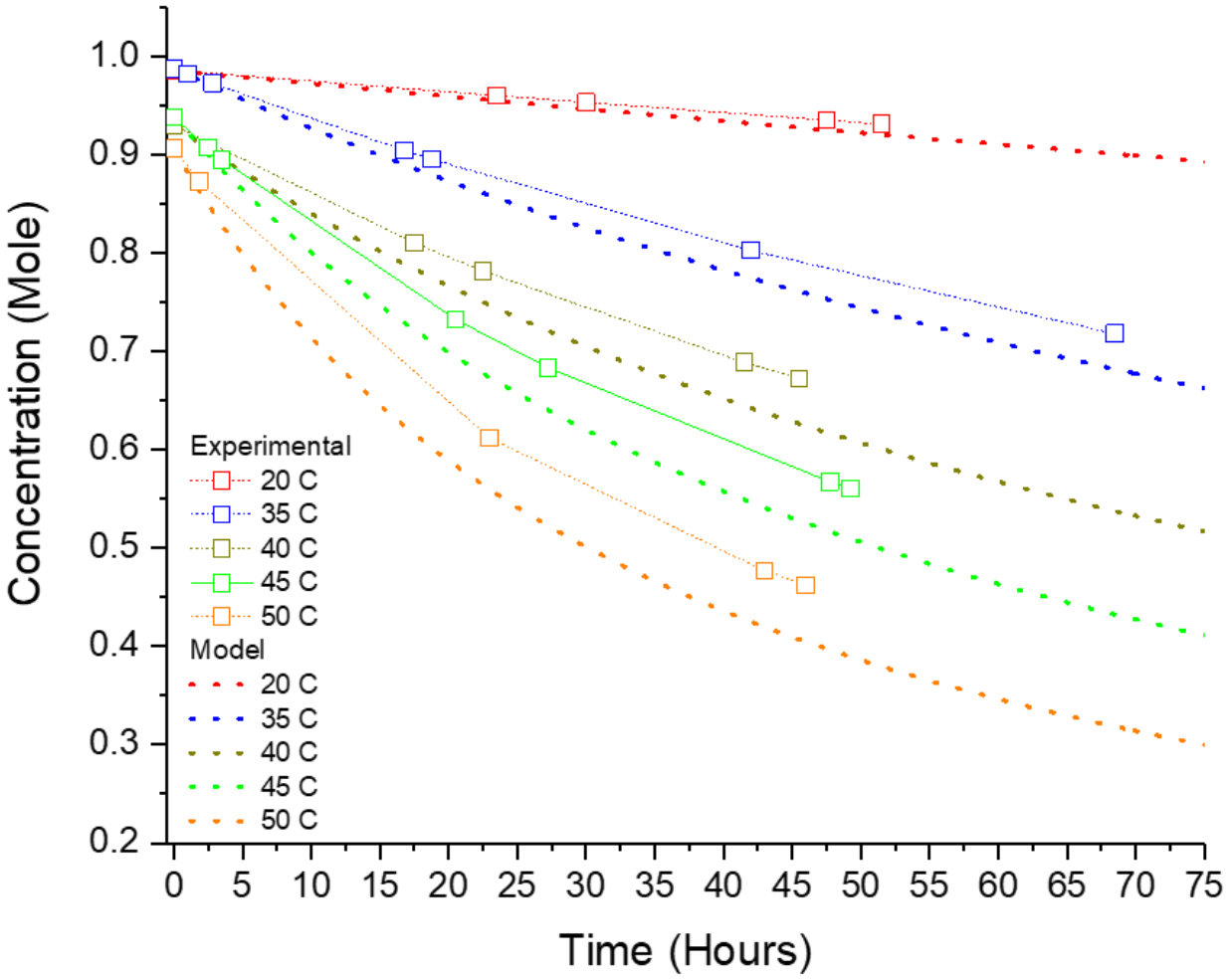

Figure 5-10: Regenerated figure of change in the Mn concentration over time at different temperatures with both experimental and model having similar starting concentration [81]

Further analyses of the data from the experiments and the model demonstrates that the change in concentration of the electrolyte becomes smaller as the duration of the rest time increases. The concentration decrease of the Mn in the electrolyte during the first 45 hours of the experiments, compared to their starting capacity, was calculated to be 5.5%, 18.72%, 27.72%, 39.49% and 49.06% for the samples tested at temperatures of 20 °C, 35°C, 40 °C, 45 °C and 50°C respectively.

Comparing the calculated changes in the concentration of Mn^{3+} using the model and experimental data, there is a larger difference between the predicted and measured data as the temperature

increased. This can be attributed to the impact of titanium additives in supressing the disproportionation of the Mn^{3+}. However, it is important to note that titanium precipitation also contributes to a decrease in the concentration of manganese in the electrolyte.

The change in the concentration of titanium occurs with respect to two competing mechanisms: the first mechanism is caused by the evaporation of water in the electrolyte, which increases the concentration of the titanium; the second mechanism relates to the precipitation of the $Ti(SO_4)_2$, which would decrease the concentration of Ti in the electrolyte [219,220]. Therefore, it is hypothesised that at lower temperatures, if evaporation of water is the dominant mechanism, the concentration of the Ti will increase slightly, thus enhancing its suppression effect on Mn^{3+} disproportionation. However, by increasing the temperature, the thermal hydrolysis effect on $Ti(SO_4)_2$ increases and Ti precipitation becomes the dominant mechanism. Reduction in Ti concentration will decrease the suppression effect on Mn stability.

5.1.4.2 Effect of Temperature on Performance of the RHMnFC

In the previous section, the effect of temperature on the stability of the electrolyte was examined. To further develop the understanding on the effect of temperature on the system performance, the RHMnFC was tested over a number of charge and discharge cycles at a constant current density (100 mA/cm^2) while increasing the cell temperature above room temperature. In these experiments, as explained in Section 3.2.5, to eliminate any impact contributed to the overall performance of the cell, caused by instability of the electrolyte at higher temperatures, only the flow cell's internal components were heated.

Initially, similar to every experiment in this project, to obtain a baseline performance, the cell was charged and discharged at a constant current density of 100 mA/cm^2 at room temperature (20 °C). According to these tests, the average EE of the cell was evaluated to be 77.18%, with an average achievable specific capacity of 25.32 Ah/L (92.67% of the theoretical capacity) over 10 cycles. In the second stage of these experiments, the temperature of the flow cell was increased to 30 °C. Based on the initial 10 cycles, there was a significant increase in the EE of the cell, when operating at 30 °C.

Figure 5-11 compares the performance of the cell at 30 °C to the cell operating at 20 °C. Based on the evaluated performance indexes, the EE and VE of the cell operating at a higher temperature was improved by approximately 4% on average over 10 cycles. However, there was a gradual decrease of the specific capacity in the cell operating at a higher temperature. This decay in achievable capacities over 10 cycles was calculated to decrease from 26.63 Ah/L (99% of theoretical capacity) at first cycle to 24.21 Ah/L (90.34% pf theoretical capacity) in last cycle.

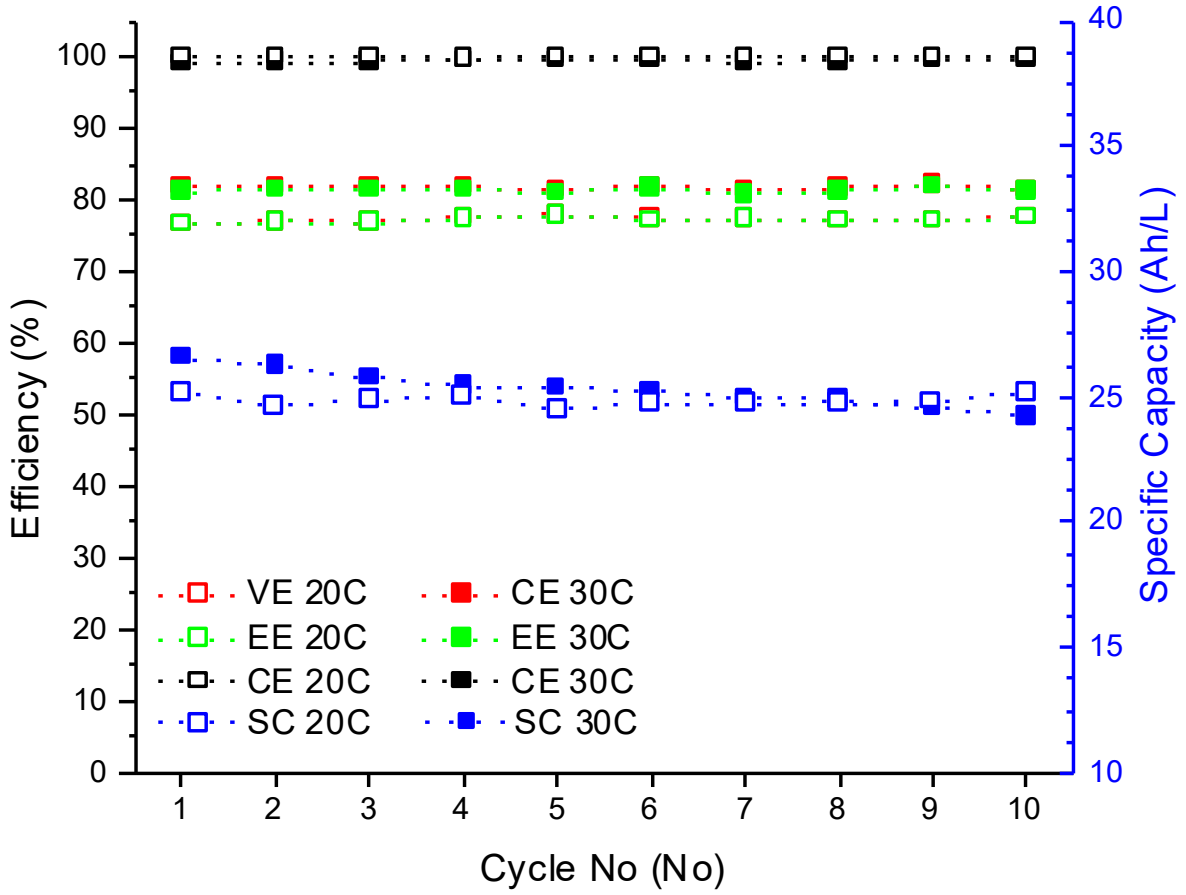

Figure 5-11: Performance comparison of RHMnFC operating at 20 °C and 30°C, charge and discharged at a constant current density of 100 mA/cm²

To further investigate the mechanisms contributing to this loss in capacity, as well as the potential reversibility of these losses, the performance of the cell operating at 30 °C was measured over 50 cycles of charge and discharge at 100 mA/cm². The evaluated performance indexes and achieved capacities, presented in Figure 5-12, shows that, although an average coulombic efficiency of 99.74% was achieved during these 50 charge and discharge cycles, the VE of the cell gradually decreased from 81.03% in first cycle to 54.62% in last cycle.

In addition to the VE drop, and thus the decrease in the EE of the cell, it is also observed that the specific capacity of the electrolyte fell from 26.16 Ah/L in the first cycle to 6.87 Ah/L in the last cycle. This 72% drop in the achievable capacity of the electrolyte can be either related to the degradation mechanisms occurring in the cell, or due to the instability of the electrolyte at higher temperatures. Although the stability of the electrolyte at different temperatures at state of charge close to 100% was investigated previously, the mechanisms that might result in the instability of the electrolyte in an operating cell will be different.

Despite the reactions that might increase the rate of disproportionation, the stability of the electrolyte in the cell during its operation at higher temperatures also depends on mechanisms such as crossover of the electrolyte through the membrane to the hydrogen half-cell, and the difference in the concentration of Ti between the electrolyte tank and inside the cell.

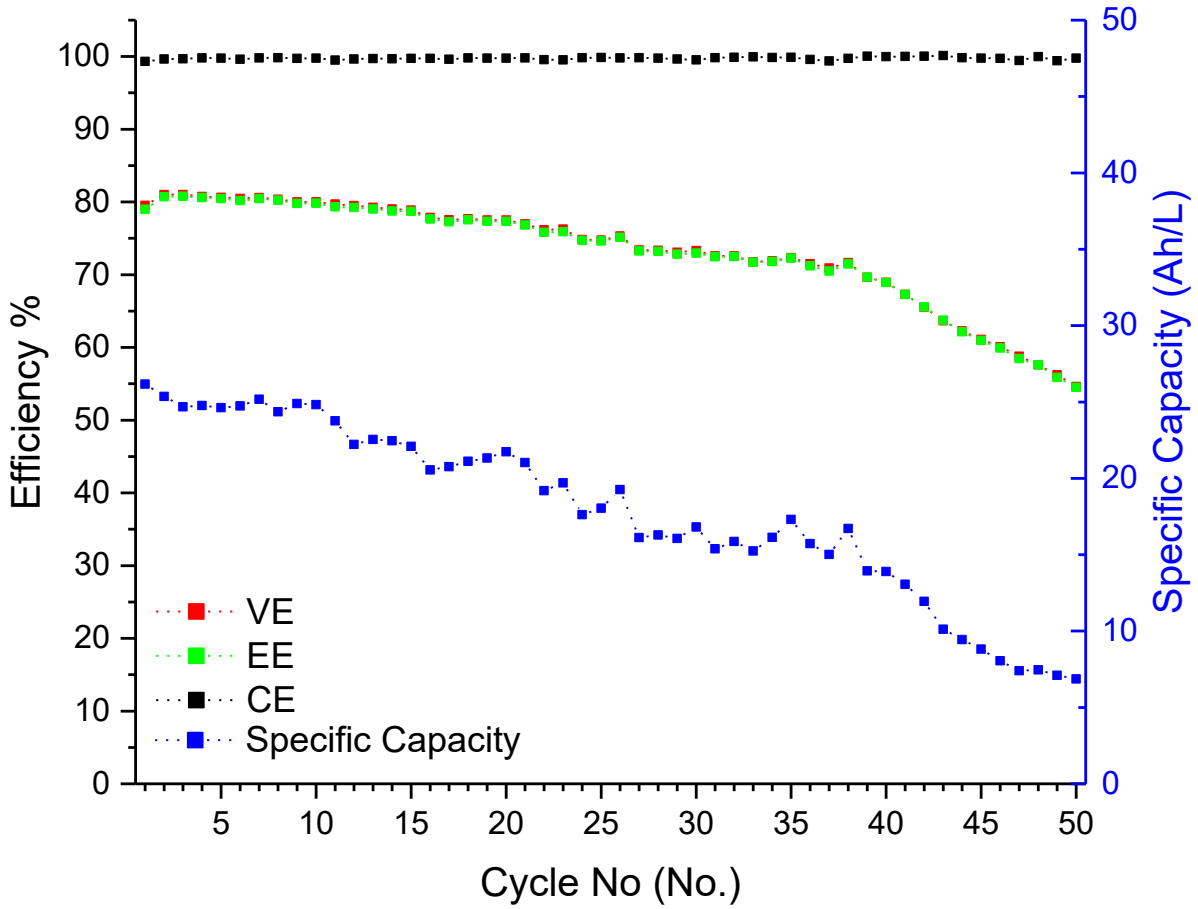

Figure 5-12: Performance of the cell operating at 30 °C over 50 cycles (Charge and discharged at a constant current density of 100 mA/cm^2)

Hence, the fade in capacity and the decrease in the VE of the cell in this experiment can be linked to three mechanisms:

- **Disproportionation of Mn^{3+}**: In this experiment, the temperature of the cell was increased, which will increase the rate of disproportionation reaction and precipitation of MnO_2. This phenomenon (highlighted previously in Section 3.2.3), can reduce the active surface area of the electrode in liquid half-cell and increase the activation overpotential of the cell. In addition, results obtained from operating 50 cycles of charge and discharge exhibit a CE close to 100%, which indicates the reversibility of the disproportionation reaction. However, as discussed in Section 4.1.7, this reversibility of MnO_2 precipitation was attributed to precipitation through an intermediate stage, where MnOOH was initially produced. It was

hypothesised that if precipitation exists in this intermediate stage, it would be possible to fully discharge the electrolyte.

- **Precipitation of TiO_2**: The hypotheses linked to the precipitation of TiO_2 due to hydrolysis of $Ti(SO_4)_2$ was discussed in Section 5.1.4.1. During operation of the cell, if TiO_2 is precipitated, it will decrease the active surface area, cause an increase in ohmic overpotential in the cell and thus decreases the VE of the cell. This will also reduce the concentration of the Ti, which will lead to an increase of Mn^{3+} disproportionation rate in the electrolyte. However, since charge and discharge cycles at a constant current density of 100 mA/cm^2 were carried out with small rest times, MnO_2 precipitation would only affect the VE, and the precipitated MnO_2 during charge half cycle, could be removed and discharged in the electrolyte.

- **Crossover of Electrolyte**: Increasing the temperature inside the cell will have a direct impact on the crossover of the electrolyte from the liquid half-cell to the hydrogen half-cell. The impact of increase in cell temperature has been discussed previously in Section 3.2.5. However, higher temperatures inside the cell could cause the aqueous electrolyte to dry inside the half-cell. This effect will lead to precipitation of both Mn and Ti oxides in the electrode and a coating on the surface of the electrode. Precipitation of these two oxides inside the electrode (in hydrogen half-cell) will increase the ohmic resistance. This will also introduce activation polarisation, due to a decrease in the Pt active surface area, where H_2 reduction or oxidation takes place during charge or discharge half-cycles.

These three hypotheses, related to possible mechanisms resulting in the degradation of the electrolyte capacity and reversibility of these losses, were investigated using various methods.

- **Disproportionation of Mn^{3+}**: In order to study the first hypothesis, where MnO_2 precipitation was assumed to cause the capacity degradation, a regeneration procedure (Section 3.2.4) was applied. By running the cell normally, no improvement in achievable capacity was observed. Also as discussed previously, MnO_2 precipitation contribution to the capacity degradation could only be valid, if a lower coulombic efficiency was obtained during charge and discharge cycles.

- **Precipitation of TiO_2**: Degradation of the capacity due to the precipitation of TiO_2 would result in the appearance of white particles inside the electrolyte tank. However, it is possible that TiO_2 precipitates were filtered inside the porous media, hence why these precipitates were not observed inside the solution. Gradual accumulation of the precipitated material (TiO_2)

inside the graphite felt could be attributed to the gradual decay in the VE of the cell during these 50 cycles. Upon deconstruction of the cell, a white layer was observed on the electrode at its interface with the Nafion membrane. Coating of the TiO_2 precipitate in the electrode and on its interface with the membrane, not only increases the charge transfer resistance of the electrode, but also reduces the proton conductivity of the membrane, which these two phenomena contribute to the inefficiencies observed in the cell performance.

- **Crossover of Electrolyte**: Initial indication of the electrolyte crossover to the hydrogen half-cell would consist of accumulated droplets in the hydrogen outlet tubing. In addition, there was no trace of any liquid droplets in the electrolyte recovery tank. When the cell was disassembled, solid material was observed inside the channels. As presented in Figure 5-13, the presence of solid material is more pronounced inside the channels closer to the inlet of the flow field (hydrogen is supplied from the top manifold), which will limit hydrogen distribution through the channels into the electrode during discharge.

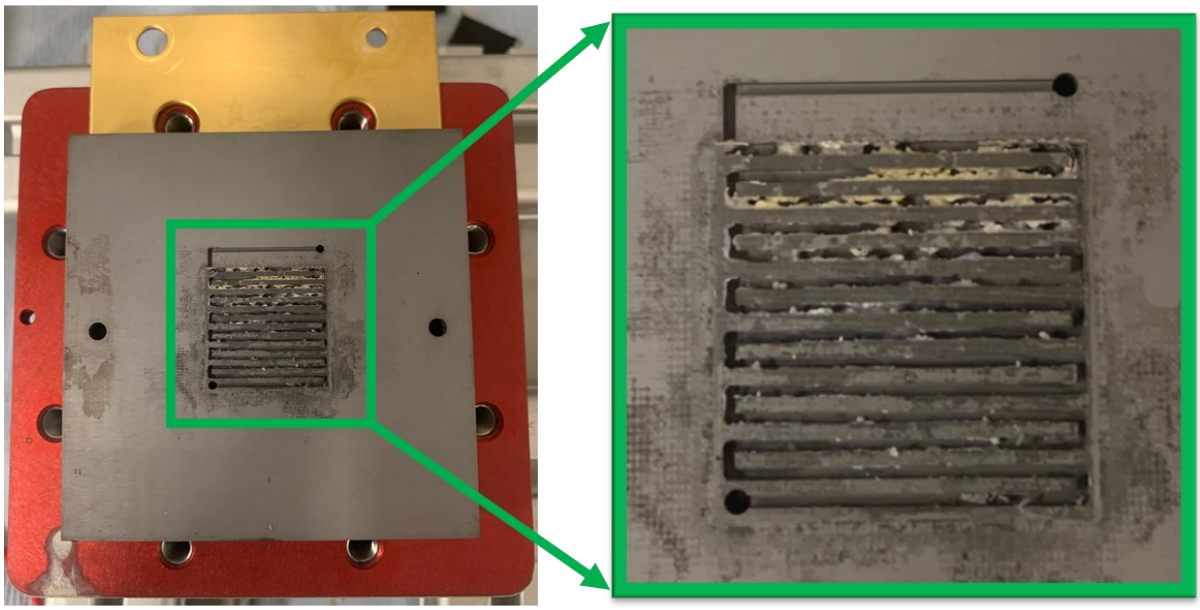

Figure 5-13: Presence of solid material inside the flow channels, due to crossover of electrolyte containing Mn and Ti metals, from liquid half-cell to the hydrogen half-cell

Following these investigations to explore the mechanisms limiting the performance of the electrochemical cell operating at 30 °C, it was hypothesised that the solidification of the material in hydrogen half-cell flow channels resulted in a significant increase of mass transport overpotential in the cell. As a consequence, the voltage of the cell would reach the cut-off voltage before utilising the full capacity of the electrolyte while charging the cell, which would directly affect the VE and achievable capacity in each cycle.

To be able to understand the losses contributed from the mechanisms discussed above, after draining the electrolyte and cleaning the cell, a cell with fresh components was assembled and conditioned. Then the electrolyte that was used to test the performance at 30 °C was used and galvanostatic charge and discharge was performed on the cell at lab temperature (20 °C). Initially, to measure the loss of electrolyte due to crossover, the volume of the electrolyte was measured. There was approximately a 5 mL loss in the electrolyte compared to the initial capacity of the electrolyte. Assuming that the amount of the electrolyte crossover contained a volumetric concentration of the active species in the electrolyte (1 M/L), a capacity loss of 0.13 Ah was estimated due to crossover.

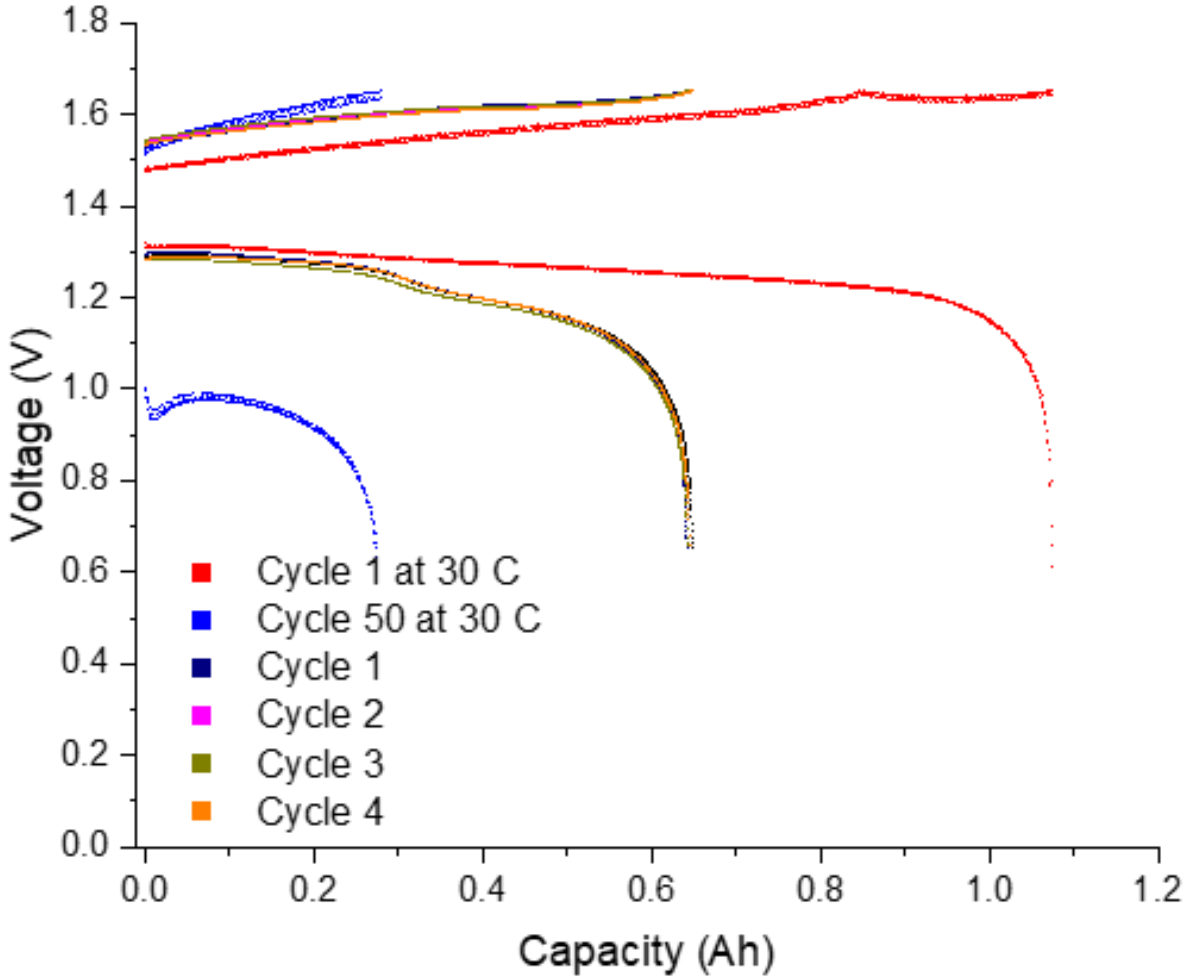

Figure 5-14: Comparison of first and last cycle of tests at 30 °C with fours cycles of the electrolyte used in a cell with fresh MEA. (Charge and discharged at a constant current density of 100 mA/cm^2)

To investigate the loss of capacity due to irreversible precipitation of the active species in the system, the electrolyte that was previously tested at 30 °C was used in a cell with fresh components. The maximum capacity achieved during galvanostatic cycling of the electrolyte, presented in Figure 5-14, was measured at 0.65 Ah (60.14% of the theoretical capacity for an electrolyte with 1 M Mn concentration). Hence, it could be hypothesised that 0.3 Ah of the capacity was degraded due to precipitation of the active species in the electrolyte.

Based on the findings from previous experiment, three different mechanism were identified to influence the measured loss in the electrolyte capacity. However, the loss of capacity caused by MnO_2 precipitation in this system requires further investigation.

5.1.5 Summary

In this chapter, the stability of the Mn electrolyte in the absence of Ti, which is used to supress the Mn^{3+} disproportionation reaction, was investigated. This experiment exhibited fade in the capacity of the electrolyte at each cycle where, after four cycles, further charge or discharge of the electrolyte (or the cell) was not possible. It was concluded that the degradation of the cell was due to the precipitation of the MnO_2, resulting in blockage of the porous electrode in the liquid half-cell.

To gain further insight into the stability of the Mn/Ti electrolyte, the reversibility of the Mn^{3+} reduction reaction was studied. In this section of the study, a fully charged electrolyte was discharged after different resting periods between the two half-cycles. The effect of an increase in the rest period between half-cycles on the stability of the charged electrolyte was a reduction on the performance of the cell which had an impact on the capacity retention of the electrolyte. In this section, the reversibility of the electrolyte was split into two half, where it was hypothesised that it is possible to fully recover the Mn^{3+} disproportionation if it existed at its intermediate state (MnOOH), and if Mn^{3+} disproportionation results in MnO_2, it is not possible to reduce the electrolyte back to Mn^{2+} during discharge.

In this work, for the first time, a method to dissolve the MnO_2 precipitate back into the electrolyte was developed and introduced. Using the electrochemical reduction of Ti^{4+} to Ti^{3+} at a redox potential of 0.1 V, the precipitates could be dissolved which regenerated the electrolyte. Reversibility of this method was shown through comparing the performance of the RHMnFC before and after running the regeneration cycle. The results were similar to the performance of the cell prior to electrolyte degradation, producing MnO_2 at 1.8 V. However, in this section, questions related to the rate of the Ti^{3+} and Mn^{4+} reaction were raised, which requires further investigation using different characterisation techniques. These methods will be discussed in more detail in Chapter 6.

Finally, the impact of increasing the temperature on the stability of the electrolyte and on the performance of the cell was studied in a series of experiments. An increase in electrolyte temperature, increased the rate of the disproportionation reaction, and consequently MnO_2 precipitation. Comparison of the experimental data with a kinetic model explained in 0 (on disproportionation of Mn^{3+}) exhibited the positive effect of Ti supressing the disproportionation reaction.

To extend this study and understand the temperature dependency of this chemistry, the effect of increasing the cell temperature on its performance was tested. Operating the cell at 30 °C exhibited an improvement in the voltage and energy efficiency of the cell in initial cycles, compared to the performance obtained operating at room temperature (20 °C). However, a small decay in the specific capacity of the cell was observed. To investigate the mechanism that impacts the achievable capacity, the number of cycles were increased to 50 cycles. In this case, there was a further decrease in the capacity (72% drop in achievable capacity). The hypotheses and mechanisms responsible for the observed fade in the capacity was discussed, where Mn^{3+} disproportionation, electrolyte crossover, and TiO_2 precipitation were assumed to be the main influencing factors.

Chapter 6 In-Situ Visualisation and Quantification of Electrodeposit Morphology Under Dynamic Conditions in Zinc Secondary Batteries

In this work, a three-electrode electrochemical cell is presented that allows the use of X-ray radiography and X-ray CT to study the morphological evolution of zinc deposits under flowing electrolyte conditions. With this bespoke cell, it is possible to perform real time visualisation of zinc electrodeposition and dissolution process which occur in zinc secondary batteries and perform non-destructive three-dimensional characterisation of the microstructure of resulting zinc deposits formed under different cell operating conditions.

6.1 Results and Discussion

This section will present the results of the electrochemical deposition of zinc using the novel in-situ three-electrode electrochemical cell. In the first part of this section, the functionality of the designed three-electrode cell is explored including the mechanical durability of the cell and the electrochemical performance of the system using cyclic voltammetry. In addition, important system parameters for zinc electrodeposition in alkaline KOH electrolyte are highlighted, such as the diffusion coefficient and limiting current density as function of Reynold's number, based on the Zn-flow battery laboratory experiments conducted by researchers at University of Exeter as part of a joint collaborative project [h] with the Electrochemical Science and Engineering group at the Imperial College London.

In second part of this section, 3D data obtained from operando visualisation of the zinc electrodeposits using X-ray tomography is presented. Also, the geometrical quantification of the different zinc deposit 3D microstructures obtained under different operating conditions of the in-situ flow cell are compared and discussed. Postprocessing of the data obtained from XCT experiments was carried out in collaboration with Oluwadamilola Taiwo, a postdoctoral researcher in Electrochemical Science and Engineering group at Imperial college London.

6.1.1 Novel Three-Electrode Cell with Dynamic Hydrogen Reference Electrode

This cell consisting of a carbon electrode as the working electrode, a Zn rod as the counter electrode and Dynamic Hydrogen Reference Electrode (DHRE) as the reference electrode was manufactured to understand the electrochemical deposition and dissolution behaviour of Zn under different operating conditions. Prior to comparing the data obtained from this cell with the data reported in the literature,

[h] Zinc-Nickel Redox Flow Battery for Energy Storage, EPSRC reference EP/P003494/1

it is important to explain or clarify the mechanisms and conditions in which this three-electrode setup operates in.

The design of the cell and use of different electrodes have been previously illustrated in Section 3.3.1. This design benefits from a dynamic hydrogen reference electrode, which enables the changes in the potential at the working electrode to be measured, independent of any changes occurring in the counter electrode. The three-electrode configuration in the in-situ flow cell allows a specific electrochemical reaction to be investigated with a higher accuracy.

In general, a standard hydrogen electrode (SHE) is used to provide a reference potential for other redox couples, and by convention has a given potential of 0 V that can be defined as the potential at which hydrogen molecule oxidise to its hydrated ionic forms, shown in eq. 6-1 By definition, the SHE must have unity activity of the hydronium (H_3O^-) ions and a hydrogen partial pressure of 1 atm [221].

$$H_2 + 2H_2O \leftrightarrow 2H_3O^+ + 2e^- \quad E^0 = 0\,V vs\,SHE \qquad \text{eq. 6-1}$$

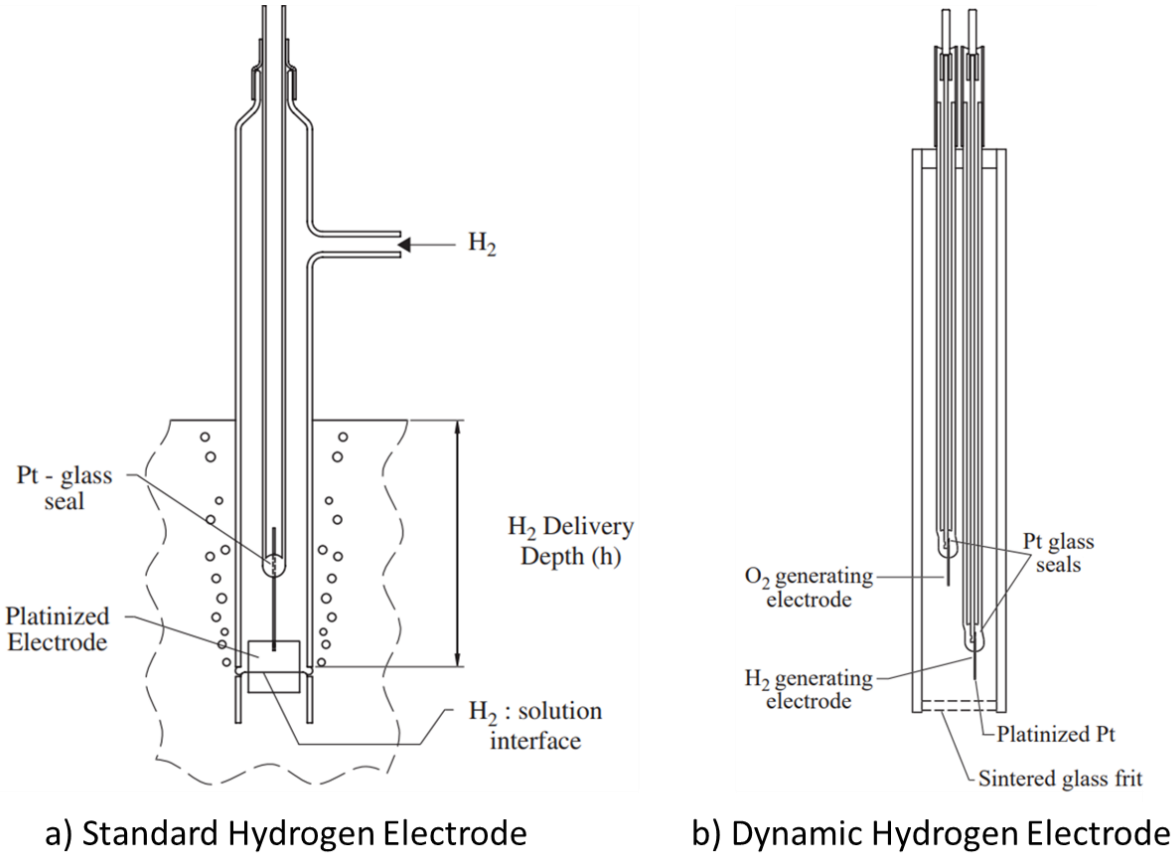

Figure 6-1: Schematic of a) a standard hydrogen electrode and b) a dynamic hydrogen electrode [221].

The SHE, presented in Figure 6-1 (a), typically consists of a platinum wire (or platinum sheet) in contact with hydrogen gas supplied to both the electrode and the electrolyte, which facilitates the catalytic

oxidation reaction of hydrogen. A DHRE, illustrated in Figure 6-1 (b), consists of a H_2 generating electrode and a O_2 generating electrode, and the potential at the electrode producing H_2 is used as the reference potential.

The DHRE assembly, unlike SHE, does not require a hydrogen supply, and is immersed in the same electrolyte as the electrolyte in which working electrode operates. Based on the explained operating principles of the DHRE, its potential correlates to the pH value of the solution and can be calculated using eq. 6-2.

$$E_0 = 0.000 - 0.059 \times pH \ (V \ vs \ SHE) \qquad \text{eq. 6-2}$$

Cyclic voltammetry (CV) experiments were conducted in the constructed three-electrode in-situ flow cell with an electrolyte solution containing 0.5 M ZnO and 6 M KOH in order to understand the electrochemical deposition and dissolution behaviour of zinc with the three-electrode cell setup at different flow rates between 0 RPM and 200 RPM. In order to obtain comparable measurements, flow rates used in these tests are presented in different form in Table 6-1. The Reynold's number (Re) corresponding to different linear flow velocities (μ), with hydraulic diameter (d_e) of 32 mm (diameter of the cylindrical portion of the in-situ flow cell at the point of measurement, shown in Figure 3-8), and kinematic viscosity (v) of the solution (measured by David Trudgeon [154] to be 1.887 mm^2/s) , is calculated using eq. 6-3.

$$Re = \frac{\mu d_e}{v} \qquad \text{eq. 6-3}$$

Table 6-1: Electrolyte flow used to conduct experiments presented in different forms

Speed of Pump	Flow Rate	Flow Velocity	Reynolds Number
RPM	**$mL.min^{-1}$**	**$cm.s^{-1}$**	**-**
0	0	0	0
50	248.55	0.53	89.54
100	497.09	1.06	179.08
150	745.63	1.58	268.62
200	994.18	2.11	358.15

Cyclic voltammograms obtained from this experiment, presented in Figure 6-2, shows that by increasing the flow rate, the maximum achievable deposition current density at -1.7 V (vs SHE) improves from -85 mA/cm^2 at no flow to -100 mA/cm^2 at a pump rotation speed of 200 RPM. This increase in the magnitude of deposition current density is due to the better mixing of the electrolyte, as well as a decrease in the length of the Nernst diffusion layer caused by forced convection [150].

The obtained CV measurements shows a linear increase in the magnitude of the measured current density as the overpotential in the working electrode decreases. According to several studies in the literature [160,164,169,222], CVs obtained from the electrodeposition of the Zn on the carbon substrate exhibit a reduction peak at voltages close to -1.4 V (vs SHE) [222]; however, no reduction peak can be observed in this experiment. This can be attributed to the difference in the surface morphology of the graphite-composite electrode used in this cell, compared to the glassy carbon electrode typically used in three-electrode cell measurements.

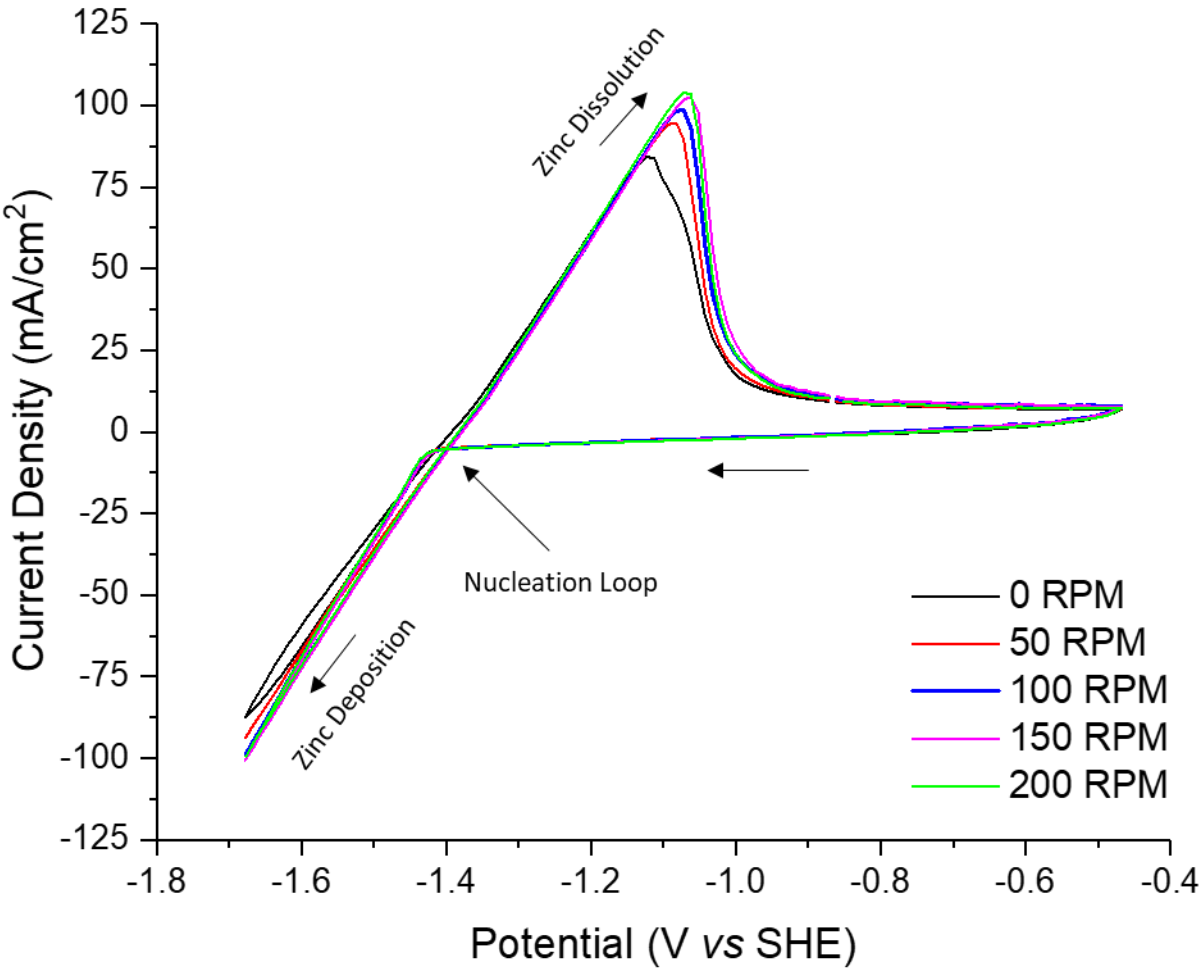

Figure 6-2: Initial Cyclic Voltammograms cycles of Zn deposition on the carbon electrode at different flow rates in the three-electrode cell, containing 0.5M ZnO and 6 M KOH electrolyte solution. Potential sweep rate 10mV/s at room temperature

As discussed in Section 3.3.1, the graphite electrode used in this setup, was machined to produce a conical tip, which results in having a microporous on the surface. This surface roughness will result in a higher local current as there will be a higher surface area available on the surface for the deposition of Zn [124]. In three-electrode rotating disk electrode (RDE) experiments, a very flat surface on the glassy carbon (working electrode) is usually accomplished by polishing the surface using 1 µm diamond paste, which mitigates the development of localised currents caused by the scratches or defects on

the surface. In addition, as explained in Section 2.4.4.1, HER could compete with the zinc electrodeposition process. Hence at more negative overpotentials, measured current response is the combination of both the Zn electrodeposition reaction and HER.

6.1.2 Operando visualisation and Characterisation of Zn Electrodeposition at Different Conditions

Figure 6-3 shows an X-ray radiograph of the tip of the carbon rod in the assembled in-situ flow cell, before (Figure 6-3 (a)) and after filling the cell with the electrolyte (Figure 6-3 (b)). Due to the X-ray attenuation by the electrolyte, it was challenging to obtain a high signal-to-noise ratio image for the carbon rod alone as in Figure 6-3 (b), once the cell was filled with the electrolyte. However, the relatively higher density of the zinc deposits provided sufficient contrast to enable their identification in the electrolyte (Figure 6-3 (c)).

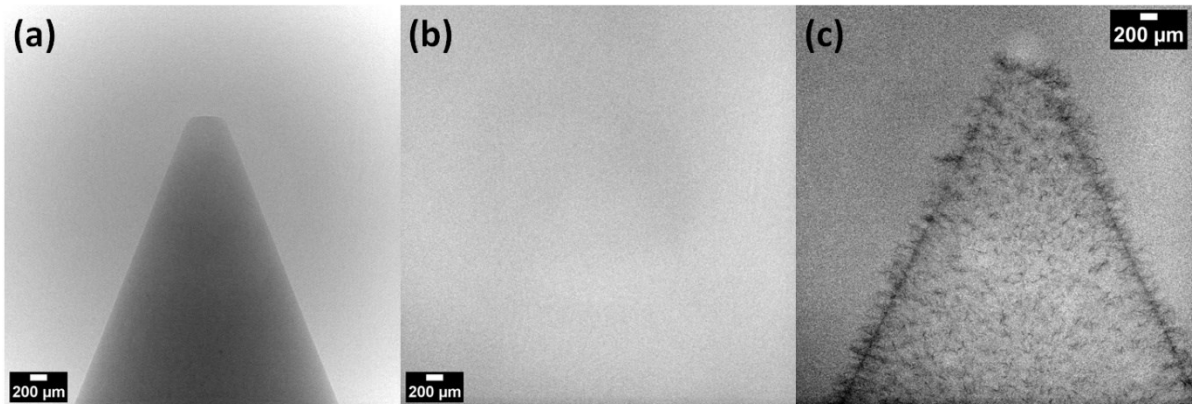

Figure 6-3: X-ray radiograph showing conical tip of extruded carbon composite rod (a) without electrolyte in the flow cell, (b) when the flow cell is filled with electrolyte, and (c) after zinc electrodeposition in the electrolyte

With the X-ray instrument in radiography mode, charge currents were applied to the cell to induce zinc deposition whilst simultaneously imaging the conical tip of the carbon composite electrode. For each experiment, the charging current was applied until an areal capacity of 5 mAh/cm^2 was achieved. In order to demonstrate the capabilities of the in-situ flow cell for both electrochemical testing and 2D/3D microstructural characterisation, experiments to observe the effect of current densities on the morphology of the Zn electrodeposition were carried out.

However, prior to presenting the data obtained from these experiments, it is important to define comparable figures of merit, which will make the results obtained from in-situ experiments comparable to the results reported in literature. Changes in different parameters, such as applied current density and flow velocity influence the distance of the system from equilibrium and the morphology of Zn deposits. However, limiting current density incorporates all of these parameters, so

the ratio between the applied current density and the limiting current is taken as a measure which indicates the distance from the equilibrium [164].

Limiting current density ($j_{lim\ (0)}$) can be calculated using eq. 6-4 for static electrolytes, and eq. 6-5, is the limiting current density (j_{lim}) for the system with flowing electrolyte, where n is the number of electron transferred in the reaction, F is the Faraday's constant, D is the diffusion coefficient of zincate in 6 M KOH at room temperature (293 K), C_0 is the concentration of zincate in the electrolyte, δ is the thickness of diffusion layer, d_e is the hydraulic diameter and Sh is Sherwood number [223].

$$j_{\mathrm{lim}\ (0)} = \frac{nFDC_0}{\delta} \qquad \text{eq. 6-4}$$

The Sherwood number can be calculated using eq. 6-5, where Re is the Reynold's number, Sc is Schmidt number, which is the ratio of the kinematic viscosity and diffusion coefficient, and L is the length of the electrode in the streamwise direction.

$$Sh = 1.8488\, Re^{1/3}\, Sc^{1/3}\, (d_e/L)^{1/3} \qquad \text{eq. 6-5}$$

Using the parameters presented in Table 6-2, limiting current densities for the electrodeposition of zinc on the carbon electrode at different electrolyte flow rates were calculated. It must be noted that, the calculated parameters are from RDE experiments, and some of these parameters will be different for electrodes with a higher surface roughness, hence, these parameters are used as a first approximation to calculate the limiting current density for the system that is produced.

Table 6-2: Input parameters to calculate limiting current densities of flowing electrolyte

Symbol	Parameter	Unit	Reference	Symbol	Parameter	Unit	Reference
$\boldsymbol{n}$	2	Electrons		D	3.0 X 10^{-6}	$m^2.s^{-1}$	124,154
$\boldsymbol{F}$	96485.33	$C.mol^{-1}$		d_e	2.5 X 10^{-3}	meter	
$\boldsymbol{C_0}$	0.5	M		L	1.0 X 10^{-3}	meter	
$\boldsymbol{v}$	1.89 X 10^{-6}	cP	154	$j_{\mathrm{lim}\ (0)}$	20	$mA.cm^{-2}$	124,224

Limiting current density at a range of operating conditions is calculated and presented in Table 6-3. Based on these values, corresponding current density ratios (CDR) are calculated for two different applied current densities, and these values will be used to compare the morphology of the depositions at different CDRs.

Table 6-3: Limiting current densities and current density ratios at different electrolyte flow rates and oprating current densities

Pump speed	Reynold's No.	j_{lim}	Current Density Ratio (CDR)	
RPM (cm/s)	**-**	**mA/cm²**	**10 mA/cm²**	**100 mA/cm²**
0 (0)	0	20.00	0.50	5.00
100 (1.06)	179.77	93.30	0.11	1.07
200 (2.11)	357.84	117.37	0.09	0.85

6.1.2.1 Effect of Applied Current Density on the Morphology of the Electrodeposition

Electrodeposition of the zinc active species in the alkaline media is initiated by applying a negative current to the working electrode at a redox potential of -1.248 V (*vs* SHE). However, as discussed in Section 2.4.2.4, this complex reaction is driven by both electrochemical and chemical processes. In the present system (three-electrode cell), to understand the effect of current density on the morphology of the electrodeposit, zinc was deposited on to the coned shape carbon electrode at two different current densities of 10 mA/cm^2 and 100 mA/cm^2, and this process was monitored in real-time, to gain more insight to the deposition process. The chronopotentiometry curve of zinc electrodeposition is presented in Figure 6-4 (g), with the radiograph images of this process at the start of the deposition (Figure 6-4 (a) and (d)), mid-point (Figure 6-4 (b) and (e)) and final deposition (5 mAh/cm^2) at two different current densities are also illustrated.

Based on the real-time visualisation of the electrodeposition process using X-ray radiography, it was observed that the deposition does not initiate until a critical overpotential is reached. Time taken to initiate the growth is dependent on different parameters such as, the concentration of the active species, the system operating temperature and the local current density. Following initial growth, by applying a negative current density of 10 mA/cm^2, a gradual increase in the thickness of the deposit was observed, resulting in a uniform final deposition.

After initial growth at the current density of 100 mA/cm^2, immediate dendritic growth of zinc at the tip of the electrode was observed. Furthermore, it was also seen that the formation of zinc dendrites was accompanied by hydrogen gas evolution (visible as white circles and semi-circles on the electrode in Figure 6-4 (e) and (f)), which is formed by the electroreduction of water. Although, previously in Section 2.4.4.3, was discussed that the produced hydrogen bubbles, from the HER, enhances the mass transport of the active species to the surface of the electrode, formation of hydrogen bubbles on the electrode reduces the available surface for zinc formation, and facilitates dendritic growth by increasing the mass transport over potential.

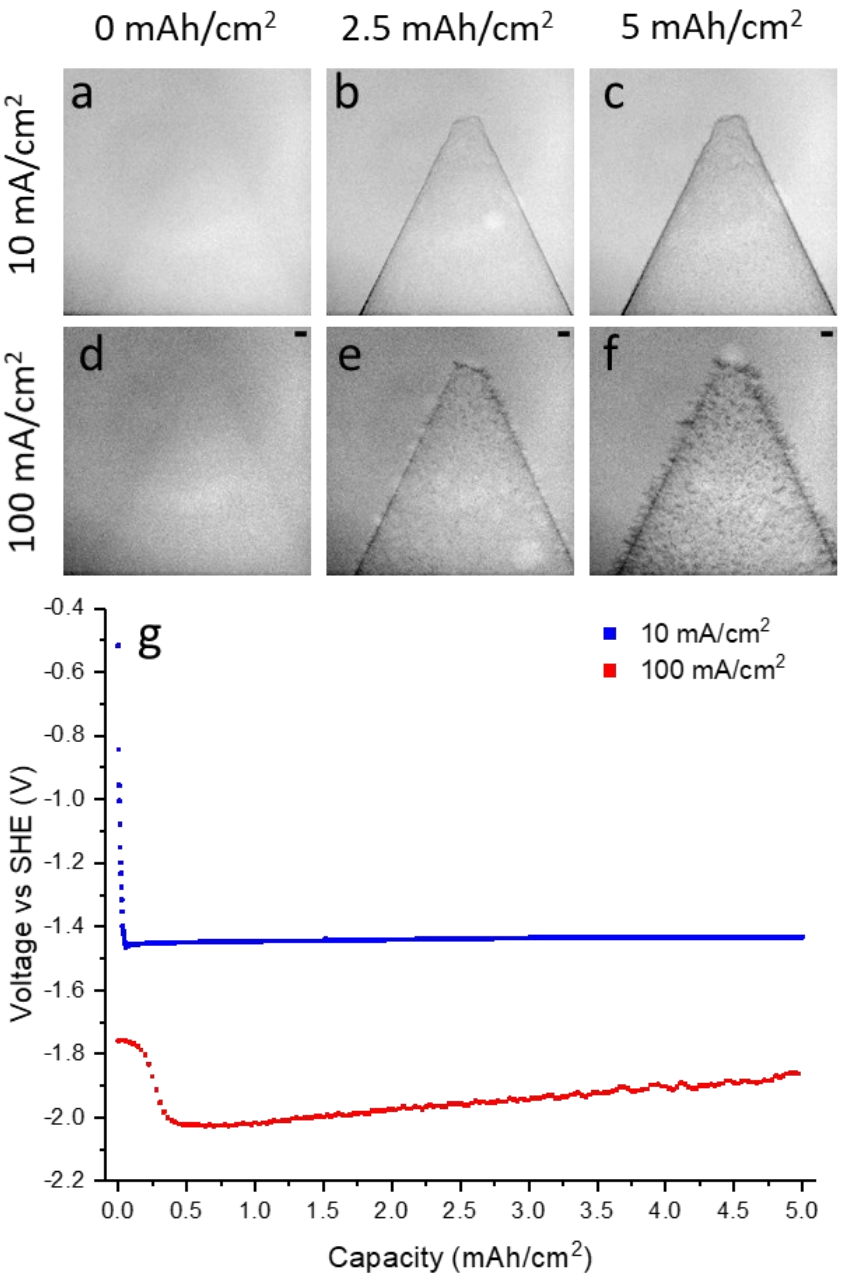

Figure 6-4: Real-Time visualisation of Zinc electrodeposition at two different current densities of 10 mA/cm^2 and 100 mA/cm^2 (a) to (f) presents the deposition at different capacity per unit area and (g) is the Chronopotentiometry curve of the zinc electrodeposition

As the deposition proceeds, the formation of dendrites is evident on various locations on the electrode. The inconsistent initiation time of dendrites in different locations can be associated with the non-uniform local surface of the working electrode, and formation of hydrogen bubbles on the electrode. These two phenomena result in a non-uniform local current density and thus affecting the effective potential of the electrode, which results in different initiation times.

After a period of sufficient deposition, secondary dendrites were observed to form on the trunk of the initial dendrites, rather than on the electrode substrate, where the growth of secondary dendrites was discussed in Section 2.4.4.2. Within the diffusion layer, it is more preferential for the ions to deposit

on these boulder agglomerates. As the deposition continues and the height of the deposits exceed the thickness of diffusion layer, the tip will be exposed to a higher concentration (equal to the concentration of the bulk electrolyte). As already deposited zinc acts as a preferential surface for Zn to deposit on, hence a secondary spherical diffusion layer will be developed around the tip, and Zn ions will diffuse from the bulk electrolyte to the surface of the tip from different directions, resulting in formation of rapid multi-directional dendrites [128,130,150].

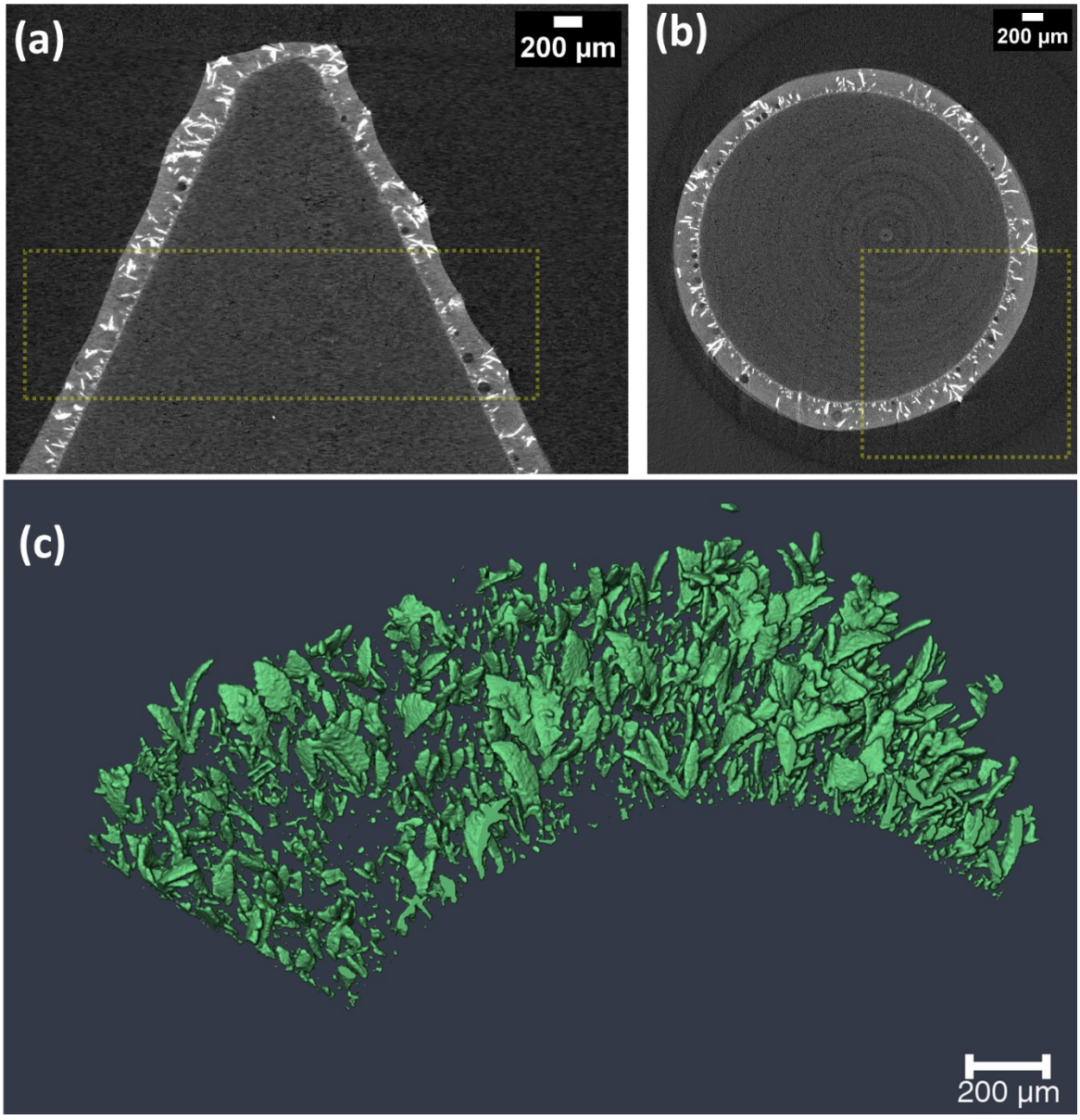

Figure 6-5: (a) Vertical and (b) horizontal cross sections through 3D reconstructed image volume of the conical tip of the carbon rod after zinc electrodeposition. The deposited zinc is distinguished by the bright shades of grey in the grayscale images due to its relatively higher X-ray attenuation. The yellow dashed lines highlight the region of interest in the reconstructed volume that was analysed, and 3D rendered in (c)

To obtain information of the microstructural parameters such as zinc deposit volume, volume specific surface area, deposit height and size distributions, tomographic reconstructions of each set of

acquired projection images obtained at two different current densities were performed. As presented in Figure 6-5, due to the large sizes of image volume data, a region of interest along the conical tip of the carbon composite rod was selected in each tomogram for subsequent analysis.

To compare the morphology and microstructure of the electrodeposits at current densities of 10 mA/cm^2 and 100 mA/cm^2, XCT scans of the area of interest were carried out at the end of each electrodeposition experiment. The laboratory X-ray instrument that was available for this research could not provide the X-ray flux to enable high contrast-high resolution radiography images of deposit growth within electrolyte. Therefore, in order to obtain higher signal to noise ratio in the radiography images during the XCT scans, the electrolyte in the cell had to be drained. However, with higher X-ray flux achievable with synchrotron X-ray sources, the need to drain the cell to obtain higher signal to noise ratio in the images would be eliminated.

Reconstructed 3D tomography scans for electrodeposition at current densities of 10 mA/cm^2 and 100 mA/cm^2 are represented in Figure 6-6. The post-processed images exhibit a difference in morphology of the deposition at different current densities; where operating at a current density lower than the limiting current density (Table 6-3) has yielded boulder type morphologies, which can be associated with mixed diffusion and charged transfer limited conditions. By increasing the effective current density higher than the limiting current density, dendritic deposition morphology is observed, which corresponds to diffusion limited deposition [158,160].

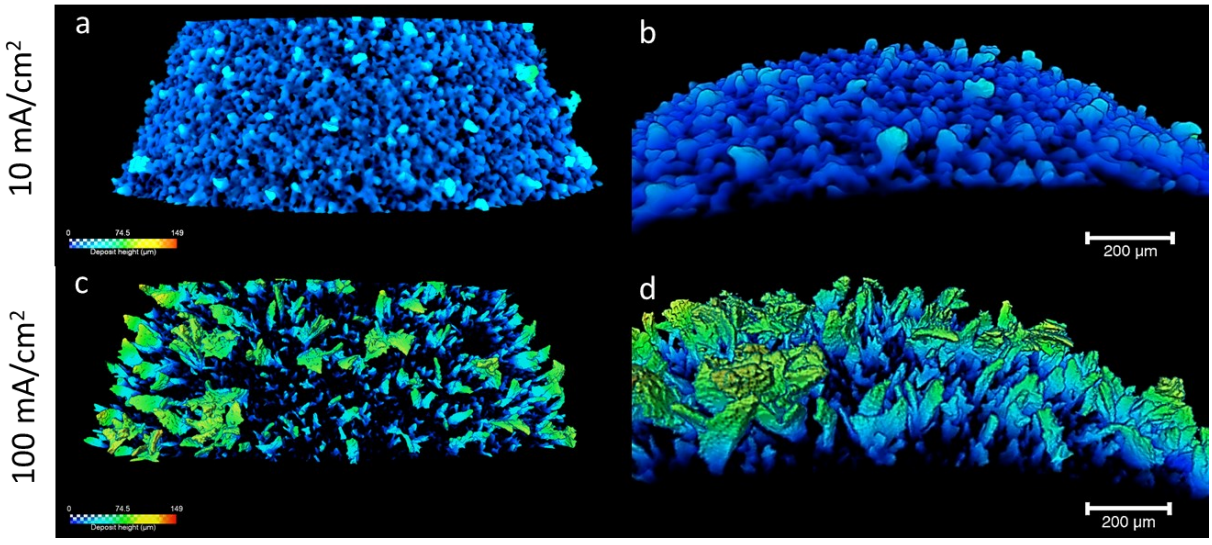

Figure 6-6: Reconstructed 3D images of zinc deposit morphologies on carbon electrode at two different current densities of (a-b) 10 mA/cm^2 and (c-d) 100 mA/cm^2

It is also clear that size of deposits and dendrites vary in height and thickness across the electrode. Figure 6-7 illustrates the distribution in the height of zinc deposits for electrodeposition at two different current densities. This indicates that, by operating the cell in a lower current density, under

a charge transfer-controlled conditions, it is possible to obtain more uniform deposits compared to the electrodeposition at a higher current density, under a diffusion limited deposition which yields in a non-uniform deposit height. Uncontrolled growth of dendrites is one of the most common failure mechanisms of the Zn-RFBs, where continued growth of dendrites may result in contact with the positive electrode and hence internal short-circuiting.

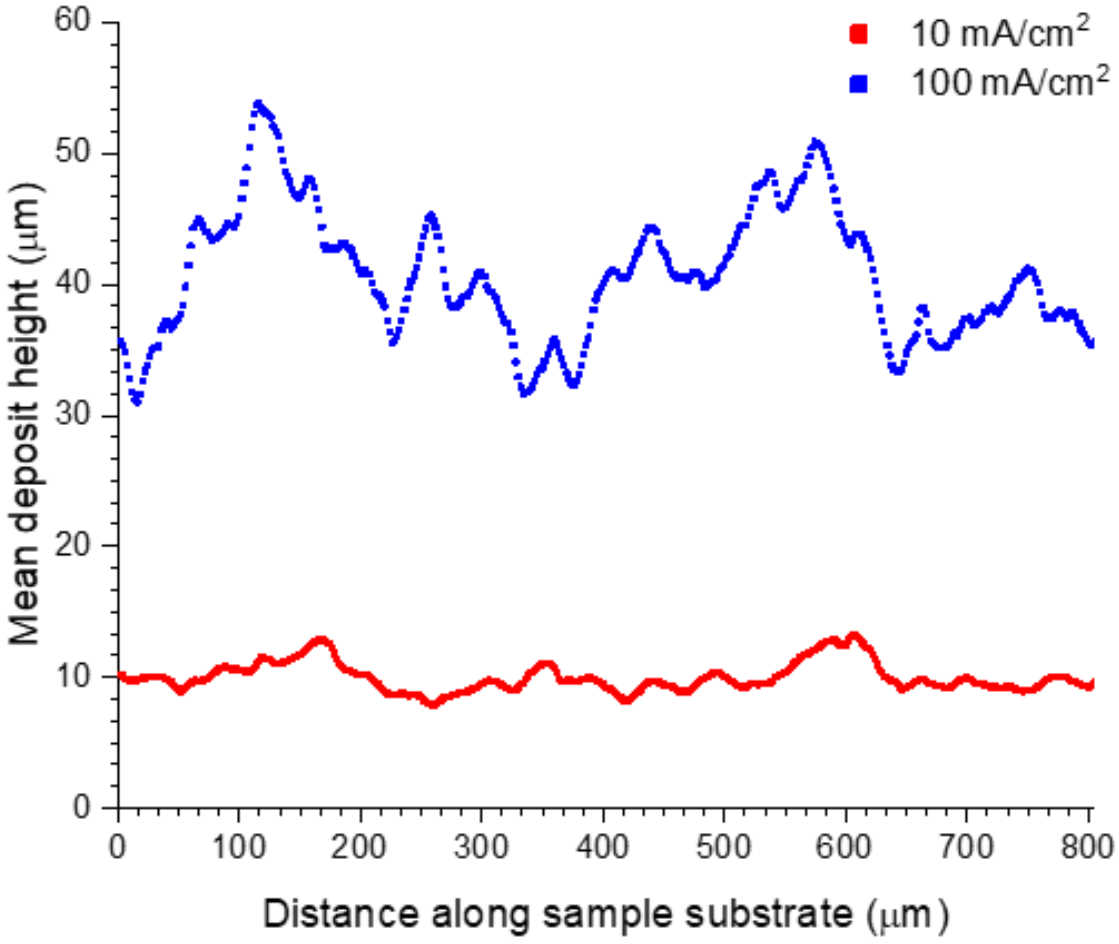

Figure 6-7: Deposit height distribution across the electrode surface for electrodepositions at a current density of 10 mA/cm^2 and 100 mA.cm^2

Quantification of the surface area, volume and mass of the deposited Zn were also performed based on reconstructed 3D tomography images (Table 6-4). It was observed that the volume of zinc deposition was 30% lower for the electrodeposition at a constant current density of 10 mA/cm^2, which indicates that a denser deposition resulted at the lower current density. Higher deposition volume at a higher current density has also yielded a higher surface area, and as highlighted in Section 2.4.4.2, higher surface area is accompanied by the increase of local current density, which facilitates the formation of the secondary dendrites on the primary dendrites rather than on the electrode.

Table 6-4: Quantified volume specific area and mass of the deposited zinc for deposition at constant current densities of 10 mA/cm² and 100 mA/cm²

Current Density	Surface Area	Volume	Volume Specific Area	Density	Mass of Zn
mA/cm²	$\mu m^2 \times 10^6$	$\mu m^3 \times 10^6$	$\mu m^2/\mu m^3$	g/mL	μg
10	6.88	52.66	0.13	7.14	0.38
100	8.99	56.07	0.16	7.14	0.4

6.1.2.2 Effect of Flowing Electrolyte on the Morphology of the Electrodeposition

For the first time known to the author, operando X-ray visualisation of the formation and morphology of zinc electrodeposition under flowing electrolyte conditions was performed using a three-electrode cell setup designed by the author. Experiments to investigate the impact of flowing electrolyte on the formation behaviour and morphology of the Zn deposition were carried out, and the results obtained from electrochemical deposition of Zn at constant current densities of 10 mA/cm² and 100 mA/cm² under flowing electrolyte, with flow velocities of 1.06 and 2.11 cm/s will be presented.

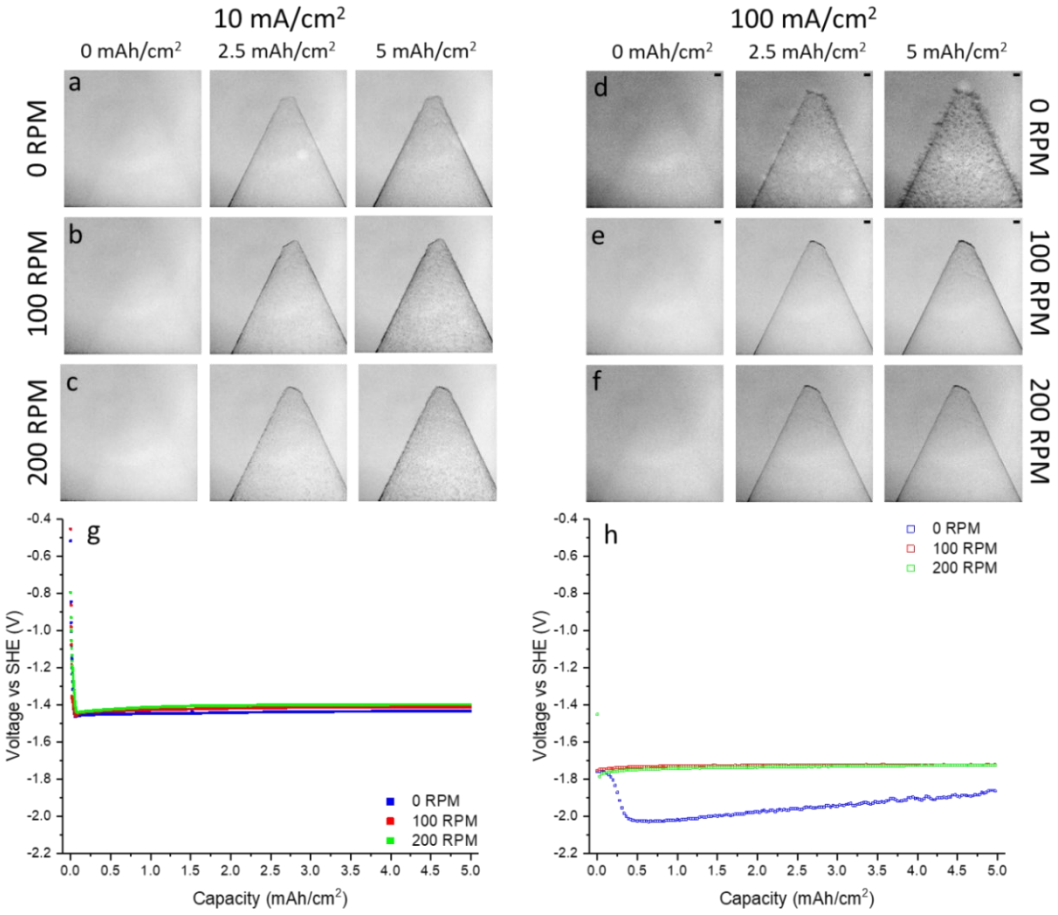

Figure 6-8: Real-Time visualisation of Zinc electrodeposition at constant current densities of 10 and 100 mA/cm2 with (a and d) static electrolyte, (b and e) at flow velocity of 1.05 cm/s and (c and f) at electrolyte flow velocity of 2.11 cm/s. (g and h) is the Chronopotentiometry curves of the zinc electrodeposition at these six conditions

Radiography images and chronopotentiometry curves of the electrodeposition at different conditions are presented in Figure 6-8. Based on the 2D projection images, no significant changes in the formation of the Zn deposit at a low current density of 10 mA/cm^2 were observed, which could be as a result of operating at a current density below the limiting current density. Hence, deposition at this current density is charge-transfer controlled, and introducing or increasing the flow will only increase or enhance the deposition.

By introducing a flow to the electrolyte while electrochemically depositing the Zn at a current density of 100 mA/cm^2, significant change in the formation of the Zn on the substrate was observed. Radiographs of Zn electrodeposition with electrolyte flow velocities of 1.05 cm/s and 2.11 cm/s (Figure 6-8 (e and f)), demonstrate a uniform growth of Zn on the surface of the electrode. The dendritic growth of Zn is suppressed in the presence of flowing electrolyte as the limiting current density has increased from 20 mA/cm^2 in a static electrolyte to limiting current densities closer to the effective current density in the experiments with the electrolyte flowing at linear velocities of 1.05 cm/s and 2.11 cm/s (see Table 6-3).

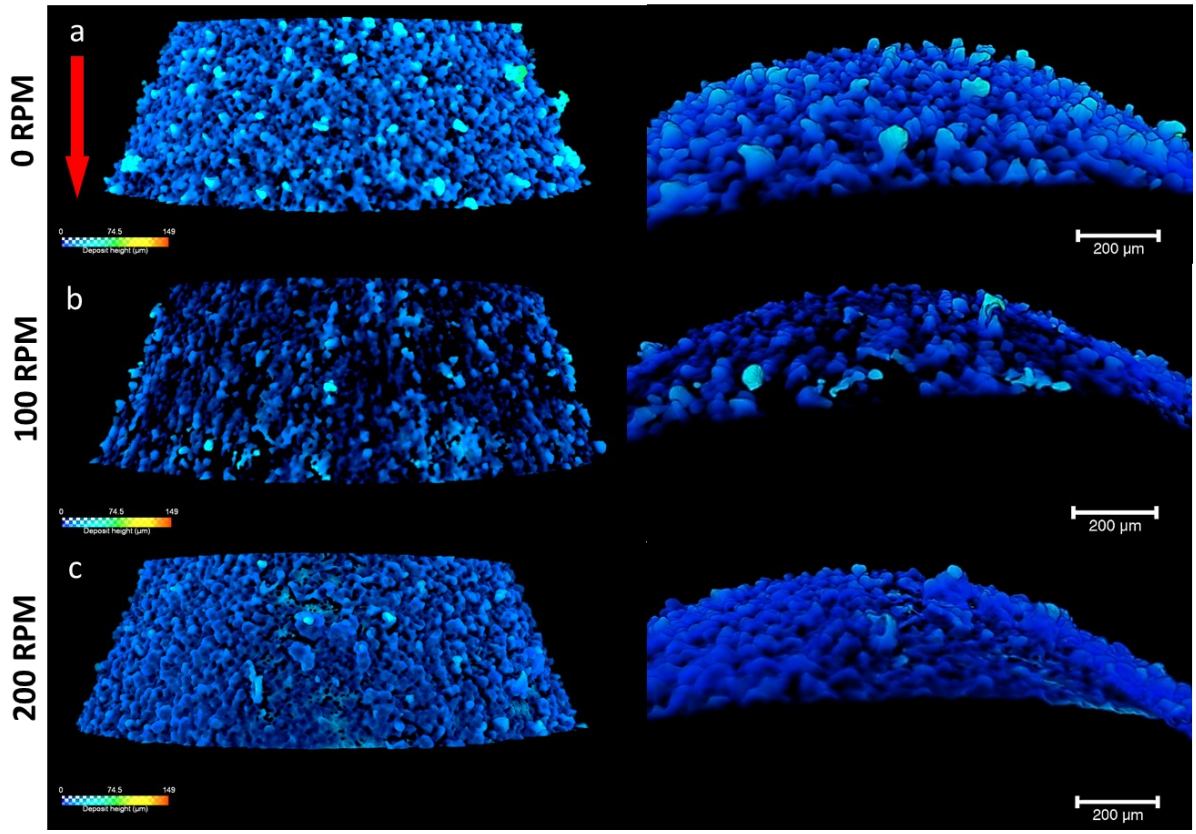

Figure 6-9: Reconstructed 3D images of zinc deposit morphologies on carbon electrode at a constant current density of 10 mA/cm^2 under (a) static electrolyte flow and (b) dynamic flow with flow velocity of 1.05 cm/s and (c) linear flow velocity of 2.11 cm/s

Moreover, based on the operando radiography of the cell at a constant current density of 100 mA/cm^2 under dynamic flow conditions, formation of the Zn initiated without any visible hydrogen bubbles on

the surface of the electrode. The linear voltage responses of the depositions under dynamic flow condition (Figure 6-8 (h)) compared to the scattered behaviour of the test with static electrolyte (0 RPM) confirms the discussion made previously in 6.1.1, that the presence of the bubbles on the surface of the electrode, increases the mass transport overpotential.

To further analyse the morphology of the deposits at different conditions, the tomography data obtained from scanning the area of the interest are processed, and the reconstructed data for the experiments at low current density of 10 mA/cm^2 and 100 mA/cm^2 under static and dynamic flow conditions are presented in Figure 6-9 and Figure 6-10 respectively.

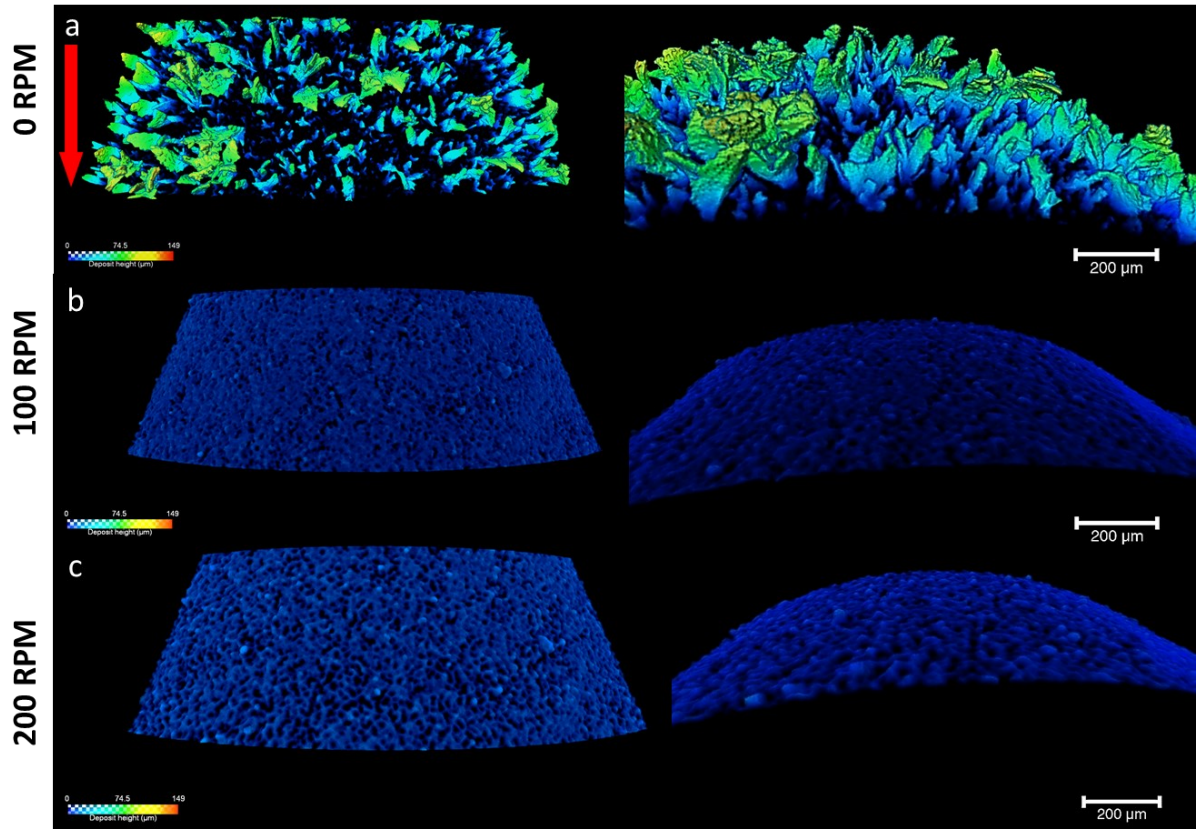

Figure 6-10: Reconstructed 3D images of zinc deposit morphologies on carbon electrode at a constant current density of 100 mA/cm2 under (a) static electrolyte flow and (b) dynamic flow with flow velocity of 1.05 cm/s and (c) linear flow velocity of 2.11 cm/s

Although the radiography images presented in Figure 6-8 (a-c) for deposition at 10 mA/cm^2 were not conclusive to identify the impact of flow on the morphology of the deposits, by reconstructing the tomography images presented in Figure 6-9, a transition from boulder deposition in static electrolyte to mossy and compact deposition in dynamic flow conditions is observed. Wang et al. reported similar morphology and found that electrodeposition of Zn at a very low constant current density (CDR<0.2) yields a highly porous and mossy deposit [138]. It is noteworthy that due to the imaging resolution limitation of the instrument and the large reliance on geometric magnification in laboratory X-ray imaging instruments, resolving any porous zinc deposition was extremely challenging.

Reconstructed data of the experiments at the higher current density (100 mA/cm^2), presented in Figure 6-10, exhibits a transition from dendritic formation in a static electrolyte to a compact deposition in the presence of a dynamic flow. This change in the morphology and suppression of the dendritic growth is indicative that reduction reactions under dynamic flows with Reynold's numbers of 179.77 and 357.84 are purely charge transfer limited.

Analysing the reconstructed 3D tomography of the deposits at different conditions has made it possible to obtain microstructural information corresponding to the formation of the deposits under different electrodeposition conditions. Figure 6-11 presents the mean deposit height across the surface of the electrode at different operating conditions. Electrodeposition at a constant current density of 10 mA/cm^2 and dynamic electrolyte with flow velocity of 2.11 cm/s exhibited a uniform and compact growth, and as it was seen in the reconstructed 3D tomography images in Figure 6-9 (b), deposition at lower flow velocity (1.05 cm/s) demonstrated a mossy growth which resulted in a deposition morphology with nonuniform mean deposit height.

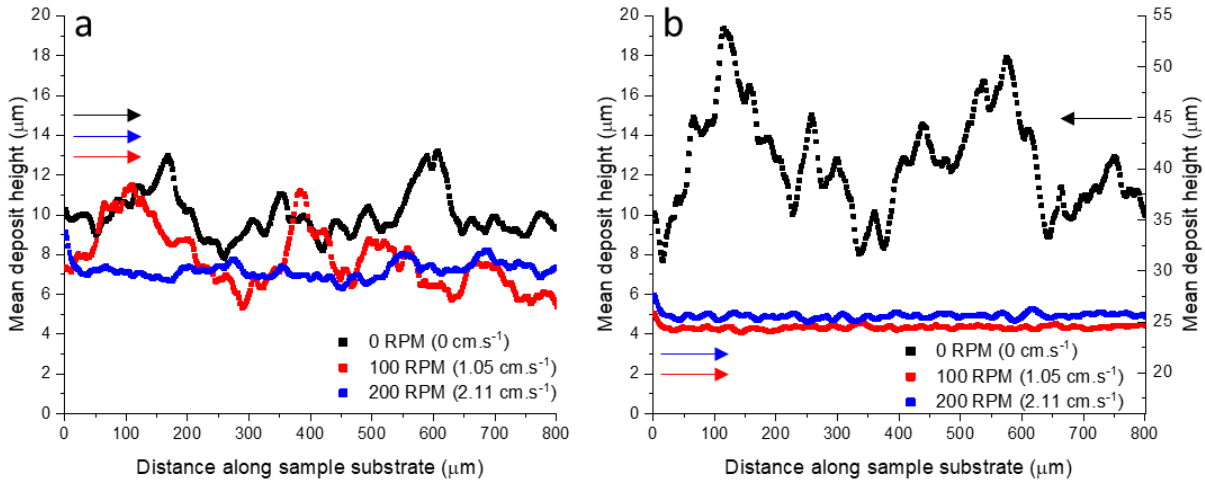

Figure 6-11: Mean deposit height of electrodeposition under static and dynamic electrolyte at constant current densities of a) 10 mA/cm^2 and b) 100 mA/cm^2

Further analysing the morphology of the electrochemical reduction of zinc at the higher current density (100 mA/cm^2) under dynamic flow, exhibits a compact growth of Zn on the surface of the electrode. According to the ratios between effective current density of 100 mA/cm^2 and limiting current densities calculated in Section 6.1.2 and presented in Table 6-3, at CDR close to 1 compact growth was expected. The compact and uniform depositions obtained from the experiments at flow velocities of 1.05 cm/s and 2.11 cm/s are in agreement with the reported literature [164].

Comparison of the quantified parameters of the deposited structures at a constant current density of 10 mA/cm^2, presented in Table 6-5, exhibits a decrease in the volume specific area for the deposits under dynamic flow compared to electrodeposition under static electrolyte. This is an indication of changes in the microstructure and size of the deposition, where Zn deposition with a linear flow

velocity of 1.05 cm/s has resulted in larger deposits and a lower surface area. While deposition at a higher velocity resulted in a compact deposit with more uniform Zn deposit grain sizes, demonstrated by the 3D topographies in Figure 6-9 (c), which yielded a lower surface area.

In addition, analysing the 3D structures for the depositions at a current density of 100 mA/cm^2 shows a decrease in volume specific area with flowing electrolyte compared to the deposition in a static electrolyte. As it was illustrated previously (Figure 6-10) Zn deposition in a dynamic flow condition resulted in supressing the dendritic growth of the deposits, hence in a compact morphology surface area of the Zn deposits is lower.

Table 6-5: Quantified volume specific area and mass of the deposited zinc for deposition at constant current densities of 10 mA/cm2 and 100 mA/cm2 under different flow conditions

Current Density	No.	Flow Velocity	Surface Area	Volume	Volume Specific Area	Density	Mass of Zn
mA/cm^2		cm/s	$\mu m^2 \times 10^6$	$\mu m^3 \times 10^6$	$\mu m^2/\mu m^3$	g/mL	μg
10	1	0	6.88	52.66	0.13	7.14	0.38
	2	1.05	3.41	58.9	0.06	7.14	0.42
	3	2.11	4.95	59.0	0.08	7.14	0.42
100	4	0	8.99	56.07	0.16	7.14	0.40
	5	1.05	3.04	37.26	0.08	7.14	0.26
	6	2.11	3.01	40.71	0.07	7.14	0.29

All the deposits were carried out to achieve an areal capacity of 5 mAh/cm^2, hence it is important to investigate the 35.0% and 27.5% reduction in the mass of deposited Zn for experiments at a constant current density of 100 mA/cm^2 with flow velocities of 1.05 cm/s and 2.11 cm/s respectively:

Microstructure of the deposits: the difference in the calculated mass of the deposits at 10 mA/cm^2 (under static and dynamic conditions) and 100 mA/cm^2 (under static electrolyte) compared to the experiments at 100 mA/cm^2 can be attributed to the low achievable imaging resolution with the laboratory X-ray instrument, which limited the ability to resolve the highly porous deposits. Hence, any porous or mossy structures of the deposits would insufficiently resolve and be reconstructed as a solid part of the deposits, resulting in a higher apparent total volume for depositions at 10 mA/cm^2 and 100 mA/cm^2 in a static electrolyte.

Location of deposits: as highlighted in Section 6.1.2, due to the large sizes of image volume data, a region of interest along the conical tip of the carbon composite rod was selected, therefore it is possible that the location of deposits on the surface of the carbon electrode is affected by the conditions in which electrodeposition is carried out.

6.1.2.3 Effect of Duty Cycle on the Morphology of the Electrodeposition

Another method to control the deposition structure and tailor the morphology to suit the application of Zn-RFBs is by controlling the frequency of electrodeposition. In this section, the effect of duty cycle on the structure of the deposits was tested by visual observation of zinc reduction and deposition on the surface of the electrode at three different duty cycles of 20%, 50% and 80%.

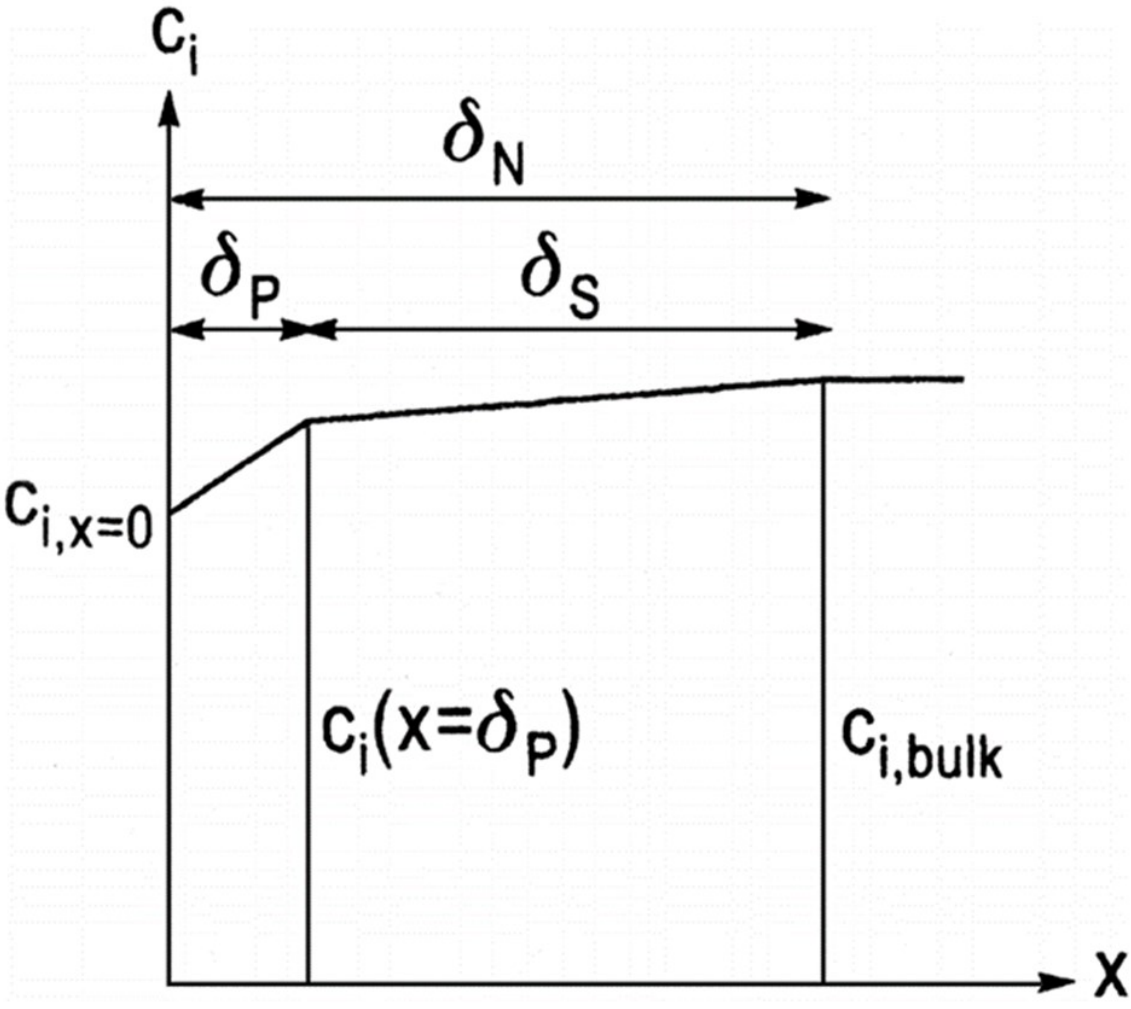

Figure 6-12: Concentration profile of the reactant at the surface of electrode during a pulse deposition [150]

One important impact of pulse electrodeposition is the modification of the diffusion layer. The Nernst diffusion layer was explained in Figure 2-16 (Section 2.4.4.2), whereas in pulse deposition the diffusion layer splits into two layers. In pulsating reduction of Zn on the working electrode, the concentration of the zincate active spices pulsates with the frequency of the pulsating current [150]. A schematic of Nernst diffusion layer model based on the pulse plating deposition is illustrated in Figure 6-12, where δ_N is the width of the Nernst diffusion Layer, δ_P refers to the thickness of the pulse diffusion layer and δ_S is the thickness of the stationary diffusion layer [150,225].

The thickness of the pulse diffusion layer (δ_P) changes as a function of the period of the pulsation, where at a shorter pulse, the thickness of the pulse diffusion layer (δ_P) becomes very small. This will result in a higher concentration profile of the active species on the surface of the electrode compared to a longer pulse period (deposition time). Consequently, higher concentration of the reactant at the surface of the electrode will result in a lower mass transport polarisation. Effective potential responses of the electrodeposition at a constant current density of 100 mA/cm^2 with duty cycles of 20%, 50% and 80% at static and dynamic flows are presented in Figure 6-13, and it is observed that the magnitude of the overpotential decreases with shorter pulses.

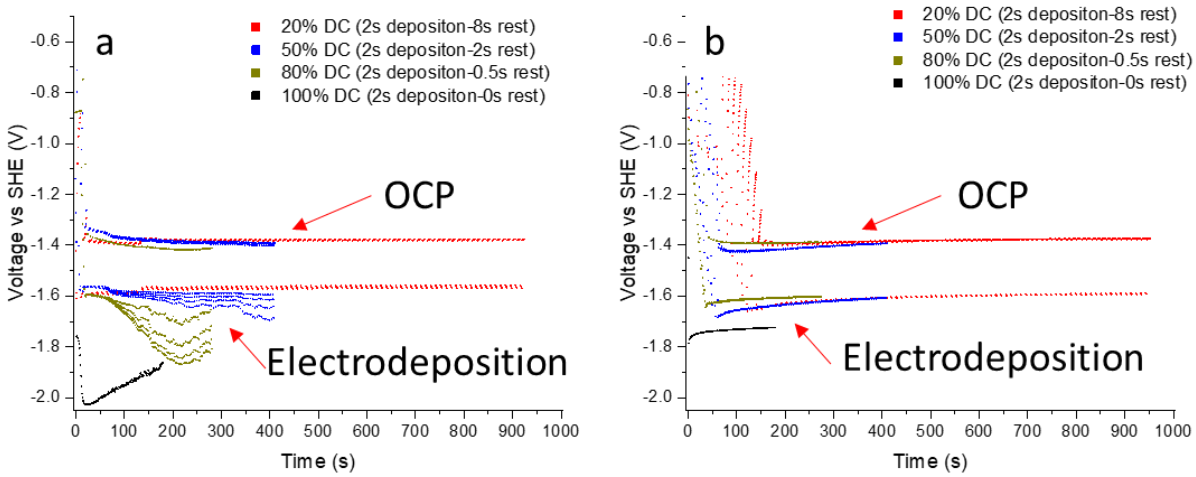

Figure 6-13: Chronopotentiometry curves of zinc electrodeposition at 100 mA/cm^2 with different duty cycles at a) static electrolyte and b) dynamic flow with linear velocity of 2.11 cm/s

Reconstructed XCT images, obtained from sets of experiments on the effect of duty cycle on the morphology of the electrodeposition in the static electrolyte, are presented in Figure 6-14. These 3D images exhibit a transition from dendritic growth at a constant current density of 100 mA/cm^2 (Figure 6-14 (a)) and duty cycle of 80% (Figure 6-14 (b)) to a compact formation of the Zn deposits at 50% and 20% duty cycles (Figure 6-14 (c)-(d)) in the static electrolyte.

The changes in the morphology of the deposition at different duty cycles are a result of the difference in the concentration of the Zn on the surface of the electrode, while deposition is occurring. The difference in the concentration of the active species on the surface of the electrode depends on the ratio of the deposit time and the rest time, where an increase in the rest time allows a higher concentration of Zn active species to migrate from the bulk electrolyte to the Nernst diffusion layer. Hence, increase in the rest time in the duty cycle, increases the concentration of the zincate at the electrode surface. Therefore, there is a transition from diffusion-controlled growth, which results in a

dendrite formation, to a charge transfer-controlled deposition, resulting in a compact formation of the deposits.

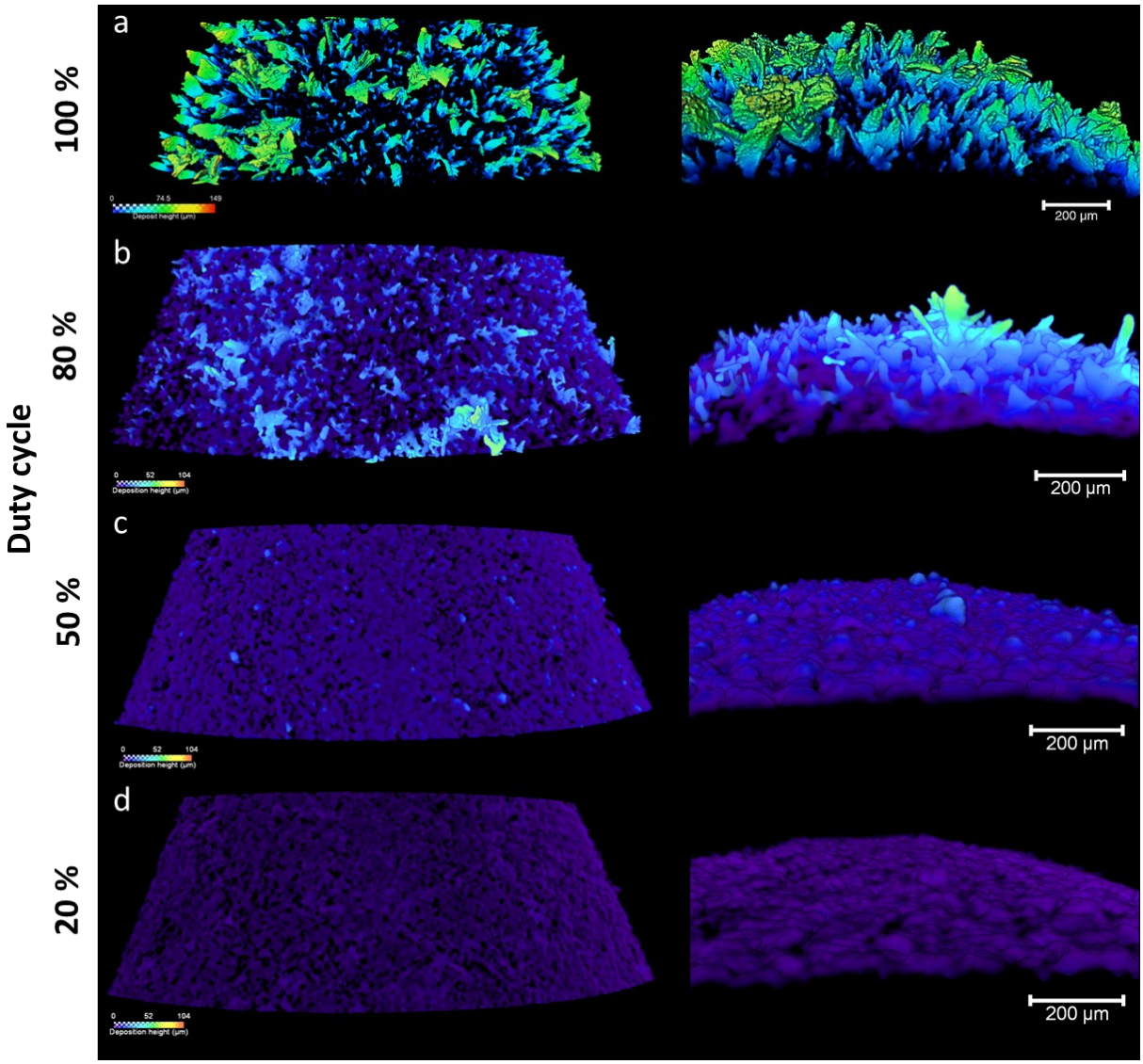

Figure 6-14: Reconstructed 3D images of zinc deposit morphologies on carbon electrode at a constant current density of 100 mA/cm2 in a static electrolyte (a) without pulsating, (b) 2s deposition and 0.5 seconds rest (80% duty cycle) (c) 2s deposition and 2 seconds rest (50% duty cycle) and (d) 2s deposition and 8 seconds rest (20% duty cycle).

Analysis of the 3D reconstructed morphology, illustrated in Figure 6-15, demonstrates the change in the thickness of the deposits as a function of duty cycle. The quantified analysis exhibits a 60.80%, 93.16% and 97.68% reduction in the difference of maximum and minimum deposit thickness of the pulsed depositis at duty cycles of 80%, 50% and 20%, compared to electrodeposition at a constant current density. There are two different mechanisms causing the transition from dendritic growth to compact formation of the deposits by increasing the wait time (decreasing duty cycle): firstly, increase in the rest period between pulses enables the transport of the active species from the bulk electrolyte

to the surface of the electrode, and results in higher surface nucleation rate on the electrode surface. Secondly, an increase in the off-load period (rest time) results in decrease in the reduction overpotential of the electrodeposition, thus formation of the hydrogen bubbles on the surface of the electrode (resulted by HER), which contributes to the dendritic growth of deposits by blocking the electrode surface area, is reduced.

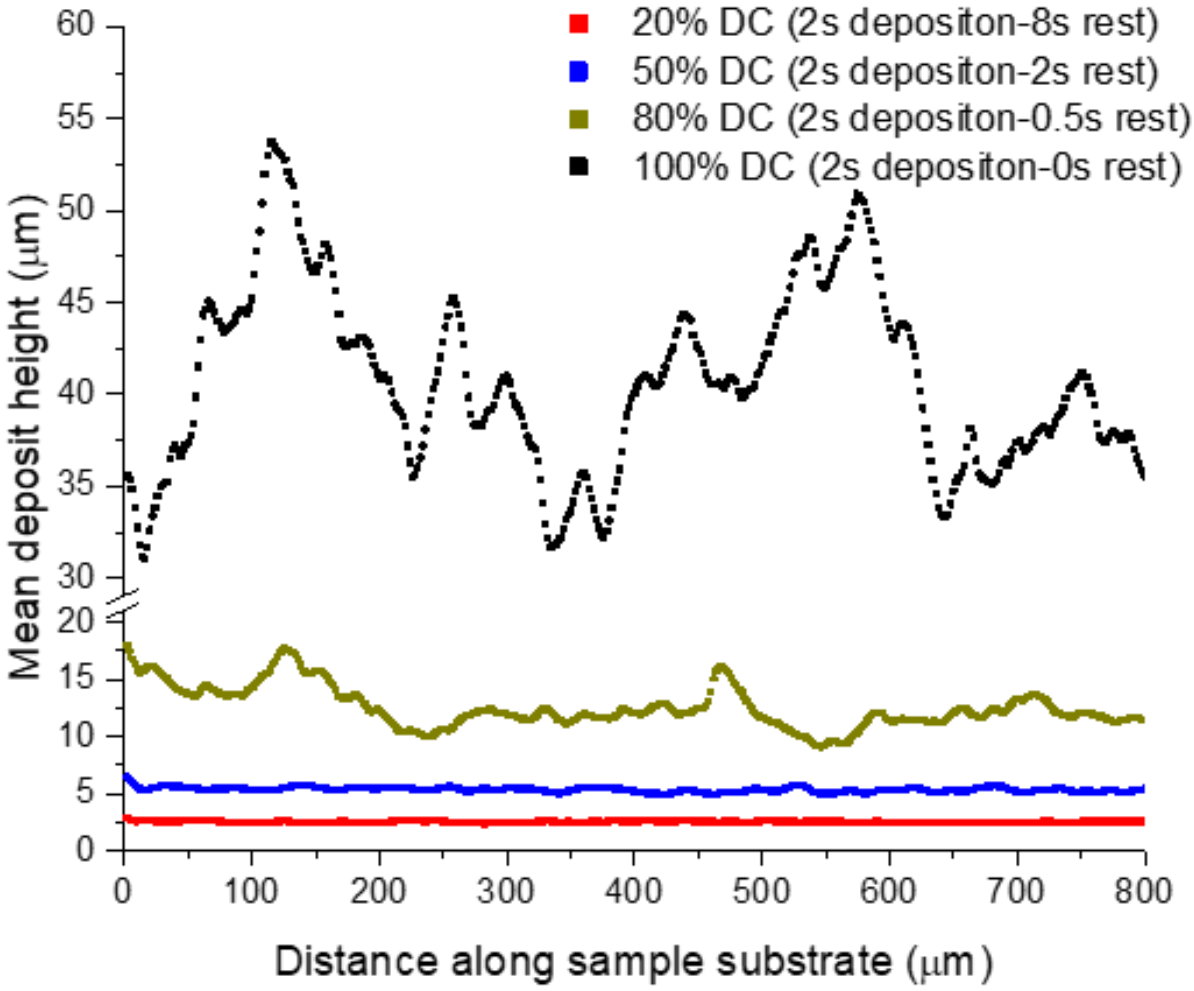

Figure 6-15: Thickness of the Zn deposits across the electrode for electrodeposition at 100 mA/cm^2 in a static electrolyte at different duty cycles

Quantitative analysis of the reconstructed structures illustrates an increase in the volume specific area as the duty cycle increases from 20% to 100% (constant current electrodeposition with no rest period). However, as discussed previously, quantified analysis of the microstructures is significantly limited by the low achievable resolution of the XCT device used to scan the samples. Therefore, difference in the evaluated deposited mass, from the reconstructed volume of the deposits, may reflect the fact that any internal porosity of the deposits may not be properly captured in the tomography images, giving an apparently higher mass of deposit.

Table 6-6: Quantified volume specific area and mass of the deposited zinc for the electrodepositions at a constant current density of 100 mA/cm2 with different duty cycles

Flow Rate	No.	Duty Cycle	Surface Area	Volume	Volume Specific Area	Density	Mass of Zn
cm/s		%	$\mu m^2 \times 10^6$	$\mu m^3 \times 10^6$	$\mu m^2/\mu m^3$	g/mL	μg
0 (0 RPM)	1	20	4.10	41.0	0.10	7.14	0.29
	2	50	3.64	42.0	0.09	7.14	0.30
	3	80	6.04	39.3	0.15	7.14	0.28
	4	100	8.99	56.07	0.16	7.14	0.40

6.1.3 Summary

In this work, a novel three-electrode electrochemical cell was presented, which for the first time allowed the use of X-ray radiography and computed tomography to study the morphological evolution of zinc deposits under different electrodeposition conditions. With this bespoke cell, it was possible to perform operando visualisation of the zinc electrodeposition process which occur in zinc secondary batteries, and perform non-destructive three-dimensional characterisation of the microstructure of zinc deposits formed under different cell operating conditions.

Using this cell, the effect of current density on the morphology of the Zn deposits was studied at current densities of 10 mA/cm^2 and 100 mA/cm^2. Deposition at a higher current density yielded a dendritic growth, which caused by the concentration overpotential, where the evolution of hydrogen bubbles on the surface of the electrode contributed to the growth of dendrite. Presence of hydrogen bubbles on the surface of the working electrode resulted in a reduction of the surface area of the working electrode, which became preferential for Zn to deposit on the primary deposits.

To investigate the effect of flowing electrolyte on the morphology, Zn electrodeposition was carried out under two different flow rates at two different current densities. It was found that at a constant current density of 10 mA/cm^2 (lower than the estimated limiting current density), increasing the linear velocity of the electrolyte resulted in a transition from compact deposition to a mossy deposition. Also, deposition at a constant current density of 100 mA/cm^2 under dynamic flow exhibited a compact growth compared to the dendritic growth obtained at a similar current density under static electrolyte, which was accompanied by reducing the formation of the hydrogen bubbles on the surface of the electrode.

Another strategy to improve the morphology of Zn deposition by suppressing the dendritic growth was tested using pulsed electrodeposition. In this set of experiments, electrodeposition with duty cycles of 20%, 50% and 80% were performed, and it was observed that by decreasing the duty cycle, more uniform and compact morphology was achievable.

Chapter 7 Conclusion and Future Work

7.1 Summary and Conclusion

Cost effective grid-scale energy storage technologies are increasingly in demand for renewable energy applications. Redox Flow Batteries (RFBs) are promising solutions to store the energy generated from renewable sources, and different RFB technologies can be deployed based on their storage capacities. This thesis focused on developing and investigating low-cost flow batteries for energy storage applications. The first part of this research project investigated and considered the performance of the novel Regenerative Hydrogen Manganese Fuel Cell (RHMnFC). The second part presented a novel method which enabled both qualitative and quantitative characterisation of the Zinc (Zn) electrodeposition in Zn-RFBs.

7.1.1 Investigation of Regenerative Hydrogen/Manganese Fuel Cell (RHMnFC)

The first phase of this work focused on the development of an innovative RHMnFC technology for energy storage applications. Typically in Mn-RFBs as the concentration of the Mn^{3+} increases during charging process, and stability of the electrolyte reduces due to the spontaneous disproportionation reaction of Mn^{3+}. Hence, it was demonstrated that the presence of Ti^{4+} additives in the electrolyte suppressed the disproportionation reaction of Mn^{3+}, resulting in a reproducible and stable charge and discharge cycles, and a new method to prepare the electrolyte was presented. Further studies to investigate the performance of different materials as the Membrane Electrode Assembly (MEA) were carried out. Polarisation and power density curves of two different hydrogen electrodes with Pt loadings of 0.4 mg_{pt}/cm^2 and 0.03 mg_{pt}/cm^2 demonstrated that at low current density, the performance of the system is not affected by the Pt loading on the catalyst layer. It was also presented that the highest performance was achievable by using a graphite felt as the liquid half-cell electrode, where an energy efficiency of 77% was obtained from the charge and discharge cycles at a constant current density of 100 mA/cm^2. From the experiments on two different membranes, it was found that the cell with Nafion® 117 provided a more stable performance compared to Nafion 212, where the decay in the achievable capacity was attributed to the crossover of the electrolyte.

The performance of the RHMnFC under different current densities was also studies and presented as a part of the technology development, and it was concluded that high theoretical capacity utilisation of 97.67% was achievable at charge and discharge current densities up to 100 mA/cm^2. Furthermore, the necessity of a conditioning step prior to normal charge and discharge cycle was highlighted, where it was shown that the diffusion limitation caused by the size of the Mn-Ti complex in the fresh electrolyte otherwise resulted in 40% lower achievable capacity.

The feasibility of scale up of the RHMnFC from a lab scale of 5 cm^2 to a large 150 cm^2 scale was investigated. The experiments on the designed 150 cm^2 cell showed that an energy efficiency of 76% was achievable from the cycles at a constant current density of 85 mA/cm^2 from the experiments on the large cell. Lower pressure drops in the large cell, compared to the 5 cm^2 cell,which results in lower convection of the electrolyte to the active media, was identified to be one of the determining mechanisms resulted in a lower performance of the cell, compared to the performance obtained from the experiments in smaller cell. Finally, the LCOS of the RHMnFC with 4 hours storage capacity was estimated and the cost advantage of this system, with 28% reduction in LCOS, compared conventional RFBs such as all-vanadium RFBs was demonstrated.

7.1.2 Regeneration of Manganese-Titanium Electrolyte

Although consistent performance was demonstrated for the RHMnFC, and the presence of titanium in the electrolyte successfully suppressed the disproportionation reaction of the Mn^{3+}, further investigation was required to understand the mechanisms in which disproportionation led to the precipitation of the Mn electrolyte. Chapter 5 of this thesis focused on studying the mechanisms, which affect the stability of the electrolyte in practical systems. Firstly, the stability of the electrolyte for the cycles with different rest periods between charge and discharge half-cycles was studied and it was found that the coulombic efficiency of the cell reduces, as the waiting period increases above 10 hours, resulting in the precipitation of MnO_2 in the system. Further analysis on the stability of the electrolyte using ICP-MS demonstrated that the rate of the precipitation reaction increases as a function of temperature, where the data obtained from this set of experiments were compared to the data from the kinetic model to estimate the Mn^{3+} disproportionation at different temperature over range of times.

In this thesis, for the first time an electrochemical method to regenerate the degraded system caused by the precipitation of the MnO_2 in the cell and the electrolyte was demonstrated. This method involves electrochemical reduction of the existing Ti^{4+} in the electrolyte to Ti^{3+}, which dissolves the precipitated MnO_2 in the system back into the electrolyte. The practicality of this method was demonstrated by overcharging the electrolyte at 1.8 V and producing MnO_2, where the degraded cell or electrolyte was recovered by discharging the cell at a constant potential of 0.1, and it was seen that after this procedure the normal performance of the cell was recovered.

Finally, the impact of the cell temperature on the performance of the cell was evaluated at 30 °C, and was compared to the performance of the cell at room temperature (20 °C). Although there was an improvement in the energy efficiency of the cell during the initial cycles, degradation in the electrolyte capacity and overall cell performance was recorded across a longer number of cycles. This was related

to the presence and precipitation of the TiO_2 on the hydrogen electrode, caused by the crossover of the electrolyte from liquid the half-cell to the hydrogen half-cell. This phenomenon resulted in blockage of the flow channels on the hydrogen half-cell, which hindered the gas transport to and from the electrode while discharging and charging the cell.

Studies on the performance of the RHMnFC, scale up, cost model and developing a sustainable method to regenerate the degraded electrolyte demonstrates the feasibility of this electrochemical system for energy storage applications. However, further studies are required to successfully transient from a research and development stage to a grid-scale commercial system.

7.1.3 In-Situ Visualisation and Quantification of Electrodeposit Morphology Under Dynamic Conditions in Zinc Secondary Batteries

In the second phase of this work, a novel three-electrode electrochemical cell was presented, that allowed the use of X-ray radiography and X-ray CT to study the morphological evolution of zinc deposits under static and dynamic electrolyte condition. The novel bespoke cell enabled a detailed assessment of the processes governing the evolution and morphology of Zn deposits across the electrode. 2D and 3D microstructure analysis of the electrodeposition at constant current densities of 10 mA/cm^2 and 100 mA/cm^2 under static and dynamic flow was demonstrated and key structural parameters, namely volume specific area and distribution in the thickness of the deposition across the electrode surface, were quantified and presented.

Observations of the evolution of Zn deposits in the static electrolyte on the surface of the electrode at the current density above limiting current density showed that dendritic growth is accompanied by evolution of hydrogen bubbles on surface of the electrode, resulted by the diffusion-controlled growth of the Zn electrodeposits. This phenomenon decreases the surface area onto which zincate can deposit, thus secondary deposits develop on the existing Zn deposits.

The investigation on the effect of dynamic flow on zinc morphology showed that by introducing a flowing electrolyte, which increases the local limiting current density, it was possible to suppress the dendritic growth of zinc deposits. These experiments demonstrated a transition from dendritic morphology to a compact deposition for electrodeposition at a current density of 100 mA/cm^2. Further studies to investigate the strategies to suppress the dendritic growth of deposits were carried out by electroplating the zinc deposits at different duty cycles. It was concluded that an increase in the rest period between pulsated deposition cycles, resulted in more uniform and compact deposition of zinc on the electrode. Therefore, the novel electrochemical cell designed and tested in this phase of the project demonstrated a suitable and reliable apparatus for a direct 3D microstructural analysis of the electrochemical reactions of the Zn-based RFBs.

7.2 Future Work

This work investigated the innovative RHMnFC and explored the feasibility of this device for energy storage applications. Although, the initial studies of this technology showed promising performance, there are scientific gaps that must be fulfilled to optimise and improve its performance. In the second phase of the project the novel three-electrode cell was demonstrated which enables investigation of the methods through which performance of the zinc-RFBs can be improved. In addition, optimising the current design according to the reactions which occur in RHMnFC will make it possible to use this technique to study the electrochemical reactions in this system.

7.2.1 Regenerative Hydrogen Manganese Fuel Cell

Future work on this novel system can be separated into three different categories: Firstly, the electrochemical properties of the system must be studied to optimise the performance of the cell, secondly mechanical challenges must be identified to produce a stack and scale up the system, and finally, the chemistry of the electrolyte, specifically interaction of Ti^{4+} additives with Mn^{3+}, must better understood.

7.2.1.1 Electrochemical Properties of The System

In this thesis, the performance of the RHMnFC was evaluated based on the charge and discharge cycles obtained from different components in the cell. Although, a reliable and promising performance was demonstrated in the initial investigations, this system can be optimised by understanding the underlying electrochemical properties of each individual component, contributing to the overall performance of the cell. To decouple the processes occurring within the anode and cathode half-cells, the reference electrode setup (schematic presented in Figure 7-1) [226], previously developed and tested to study the electrochemical processes in a Regenerative Hydrogen Vanadium Fuel Cell (RHVFC), can be used.

In Chapter 4 and 5 hypothesises were made to explain the losses affecting the performance. This system would allow us to better understand and decouple these processes which contribute to the irreversible losses in the system by measuring the independent voltage of each half-cells separately. identifying the limiting processes in of each half-cell will minimise the losses by optimising the components and achieve a higher overall performance. In addition, Rotating disc electrode experiment can be conducted to study the electrochemical properties of the manganese reaction, such as the diffusion coefficient and limiting current density as a function of Reynold's number, which will provide the necessary information to optimise the system and the flow rate of the anolyte and catholyte in the cell.

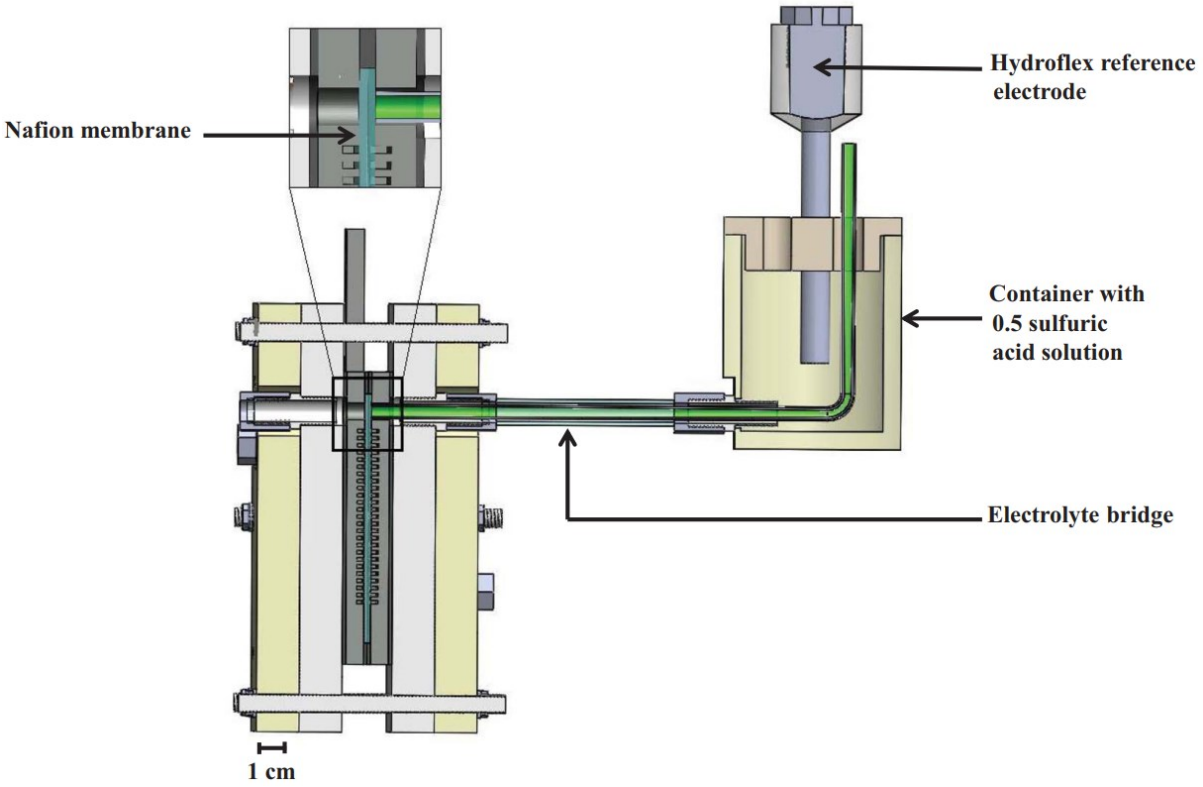

Figure 7-1: Schematic of the assembled RHVFC with the integration of the reference electrode set-up (Designed by the author for H. Dewage's PhD project) [226]

7.2.1.2 Electrolyte Properties:

Based on the initial investigation on this novel RFB technology, the most important gaps identified in this work relate to the chemistry of the electrolyte in which Ti additives supress the disproportionation reaction of the Mn^{3+} active species in the electrolyte. Characterising techniques must be used to study the stability of the electrolyte and mechanisms which facilite the precipitation of the MnO_2 in the system. A three-electrode cell, similar to the setup demonstrated in Chapter 6, could be designed and developed to qualitatively and quantitively characterise the processes through which precipitation of MnO_2 occurs. X-ray radiography with the aid of synchrotron X-ray sources would enable these processes to be monitored in real-time and identify their relationship to the potential at which the cell operates.

In addition, Chapter 5 demonstrated a novel regeneration method which enabled the dissolution of the precipitated MnO_2 in the electrolyte. According to the current response at different flow rates, while operating the cell at 0.1 V to reduce the existing Ti^{4+} to Ti^{3+}, the rate of reaction between Ti^{3+} and MnO_2 was assumed to be the rate limiting reaction. Hence, to investigate this phenomenon, Ultraviolet–visible spectroscopy (UV-VIS) can be used to monitor the change in the concentration of Ti^{3+} in the electrolyte, resulting in the reaction of the Ti^{3+} and MnO_2 which produces Ti^{4+} and Mn^{2+}, over different period of times.

7.2.1.3 Mechanical properties and Scaling up the system:

In Chapter 4 of this thesis, an attempt to investigate the feasibility of designing and developing a cell with larger active area was made and the drop in the performance of the cell, compared to the performance obtained from the cell with 5 cm^2 area, was related to the design of the cell. According to the model presented in Chapter 4, the lower pressure-drop in 150 cm^2 cell, compared to the smaller cell, was identified as the main mechanism affecting the lower performance of the cell (related to the lower convection of the electrolyte to the electrodes). Therefore, in order to use the model to optimise the design of the cell, it must initially be validated by a set of experiments.

Firstly, a set of pressure sensors can be used in-line with the flow of the electrolyte to measure the difference in the electrolyte pressure at the inlet and outlet of the cell, and use the data obtained from these measurements to validate the model. Secondly, a change in the viscosity as a function of state of charge of the electrolyte was observed during charge and discharge cycles of the RHMnFC. Hence, a method must be developed which enables the viscosity of the electrolyte to be measured as a function of the changes in the states of charge in the cell. The suggested method consists of a tube with defined geometry and two pressure sensors at the inlet and outlet of the tube, which measures the pressure drop between these two points and allows the dynamic viscosity of the electrolyte to be measured.

7.2.2 In-Situ Three-Electrode Cell

The novel cell designed and tested in Chapter 6 of this thesis accomplished the objective of the study as a method which enables the real-time evolution and formation of the zinc deposits under different conditions to be monitored. Although it was difficult to distinctly resolve individual electrodeposit structures from the radiography experiments (due to the spatial resolution and X-ray beam flux limitations of laboratory-based XCT imaging), with the aid of higher spatial and temporal X-ray image resolution achievable at synchrotron light sources, this in-situ flow cell design can facilitate measurements of the additional microstructural behaviour such as tracking of dendrite growth in 3D under flowing conditions, and determination of critical size of deposits.

Calculating the error in the quantification of the zinc deposit volumes is not trivial - the main source of error would be from the image resolution rather the automated image segmentation method applied, as the threshold-based segmentation algorithm is pixel-based and works by examining the greyscale of finite pixels and their neighbours based on their greyscale value. The experiment was carried out at the limit of the resolution limit of the laboratory XCT instrument setup, i.e. it was not possible to get any better image resolution of the zinc deposit features in the reconstructed 3D images generated from the instrument.

Obtaining an estimated error would require imaging the same deposit sample(s)/regions of interest at multiple length scales/increasing higher resolutions and performing quantitative analysis of the resulting images to not only validate the quantified parameters in the relatively lower resolution image collected, but also to see at what resolution does the quantification error become negligible.

Additionally, increasing the number of experiments for various conditions such as the current density and the flow rate during the electrochemical deposition of the zinc, will enable the mapping of changes in the evolution and morphology of the deposition as a function of these variables. This system also allows the effect of additives on the evolution and morphology of the electrodeposition to be studied, which researchers have introduced as an effective method to suppress the dendritic growth of the zinc deposits.

Dissemination

Publications:

1. B. Chakrabarti, V. Yufit, **Ashkan Kavei**, Y. Xia, G. Stevenson, E. Kalamaras, H. Luo, J. Feng, F. Tariq, O. O. Taiwo, M. Titirici, N. P. Brandon, "Charge/Discharge and Cycling Performance of Flexible Carbon Paper Electrodes In a Regenerative Hydrogen/Vanadium Fuel Cell", International Journal of Hydrogen Energy, vol. 44, no.57, pp. 3009-30107, 2019 (DOI: 10.1016/j.ijhydene.2019.09.151)
2. J. Rubio-Garcia, **A. Kavei**, A. Kucernak, V. Yufit, N. P. Brandon "In-Situ Electrochemical Regeneration of Manganese Electrolyte" In Preparation
3. **A. Kavei**, J. Rubio-Garcia, A. Kucernak, V. Yufit, N. P. Brandon, "Investigation of Regenerative Hydrogen-Manganese Fuel Cell for Energy Storage Applications", In Preparation
4. **A. Kavei,** O. O. Taiwo, V. Yufit, F. Tariq, X. Li, N. P. Brandon "In-situ Visualisation and Quantification of Electrodeposit Morphology Under Dynamic Conditions in Zinc Secondary Batteries, In Preparation

Talks and Posters Conference Participations:

1. Vanadium-Hydrogen Flow Battery for Energy Storage Applications - A Feasibility Study, UK Energy Storage Conference, Bath, UK, 2015
2. Development of a Segmented Fuel Cell-Supercapacitor Passive Hybrid System, H2SuperGen, Belfast, UK, 2016
3. Development of a Segmented Fuel Cell-Supercapacitor Passive Hybrid System, CDT Annual Meeting, University of Nottingham, Nottingham, United Kingdom, 2016
4. Hybrid Fuel Cell-Supercapacitor system for Automotive Applications, Fuel Cell Hydrogen Conference, Birmingham, UK, 2016
5. Electric vehicle Showcase, Fuel Cell Hydrogen Conference, Birmingham, UK, 2017
6. Development and Characterisation of Advanced Energy Storage Devices for Stationary Applications, International Flow Battery Forum, Lyon, France, 2019 (Prize Winner for "Best Pitch" presentation)

References

1. BP. *BP Statistical Review of World Energy 2019|68th Edition*. *BP World Energy* vol. 68 https://www.bp.com/content/dam/bp/business-sites/en/global/corporate/pdfs/energy-economics/statistical-review/bp-stats-review-2019-full-report.pdf (2019).

2. Newell, R. G., Raimi, D. & Aldana, G. Global Energy Outlook 2019 : The Next Generation of Energy. (2019).

3. Andoni, M. *et al.* Blockchain technology in the energy sector: A systematic review of challenges and opportunities. *Renew. Sustain. Energy Rev.* **100**, 143–174 (2019).

4. OECD/IEA. International Comparison of Light-duty Vehicle Fuel Economy 2005-2015 Ten years of fuel economy benchmarking. *Int. Energy Agency* (2017).

5. BP Energy. BP Energy Outlook 2019. *BP Energy Outlook 2019* 73 (2019).

6. IEA. *World Energy Outlook 2019*. (2019).

7. Diehl, A. Why is Energy Storage Such an Important Part of the Renewables Mix. https://www.civicsolar.com/article/why-energy-storage-such-important-part-renewables-mix (2015).

8. Few, S., Schmidt, O. & Gambhir, A. Electrical energy storage for mitigating climate change. *Gratham Institute, Imp. Coll. Sci.* 24 (2016).

9. International Energy Agency. Energy Storage in the UK: An Overview. (2014).

10. Luo, X., Wang, J., Dooner, M. & Clarke, J. Overview of current development in electrical energy storage technologies and the application potential in power system operation. *Appl. Energy* **137**, 511–536 (2015).

11. Singh, A. *Talking Renewables: A renewable energy primer for everyone*. (IOP Publishing, 2018). doi:10.1088/978-1-6817-4901-3.

12. Nikolaidis, P. & Poullikkas, A. Cost metrics of electrical energy storage technologies in potential power system operations. *Sustain. Energy Technol. Assessments* **25**, 43–59 (2018).

13. Arenas, L. F., Ponce de León, C. & Walsh, F. C. Redox flow batteries for energy storage: their promise, achievements and challenges. *Curr. Opin. Electrochem.* **16**, 117–126 (2019).

14. Krivik, P. & Bac, P. Electrochemical Energy Storage. in *Energy Storage - Technologies and Applications* (InTech, 2013). doi:10.5772/52222.

15. Alotto, P., Guarnieri, M. & Moro, F. Redox flow batteries for the storage of renewable energy: A review. *Renew. Sustain. Energy Rev.* **29**, 325–335 (2014).

16. Rubio-Garcia, J. *et al.* Hydrogen/manganese hybrid redox flow battery. *J. Phys. Energy* **1**, 015006 (2018).

17. U.S. Department of Energy. ARPA-E Duration Addition to Electricity Storage (DAYS) Technical Overview Document. 1–17 (2018).

18. Skyllas-Kazacos, M., Chakrabarti, M. H., Hajimolana, S. A., Mjalli, F. S. & Saleem, M. Progress in Flow Battery Research and Development. *J. Electrochem. Soc.* **158**, R55 (2011).

19. Thaller, L. H. Electrically Rechargeable Redox Flow Cell. (1986).

20. Divya, K. C. & Østergaard, J. Battery energy storage technology for power systems-An overview. *Electr. Power Syst. Res.* **79**, 511–520 (2009).

21. Skyllas-Kazacos, Maria, Robins, R. All-vanadium Redox Battery. (1986).

22. Leung, P. *et al.* Progress in redox flow batteries, remaining challenges and their applications in energy storage. *RSC Adv.* **2**, 10125–10156 (2012).

23. Chen, R., Kim, S. & Chang, Z. Redox Flow Batteries: Fundamentals and Applications. in *Redox - Principles and Advanced Applications* (InTech, 2017). doi:10.5772/intechopen.68752.

24. Bartolozzi, M. Development of redox flow batteries. A historical bibliography. *J. Power Sources* **27**, 219–234 (1989).

25. Zhang, L. *et al.* Study of zinc electrodes for single flow zinc/nickel battery application. *J. Power Sources* **179**, 381–387 (2008).

26. Ulaganathan, M. *et al.* Recent Advancements in All-Vanadium Redox Flow Batteries. *Adv. Mater. Interfaces* **3**, 1500309 (2016).

27. Parasuraman, A., Lim, T. M., Menictas, C. & Skyllas-Kazacos, M. Review of material research and development for vanadium redox flow battery applications. *Electrochim. Acta* **101**, 27–40 (2013).

28. Rychcik, M. & Skyllas-Kazacos, M. Characteristics of a new all-vanadium redox flow battery. *J. Power Sources* **22**, 59–67 (1988).

29. Bryans, D., Amstutz, V., Girault, H. & Berlouis, L. Characterisation of a 200 kW/400 kWh Vanadium Redox Flow Battery. *Batteries* **4**, 54 (2018).

30. Yang, Z. *et al.* Electrochemical Energy Storage for Green Grid. *Chem. Rev.* **111**, 3577–3613 (2011).

31. Joerissen, L., Garche, J., Fabjan, C. & Tomazic, G. Possible use of vanadium redox-flow batteries for energy storage in small grids and stand-alone photovoltaic systems. *J. Power Sources* **127**, 98–104 (2004).

32. Skyllas-Kazacos, M., Kazacos, G., Poon, G. & Verseema, H. Recent advances with UNSW vanadium-based redox flow batteries. *Int. J. Energy Res.* **34**, 182–189 (2010).

33. Skyllas-Kazacos, M. Novel vanadium chloride/polyhalide redox flow battery. *J. Power Sources* **124**, 299–302 (2003).

34. Kimura, N. *et al.* Membrane potential across anion-exchange membranes in acidic solution system. *J. Colloid Interface Sci.* **286**, 288–293 (2005).

35. Linden, D. & Reddy, T. B. *Handbook of Batteries*. (2002).

36. Bass, K., Mitchell, P. J., Wilcox, G. D. & Smith, J. Methods for the reduction of shape change and dendritic growth in zinc-based secondary cells. *J. Power Sources* **35**, 333–351 (1991).

37. Cheng, J. *et al.* Preliminary study of single flow zinc-nickel battery. *Electrochem. commun.* **9**, 2639–2642 (2007).

38. Ulaganathan, M. *et al.* Recent Advancements in All-Vanadium Redox Flow Batteries. *Adv. Mater. Interfaces* **3**, (2016).

39. Yufit, V., Hale, B., Matian, M., Mazur, P. & Brandon, N. P. Development of a Regenerative Hydrogen-Vanadium Fuel Cell for Energy Storage Applications. *J. Electrochem. Soc.* **160**, A856–A861 (2013).

40. Tucker, M. C., Weiss, A. & Weber, A. Z. Improvement and analysis of the hydrogen-cerium redox flow cell. *J. Power Sources* **327**, 591–598 (2016).

41. GLASS, W. & BOYLE, G. H. Performance of Hydrogen-Bromine Fuel Cells. in 203–220 (1969). doi:10.1021/ba-1965-0047.ch015.

42. Braff, W. A., Bazant, M. Z. & Buie, C. R. Membrane-less hydrogen bromine flow battery. *Nat. Commun.* **4**, 2346 (2013).

43. Cho, K. T., Tucker, M. C. & Weber, A. Z. A Review of Hydrogen/Halogen Flow Cells. *Energy Technol.* **4**, 655–678 (2016).

44. Jorne, J., Kim, J. T. & Kralik, D. The zinc-chlorine battery: half-cell overpotential measurements. *J. Appl. Electrochem.* **9**, 573–579 (1979).

45. Hagedorn, N. H. NASA Redox Storage System Development Project. Final report. (1984).

46. Ma, X., Zhang, H., Sun, C., Zou, Y. & Zhang, T. An optimal strategy of electrolyte flow rate for vanadium redox flow battery. *J. Power Sources* **203**, 153–158 (2012).

47. Wang, W. *et al.* A new redox flow battery using Fe/V redox couples in chloride supporting electrolyte. *Energy Environ. Sci.* **4**, 4068 (2011).

48. Xue, F.-Q., Wang, Y.-L., Wang, W.-H. & Wang, X.-D. Investigation on the electrode process of the Mn(II)/Mn(III) couple in redox flow battery. *Electrochim. Acta* **53**, 6636–6642 (2008).

49. Fang, B. A study of the Ce(III)/Ce(IV) redox couple for redox flow battery application. *Electrochim. Acta* **47**, 3971–3976 (2002).

50. Zhou, H., Zhang, H., Zhao, P. & Yi, B. A comparative study of carbon felt and activated carbon based electrodes for sodium polysulfide/bromine redox flow battery. *Electrochim. Acta* **51**, 6304–6312 (2006).

51. Lim, H. S. Zinc-Bromine Secondary Battery. *J. Electrochem. Soc.* **124**, 1154 (1977).

52. Ulaganathan, M., Suresh, S., Mariyappan, K., Periasamy, P. & Pitchai, R. New Zinc–Vanadium (Zn–V) Hybrid Redox Flow Battery: High-Voltage and Energy-Efficient Advanced Energy Storage System. *ACS Sustain. Chem. Eng.* **7**, 6053–6060 (2019).

53. Pan, J. *et al.* Preliminary study of alkaline single flowing Zn–O2 battery. *Electrochem. commun.* **11**, 2191–2194 (2009).

54. Hosseiny, S. S., Saakes, M. & Wessling, M. A polyelectrolyte membrane-based vanadium/air redox flow battery. *Electrochem. commun.* **13**, 751–754 (2011).

55. Cho, K. T. *et al.* High Performance Hydrogen/Bromine Redox Flow Battery for Grid-Scale Energy Storage. *J. Electrochem. Soc.* **159**, A1806–A1815 (2012).

56. Kreutzer, H., Yarlagadda, V. & Van Nguyen, T. Performance Evaluation of a Regenerative Hydrogen-Bromine Fuel Cell. *J. Electrochem. Soc.* **159**, F331–F337 (2012).

57. Anderson, D. L. *Theory of the Earth*. (1989).

58. O'Conner, B. An Introduction to Redflow. in (2019).

59. McGregor Scott. redT energy. 2–4.

60. Buschmann, H. Schmid Energy Systems Gmbh. in (2019).

61. Shibata, T. Performance evaluation of 60MWh vanadium flow battery system over three years of operation. in 1–14 (2019).

62. Akhil, A. A. *et al. DOE/EPRI Electricity Storage Handbook in Collaboration with NRECA*. http://www.osti.gov/servlets/purl/1431469/ (2016) doi:10.2172/1431469.

63. Zhang, M., Moore, M., Watson, J. S., Zawodzinski, T. A. & Counce, R. M. Capital Cost Sensitivity Analysis of an All-Vanadium Redox-Flow Battery. *J. Electrochem. Soc.* **159**, A1183–A1188 (2012).

64. Xu, Q. *et al.* Evaluation of redox flow batteries goes beyond round-trip efficiency: A technical review. *J. Energy Storage* **16**, 108–115 (2018).

65. Kosek, J. A. & Laconti, A. B. Advanced hydrogen electrode for a hydrogen-bromine battery. *J. Power Sources* **22**, 293–300 (1988).

66. Singh, V., Kim, S., Kang, J. & Byon, H. R. Aqueous organic redox flow batteries. *Nano Res.* **12**, 1988–2001 (2019).

67. Zhao, Y., Wang, L. & Byon, H. R. High-performance rechargeable lithium-iodine batteries using triiodide/iodide redox couples in an aqueous cathode. *Nat. Commun.* **4**, 1896 (2013).

68. Hu, B., DeBruler, C., Rhodes, Z. & Liu, T. L. Long-Cycling Aqueous Organic Redox Flow Battery (AORFB) toward Sustainable and Safe Energy Storage. *J. Am. Chem. Soc.* **139**, 1207–1214 (2017).

69. Winsberg, J., Hagemann, T., Janoschka, T., Hager, M. D. & Schubert, U. S. Redox-Flow Batteries: From Metals to Organic Redox-Active Materials. *Angew. Chemie Int. Ed.* **56**, 686–711 (2017).

70. Kowalski, J. A., Su, L., Milshtein, J. D. & Brushett, F. R. Recent advances in molecular engineering of redox active organic molecules for nonaqueous flow batteries. *Curr. Opin. Chem. Eng.* **13**, 45–52 (2016).

71. Chen, Q., Eisenach, L. & Aziz, M. J. Cycling Analysis of a Quinone-Bromide Redox Flow Battery. *J. Electrochem. Soc.* **163**, A5057–A5063 (2016).

72. Huskinson, B. *et al.* A metal-free organic–inorganic aqueous flow battery. *Nature* **505**, 195–198 (2014).

73. Li, Z. *et al.* Electrochemical Properties of an All-Organic Redox Flow Battery Using 2,2,6,6-

Tetramethyl-1-Piperidinyloxy and N-Methylphthalimide. *Electrochem. Solid-State Lett.* **14**, A171 (2011).

74. Dmello, R., Milshtein, J. D., Brushett, F. R. & Smith, K. C. Cost-driven materials selection criteria for redox flow battery electrolytes. *J. Power Sources* **330**, 261–272 (2016).

75. Agar, E., Knehr, K. W., Chen, D., Hickner, M. A. & Kumbur, E. C. Species transport mechanisms governing capacity loss in vanadium flow batteries: Comparing Nafion® and sulfonated Radel membranes. *Electrochim. Acta* **98**, 66–74 (2013).

76. Dong, Y.-R., Kaku, H., Hanafusa, K., Moriuchi, K. & Shigematsu, T. A Novel Titanium/Manganese Redox Flow Battery. *ECS Trans.* **69**, 59–67 (2015).

77. Tokuda, K., Iihara, J., Saito, Y., Masuno, A. & Inoue, H. Structural analysis of sulfuric acid solutions containing Ti and Mn using x-ray diffraction, x-ray absorption fine structure, and molecular dynamics simulation. *J. Chem. Phys.* **149**, 014503 (2018).

78. Davies, G. Some aspects of the chemistry of manganese(III) in aqueous solution. *Coord. Chem. Rev.* **4**, 199–224 (1969).

79. Belcher, R. & West, T. S. Trivalent manganese as an oxidimetric reagent. *Anal. Chim. Acta* **6**, 322–332 (1952).

80. Kaku, H., Dong, Y.-R., Hanafusa, K., Moriuchi, K. & Shigematsu, T. Effect of Ti(IV) Ion on Mn(III) Stability in Ti/Mn Electrolyte for Redox Flow Battery. *ECS Trans.* **72**, 1–9 (2016).

81. Tan, A., Rubio-Garcia, J. & Kucernak, A. A Study of the Mn/Ti Electrolyte Used in Redox Flow Batteries. (Imperial College London, 2018).

82. Chen, W. *et al.* A manganese–hydrogen battery with potential for grid-scale energy storage. *Nat. Energy* **3**, 428–435 (2018).

83. Zhang, Q., Dong, Q.-F., Zheng, M.-S. & Tian, Z.-W. Electrochemical Energy Storage Device for Electric Vehicles. *J. Electrochem. Soc.* **158**, A443 (2011).

84. Kersey, J., Sprengel, M., Babbitt, G. & Johnson, T. Hybrid Power Generation for Improved Fuel Efficiency and Performance. 1–10.

85. Qu, D. Y., Bai, L., Castledine, C. G., Conway, B. E. & Adams, W. A. Spectro-electrochemical studies on production and role of soluble Mn(III) species in discharge and recharge of various MnO2 cathode materials. *J. Electroanal. Chem.* **365**, 247–259 (1994).

86. Godunov, E. B., Izotov, A. D. & Gorichev, I. G. Dissolution of Manganese Oxides of Various Compositions in Sulfuric Acid Solutions Studied by Kinetic Methods. *Inorg. Mater.* **54**, 66–71 (2018).

87. Chandra, S. *Comprehensive Inorganic Chemistry Vol. Ii*. (New Age International (P) Limited, 2006).

88. Martin, S. Precipitation and Dissolution of Iron and Manganese Oxides. in *Environmental Catalysis* 61–82 (CRC Press, 2005). doi:10.1201/9781420027679.ch3.

89. Sun, W., Kitchaev, D. A., Kramer, D. & Ceder, G. Non-equilibrium crystallization pathways of manganese oxides in aqueous solution. *Nat. Commun.* **10**, 573 (2019).

90. Perez-Benito, J. F. Reduction of Colloidal Manganese Dioxide by Manganese(II). *J. Colloid Interface Sci.* **248**, 130–135 (2002).

91. Park, S., Lee, H. J., Lee, H. & Kim, H. Development of a Redox Flow Battery with Multiple Redox Couples at Both Positive and Negative Electrolytes for High Energy Density. *J. Electrochem. Soc.* **165**, A3215–A3220 (2018).

92. Marković, N. M., Schmidt, T. J., Stamenković, V. & Ross, P. N. Oxygen Reduction Reaction on Pt and Pt Bimetallic Surfaces: A Selective Review. *Fuel Cells* **1**, 105–116 (2001).

93. Mayrhofer, K. J. J. *et al.* Measurement of oxygen reduction activities via the rotating disc electrode method: From Pt model surfaces to carbon-supported high surface area catalysts. *Electrochim. Acta* **53**, 3181–3188 (2008).

94. Durst, J., Simon, C., Hasché, F. & Gasteiger, H. A. Hydrogen Oxidation and Evolution Reaction Kinetics on Carbon Supported Pt, Ir, Rh, and Pd Electrocatalysts in Acidic Media. *J. Electrochem. Soc.* **162**, F190–F203 (2015).

95. Neyerlin, K. C., Gu, W., Jorne, J. & Gasteiger, H. A. Study of the Exchange Current Density for the Hydrogen Oxidation and Evolution Reactions. *J. Electrochem. Soc.* **154**, B631 (2007).

96. Ishigami, Y. *et al.* Corrosion of carbon supports at cathode during hydrogen/air replacement at anode studied by visualization of oxygen partial pressures in a PEFC—Start-up/shut-down simulation. *J. Power Sources* **196**, 3003–3008 (2011).

97. Liu, J. & Hou, Z. Carbon Corrosion in Polymer Electrolyte Membrane Fuel Cell Catalysts and its Mitigation Strategies. in *Eco- and Renewable Energy Materials* 53–72 (Springer Berlin Heidelberg, 2013). doi:10.1007/978-3-642-33497-9_3.

98. Davies, T. & Tummino, J. High-Performance Vanadium Redox Flow Batteries with Graphite Felt Electrodes. *C* **4**, 8 (2018).

99. Bhattarai, A. *et al.* Advanced porous electrodes with flow channels for vanadium redox flow battery. *J. Power Sources* **341**, 83–90 (2017).

100. Oh, K., Won, S. & Ju, H. Numerical study of the effects of carbon felt electrode compression in all-vanadium redox flow batteries. *Electrochim. Acta* **181**, 13–23 (2015).

101. Park, S. K. *et al.* The influence of compressed carbon felt electrodes on the performance of a vanadium redox flow battery. *Electrochim. Acta* **116**, 447–452 (2014).

102. Ghimire, P. C. *et al.* A comprehensive study of electrode compression effects in all vanadium redox flow batteries including locally resolved measurements. *Appl. Energy* **230**, 974–982 (2018).

103. Brown, L. D. *et al.* The effect of felt compression on the performance and pressure drop of all-vanadium redox flow batteries. *J. Energy Storage* **8**, 91–98 (2016).

104. Tsai, B.-T. *et al.* Effects of flow field design on the performance of a PEM fuel cell with metal foam as the flow distributor. *Int. J. Hydrogen Energy* **37**, 13060–13066 (2012).

105. Aaron, D. S. *et al.* Dramatic performance gains in vanadium redox flow batteries through modified cell architecture. *J. Power Sources* **206**, 450–453 (2012).

106. Sun, B. & Skyllas-Kazacos, M. Modification of graphite electrode materials for vanadium redox flow battery application—I. Thermal treatment. *Electrochim. Acta* **37**, 1253–1260 (1992).

107. Dixon, D. *et al.* Effect of oxygen plasma treatment on the electrochemical performance of the rayon and polyacrylonitrile based carbon felt for the vanadium redox flow battery application. *J. Power Sources* **332**, 240–248 (2016).

108. Prifti, H., Parasuraman, A., Winardi, S., Lim, T. M. & Skyllas-Kazacos, M. Membranes for Redox Flow Battery Applications. *Membranes (Basel).* **2**, 275–306 (2012).

109. Shi, Y. *et al.* Recent development of membrane for vanadium redox flow battery applications: A review. *Appl. Energy* **238**, 202–224 (2019).

110. Smitha, B., Sridhar, S. & Khan, A. A. Solid polymer electrolyte membranes for fuel cell applications—a review. *J. Memb. Sci.* **259**, 10–26 (2005).

111. Arora, P. & Zhang, Z. (John). Battery Separators. *Chem. Rev.* **104**, 4419–4462 (2004).

112. Kim, Y. S. & Pivovar, B. S. Polymer Electrolyte Membranes for Direct Methanol Fuel Cells. in 187–234 (2007). doi:10.1016/S1752-301X(07)80009-3.

113. Junoh, H. *et al.* A Review on the Fabrication of Electrospun Polymer Electrolyte Membrane for Direct Methanol Fuel Cell. *J. Nanomater.* **2015**, 1–16 (2015).

114. Xi, J. *et al.* Self-assembled polyelectrolyte multilayer modified Nafion membrane with suppressed vanadium ion crossover for vanadium redox flow batteries. *J. Mater. Chem.* **18**, 1232 (2008).

115. Zuo, Z., Fu, Y. & Manthiram, A. Novel Blend Membranes Based on Acid-Base Interactions for Fuel Cells. *Polymers (Basel).* **4**, 1627–1644 (2012).

116. Jiang, B., Wu, L., Yu, L., Qiu, X. & Xi, J. A comparative study of Nafion series membranes for vanadium redox flow batteries. *J. Memb. Sci.* **510**, 18–26 (2016).

117. Jeong, S., Kim, L.-H., Kwon, Y. & Kim, S. Effect of nafion membrane thickness on performance of vanadium redox flow battery. *Korean J. Chem. Eng.* **31**, 2081–2087 (2014).

118. Xi, J., Dai, W. & Yu, L. Polydopamine coated SPEEK membrane for a vanadium redox flow battery. *RSC Adv.* **5**, 33400–33406 (2015).

119. Dai, W. *et al.* Sulfonated Poly(Ether Ether Ketone)/Graphene composite membrane for vanadium redox flow battery. *Electrochim. Acta* **132**, 200–207 (2014).

120. Choi, S.-W. *et al.* Hydrocarbon membranes with high selectivity and enhanced stability for vanadium redox flow battery applications: Comparative study with sulfonated poly(ether sulfone)s and sulfonated poly(thioether ether sulfone)s. *Electrochim. Acta* **259**, 427–439 (2018).

121. Gundlapalli, R., Kumar, S. & Jayanti, S. Stack Design Considerations for Vanadium Redox Flow Battery. *Ina. Lett.* **3**, 149–157 (2018).

122. Harting, K., Kunz, U. & Turek, T. Zinc-air Batteries: Prospects and Challenges for Future Improvement. *Zeitschrift für Phys. Chemie* **226**, 151–166 (2012).

123. Pei, P., Wang, K. & Ma, Z. Technologies for extending zinc–air battery's cyclelife: A review. *Appl. Energy* **128**, 315–324 (2014).

124. Yufit, V. *et al.* Operando Visualization and Multi-scale Tomography Studies of Dendrite Formation and Dissolution in Zinc Batteries. *Joule* 1–18 (2018) doi:10.1016/j.joule.2018.11.002.

125. Bockris, J. O., Nagy, Z. & Drazic, D. On the Morphology of Zinc Electrodeposition from Alkaline Solutions. *J. Electrochem. Soc.* **120**, 30 (1973).

126. Cachet, C. The Behavior of Zinc Electrode in Alkaline Electrolytes. *J. Electrochem. Soc.* **138**, 678 (1991).

127. Despić, A. R., Jovanović, D. & Rakić, T. Kinetics and mechanism of deposition of zinc from zincate in concentrated alkali hydroxide solutions. *Electrochim. Acta* **21**, 63–77 (1976).

128. Bockris, J. O., Nagy, Z. & Damjanovic, A. On the Deposition and Dissolution of Zinc in Alkaline Solutions. *J. Electrochem. Soc.* **119**, 285 (1972).

129. Yi, J. *et al.* Challenges, mitigation strategies and perspectives in development of zinc-electrode materials and fabrication for rechargeable zinc–air batteries. *Energy Environ. Sci.* **11**, 3075–3095 (2018).

130. Khor, A. *et al.* Review of zinc-based hybrid flow batteries: From fundamentals to applications. *Mater. Today Energy* **8**, 80–108 (2018).

131. Fleischmann, M., Hill, I. R. & Sundholm, G. A Raman spectroscopic study of thiourea adsorbed on silver and copper electrodes. *J. Electroanal. Chem. Interfacial Electrochem.* **157**, 359–368 (1983).

132. Li, X., Ponce de Léon, C., Walsh, F. C., Wills, R. G. A. & Pletcher, D. Zinc-based flow batteries for medium- and large-scale energy storage. in *Advances in Batteries for Medium and Large-Scale Energy Storage* 293–315 (Elsevier, 2015). doi:10.1016/B978-1-78242-013-2.00008-X.

133. Gong, K., Fang, Q., Gu, S., Li, S. F. Y. & Yan, Y. Nonaqueous redox-flow batteries: organic solvents, supporting electrolytes, and redox pairs. *Energy Environ. Sci.* **8**, 3515–3530 (2015).

134. Weber, A. Z. *et al.* Redox flow batteries: a review. *J. Appl. Electrochem.* **41**, 1137–1164 (2011).

135. Ponce de León, C., Frías-Ferrer, A., González-García, J., Szánto, D. A. & Walsh, F. C. Redox flow cells for energy conversion. *J. Power Sources* **160**, 716–732 (2006).

136. Shin, S.-H., Yun, S.-H. & Moon, S.-H. A review of current developments in non-aqueous redox flow batteries: characterization of their membranes for design perspective. *RSC Adv.* **3**, 9095 (2013).

137. Hu, J., Ding, J., Du, Z., Duan, H. & Yang, S. Zinc anode with artificial solid electrolyte interface for dendrite-free Ni-Zn secondary battery. *J. Colloid Interface Sci.* **555**, 174–179 (2019).

138. Wang, R. Y., Kirk, D. W. & Zhang, G. X. Effects of Deposition Conditions on the Morphology of Zinc Deposits from Alkaline Zincate Solutions. *J. Electrochem. Soc.* **153**, C357 (2006).

139. R. Mainar, A. *et al.* Alkaline aqueous electrolytes for secondary zinc-air batteries: an overview. *Int. J. Energy Res.* **40**, 1032–1049 (2016).

140. Fordyce, J. S. & Baum, R. L. Vibrational Spectra of Solutions of Zinc Oxide in Potassium Hydroxide. *J. Chem. Phys.* **43**, 843–846 (1965).

141. Newman, G. H. & Blomgren, G. E. NMR Study of Complex Ions in the Aqueous ZnO–KOH System. *J. Chem. Phys.* **43**, 2744–2747 (1965).

142. Pereira, M. S., Barbosa, L. L., Souza, C. A. C., de Moraes, A. C. M. & Carlos, I. . . The influence of sorbitol on zinc film deposition, zinc dissolution process and morphology of deposits obtained from alkaline bath. *J. Appl. Electrochem.* **36**, 727–732 (2006).

143. Trejo, G. Nucleation and Growth of Zinc from Chloride Concentrated Solutions. *J. Electrochem. Soc.* **145**, 4090 (1998).

144. Leung, P. K., Ponce-de-León, C., Recio, F. J., Herrasti, P. & Walsh, F. C. Corrosion of the zinc negative electrode of zinc–cerium hybrid redox flow batteries in methanesulfonic acid. *J. Appl. Electrochem.* **44**, 1025–1035 (2014).

145. Budevski, E., Staikov, G. & Lorenz, W. J. Electrocrystallization: Nucleation and growth phenomena. *Electrochim. Acta* **45**, 2559–2574 (2000).

146. Walsh, F. C. & Herron, M. E. Electrocrystallization and electrochemical control of crystal growth: fundamental considerations and electrodeposition of metals. *J. Phys. D. Appl. Phys.* **24**, 217–225 (1991).

147. Thanh, N. T. K., Maclean, N. & Mahiddine, S. Mechanisms of Nucleation and Growth of Nanoparticles in Solution. *Chem. Rev.* **114**, 7610–7630 (2014).

148. Wranglén, G. Dendrites and growth layers in the electrocrystallization of metals. *Electrochim. Acta* **2**, 130–143 (1960).

149. Ertl, G. Pattern formation at electrode surfaces. *Electrochim. Acta* **43**, 2743–2750 (1998).

150. Schlesinger, M. & Paunovic, M. *Modern Electroplating*. (John Wiley & Sons, Inc., 2010). doi:10.1002/9780470602638.

151. Wang, K. *et al.* Dendrite growth in the recharging process of zinc–air batteries. *J. Mater. Chem.*

A **3**, 22648–22655 (2015).

152. Iwakura, C., Murakami, H., Nohara, S., Furukawa, N. & Inoue, H. Charge–discharge characteristics of nickel/zinc battery with polymer hydrogel electrolyte. *J. Power Sources* **152**, 291–294 (2005).

153. Leistner, K. *et al.* Role of Hydrogen Evolution during Epitaxial Electrodeposition of Fe on GaAs. *J. Electrochem. Soc.* **165**, H3076–H3079 (2018).

154. Trudgeon, D. P. Study and Development of the Zinc Electrode for the Alkaline Zinc-Nickel Redox Flow Battery. (2019).

155. Dundálek, J. *et al.* Zinc electrodeposition from flowing alkaline zincate solutions: Role of hydrogen evolution reaction. *J. Power Sources* **372**, 221–226 (2017).

156. Li, Y. & Dai, H. Recent advances in zinc–air batteries. *Chem. Soc. Rev.* **43**, 5257–5275 (2014).

157. Grier, D., Ben-Jacob, E., Clarke, R. & Sander, L. M. Morphology and Microstructure in Electrochemical Deposition of Zinc. *Phys. Rev. Lett.* **56**, 1264–1267 (1986).

158. Ito, Y. *et al.* Zinc morphology in zinc–nickel flow assisted batteries and impact on performance. *J. Power Sources* **196**, 2340–2345 (2011).

159. Wang, K. *et al.* Morphology control of zinc regeneration for zinc–air fuel cell and battery. *J. Power Sources* **271**, 65–75 (2014).

160. Naybour, R. D. The Effect of Electrolyte Flow on the Morphology of Zinc Electrodeposited from Aqueous Alkaline Solution Containing Zincate Ions. *J. Electrochem. Soc.* **116**, 520 (1969).

161. Turney, D. E. *et al.* Rechargeable Zinc Alkaline Anodes for Long-Cycle Energy Storage. *Chem. Mater.* **29**, 4819–4832 (2017).

162. Moseley, P. T. & Jürgen, G. *Electrochemical Energy Storage for Renewable Sources and Grid Balancing*. (Elsevier, 2015). doi:10.1016/C2012-0-01253-7.

163. Chamoun, M. *et al.* Hyper-dendritic nanoporous zinc foam anodes. *NPG Asia Mater.* **7**, e178–e178 (2015).

164. Ito, Y., Wei, X., Desai, D., Steingart, D. & Banerjee, S. An indicator of zinc morphology transition in flowing alkaline electrolyte. *J. Power Sources* **211**, 119–128 (2012).

165. Yu, W. *et al.* Achieving a stable zinc electrode with ultralong cycle life by implementing a flowing electrolyte. *J. Power Sources* **453**, 227856 (2020).

166. Torrent-Burgués, J., Guaus, E. & Sanz, F. Initial stages of tin electrodeposition from sulfate baths in the presence of gluconate. *J. Appl. Electrochem.* **32**, 225–230 (2002).

167. Volmer, M. & Weber, A. Keimbildung in übersättigten Gebilden. *Zeitschrift für Phys. Chemie* **119U**, (1926).

168. McBreen, J. & Gannon, E. The electrochemistry of metal oxide additives in pasted zinc electrodes. *Electrochim. Acta* **26**, 1439–1446 (1981).

169. Trudgeon, D. P. *et al.* Screening of effective electrolyte additives for zinc-based redox flow battery systems. *J. Power Sources* **412**, 44–54 (2019).

170. Diggle, J. W. & Damjanovic, A. The Inhibition of the Dendritic Electrocrystallization of Zinc from Doped Alkaline Zincate Solutions. *J. Electrochem. Soc.* **119**, 1649 (1972).

171. Banik, S. J. & Akolkar, R. Suppressing Dendritic Growth during Alkaline Zinc Electrodeposition using Polyethylenimine Additive. *Electrochim. Acta* **179**, 475–481 (2015).

172. Popoola, P., Fayomi, O. S. I. & Popoola, O. Comparative Studies of Microstructural, Tribological and Corrosion Properties of Plated Zn and Zn-alloy Coatings. *Int. J. Electrochem. Sci.* **7**, (2012).

173. Wu, L., Ashworth, M. A. & Wilcox, G. D. Investigation of Whisker Growth from Alkaline Non-cyanide Zinc Electrodeposits. *J. Electron. Mater.* **46**, 1114–1127 (2017).

174. Gallaway, J. W. *et al.* An In Situ Synchrotron Study of Zinc Anode Planarization by a Bismuth Additive. *J. Electrochem. Soc.* **161**, A275–A284 (2014).

175. Biton, M., Tariq, F., Yufit, V., Chen, Z. & Brandon, N. Integrating multi-length scale high resolution 3D imaging and modelling in the characterisation and identification of mechanical failure sites in electrochemical dendrites. *Acta Mater.* **141**, 39–46 (2017).

176. Cai, B. *et al.* In situ synchrotron tomographic quantification of granular and intragranular deformation during semi-solid compression of an equiaxed dendritic Al–Cu alloy. *Acta Mater.* **76**, 371–380 (2014).

177. Cai, B. *et al.* 4D synchrotron X-ray tomographic quantification of the transition from cellular to dendrite growth during directional solidification. *Acta Mater.* **117**, 160–169 (2016).

178. Yang, M., Xiong, S.-M. & Guo, Z. Characterisation of the 3-D dendrite morphology of magnesium alloys using synchrotron X-ray tomography and 3-D phase-field modelling. *Acta Mater.* **92**, 8–17 (2015).

179. Terzi, S., Salvo, L., Suery, M. & Dahle, A. K. Coarsening mechanisms during isothermal holding of a dendritic Al-10wt%Cu alloy. *Trans. Indian Inst. Met.* **62**, 447–449 (2009).

180. Shuai, S. *et al.* Fast synchrotron X-ray tomographic quantification of dendrite evolution during the solidification of Mg Sn alloys. *Acta Mater.* **118**, 260–269 (2016).

181. Drummond, J. L., De Carlo, F. & Super, B. J. Three-dimensional tomography of composite fracture surfaces. *J. Biomed. Mater. Res. Part B Appl. Biomater.* **74B**, 669–675 (2005).

182. Ketcham, R. X-ray Computed Tomography (CT). https://serc.carleton.edu/research_education/geochemsheets/techniques/CT.html.

183. Taiwo, O. O. 3D and 4D Characterisation of Lithium Ion Battery Electrode Microstructures using X-ray Tomography. (University College of London, 2016).

184. Ketcham, R. A. & Carlson, W. D. Acquisition, optimization and interpretation of X-ray computed tomographic imagery: applications to the geosciences. *Comput. Geosci.* **27**, 381–400 (2001).

185. Perez, N. Kinetics of Activation Polarization. in *Electrochemistry and Corrosion Science* 101–150 (Springer International Publishing, 2016). doi:10.1007/978-3-319-24847-9_5.

186. Guidelli, R. *et al.* Defining the transfer coefficient in electrochemistry: An assessment (IUPAC Technical Report). *Pure Appl. Chem.* **86**, 245–258 (2014).

187. Mavrič, T. *et al.* Electrochemical Biosensor Based on TiO 2 Nanomaterials for Cancer Diagnostics. in 63–105 (2018). doi:10.1016/bs.abl.2017.12.003.

188. Orazem, M. E. & Tribollet, B. *Electrochemical Impedance Spectroscopy*. (John Wiley & Sons, Inc., 2008). doi:10.1002/9780470381588.

189. Lvovich, V. F. *Impedance Spectroscopy*. (John Wiley & Sons, Inc., 2012). doi:10.1002/9781118164075.

190. Fickett, A. P. Electrochemical systems, John S. Newman, Prentice-Hall, Inc., Englewood Cliffs, New Jersey(1973). 432 pages. *AIChE J.* **19**, 879–879 (1973).

191. Wu, B. Fuel Cell Hybrid Electric Vehicle Powertrain Modelling and Testing. (2014).

192. Lasia, A. Electrochemical Impedance Spectroscopy and its Applications. in *Modern Aspects of Electrochemistry* 143–248 (Kluwer Academic Publishers). doi:10.1007/0-306-46916-2_2.

193. Li, D. & Kucernak, A. Optimisation of the Performance in a Regenerative Hydrogen-Manganese Fuel cell. (2017).

194. Gandomi, Y. A. *et al.* Critical Review—Experimental Diagnostics and Material Characterization Techniques Used on Redox Flow Batteries. *J. Electrochem. Soc.* **165**, A970–A1010 (2018).

195. Xing, F., Zhang, H. & Ma, X. Shunt current loss of the vanadium redox flow battery. *J. Power Sources* **196**, 10753–10757 (2011).

196. Skyllas-Kazacos, M., McCann, J., Li, Y., Bao, J. & Tang, A. The Mechanism and Modelling of Shunt Current in the Vanadium Redox Flow Battery. *ChemistrySelect* **1**, 2249–2256 (2016).

197. Feldkamp, L., Davis, L. C. & Kress, J. Practical Cone-Beam Algorithm. *J. Opt. Soc. Am* **1**, 612–619 (1984).

198. Schindelin, J. *et al.* Fiji: an open-source platform for biological-image analysis. *Nat. Methods* **9**, 676–682 (2012).

199. Arenas, L. F., Ponce de León, C. & Walsh, F. C. Engineering aspects of the design, construction and performance of modular redox flow batteries for energy storage. *J. Energy Storage* **11**, 119–153 (2017).

200. Zhao, Y., Liu, L., Qiu, X. & Xi, J. Revealing sulfuric acid concentration impact on comprehensive performance of vanadium electrolytes and flow batteries. *Electrochim. Acta* **303**, 21–31 (2019).

201. Johnson, D. A. & Nelson, P. G. Improvements in Estimated Entropies and Related Thermodynamic Data for Aqueous Metal Ions. *Inorg. Chem.* **51**, 6116–6128 (2012).

202. Lee, J. A., Maskell, W. C. & Tye, F. L. The electrochemical reduction of manganese dioxide in acidic solutions. *J. Electroanal. Chem. Interfacial Electrochem.* **79**, 79–104 (1977).

203. Mansoor, M. A. *et al.* Photoelectrocatalytic activity of Mn2O3–TiO2 composite thin films engendered from a trinuclear molecular complex. *Int. J. Hydrogen Energy* **41**, 9267–9275 (2016).

204. Wei, Z. *et al.* Real-time monitoring of capacity loss for vanadium redox flow battery. *J. Power Sources* **390**, 261–269 (2018).

205. Wei, Z., Zhao, J., Skyllas-Kazacos, M. & Xiong, B. Dynamic thermal-hydraulic modeling and stack flow pattern analysis for all-vanadium redox flow battery. *J. Power Sources* **260**, 89–99 (2014).

206. Cengel, Y. & Ghajar, A. *Heat and Mass Transfer: Fundamentals and Applications*. (2014).

207. Baek, S. M., Jeon, D. H., Nam, J. H. & Kim, C.-J. Pressure drop and flow distribution characteristics of single and parallel serpentine flow fields for polymer electrolyte membrane

fuel cells. *J. Mech. Sci. Technol.* **26**, 2995–3006 (2012).

208. Singh, N. & McFarland, E. W. Levelized cost of energy and sensitivity analysis for the hydrogen–bromine flow battery. *J. Power Sources* **288**, 187–198 (2015).

209. IRENA. Costs and Markets to 2030. *Electr. Storage Renewables Costs Mark. to 2030, https//www.irena.org/publications/2017/Oct/Electricity-storage-and-renewables-costs-and-markets* (2017).

210. Zhang, L., Finch, J., Gontarz, G. & Wang, C. Development of Low Cost PEMFC Metal Bipolar Plate. in 955–961 (2010). doi:10.1149/1.3484589.

211. Minke, C. & Turek, T. Materials, system designs and modelling approaches in techno-economic assessment of all-vanadium redox flow batteries – A review. *J. Power Sources* **376**, 66–81 (2018).

212. Cho, K. T. *et al.* Optimization and Analysis of High-Power Hydrogen/Bromine-Flow Batteries for Grid-Scale Energy Storage. *Energy Technol.* **1**, 596–608 (2013).

213. Kear, G., Shah, A. A. & Walsh, F. C. Development of the all-vanadium redox flow battery for energy storage: A review of technological, Financial and policy aspects. *Int. J. Energy Res.* **36**, 1105–1120 (2012).

214. Xia, Y. Development and Characterisation of Anode Materials for Polysulphide-Air Redox Flow Battery. (2019).

215. Li, Z. *et al.* Air-Breathing Aqueous Sulfur Flow Battery for Ultralow-Cost Long-Duration Electrical Storage. *Joule* **1**, 306–327 (2017).

216. Tsagareli, G., Makhatadze, S., Soselia, M. & Maisuradze, N. Chemical and electrochemical behavior of manganese dioxide film in various solutions. *Dusunen Adam* **10**, 125–133 (2019).

217. Cosnett, I. R. & Kennedy, J. F. Environmental Chemistry a global perspective Gary W. Vanloon and Stephen J. Duffy Oxford University Press, Inc., New York, 2000, 492pp £23.99, ISBN 0-]-856440-6. *Bioseparation* **9**, 326–327 (2000).

218. Zhang, C., Zhao, T. S., Xu, Q., An, L. & Zhao, G. Effects of operating temperature on the performance of vanadium redox flow batteries. *Appl. Energy* **155**, 349–353 (2015).

219. Hixson, A. W. & Plechner, W. W. Hydrated Titanium Oxide. Thermal Precipitation from Titanium Sulfate Solutions. *Ind. Eng. Chem.* **25**, 262–274 (1933).

220. Wang, W. *et al.* Mechanism and kinetics of titanium hydrolysis in concentrated titanyl sulfate solution based on infrared and Raman spectra. *Chem. Eng. Sci.* **134**, 196–204 (2015).

221. Smith, T. J. & Stevenson, K. J. 4 - Reference Electrodes. in *Handbook of Electrochemistry* (ed. Zoski, C. G. B. T.-H. of E.) 73–110 (Elsevier, 2007). doi:https://doi.org/10.1016/B978-044451958-0.50005-7.

222. Shimizu, M., Hirahara, K. & Arai, S. Morphology control of zinc electrodeposition by surfactant addition for alkaline-based rechargeable batteries. *Phys. Chem. Chem. Phys.* **21**, 7045–7052 (2019).

223. Newman, J. & Thomas-Alyea, K. *Electrochemical Systems*. (2004).

224. Diggle, J. W., Despic, A. R. & Bockris, J. O. The Mechanism of the Dendritic Electrocrystallization of Zinc. *J. Electrochem. Soc.* **116**, 1503 (1969).

225. Ibl, N. Some theoretical aspects of pulse electrolysis. *Surf. Technol.* **10**, 81–104 (1980).

226. Dewage, H. H., Yufit, V. & Brandon, N. P. Study of Loss Mechanisms Using Half-Cell Measurements in a Regenerative Hydrogen Vanadium Fuel Cell. *J. Electrochem. Soc.* **163**, A5236–A5243 (2016).